Technical Report
TR-18-08
December 2019

Copper Sulfide Model (CSM)

Model improvements, sensitivity analyses, and results from the Integrated Sulfide Project inter-model comparison exercise

Fraser King
Miroslav Kolář

SVENSK KÄRNBRÄNSLEHANTERING AB

SWEDISH NUCLEAR FUEL
AND WASTE MANAGEMENT CO

Box 3091, SE-169 03 Solna
Phone +46 8 459 84 00
skb.se

SVENSK KÄRNBRÄNSLEHANTERING

ISSN 1404-0344
SKB TR-18-08
ID 1692666
December 2019

Copper Sulfide Model (CSM)

Model improvements, sensitivity analyses, and results from the Integrated Sulfide Project inter-model comparison exercise

Fraser King, Integrity Corrosion Consulting Ltd

Miroslav Kolář, LS Computing Ltd

Permission Figure 2-7a

Summary

The Copper Sulfide Model (CSM) was developed to predict the long-term evolution of the corrosion behaviour of copper canisters in a deep geological repository. The model is based on the coupling of the interfacial electrochemical reactions involved in the corrosion of the canister to processes occurring in the repository near- and far-fields. A key feature of the CSM is the incorporation of a mixed-potential model for the interfacial electrochemical reactions which allows the prediction of both the corrosion rate and the corrosion potential, an important parameter in corrosion science. In this way, the model is capable of predicting not only the long-term corrosion behaviour of the canister but also the evolution of the near-field corrosive environment as conditions evolve from warm and oxidising initially to cool and sulfide-dominated in the long term.

Since the model was first developed in 2007, there have been a number of improvements to the mechanistic understanding of the corrosion process in sulfide environments. This improved mechanistic information, as well as other additions to the code, have been incorporated in a number of updates to the original model. The code updates that address either improved mechanistic understanding or to correct earlier omissions from the code include: exclusion of the anaerobic dissolution of pyrite as a source of sulfide, updated stoichiometry for the oxidative dissolution of pyrite, updated kinetic expression for the microbial reduction of sulfate, inclusion of the chemical conversion of Cu_2O to Cu_2S, addition of the cathodic reduction of H_2O, and a correction to the treatment of the evolution of H_2 from the cathodic reduction of the proton in the HS^- ion. In addition to these relatively minor updates to the code, a second major improvement to the treatment of microbial sulfate reduction has been implemented involving the use of Monod kinetic expressions for both organotrophic and chemotrophic sulfate reduction pathways, as well as the possible limitation by the availability of organic carbon and/or sulfate (gypsum). A number of other changes have been made to the code to extend the range of application of the model. For example, the effect of gaseous H_2S in an unsaturated repository has been addressed in a version of the code. The effect of spatial separation of anodic and cathodic reactions and an alternative bentonite model based on a single inter-layer porosity treatment have also been implemented.

The mechanistic basis of these model improvements and the results of the various resulting versions of the code are described in some detail. With these various updates and improvements, the CSM is considered to satisfactorily predict the long-term corrosion behaviour of the canister and the evolution of the near-field corrosive environment. In addition to a best-estimate simulation of the expected behaviour in the repository, the results from the CSM have also been compared with those from two thermodynamically based reactive-transport models in an inter-model comparison exercise.

The results from the CSM simulations indicate that the extent of corrosion of copper canisters in a KBS-3 design repository will be limited. Based on the best-estimate simulation, the depth of general corrosion due to both the initially trapped oxygen and sulfide produced by microbial activity or present in the ground water is predicted to be < 10 μm after one million years.

Contents

1 Introduction 7

2 Updates to CSM 9
2.1 History and nomenclature of various versions of the CSM 9
2.2 Improvements to the CSM Version 1.1 17
2.2.1 Implementation of Henry's law treatment for O_2 (CSM V1.1eq) 17
2.2.2 Other improvements to the code and subroutines 19
2.3 Improvements to reaction scheme 20
2.3.1 Exclusion of anaerobic dissolution of pyrite as a source of sulfide 20
2.3.2 Updated mechanism for the oxidative dissolution of pyrite 20
2.3.3 Microbial reduction of sulfate 22
2.3.4 Conversion of cuprous oxide to cuprous sulfide 23
2.3.5 Cathodic reduction of water 23
2.3.6 Improvement to treatment of cathodic reduction of sulfide 26
2.3.7 Improved treatment of microbial sulfate reduction 27
2.3.8 Treatment of gaseous H_2S 33
2.4 Spatial separation of anodic and cathodic processes 37
2.5 Alternative film formation process 39
2.6 Alternative bentonite model 40
2.6.1 Background 40
2.6.2 Changes to CSM for the single inter-layer model 41

3 Results of simulations with updated versions of the CSM 45
3.1 Reference simulation with CSM Version 1.1eq 45
3.2 Improvements to reaction scheme CSM Versions 1.2a–1.2h 53
3.2.1 Modification to the reaction scheme CSM Versions 1.2a to 1.2f 53
3.2.2 Improved treatment of microbial sulfate reduction CSM Version 1.2g 58
3.2.3 Treatment of gaseous H_2S CSM Version 1.2a-h 61
3.3 Spatial separation of anodic and cathodic processes CSM Version 1.3 64
3.4 Alternative film formation process CSM Version 1.4 66
3.5 Alternative bentonite model CSM Version 2.0 66

4 Default or "best-estimate" CSM simulation and sensitivity analyses 69
4.1 Definition of "best-estimate" scenario 69
4.2 Results of "best-estimate" simulation 74
4.2.1 Corrosion 74
4.2.2 Oxygen balance 78
4.2.3 Sulfide balance 79
4.2.4 Fe(II) balance 80
4.2.5 Microbial aspects 82
4.3 Sensitivity analyses 87
4.3.1 Impact of allowing microbial activity in the buffer 89
4.3.2 Impact of assumption of microbial death 92
4.3.3 Buffer and backfill saturation time 93
4.3.4 Horizontal versus vertical diffusion 97

5 Integrated Sulfide Project benchmarking exercise 101
5.1 Background 101
5.2 Definition of Base Case and variants 103
5.2.1 Definition of Base Case 103
5.2.2 Definition of variant cases 104
5.3 Results of simulations 110
5.3.1 Base Case 110
5.3.2 Variant cases 119
5.3.3 Discussion of the results of the Base Case and variant cases 131

6 Discussion 133
6.1 Nature of the repository environment and the evolution of the corrosion behaviour of the canister 133
6.2 Implications of CSM predictions for localised corrosion and SCC of the canister 134
6.2.1 Pitting 134
6.2.2 Stress corrosion cracking 135
6.3 Cathodic reaction under anaerobic conditions 135
6.4 Spatial separation of anodic and cathodic processes 136
6.5 The nature of the Cu_2S film 138
6.6 Effect of gaseous H_2S 138
6.7 Status and future development of the CSM 138

7 Conclusions 141

References 143

Appendix A Derivation of parameter values for cathodic reduction of H_2O on copper 151

Appendix B Derivation of surface area factor for cathodic reaction on surface and within pores of Cu_2S film 153

Appendix C Data input file 157

Appendix D Definition of Base Case and Variant calculations for WP3 of the Integrated Sulfide Project 181

1 Introduction

The Copper Sulfide Model (CSM) is a reactive-transport model for predicting the long-term corrosion behaviour of copper canisters in an underground repository. The model is structured so that physical, chemical, microbial, and mass-transport processes in the near- and far-fields are coupled to the interfacial electrochemical reactions that constitute the overall corrosion reaction. In this way, the model is capable of predicting the evolution of the corrosion behaviour as the environmental conditions within the repository change over time. Thus, the model accounts for not only the corrosion behaviour during the early aerobic phase, but also the corrosion of the canister due to the presence of sulfide during the long-term anaerobic period.

The CSM is a custom-designed code written in the C computer language. The code is structured around a series of linear, one-dimensional (1-D) reaction-diffusion (mass-balance) equations, one for each chemical species included in the model plus a heat-conduction equation to predict the spatial and temporal variation in temperature. These mass-balance equations are discretized and numerically solved using finite-difference methods with the aid of the TRANSIENT solver for sparse matrices (Kolář 2016). The basic output of the code is the spatial and temporal variation of the concentration of each of the species, plus temperature. Because of the use of a mixed-potential boundary condition for the electrochemical reactions on the canister surface, the code also predicts the time dependence of the corrosion potential (E_{CORR}) and the corrosion rate (as the corrosion current density i_{CORR}). The spatial variation in the rates of the various reactions included in the model are also predicted. Integrating these rates over time and/or space provides information about the total extent of the various processes that are responsible for the evolution of the repository environment.

Figure 1-1 illustrates how the model represents the various components of the multi-barrier disposal system. The CSM can handle an arbitrary number of layers and in the work described in this report a total of either six or nine layers are used. Each of these layers represents one of the engineered or natural barriers which, from the canister surface outwards, include: (i) a layer of precipitated porous Cu_2S (not shown in the figure), (ii) compacted bentonite-based buffer material, (iii) clay-based backfill, (iv) excavation-damaged or -disturbed rock, and (v) intact host rock. The right-hand boundary of the model is a groundwater-bearing fracture that maintains constant chemical conditions. The backfill layer(s) is excluded for simulations representing a horizontal orientation from the canister surface across the deposition hole and into the host rock. In contrast, transport of species in the vertical direction across the deposition tunnel can be simulated by including the backfill layer. For better representation of the spatial variation in the degree of saturation, which is treated as an external input in the model, the buffer and backfill layers are commonly sub-divided into three and two sub-layers, respectively. The excavation-damaged rock is also sometimes sub-divided into two layers in order to represent differing degrees of damage with distance from the excavation opening. Finally, in order to properly represent the inventory of species (especially the initially trapped O_2) in the system, the dimensions of the buffer and backfill layers are based on the respective barrier volume to canister surface area ratios. Consequently, the dimensions of these layers in the model differ from the geometric dimensions in the repository.

The CSM has undergone various revisions since it was first developed in 2007 (King 2008). This report is a description of the further development and application of the CSM over the period 2015–2018. In 2015, the focus was on the further development of the code through changes to the associated reaction scheme and correction of earlier errors and omissions. Further improvement to the treatment of the microbial reduction of sulfate was achieved in 2016 and the updated model was used in an inter-model comparison (or benchmarking) exercise as part of the SKB-Posiva Integrated Sulfide Project (ISP). The effects of gaseous H_2S were incorporated in 2018, along with further inter-model comparisons.

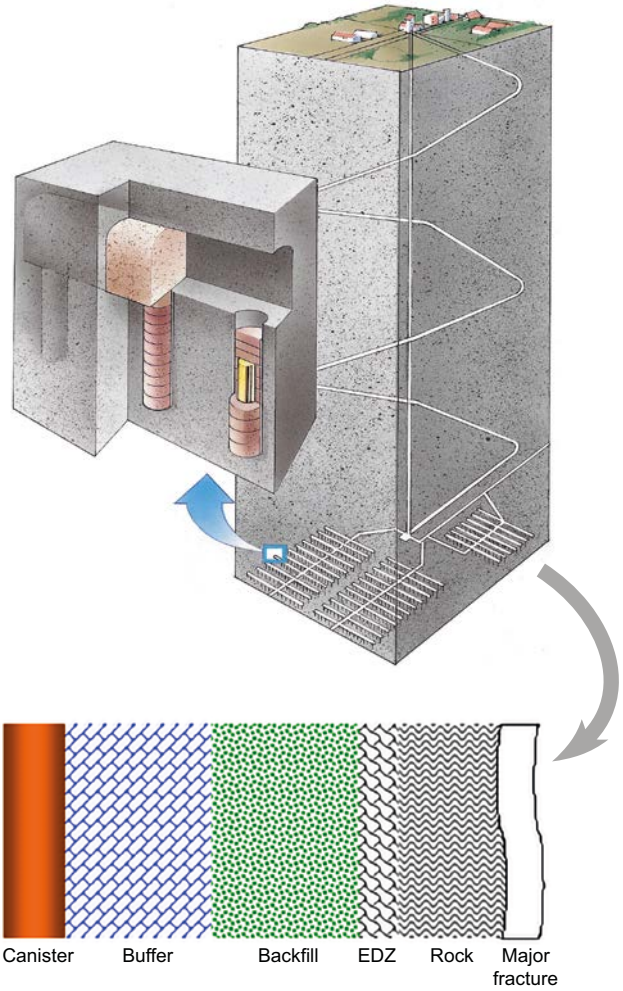

Figure 1-1. *Schematic illustration of the translation of the repository geometry into a 1-D multi-layer representation for modelling purposes.*

Here, various modifications to an earlier version of the code (CSM Version 1.1) are described, including (a) improvements and corrections to various aspects of the reaction mechanism on which the model is based, (b) a provision to allow the spatial separation of anodic and cathodic processes, (c) an alternative treatment of Cu_2S film formation, (d) an alternative treatment for the properties of the bentonite buffer, (e) a more-mechanistic treatment of the kinetics of microbial sulfate reduction, and (f) the formation, transport, and reaction of gaseous H_2S. The ISP benchmarking simulations were run using hypothetical scenarios defined to allow inter-comparison of different codes. For example, fully saturated, isothermal conditions with no initially trapped atmospheric O_2 were assumed for the base case simulation. Although such assumptions were useful for comparing different models, they do not properly reflect the expected evolution of the corrosion behaviour of canisters in the repository.

Section 2 of this report describes the history and nomenclature of the CSM development, as well as the code changes required to implement the modifications described above. The results of simulations using the improved versions of the CSM are described in Section 3 by comparison with the results of a reference simulation using the CSM Version 1.1. The current best estimate of the evolution of the corrosion behaviour of the canister is presented in Section 4, along with the results of sensitivity analyses. The results of the CSM simulations performed as part of the ISP code-comparison exercise are described in Section 5. Finally, the current status of the model and the implications of the CSM predictions are considered in Section 6. A number of appendices support the main text, including (a) a description of the derivation of parameters for the interfacial reduction of H_2O, (b) the derivation of the surface area factor for the simulation of the spatial separation of anodic and cathodic processes, (c) the default input parameter values for Version 1.1eq and the respective sources, and (d) a description of the input data for the ISP benchmarking base case and variant calculations.

2 Updates to CSM

2.1 History and nomenclature of various versions of the CSM

Various versions of the CSM have been developed, both historically and in the current program. Table 2-1 summarizes the various versions of the code, provides a brief description of the model and/or the changes from the prior version(s), and gives applicable references.

The first version of the CSM was developed in 2007 (King 2008), although no results of simulations were presented. That version of the code was referred to as the CSM Version 1.0 and was based on an earlier Copper Corrosion Model (CCM) with the addition of various interfacial, mass transport, redox and precipitation processes involving sulfide and various sulfide-containing species. Figure 2-1 shows the reaction scheme for CSM Version 1.0, with the additions made to the reaction scheme for the CCM Version 1.1 (King and Kolář 2006, King et al. 2008) highlighted in red.

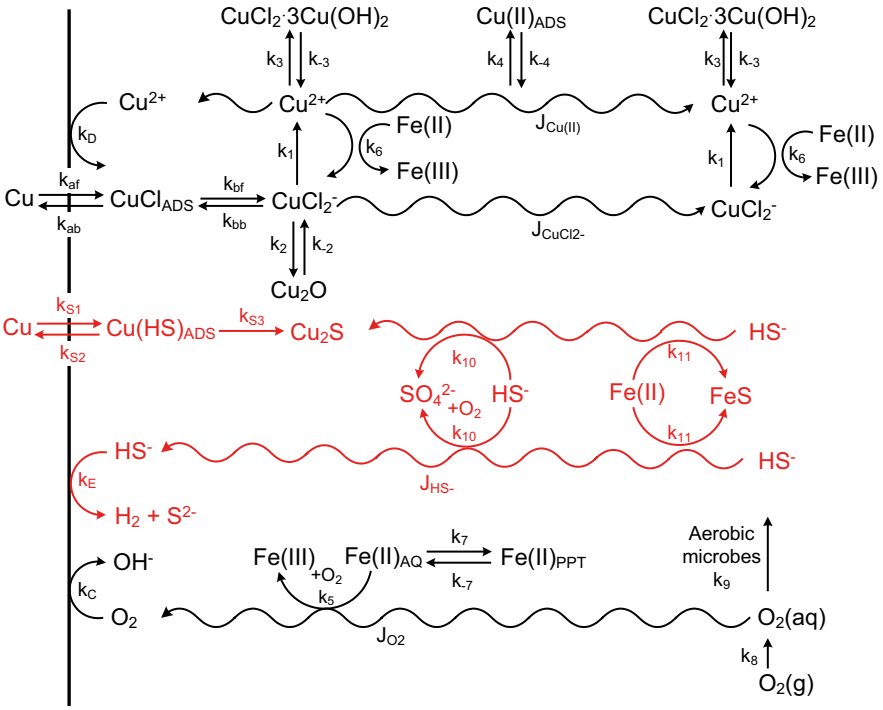

Figure 2-1. *Reaction mechanism for CSM Version 1.0 (King 2008). The red-highlighted processes indicate the additions made to the earlier CCM Version 1.1 reaction mechanism (King and Kolář 2006, King et al. 2008).*

Table 2-1. Summary of the various versions of the Copper Sulfide Model.

Version	Summary of code changes	Comments	Reference(s)
1.0	Based on CCM V1.1 with addition of (i) anodic dissolution of Cu to form Cu_2S supported by the cathodic reduction of HS^-, (ii) diffusive transport of HS^-, (iii) oxidation of HS^- by O_2, and (iv) precipitation of FeS.	No simulations performed with V1.0.	King (2008)
1.1	Based on CSM V1.0 with addition of (i) oxidation of pyrite (FeS_2) by O_2, (ii) reduction of sulfate by SRB, and (iii) dissolution of FeS_2 to produce HS^- and Fe(II). The following processes from V1.0 were excluded from the reaction mechanism for V1.1: (a) oxidation of HS^- by O_2, (b) the dissolution of an Fe(II) mineral to produce dissolved Fe(II), (c) the precipitation of an Fe(II) secondary phase, and (d) the oxidation of Fe(II) by O_2.	See rationale for changes in text. Changes require the addition of mass-balance equations for SO_4^{2-} and pyrite.	King et al. (2011a, b)
1.1eq	Replacement of the kinetic treatment of the dissolution of gaseous O_2 by an equilibrium between gaseous and dissolved O_2.	Change made to make the treatment of gaseous and dissolved O_2 the same as gaseous and dissolved H_2 as introduced in V1.2. Removes one mass-balance equation from the code (gaseous O_2).	This report. Sections 2.2.1 and 3.1.
1.2a	Remove anaerobic pyrite dissolution as a source of HS^- from the reaction scheme for Version 1.1eq.	Based on the review of King (2013), anaerobic pyrite dissolution is not considered to be a significant source of HS^- because of the low solubility of FeS_2.	This report. Sections 2.3.1 and 3.2.1.
1.2b	Update the mechanism of the oxidative dissolution of pyrite in the reaction scheme for Version 1.1eq.	Review of the literature on pyrite oxidation indicates an alternative stoichiometry for the oxidative dissolution reaction (King 2013).	This report. Sections 2.3.2 and 3.2.1.
1.2c	Modify/update the rate and/or mechanism of the reduction of SO_4^{2-} by SRB in the reaction scheme for Version 1.1eq.	As part of the overall Integrated Sulfide Project, Bengtsson et al. (2017) have published new data on the reduction of sulfate by SRB in compacted bentonite.	This report. Sections 2.3.3 and 3.2.1.
1.2d	Add the conversion of Cu_2O to Cu_2S by HS^- to the reaction scheme for Version 1.1eq.	Based on data from Smith et al. (2007a), Cu_2O has been shown to convert to Cu_2S in the presence of HS^-	This report. Sections 2.3.4 and 3.2.1.
1.2e	Add the cathodic reduction of H_2O to the reaction scheme for Version 1.1eq. Add gaseous and dissolved H_2 species to the model.	There is a current debate about which species is undergoing electrochemical reduction to produce the H_2 formed by the corrosion of copper in sulfide solutions (Macdonald et al. 2016). If the source of hydrogen is HS^- then the cathodic reaction could be transport limited. However, H_2O is present in much higher concentration than HS^- and could be the source of the H_2.	This report. Sections 2.3.5 and 3.2.1.
1.2f	Correct treatment of the cathodic reduction of HS^- in the reaction scheme for Version 1.1eq.	In Version 1.1eq, HS^- is cathodically reduced to produce ½ H_2 and S^{2-}. The S^{2-} species is not accounted for in the code and is essentially lost from the system. However, S^{2-} is not stable at pH < 14 and would protonate to from HS^-. We need to properly account for all sulfide species in the code.	This report. Sections 2.3.6 and 3.2.1.

Version	Summary of code changes	Comments	Reference(s)
1.2g	Improved treatment of microbial sulfate reduction.	Changes made to improve treatment of microbial sulfate reduction to make CSM consistent with treatment in similar Unibern and Amphos 21/Clay Technology models for purposes of SKB/Posiva Integrated Sulfide Project benchmarking exercise. Species added to code: gypsum, dissolved and solid organic matter, two additional sources (and sinks) for Fe(II), chemotrophic and organotrophic SRB. Monod kinetics used to model rates of sulfate reduction. Inclusion of gypsum overcomes problem of high initial rates of sulfate reduction due to need to assume all gypsum initially dissolved in pore water. Specific modelling of organic matter dissolution avoids issues due to assuming all organic C initially dissolved in porewater.	This report. Sections 2.3.7 and 3.2.2.
1.2h	Treatment of gaseous H_2S.	Addresses questions raised about possibility of rapid H_2S transport and corrosion during unsaturated phase. Additional, non-electrochemical interfacial reaction due to reaction of Cu with $H_2S(g)$.	This report. Sections 2.3.8 and 3.2.3.
1.2a-f	Overall version incorporating all changes in Versions 1.2a to 1.2f.	Outcome of model development activities in 2015 and basis for Versions 1.3 and 2.	This report. Section 3.2.1
1.2a-g	Overall version incorporating all changes in Versions 1.2a to 1.2g.	Used for Integrated Sulfide Project inter-model comparison exercise.	This report. Sections 4 and 5.
1.2a-h	Overall version incorporating all changes in Versions 1.2a to 1.2h.	-	This report. Section 3.2.3.
1.3a	Spatial separation of anodic and cathodic processes. Cathodic reaction on surface of Cu_2S film only.	Simplified treatment using different fractional surface areas for anodic and cathodic reactions. Based on CSM Version 1.2a-f.	This report. Sections 2.4 and 3.3.
1.3b	Spatial separation of anodic and cathodic processes. Cathodic reaction on surface and within pores of Cu_2S film.	Simplified treatment using different fractional surface areas for anodic and cathodic reactions. Based on CSM Version 1.2a-f.	This report. Sections 2.4 and 3.3.
1.4	Alternative film formation process in which the film is allowed to grow at the location at which precipitation occurs and the porosity is predicted within the code.	Not developed as the proposed format (based on the possibility of transport and spatially distributed precipitation of dissolved copper species) is inappropriate for Cu in sulfide environments due to the absence of dissolved copper.	This report. Sections 2.5 and 3.4.
2.0	Alternative bentonite model.	Attempt to implement a single inter-layer pore model for the highly compacted bentonite in place of the default multi-porosity model. Based on CSM Version 1.2a-f.	This report. Sections 2.6 and 3.5.

The changes made to the CCM V1.1 in the development of the CSM V1.0 included:

- Additional interfacial reactions in the form of the anodic dissolution of Cu to form Cu_2S supported by the cathodic reduction of the proton in the HS^- ion to produce H_2.
- Addition of the diffusive transport of HS^-.
- Addition of the oxidation of HS^- by O_2.
- Addition of the precipitation of HS^- as FeS in the presence of Fe(II).

Version 1.0 of the CSM is described by King (2008), but no simulations using the model were ever published.

King et al. (2011a, b) describe the first results of simulations using the CSM and were based on the CSM V1.1. (King et al. (2011a) erroneously describe the version of the code they used as V1.0). Version 1.1 was developed from the CSM V1.0 by making the following changes to the reaction scheme:

- Addition of the oxidation of pyrite (FeS_2) by O_2.
- Addition of the reduction of sulfate by sulfate reducing bacteria (SRB).
- Addition of the anaerobic dissolution of FeS_2 to produce HS^- and Fe(II).
- Removal of the oxidation of HS^- by O_2.
- Removal of the dissolution of an unidentified Fe(II) mineral to produce dissolved Fe(II).
- Removal of the precipitation of a non-sulfide Fe(II) secondary phase.
- Removal of the oxidation of Fe(II) by O_2.

The reaction scheme for CSM V1.1 is shown in Figure 2-2, with additions to the reaction scheme for V1.0 highlighted in red and exclusions shown in crossed-out text in blue font. For V1.1, it was considered important to include processes associated with the presence of pyrite since FeS_2 is a major accessory mineral in bentonite and can also be present on fracture surfaces. Pyrite oxidation could be a major cause of O_2 consumption in the repository and is assumed to be a source of sulfide for safety assessments (SKB 2010). Sulfate reduction by SRB was considered to be another potential source of HS^-, especially in the backfill and host rock. In contrast, oxygen consumption by HS^- oxidation was not considered to be an important process as it is likely that the initially trapped O_2 will have been consumed by other processes (including the oxidation of pyrite included in V1.1) before HS^- diffuses into the buffer from the far-field. Finally, in the CCM and CSM V1.0, it was assumed that dissolution of an Fe(II)-containing mineral was the source of dissolved Fe(II) in the repository, which could then lead to the consumption of O_2 and/or precipitate as an Fe(II)-containing secondary phase if present in amounts in excess of the solubility of the Fe(II) phase. With the inclusion of pyrite in the reaction scheme, it was deemed unnecessary to also include this prior Fe(II)-containing mineral phase in the reaction scheme.

With these changes to the reaction scheme, it was necessary to add reaction-diffusion equations for SO_4^{2-} and FeS_2 to the code. In the latter case, although pyrite is immobile, it is present in a limited quantity and it is necessary to keep track of the quantity remaining in the repository as it undergoes reaction.

To help in understanding the further changes made to the code as part of this study, the notation for the species considered in Version 1.1 and the corresponding mass-balance expressions are given in Table 2-2 and Equations (2-1) to (2-14), respectively. In all versions of the CSM, concentrations of dissolved species refer to unit volume of pore water and the concentration of solid species is referred to unit volume of the system (solid plus pores). The concentration of adsorbed Cu(II) is referred to unit mass of the adsorbent. It should also be noted that, as the CSM is currently a 1-D model, various quantities are expressed per unit cross-sectional area, for example, the inventory of the different species.

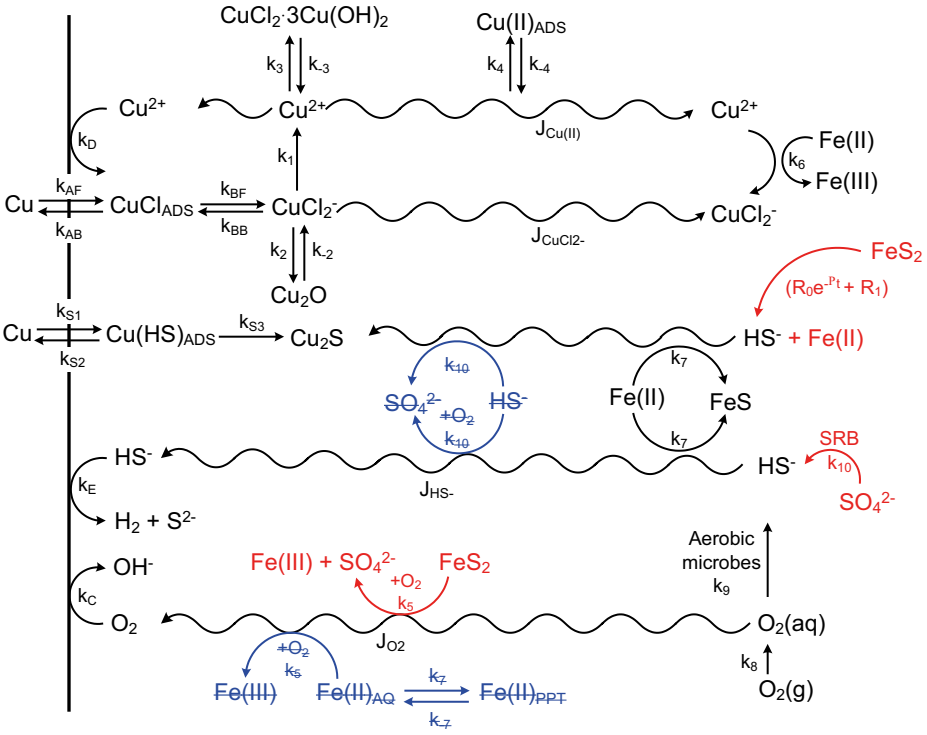

Figure 2-2. *Reaction mechanism for CSM Version 1.1 (King et al. 2011a, b). The red-highlighted processes indicate the additions made to the earlier CSM Version 1.0 reaction mechanism and the blue struck-through items identify those processes removed from the earlier version of the model.*

Table 2-2. Species included in the Copper Sulfide Model Version 1.1.

Notation	Species	Species Name
c_A	$O_2(g)$	Gaseous oxygen
c_0	$O_2(aq)$	Dissolved oxygen
c_1	$CuCl_2^-$	Dissolved cuprous chloride complex ion
c_2	Cu_2O	Precipitated cuprous oxide
c_3	Cu^{2+}	Dissolved cupric ions
c_4	$CuCl_2{\cdot}3Cu(OH)_2$	Precipitated basic cupric chloride
c_5	Cu(II)(ads)	Adsorbed cupric species
c_6	Cl^-	Dissolved chloride ions
c_7	Fe(II)(aq)	Dissolved ferrous ions
c_8	FeS	Precipitated ferrous sulfide
c_9	HS^-	Dissolved sulfide ions
c_{10}	FeS_2	Pyrite
c_{11}	SO_4^{2-}	Sulfate ions
T	-	Temperature

The mass-balance (reaction-diffusion) equations for each of these species (and temperature) are given below.

$$\varepsilon_a \frac{\partial[(1-S)c_A]}{\partial t} = \frac{\partial}{\partial x}\left(\tau_f(1-S)^3\varepsilon_e D_A \frac{\partial c_A}{\partial x}\right) - \varepsilon_a S k_8 (c_0^{sat} - c_0)(1-S)c_A \quad (2\text{-}1)$$

$$\varepsilon_a \frac{\partial(Sc_0)}{\partial t} = \frac{\partial}{\partial x}\left(\tau_f\varepsilon_e S D_0 \frac{\partial c_0}{\partial x}\right) - \varepsilon_a S\left[\frac{k_1}{4}c_0c_1 + 3.75A_P k_5 c_0^{1/2}\theta(c_{10}) + k_9 c_0 \theta(S - S_{MIC})\right] \quad (2\text{-}2)$$
$$+\varepsilon_a S k_8 (c_0^{sat} - c_0)(1-S)c_A$$

$$\varepsilon_a \frac{\partial(Sc_1)}{\partial t} = \frac{\partial}{\partial x}\left(\tau_f \varepsilon_e S D_1 \frac{\partial c_1}{\partial x}\right) + \varepsilon_a S[-k_1 c_0 c_1 + k_6 c_3 c_7 - k_2 \max(0, c_1 - c_1^{sat})] + 2k_{-2} c_2 \quad (2\text{-}3)$$

$$\frac{\partial c_2}{\partial t} = \varepsilon_a S \frac{k_2}{2} \max(0, c_1 - c_1^{sat}) - k_{-2} c_2 \quad (2\text{-}4)$$

$$\varepsilon_a \frac{\partial(Sc_3)}{\partial t} = \frac{\partial}{\partial x}\left(\tau_f \varepsilon_e S D_3 \frac{\partial c_3}{\partial x}\right) \varepsilon_a S\left[k_1 c_0 c_1 - k_6 c_3 c_7 - k_3 \max(0, c_3 - c_3^{sat}) - k_4 c_3 (c_5^{max} - c_5)\rho_d\right] + 4k_{-3} c_4 + k_{-4} c_5 \rho_d \quad (2\text{-}5)$$

$$\frac{\partial c_4}{\partial t} = \varepsilon_a S \frac{k_3}{4} \max(0, c_3 - c_3^{sat}) - k_{-3} c_4 \quad (2\text{-}6)$$

$$\rho_d \frac{\partial c_5}{\partial t} = \varepsilon_a S k_4 c_3 (c_5^{max} - c_5)\rho_d - k_{-4} c_5 \rho_d \quad (2\text{-}7)$$

$$\varepsilon_a S \frac{\partial c_6}{\partial t} = \frac{\partial}{\partial x}\left(\tau_f \varepsilon_e S f_{D6} D_6 \frac{\partial c_6}{\partial x}\right) + \varepsilon_a S\left[2k_1 c_0 c_1 - 2k_6 c_3 c_7 + 2k_2 \max(0, c_1 - c_1^{sat}) - \frac{k_3}{2}\max(0, c_3 - c_3^{sat})\right] + 2k_{-3} c_4 - 4k_{-2} c_2 \quad (2\text{-}8)$$

$$\varepsilon_a \frac{\partial(Sc_7)}{\partial t} = \frac{\partial}{\partial x}\left(\tau_f \varepsilon_e S D_7 \frac{\partial c_7}{\partial x}\right) + \varepsilon_a S A_P [R_0 e^{-\alpha_P t} + R_1]\theta(c_{10}) - \varepsilon_a S[k_6 c_3 c_7 + k_7 \max(0, c_7 - c_7^{sat}) c_9] \quad (2\text{-}9)$$

$$\frac{\partial c_8}{\partial t} = \varepsilon_a S k_7 \max(0, c_7 - c_7^{sat}) c_9 \quad (2\text{-}10)$$

$$\varepsilon_a \frac{\partial(Sc_9)}{\partial t} = \frac{\partial}{\partial x}\left(\tau_f \varepsilon_e S D_9 \frac{\partial c_9}{\partial x}\right) + \varepsilon_a S\left[\begin{matrix} k_{10}\theta(c_{11})\theta(S - S_{MIC}) + 1.5 A_P (R_0 e^{-\alpha_P t} + R_1)\theta(c_{10}) \\ -k_7 \max(0, c_7 - c_7^{sat}) c_9 \end{matrix}\right] \quad (2\text{-}11)$$

$$\frac{\partial c_{10}}{\partial t} = -\varepsilon_a S A_P\left[k_5 c_0^{1/2} + (R_0 e^{-\alpha_P t} + R_1)\right]\theta(c_{10}) \quad (2\text{-}12)$$

$$\varepsilon_a S \frac{\partial c_{11}}{\partial t} = \frac{\partial}{\partial x}\left(\tau_f \varepsilon_e S D_{11} \frac{\partial c_{11}}{\partial x}\right) + \varepsilon_a S\left[2A_P k_5 c_0^{1/2}\theta(c_{10}) - k_{10}\theta(c_{11})\theta(S - S_{MIC})\right] \quad (2\text{-}13)$$

and

$$\rho C \frac{\partial T}{\partial t} = \frac{\partial}{\partial x}\left(K \frac{\partial T}{\partial x}\right) \quad (2\text{-}14)$$

where the different symbols are defined in Table 2-3. Values for many of these parameters are given in Appendix C.

Table 2-3. Definition of symbols for the Copper Sulfide Model Version 1.1.

Symbol	Species Name
c_A	Concentration of gaseous oxygen O_2(g)
c_0	Concentration of dissolved oxygen O_2(aq)
c_0^{sat}	Solubility of dissolved O_2
c_1	Concentration of dissolved cuprous chloride complex ion $CuCl_2^-$
c_1^{sat}	Saturated concentration of $CuCl_2^-$ in equilibrium with Cu_2O
c_2	Concentration of precipitated cuprous oxide Cu_2O
c_3	Concentration of dissolved cupric ions Cu^{2+}
c_3^{sat}	Saturated concentration of Cu^{2+} in equilibrium with $CuCl_2{\cdot}3Cu(OH)_2$
c_4	Concentration of precipitated basic cupric chloride $CuCl_2{\cdot}3Cu(OH)_2$
c_5	Concentration of adsorbed cupric species Cu(II)(ads)
c_5^{max}	Maximum concentration of adsorbed Cu^{2+} (equivalent to the cation exchange capacity of the adsorbate)
c_6	Concentration of dissolved chloride ions Cl^-
c_7	Concentration of dissolved ferrous ions Fe(II)(aq)
c_7^{sat}	Saturated concentration of Fe(II) in equilibrium with FeS

Symbol	Species Name
c_8	Concentration of precipitated ferrous sulfide FeS
c_9	Concentration of dissolved sulfide ions HS^-
c_{10}	Concentration of pyrite FeS_2
c_{11}	Concentration of sulfate ions SO_4^{2-}
f_{D6}	Enhancement factor for the diffusivity of Cl^- to account for gravitational flow due to density differences for saline ground waters
k_1	Rate constant for the irreversible oxidation of $CuCl_2^-$ by dissolved O_2
k_2	Rate constant for the precipitation of $CuCl_2^-$ as Cu_2O
k_{-2}	Rate constant for the dissolution of Cu_2O
k_3	Rate constant for the precipitation of Cu^{2+} as $CuCl_2 \cdot 3Cu(OH)_2$
k_{-3}	Rate constant for the dissolution of $CuCl_2 \cdot 3Cu(OH)_2$
k_4	Rate constant for the adsorption of Cu^{2+}
k_{-4}	Rate constant for the desorption of Cu^{2+}
k_5	Rate constant for the oxidative dissolution of pyrite
k_6	Rate constant for the irreversible reduction of Cu^{2+} by Fe(II)
k_7	Rate constant for the precipitation of FeS
k_8	Rate constant for the dissolution of gaseous O_2
k_9	Rate constant for the consumption of O_2 by aerobic microbes
k_{10}	Rate constant for the reduction of SO_4^{2-} by SRB
k_{AF}	Interfacial rate constant for the forward step to form $CuCl_{ADS}$
k_{AB}	Interfacial rate constant for backward step to form Cu from $CuCl_{ADS}$
k_{BF}	Interfacial rate constant for the forward step to form $CuCl_2^-$
k_{BB}	Interfacial rate constant for the backward step to form $CuCl_{ADS}$ from $CuCl_2^-$
k_C	Interfacial rate constant for the reduction of dissolved O_2
k_D	Interfacial rate constant for the reduction of Cu^{2+}
k_E	Interfacial rate constant for the reduction of the proton in the HS^- ion
k_{S1}	Interfacial rate constant for the forward step to form $CuHS_{ADS}$
k_{S2}	Interfacial rate constant for the backward step to form Cu from $CuHS_{ADS}$
k_{S3}	Interfacial rate constant for the formation of Cu_2S from $CuHS_{ADS}$
max	Mathematical operator that takes the value of the maximum value of the parameters in the argument
t	Time
x	Distance
A_p	Specific surface area of pyrite
C	Heat capacity
D_A	Diffusion coefficient of gaseous O_2 in air
D_0	Bulk solution diffusion coefficient of dissolved O_2
D_1	Bulk solution diffusion coefficient of $CuCl_2^-$
D_3	Bulk solution diffusion coefficient of Cu^{2+}
D_6	Bulk solution diffusion coefficient of Cl^-
D_7	Bulk solution diffusion coefficient of dissolved Fe(II)
D_9	Bulk solution diffusion coefficient of HS^-
D_{11}	Bulk solution diffusion coefficient of SO_4^{2-}
F	Faraday constant
K	Thermal conductivity
R	Gas constant
R_0	Instantaneous rate of anaerobic dissolution of pyrite
R_1	Long-term rate of anaerobic dissolution of pyrite
S	Degree of saturation
S_{MIC}	Threshold degree of saturation above which microbial activity is possible
T	Temperature (absolute)
α_p	Time constant for the anaerobic dissolution of pyrite
ε_a	Accessible porosity
ε_e	Effective porosity for mass transport
ε_{film}	Porosity of the Cu_2S film
θ	Mathematical operator that takes the value of 1 if the argument has a value greater than zero and 0 if the argument is ≤ 0
ρ	Particle density (for calculation of thermal properties)
ρ_d	Dry density
τ_f	Tortuosity factor

It was intended to use the results from simulations using CSM Version 1.1 as a reference case against which to compare the results of the further improvements to the model. However, it was realized that there would be an inconsistent treatment of species that can partition between the gaseous and dissolved forms (i.e., O_2 and H_2) between Version 1.1 and the newer versions of the code that include partitioning and transport of H_2. In CSM Version 1.1, gaseous O_2 is assumed to dissolve into the aqueous phase where it participates in various interfacial and homogeneous processes. Gaseous O_2 can diffuse but does not participate in reactions. This treatment is reasonable in the case of O_2 where the gaseous phase primarily acts as a reservoir for the initially trapped atmospheric O_2 and where the extent of exsolution of dissolved O_2 back into the gas phase is expected to be minimal. In the case of H_2, however, exchange of hydrogen between the gaseous and dissolved forms is more important as H_2 is accumulating in the system (as opposed to being consumed) and could remain in the system for the entire duration of the simulation. (In addition, for the improved treatment of microbial sulfate reduction described in Section 2.3.7, dissolved H_2 can be consumed by SRB so it is important to consider the partitioning of hydrogen between gas and liquid phases.)

The reversible dissolution and exsolution of O_2 (and H_2) is best treated in the model by assuming that the dissolved and gaseous species are in equilibrium, with their respective concentrations governed by Henry's law

$$c_0 = H_0 c_A \qquad (2\text{-}15)$$

where H_0 is the temperature-dependent Henry's law constant for O_2. The CSM Version 1.1 was modified to include equilibrium between dissolved and gaseous O_2 and resulted in a new version of the model denoted CSM Version 1.1eq (Table 2-1). The details of the changes required for the development of Version 1.1eq are described in Section 2.2.1.

With CSM Version 1.1eq as the reference version of the model, further changes were made to the code to incorporate the various improvements identified here. A number of these updates were corrections or improvements to the treatment of processes associated with the reaction mechanism, for example, changes to the stoichiometry for the oxidative dissolution of pyrite in Version 1.2b. These changes resulted in new versions of the code referred to as Versions 1.2a to 1.2h. An overall updated code, referred to as Version 1.2a-h, was also developed that incorporated all of the changes and improvements to the reaction scheme. For the ISP inter-model comparison, a version of the code incorporating all changes 1.2a through 1.2g (denoted as Version 1.2a-g) was used.

The details of the changes are described in Section 2.3, but briefly the various changes and the various model versions are (Table 2-1):

- Version 1.2a – remove the anaerobic dissolution of pyrite as a source of dissolved HS^-, based on the review by King (2013).
- Version 1.2b – change the stoichiometry of the oxidative dissolution of FeS_2.
- Version 1.2c – modify the rate and/or mechanism for the reduction of SO_4^{2-} by SRB based on data from Bengtsson et al. (2017).
- Version 1.2d – incorporate the chemical conversion of Cu_2O to Cu_2S by HS^- based on the study of Smith et al. (2007a).
- Version 1.2e – add the cathodic reduction of H_2O as an interfacial process and gaseous and dissolved H_2 as additional species.
- Version 1.2f – correct the treatment of the reduction of HS^- to ensure that we properly account for all sulfide in the system.
- Version 1.2g – improve the treatment of sulfate reduction using Monod kinetics for both chemotrophic and organotrophic SRB and proper accounting of inventories of gypsum and organic matter.
- Version 1.2h – treatment of gaseous H_2S including an additional interfacial reaction and enhanced mass-transport of $H_2S(g)$.
- Version 1.2a-f – incorporates all changes/improvements in Versions 1.2a to 1.2f and used as basis for Versions 1.3 and 2.0.
- Version 1.2a-g – incorporates all changes/improvements in Versions 1.2a to 1.2g and used for the ISP benchmarking exercise.
- Version 1.2a-h – incorporates all changes/improvements in Versions 1.2a to 1.2h.

With the exception of the overall Versions 1.2a-f, 1.2a-g, and 1.2a-h, each of these sets of changes were made separately to the CSM Version 1.1eq so that the effect of each individual change could be determined by comparison with the results from the original code.

The CSM Version 1.3 allowed the option to specify spatial separation of the anodic and cathodic processes (Table 2-1). The default assumption is that both anodic and cathodic processes occur at the metal/solution interface at the bottom of pores in the (electrically insulating) Cu_2S film. However, there is experimental evidence (Chen J 2015, private communication) to suggest that the cathodic reaction occurs on the Cu_2S film. Starting with the CSM Version 1.2a-f, two variant models were developed:

- Version 1.3a – cathodic reaction on the upper surface of the Cu_2S film only.
- Version 1.3b – cathodic reaction on the Cu_2S film both on the upper surface and within the pores.

Further details of the development of CSM Versions 1.3a and 1.3b are given in Section 2.4.

Film formation can be treated in the model in one of two ways. Usually, the film is assumed to grow at the film/solution interface (Martino et al. 2017) with a user-defined (constant) porosity ε_{film}. Thus, regardless of where the precipitation reaction occurs, all precipitated Cu_2S is "moved" to the film/solution interface. This treatment of film formation is used for all versions of the model including Version 1.0, Version 1.1, Versions 1.2a to 1.2h, Version 1.3, and for Version 2.0 described below. Alternatively, the film could form at the location at which the precipitation reaction occurs, typically within the pores of the film close to the metal/solution interface as this is where the concentration of dissolved metal ions is highest. The film porosity then becomes a parameter which is predicted within the model rather than being user-specified.

Consideration was given to implementing the spatially distributed film formation process in the CSM (Version 1.4). However, it was subsequently realized that such a treatment is inappropriate for Cu_2S films because of the absence of dissolved copper species as a result of the low solubility of the solid phase. Therefore, this version of the model (Version 1.4) was not developed (Table 2-1). Further details of this alternative film formation treatment are given in Section 2.5.

Currently, mass transport and reactions within the buffer (and backfill) are treated assuming a multi-porosity model for the highly compacted bentonite (HCB). Thus, we distinguish between accessible and non-accessible pores, as well as through and dead-end pores. Among others, Birgersson and Karnland (2009) have suggested that the bentonite pore structure is better represented by a single inter-layer porosity taking into account the effects of Donnan equilibrium across the pore/bulk water interface. Adaptation of the CSM Version 1.2a-f to simulate the effects of this alternative bentonite model were implemented in CSM Version 2.0 (Table 2-1). (The notation Version 2.0 was used, rather than Version 1.X, as the choice of bentonite model represents a fundamental, as opposed to an incremental, change in the structure of the code). Further details of the development of CSM Version 2.0 are given in Section 2.6.

2.2 Improvements to the CSM Version 1.1

2.2.1 Implementation of Henry's law treatment for O_2 (CSM V1.1eq)

The CSM Version 1.1 treats O_2 dissolution/exsolution as a 2nd-order kinetic process (rate constant k_8) in which the rate of dissolution is proportional to the degree of under-saturation of the solution ($c_0^{sat} - c_0$). Thus, dissolution of O_2 is treated as a reversible process since exsolution will occur if $c_0 > c_0^{sat}$. An alternative treatment for species that can partition between the gaseous and aqueous phases is to assume that the dissolved and gaseous species are in equilibrium with concentrations determined by Henry's law. The Henry's law treatment has been used for H_2 in other reactive-transport models and is used for the CSM Version 1.2eq. To maintain consistency of the treatment of gaseous species, Henry's law was also applied here to dissolved and gaseous O_2.

Therefore, Version 1.1 of the CSM was modified to treat gaseous (species A) and dissolved O_2 (species 0) as being in equilibrium. This new version of the model is referred to as Version 1.1eq and the corresponding reaction mechanism is illustrated in Figure 2-3.

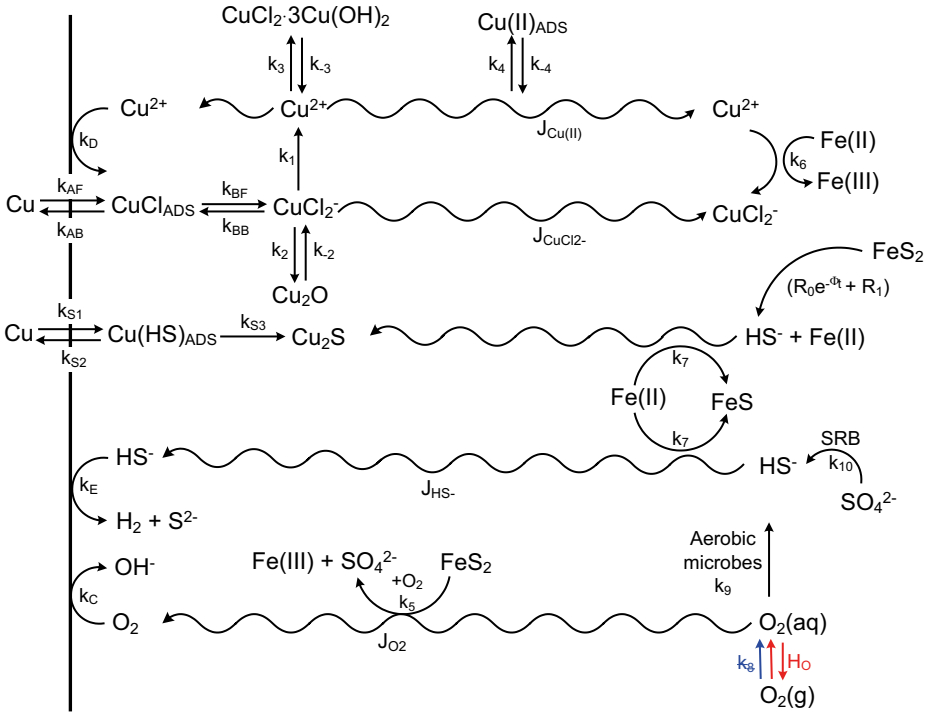

Figure 2-3. *Reaction mechanism for CSM Version 1.1eq. The red-highlighted process indicate the addition made to the earlier CSM Version 1.1 reaction mechanism and the blue struck-through item identifies the processes deleted from the earlier version.*

Because the dissolved and gaseous O_2 are assumed to be in equilibrium, we can eliminate one of the two mass-balance equations (MBE) describing these species (Equations (2-1) and (2-2)), based on the relationship.

$$c_A = \tilde{H}_O c_0 \tag{2-16}$$

where $\tilde{H}_o$ is the inverse Henry's law constant for O_2. Equations (2-1) and (2-2) can be combined to give the single MBE

$$\frac{\partial}{\partial t}\left(\varepsilon_a\left[S + (1-S)\tilde{H}_O\right]c_0\right) = \frac{\partial}{\partial x}\left(\tau_f\varepsilon_e\left[SD_0 + (1-S)^3 D_A\tilde{H}_O\right]\frac{\partial c_0}{\partial x}\right) - \varepsilon_a S\left[\frac{k_1}{4}c_0c_1 + 3.75A_P k_5 c_0^{1/2}\theta(c_{10}) + k_9 c_0\theta(S - S_{MIC})\right] \tag{2-17}$$

The equilibrium treatment for O_2 also necessitates a change in the relationship between the cathodic current density for the reduction of O_2 (i_c) and the interfacial flux of **both** dissolved and gaseous O_2

$$i_C = -n_0 F\tau_f\varepsilon_e\left[D_0 S + (1-S)^3 D_A\tilde{H}_O\right]\frac{\partial c_0}{\partial x}\Big|_{x=0} \tag{2-18}$$

Based on Sander (1999), the mean value for the Henry's law constant H_O for O_2 is 1.3×10^{-3} mol·dm^{-3}·atm^{-1} at 25 °C, corresponding to the expression c_0/p_{O2} where p_{O2} is the pressure of gaseous O_2. At 25 °C, 1 atm of an ideal gas is equivalent to a concentration of 0.040876 mol·dm^{-3}·atm^{-1}. Thus, the inverse Henry's law constant for O_2 is given by

$$\tilde{H}_O = \frac{1}{H_O} = \frac{0.040876\,\text{mol dm}^{-3}\text{atm}^{-1}}{1.3\text{x}10^{-3}\,\text{mol dm}^{-3}\text{atm}^{-1}} = 31.4 \tag{2-19}$$

The temperature dependence of the Henry's law constant (and, by inference, of the inverse Henry's law constant) is described by an Arrhenius relationship (Sander 1999). The activation energy for $\tilde{H}_o$ will be equal but of opposite sign to that of H_O. The mean activation energy for H_O according to Sander (1999) is 14 100 J/mol, so that for $\tilde{H}_o$ ($\Delta H_{\tilde{H}o}$) is taken to be $\Delta H_{\tilde{H}o} = -14\,100$ J/mol.

Simulations with CSM Version 1.1eq

To allow comparison to earlier predictions using the CSM Version 1.1, the same input data as used for the "Forsmark Base Case" described by King et al. (2011b) were used to develop a reference simulation using CSM Version 1.1eq for the current study. The repository geometry is described by a series of nine layers in the model representing the properties of the precipitated Cu_2S film, HCB (three sub-layers), backfill material (two sub-layers), excavation-damaged (EDZ) and excavation-disturbed (EdZ) zones, and intact host rock.

For comparison with the results of the simulations with the new CSM Version 2.0 (in which, conceptually we assume there is no backfill and the HCB is in direct contact with the EDZ), we also ran Version 1.1eq as a six-layer model. In this case, the six layers represented the precipitated Cu_2S film, HCB (three sub-layers), excavation-damaged zone EDZ, and host rock.

Table 2-4 summarizes these and all of the other simulations performed for this study. The input data for the reference simulation with the 9-layer model (Run 1.1eq(a)) are given in Appendix C.

Table 2-4. Summary of runs for the reference and various updated versions of the model.

CSM Version	Run	Comments
1.1eq	1.1eq(a)	Reference simulation 9-layer model.
	1.1eq(b)	Reference simulation 6-layer model.
1.2a	1.2a	Same input data as V1.1eq(a).
1.2b	1.2b	Same input data as V1.1eq(a).
1.2c	1.2c1	S_{MIC} = 1 (microbial activity not allowed in layers 1, 2, 3, and 4).
	1.2c2	S_{MIC} = 0 (microbial activity allowed in layers 1, 2, 3, and 4).
1.2d	1.2d	Same input data as V1.1eq(a), with addition of conversion term for Cu_2O.
1.2e	1.2e	Same input data as V1.1eq(a), with addition of terms related to generation and equilibrium of H_2.
1.2f	1.2f	Same input data as V1.1eq(a).
1.2a-f	1.2a-f.1	S_{MIC} = 1 (microbial activity not allowed in layers 1, 2, 3, and 4).
	1.2a-f.2	S_{MIC} = 0 (microbial activity allowed in layers 1, 2, 3, and 4).
1.2g	1.2g1	S_{MIC} = 1 (microbial activity not allowed in layers 1, 2, 3, and 4).
	1.2g2	S_{MIC} = 0 (microbial activity not allowed in layers 1, 2, 3, and 4).
1.2a-g	1.2a-g1 (death)	S_{MIC} = 1 (microbial activity not allowed in layers 1, 2, 3, and 4), death of microbes due to cell maintenance.
	1.2a-g1 (no death)	S_{MIC} = 1 (microbial activity not allowed in layers 1, 2, 3, and 4), no death of microbes due to cell maintenance.
	1.2a-g2 (death)	S_{MIC} = 0 (microbial activity allowed in layers 1, 2, 3, and 4), death of microbes due to cell maintenance.
	1.2a-g2 (no death)	S_{MIC} = 0 (microbial activity allowed in layers 1, 2, 3, and 4), no death of microbes due to cell maintenance.
1.2h	-	No runs performed with standalone Version 1.2h.
1.2a-h	1.2a-h	Based on best-estimate input data used for rin 1.2a-g1 (death), plus additional input parameters for treatment of gaseous H_2S.
1.3	1.3a	Cathodic reaction on surface of Cu_2S film only.
	1.3b	Cathodic reaction on surface of Cu_2S film and within pores.
1.4	-	Version not developed.
2.0	2.0	S_{MIC} = 1, microbial activity not allowed in layers 1, 2, 3, and 4.

2.2.2 Other improvements to the code and subroutines

A number of other improvements have been made to the software in order to improve the stability and execution of the code. These miscellaneous improvements included:

- Improved conservation of O_2 by modifying the MBE for O_2 by placing the inverse Henry's law constant inside the derivative (as it is temperature dependent and, hence, depends on x and t).
- Line-by-line debugging of code to correct typos and other errors.
- Improvement to the TRANSIENT solver and internal memory allocation algorithms.
- Improvements to the time-stepping algorithm in TRANSIENT.

2.3 Improvements to reaction scheme

2.3.1 Exclusion of anaerobic dissolution of pyrite as a source of sulfide

King (2013) has reviewed the properties of pyrite and, in particular, those relevant to the long-term anaerobic phase in the repository evolution. The solubility of pyrite is so low that the activity of HS^- in equilibrium with pyrite at pH 8 according to the reaction

$$FeS_2 + H^+ \rightleftarrows Fe^{2+} + HS^- + S^0 \quad (2\text{-}20)$$

is predicted to be 5×10^{-18} mol·dm^{-3} for a typical dissolved Fe^{2+} concentration of 10^{-5} mol × dm^{-3} (King 2013). Such a low concentration is unlikely to have any effect on the corrosion behaviour of copper canisters, even over a 10^6-year period. Therefore, the anaerobic dissolution of pyrite is considered to be an insignificant source of HS^- and can be excluded from the reaction scheme.

Exclusion of the anaerobic dissolution of pyrite from the code is achieved by the following modifications:

- Removal of the term $(R_0 e^{-\alpha_p t} + R_1)$ from the mass-balance equation for FeS_2 (species c_{10}) (Equation (2-12)).
- Removal of the term $(R_0 e^{-\alpha_p t} + R_1)$ from the mass-balance equation for HS^- (species c_9) (Equation (2-11)).
- Removal of the term $(R_0 e^{-\alpha_p t} + R_1)$ from the mass-balance equation for Fe(II) (species c_7) (Equation (2-9)).

The intermediate version of the CSM incorporating these changes is CSM Version 1.2a. These changes to the reaction mechanism are also highlighted in Figure 2-4, along with the other changes for the CSM Versions 1.2a to 1.2f.

Simulations with CSM Version 1.2a

Since the modification to the code does not introduce new parameters, the same set of input parameters as used above for the 9-layer Version 1.1eq simulation were used here to determine the impact of excluding anaerobic pyrite dissolution as a source of HS^- (Table 2-4).

2.3.2 Updated mechanism for the oxidative dissolution of pyrite

In the CSM Version 1.1/1.1eq, the oxidative dissolution of FeS_2 is given by:

$$FeS_2 + 3.5H_2O + 3.75O_2 \rightarrow Fe(OH)_3 + 2SO_4^{2-} + 4H^+ \quad (2\text{-}21)$$

with a rate constant $k_5 = 6.6 \times 10^{-11}$ mol$^{1/2}$·dm$^{-1/2}$·s^{-1} and an activation energy $\Delta H_5 = 56\,900$ J/mol.

A more appropriate expression for the oxidative dissolution of FeS_2 is (King 2013) (Figure 2-4):

$$FeS_2 + H_2O + 3.5O_2 \rightarrow Fe^{2+} + 2SO_4^{2-} + 4H^+ \quad (2\text{-}22)$$

This alternative mechanism is based on the review of Vaughan (2005) and, in addition to a slight decrease in the number of moles of O_2 consumed, also results in the formation of Fe^{2+} rather than a ferric species.

This change in mechanism results in changes to two MBE, that for dissolved O_2 (since 3.5 mol O_2 is now consumed per mol FeS_2 instead of 3.75) and Fe(II) (since this is now a product of the oxidation of pyrite, rather than Fe(III) assumed for Version 1.1/1.1eq). The MBE for FeS_2 and SO_4^{2-} do not require changing as the stoichiometry is the same for both species in both Reactions (2-21) and (2-22). There are no changes required for $Fe(OH)_3$ or H^+ as neither species is tracked in the model (i.e., they are not represented by an MBE in the code).

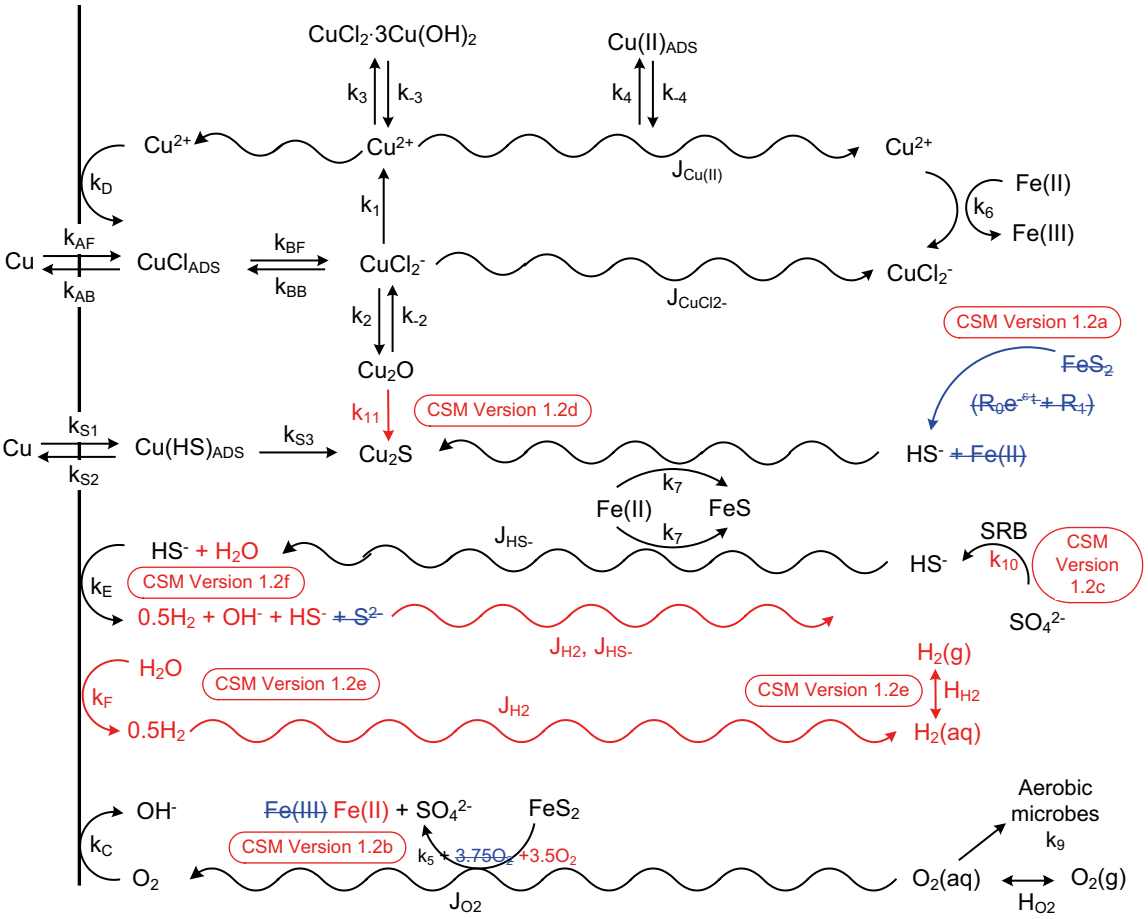

Figure 2-4. *Reaction mechanism for CSM Versions 1.2a to 1.2f. The red-highlighted processes indicate the additions made to the earlier CSM Version 1.1eq reaction mechanism and the blue struck-through items identify those processes deleted from the earlier version.*

Based on these changes, the MBE for O_2 for Version 1.2b is given by:

$$\frac{\partial}{\partial t}\left(\varepsilon_a\left[S+(1-S)\tilde{H}_O\right]c_0\right)=\frac{\partial}{\partial x}\left(\tau_f\varepsilon_e\left[SD_0+(1-S)^3D_A\tilde{H}_O\right]\frac{\partial c_0}{\partial x}\right) \\ -\varepsilon_a S\left[\frac{k_1}{4}c_0c_1+3.5A_Pk_5c_0^{1/2}\theta(c_{10})+k_9c_0\theta(S-S_{MIC})\right] \quad (2\text{-}23)$$

and the MBE for Fe(II) is:

$$\varepsilon_a\frac{\partial(Sc_7)}{\partial t}=\frac{\partial}{\partial x}\left(\tau_f\varepsilon_eSD_7\frac{\partial c_7}{\partial x}\right)+\varepsilon_aSA_P[R_0e^{-\alpha_Pt}+R_1]\theta(c_{10}) \\ +\varepsilon_aSA_pk_5c_0^{1/2}\theta(c_{10})-\varepsilon_aS[k_6c_3c_7+k_7\max(0,c_7-c_7^{sat})c_9] \quad (2\text{-}24)$$

The $(R_0e^{-\alpha_pt}+R_1)$ term in Equation (2-24) represents the time-dependent dissolution of an Fe(II)-containing solid phase based on a shrinking core mechanism. Here it is used to represent the anaerobic dissolution of pyrite, but a similar expression is also used in other versions of the CSM to represent the release of Fe(II) from the dissolution of biotite. In both cases, the R_1 term represents the instantaneous dissolution rate and the time-dependent exponential term represents the longer-term release controlled by the build-up of an Fe(II)-depleted layer around an unaltered core.

The intermediate version of the CSM incorporating these changes is CSM Version 1.2b. As noted above, these changes were applied to the original CSM Version 1.1eq, **not** to the new Version 1.2a. Thus, Version 1.2b retains the reactions for the anaerobic dissolution of FeS_2.

The values for k_5 and ΔH_5 remain the same for Version 1.2b.

Simulations with CSM Version 1.2b

This modification involves changes to the MBE only and does not introduce new parameters. Therefore, a single simulation was run using the same input parameters as the 9-layer simulation for Version 1.1eq (Table 2-4).

2.3.3 Microbial reduction of sulfate

In the CSM Version 1.1eq, the microbial reduction of sulfate is treated as a zero-order kinetic expression based on the stoichiometry:

$$SO_4^{2-} + 5H_2O + 8e^- \xrightarrow{k_{10}} HS^- + 9OH^- \quad (2\text{-}25)$$

and proceeds subject to the *presence* of SO_4^{2-} (but not its concentration) and a threshold degree of saturation for microbial activity S_{MIC}. No attempt is made to model the population of sulfate-reducing bacteria (SRB) or to achieve electron-balance for this reaction. The value of k_{10} is derived from the study of Masurat et al. (2010) and an activation energy of 60 000 J/mol is assumed.

For the updated version of the model (Version 1.2c), the sulfate reduction reaction is modified to be first-order with respect to the sulfate concentration; namely:

$$-\frac{d[SO_4^{2-}]}{dt} = \frac{d[HS^-]}{dt} = k_{10}[SO_4^{2-}]\theta(S - S_{MIC}) \quad (2\text{-}26)$$

This then results in changes to the MBE for HS^- (species 9) and SO_4^{2-} (species 11); namely

$$\varepsilon_a \frac{\partial(Sc_9)}{\partial t} = \frac{\partial}{\partial x}\left(\tau_f \varepsilon_e S D_9 \frac{\partial c_9}{\partial x}\right) + \varepsilon_a S \left[\begin{matrix} k_{10} c_{11} \theta(S - S_{MIC}) + 1.5 A_P (R_0 e^{-\alpha_P t} + R_1)\theta(c_{10}) \\ -k_7 \max(0, c_7 - c_7^{sat}) c_9 \end{matrix}\right] \quad (2\text{-}27)$$

and

$$\varepsilon_a \frac{\partial(Sc_{11})}{\partial t} = \frac{\partial}{\partial x}\left(\tau_f \varepsilon_e S D_{11} \frac{\partial c_{11}}{\partial x}\right) + \varepsilon_a S\left[2 A_P k_5 c_0^{1/2} \theta(c_{10}) - k_{10} c_{11} \theta(S - S_{MIC})\right] \quad (2\text{-}28)$$

As part of the joint SKB-Posiva Integrated Sulfide Project, the rate of sulfate reduction by SRB in compacted bentonite has been determined by Bengtsson et al. (2017). The rate of sulfate reduction is based on the measured amount of Cu_2S formation on copper samples. The rate of sulfate reduction is then back-calculated based on assumed diffusion coefficients for SO_4^{2-} and HS^-. There is a lot of scatter in the data, but the maximum rate for MX-80 with a density of 2 000 kg·m^{-3} is 6.1×10^{-9} mol·m^{-3}·s^{-1}. Bengtsson et al. (2017) also give a measured sulfate concentration in the pore water, but not the concentration of organic carbon.

It is not clear from the report of Bengtsson et al. (2017) whether the rate of sulfate reduction is expressed per unit volume of pore water or per unit volume of HCB. Given the variability in the estimated rate, this uncertainty is relatively minor and it is assumed here that the reported rate refers to the pore volume only. Thus, the experimental value of 6.1×10^{-9} mol·m^{-3}·s^{-1} is equivalent to the term $d[SO_4^{2-}]/dt$ in Equation (2-26).

In order to determine the value of k_{10}, we need a value for the corresponding pore-water $[SO_4^{2-}]$. Bengtsson et al. (2017) report the results of leaching experiments on fresh bentonite and from samples taken from the experiments, expressed as a total concentration in the corresponding pore water for the given HCB density. The authors reported that the amount of sulfate leached was independent of the amount of water added and that no sulfate was leached after a second contact, the implication being that the reported sulfate concentrations represent the actual pore-water composition.

The concentration of leachable sulfate decreased during the course of the experiment. This decrease is presumably a consequence of both sulfate reduction and diffusive loss into the solution phase surrounding the HCB. The reported initial pore-water sulfate concentration for MX-80 bentonite was 0.04–0.06 mol/L (Bengtsson et al. 2017). Following the tests, the remaining sulfate concentration ranged from 0.01–0.15 mol/L (Bengtsson et al. 2017, Figure 3-5). The mean sulfate concentration during the experiment is assumed here to be 0.1 mol/L. Based on the reported rate of sulfate reduction of 6.1×10^{-9} mol·m^{-3}·s^{-1} (6.1×10^{-12} mol·dm^{-3}·s^{-1}), the value of k_{10} is, therefore, 6.1×10^{-11} s^{-1}.

The intermediate version of the CSM incorporating these changes is CSM Version 1.2c (Table 2-1).

Simulations with CSM Version 1.2c

Two runs were performed with Version 1.2c, in which microbial activity was either allowed or not allowed to occur in the bentonite (and Cu_2S film) (Table 2-4).

- Run 1.2c1: $S_{MIC} = 1$ (microbial activity not allowed in layers 1, 2, 3, and 4).
- Run 1.2c2: $S_{MIC} = 0$ (microbial activity allowed in layers 1, 2, 3, and 4).

2.3.4 Conversion of cuprous oxide to cuprous sulfide

There is evidence that Cu_2O is converted to Cu_2S in the presence of HS^- most likely due to an irreversible chemical conversion process, which can be described stoichiometrically as (Smith et al. 2007a):

$$Cu_2O + HS^- \rightarrow Cu_2S + OH^- \quad (2\text{-}29)$$

This change in the mechanism is likely to result in relatively minor changes to the results of the model. Typically, we predict the formation of a maximum of 10^{-5} mol/dm^2 of Cu_2O compared with > 0.1 mol/dm^2 of Cu_2S. The Cu_2O that is formed is currently predicted to dissolve as $CuCl_2^-$ prior to the end of the simulation.

The experimental data of Smith et al. (2007a) suggest that Reaction (2-29) is rapid. Here we assume first-order kinetics with respect to both [Cu_2O] and [HS^-] (i.e., second-order overall), with a pseudo first-order rate constant of 1.99×10^{-4} s^{-1} determined from the decrease in the amount of Cu_2O with time upon exposure to 10^{-4} mol/L HS^- reported by Smith et al. (2007a). Thus, the second order rate constant is $k_{11} = 1.99$ dm^3·mol^{-1}·s^{-1}. In the absence of any specific information, we assume an activation energy of 60 000 J/mol.

This modification to the reaction mechanism (Figure 2-4), requires changes to the MBE for Cu_2O (species c_2) and HS^- (species c_9) and for the expression by which we track the amount of Cu_2S formed (Cu_2S is not assigned an MBE in Version 1.1eq).

The expressions for the loss of Cu_2O and HS^- (and for the gain of Cu_2S) due to this process are given by:

$$-\frac{\partial c_2}{\partial t} = -\frac{\partial c_9}{\partial t} = k_{11} c_9 c_2 \quad (2\text{-}30)$$

Clearly, conversion of Cu_2O only occurs as long as Cu_2O exists.

The revised MBE for Cu_2O is given by:

$$\frac{\partial c_2}{\partial t} = \varepsilon_a S \frac{k_2}{2} \max(0, c_1 - c_1^{sat}) - k_{-2} c_2 - S \varepsilon_a k_{11} c_9 c_2 \quad (2\text{-}31)$$

and the revised MBE for HS^- is given by:

$$\varepsilon_a \frac{\partial (Sc_9)}{\partial t} = \frac{\partial}{\partial x}\left(\tau_f \varepsilon_e S D_9 \frac{\partial c_9}{\partial x}\right) + \varepsilon_a S \begin{bmatrix} k_{10}\theta(c_{11})\theta(S - S_{MIC}) + 1.5 A_P (R_0 e^{-\alpha_P t} + R_1)\theta(c_{10}) \\ -k_7 \max(0, c_7 - c_7^{sat}) c_9 - k_{11} c_9 c_2 \end{bmatrix} \quad (2\text{-}32)$$

As for other intermediate versions of the code, these changes to the MBE are applied to the equations from Version 1.1eq, *not* to earlier intermediate versions of Version 1.2.

The intermediate version of the CSM incorporating these changes is CSM Version 1.2d (Table 2-1).

Simulations with CSM Version 1.2d

A single run with Version 1.2d was performed using the new parameter values (Table 2-4):

- $k_{11} = 1.99$ dm^3·mol^{-1}·s^{-1}
- activation energy DeH11 = 60 000 J/mol

2.3.5 Cathodic reduction of water

In Version 1.1eq, the three cathodic reactions are the reduction of the proton in the HS^- ion under anaerobic conditions and the reduction of either O_2 or Cu^{2+} under aerobic conditions (Figure 2-3). The nature of the cathodic reaction under anaerobic conditions is debated (Macdonald et al. 2016), and could involve the reduction of H_2O as well as, or instead of, the reduction of HS^-. The nature of the

cathodic reactant may be important when we consider the possible spatial separation of the anodic and cathodic reactions as the reduction of HS^- is likely to be transport limited (and, therefore, dependent only on the geometric surface area), whereas H_2O is assumed to be in plentiful supply and its reduction will not be transport limited. The equilibrium potentials for the HS^-/H_2 and H_2O/H_2 couples are also likely to be different and may impact the value of E_{CORR}.

Hydrogen was not accounted for in Version 1.1eq. For Version 1.2e, both gaseous and dissolved H_2 will be considered, requiring additional MBE and the definition of the associated interfacial (left-hand) and right-hand boundary conditions. Because the rate of H_2 generation could be relatively slow (equivalent to a corrosion rate of the order of 1 nm/yr, SKB 2010), it is not unreasonable to assume that transport of H_2 will occur by diffusion of dissolved and/or gaseous H_2 only and that we do not need to consider the build-up and release of H_2 at elevated pressure as is necessary when modelling the corrosion of C-steel canisters (King et al. 2014).

For the CSM Version 1.2e, we treat dissolved and gaseous H_2 as being in equilibrium (based on Henry's law) and then eliminate the MBE for gaseous H_2.

In summary, the changes to the CSM V1.1eq to accommodate the addition of the reduction of H_2O as a cathodic reaction involve:

1. Addition of another cathodic interfacial process, with the rate given by a corresponding Butler–Volmer expression.
2. Modification of the left-hand boundary condition and mixed-potential model.
3. Introduction of new MBEs for dissolved and gaseous H_2, with the two species assumed to be in equilibrium according to Henry's law.

These modifications result in changes to the number and nomenclature of species in the CSM (Table 2-5). Dissolved H_2 is produced by the cathodic reduction of both HS^- and H_2O and can diffuse away from the corroding interface, but does not otherwise react with any other species in the model (other than being in equilibrium with gaseous H_2). Gaseous H_2 can similarly diffuse to and away from the canister surface, but again does not otherwise react with any other species in the model (other than being in equilibrium with dissolved H_2). The modified reaction scheme is shown in Figure 2-4.

The interfacial reduction of H_2O is given by:

$$H_2O + e^- \rightarrow \tfrac{1}{2}H_2 + OH^- \quad (2\text{-}33)$$

for which the corresponding Butler–Volmer expression is given by:

$$i_F = -n_F F \varepsilon_{film} k_F \exp\left\{-\frac{\alpha_F F}{RT}(E - E_F^0)\right\} \quad (2\text{-}34)$$

where the reaction is denoted by the subscript F (Figure 2-4).

Table 2-5. Extended list of species for the CSM Version 1.2e.

Notation	Species	Species Name
c_A	$O_2(g)$	Gaseous oxygen
c_0	$O_2(aq)$	Dissolved oxygen
c_1	$CuCl_2^-$	Dissolved cuprous chloride complex ion
c_2	Cu_2O	Precipitated cuprous oxide
c_3	Cu^{2+}	Dissolved cupric ions
c_4	$CuCl_2{\cdot}3Cu(OH)_2$	Precipitated basic cupric chloride
c_5	Cu(II)(ads)	Adsorbed cupric species
c_6	Cl^-	Dissolved chloride ions
c_7	Fe(II)(aq)	Dissolved ferrous ions
c_8	FeS	Precipitated ferrous sulfide
c_9	HS^-	Dissolved sulfide ions
c_{10}	FeS_2	Pyrite
c_{11}	SO_4^{2-}	Sulfate ions
c_{12}	$H_2(aq)$	Dissolved H_2
c_{13}	$H_2(g)$	Gaseous H_2
T	-	Temperature

The values of the various electrochemical parameters are (Appendix A):

- kFroom ($k_F = 6.8 \times 10^{-9}$ mol·dm^{-2}·s^{-1})
- DeHF ($\Delta H_F = 31\,200$ J/mol)
- nF ($n_F = 1$)
- alfaF ($\alpha_F = 0.15$)
- E0Froom ($E_F^0 = -0.764$ V_{SCE})
- DeE0F ($dE_F^0/dT = -0.0019$ V/K)

The addition of another interfacial electrochemical process requires changes to the left-hand boundary conditions and the mixed-potential expression. At the corrosion potential (E_{CORR}), the sum of the anodic and cathodic current densities is zero and is given by:

$$i_A(t) + i_C(t) + i_D(t) + i_E(t) + i_F(t) + i_S(t) = 0 \tag{2-35}$$

The interfacial flux of dissolved H_2 (species 12) is given by:

$$\frac{i_E}{n_E} + \frac{i_F}{n_F} = 2FS\tau_f\varepsilon_e\left[D_{12}S + (1-S)^3 D_{13}\tilde{H}_H\right]\frac{\partial c_{12}}{\partial x}\Big|_{x=0} \tag{2-36}$$

For the current work, a zero-flux right-hand boundary condition has been used for dissolved H_2. The new MBEs introduced for dissolved hydrogen (species 12) and gaseous H_2 (species 13) are given by:

$$\frac{\partial(\varepsilon_a S c_{12})}{\partial t} = \frac{\partial}{\partial x}\left(\tau_f\varepsilon_e S D_{12}\frac{\partial c_{12}}{\partial x}\right) + R_H \tag{2-37}$$

where R_H is the rate constant for the dissolution of H_2.

The MBE for gaseous H_2 (species 13) is given by:

$$\frac{\partial((1-S)\varepsilon_a c_{13})}{\partial t} = \frac{\partial}{\partial x}\left(\tau_f\varepsilon_e(1-S)^3 D_{13}\frac{\partial c_{13}}{\partial x}\right) - R_H \tag{2-38}$$

However, the reaction rate R_H between dissolved and gaseous H_2 is assumed to be fast so that equilibrium can be assumed

$$c_{13} = \tilde{H}_H c_{12} \tag{2-39}$$

where $\tilde{H}_H$ is the inverse Henry's law constant for H_2. Equations (2-37) and (2-38) can then be combined to a single MBE

$$\frac{\partial}{\partial t}\left(\varepsilon_a\left[S + (1-S)\tilde{H}_H\right]c_{12}\right) = \frac{\partial}{\partial x}\left(\tau_f\varepsilon_e\left[SD_{12} + (1-S)^3 D_{13}\tilde{H}_H\right]\frac{\partial c_{12}}{\partial x}\right) \tag{2-40}$$

Based on Sander (1999), the mean value for the Henry's law constant for H_2 is 7.8×10^{-4} mol·dm^{-3}·atm^{-1} at 25 °C, corresponding to the expression c_{12}/p_{13} where p_{13} is the pressure of gaseous H_2. At 25 °C, 1 atm of an ideal gas is equivalent to a concentration of 0.040876 mol·dm^{-3}·atm^{-1}. Thus, the inverse Henry's law constant for H_2 is given by

$$\tilde{H}_H = \frac{1}{H_H} = \frac{0.040876 \text{mol dm}^{-3}\text{atm}^{-1}}{7.8\text{x}10^{-4}\text{mol dm}^{-3}\text{atm}^{-1}} = 52.4 \tag{2-41}$$

The temperature dependence of the Henry's law constant (and, by inference, of the inverse Henry's law constant) is described by an Arrhenius relationship. The activation energy for $\tilde{H}_H$ will be equal but of opposite sign to that of H_H. The mean activation energy for H_H according to Sander (1999) is 4 500 J/mol, so that for $\tilde{H}_H$ is taken to be

$$\Delta H_{\tilde{H}_H} = -4{,}500 \text{ J/mol} \tag{2-42}$$

Simulations with CSM Version 1.2e

A single run with Version 1.2e was performed using the new parameter values defined below (Table 2-4):

- kFroom ($k_F = 6.8 \times 10^{-9}$ mol·dm^{-2}·s^{-1})
- DeHF ($\Delta H_F = 31\,200$ J/mol)
- nF ($n_F = 1$)
- alfaF ($\alpha_F = 0.15$)
- E0Froom ($E_F^0 = -0.764$ V_{SCE})
- DeE0F ($dE_F^0/dT = -0.0019$ V/K)
- $\widetilde{H}_H = 52.4$
- $\Delta H_{\tilde{H}_H} = -4\,500$ J/mol

2.3.6 Improvement to treatment of cathodic reduction of sulfide

For the CSM Version 1.1/1.1eq, the interfacial reduction of HS^- to produce H_2 (rate constant k_E) was described by (Figure 2-3):

$$HS^- + e^- \rightarrow \tfrac{1}{2}H_2 + S^{2-} \quad (2\text{-}43)$$

Because S^{2-} (sulfide anion) is not a species included in the model, we do not properly account for the total amount of sulfide being transported to the canister surface. In other words, the S^{2-} product is lost from the system. This is an important omission for a system in which the corrosion rate is likely to be controlled by the rate of supply of sulfide to the canister surface.

Furthermore, the species S^{2-} does not exist in aqueous solutions at normal pH values and would immediately convert to HS^- by reaction with H_2O:

$$H_2O + S^{2-} \rightleftarrows HS^- + OH^- \quad (2\text{-}44)$$

We can re-write the interfacial reaction for the reduction of HS^- as (Figure 2-4):

$$HS^- + H_2O + e^- \rightarrow \tfrac{1}{2}H_2 + HS^- + OH^- \quad (2\text{-}45)$$

using the same values for the various electrochemical parameters describing the rate of this interfacial reaction. In this way, the sulfide species is conserved and not lost from the system.

There is no need to adjust the MBE for HS^- (species 9) or the electrochemical expression for the reduction of HS^- as a result of the change in mechanism, but there is a need to change the equation relating the interfacial flux of HS^- to the various current densities for the reactions involving HS^-.

The existing relationship between the sulfide flux and the current densities for reactions involving HS^- is:

$$-\frac{i_S}{n_S} + \frac{i_E(t)}{n_e} = -FS\tau_f\varepsilon_e D_9 \frac{\partial c_9(0,t)}{\partial x} \quad (2\text{-}46)$$

Because HS^- is no longer consumed by Reaction E (Figure 2-4), this equation should read:

$$-\frac{i_S}{n_S} = -FS\tau_f\varepsilon_e D_9 \frac{\partial c_9(0,t)}{\partial x} \quad (2\text{-}47)$$

Simulations with CSM Version 1.2f

This modification involves changes to the left-hand boundary conditions only and does not introduce new parameters. Therefore, a single run using the same input parameters as the 9-layer reference simulation Run 1.1eq(a) was performed (Table 2-4).

2.3.7 Improved treatment of microbial sulfate reduction

There are a number of issues with the current treatment of SRB activity, even following the improved treatment in V1.2c. These issues include:

- Microbial activity is limited only by the availability of SO_4^{2-} and the threshold water activity (a_W), and implicitly assumes sufficient nutrient and organic carbon.
- Because gypsum is not included as a species in the code, the entire inventory is assumed to be immediately dissolved in the bentonite pore water in order that the availability of sulfate from this source is not under-estimated. However, since the sulfate reduction kinetics are assumed to be first-order with respect to $[SO_4^{2-}]$ in Version 1.2c, this then results in very high sulfate reduction kinetics and all of the sulfate is consumed within a short period at the start of the simulation.
- The current treatment does not take into account the available biomass or microbial growth or death.
- Since there is no longer a source of dissolved Fe(II) following the removal of the anaerobic dissolution of pyrite (V1.2a), there is no way to simulate the precipitation of FeS as a sink for sulfide produced from sulfate reduction.

King et al. (1999) previously developed the Microbial Activity Model (MAM) to predict the effect of sulfate reduction on the extent of copper corrosion. Both chemotrophic (based on H_2 as an energy source) and organotrophic (based on dissolved organic carbon as an energy source, represented by acetate in the model) sulfate reduction were modelled using Monod kinetic expressions that incorporated the effect of biomass. Microbial growth, death, and the recycling of dead cell material were considered. Precipitation of FeS was also included in the model. A similar treatment is incorporated here into the CSM, but excluding the effects of radiation on microbial activity/mortality and the radiolytic production of acetate and H_2 considered by King et al. (1999).

The incorporation of a more-complex microbial sulfate reduction scheme requires the addition of a number of new species into the model:

- Gypsum ($CaSO_4 \cdot 2H_2O$).
- Organic carbon (dissolved and un-dissolved).
- Biotite ($K(Mg_{0.6–1.8}Fe^{II}_{2.4–1.2})(Si_3Al)O_{10}(OH,F)_2$.
- A second Fe(II)-containing solid phase (e.g., siderite $FeCO_3$).
- Chemotrophic and organotrophic SRB.

The inclusion of gypsum as a species avoids the need to initially dissolve the entire inventory and allows the dissolution (and precipitation) to be explicitly modelled. Similarly, by including both dissolved and solid organic carbon we can simulate the possibly slow release of organic carbon from the bentonite. The inclusion of two additional Fe(II)-bearing species allows additional sources of Fe(II) to be included, thus allowing the potentially important precipitation of FeS to be simulated. Finally, both chemotrophic and organotrophic sulfate-reduction pathways are included in the model, as are the growth, death, and recycling of cell material.

Table 2-6 list the species and corresponding notation for CSM Version 1.2g and Figure 2-5 illustrates the additions and deletions made to the reaction scheme for Version 1.2a to V1.2f inclusive.

Table 2-6. List of species and their notation for CSM Version 1.2g and for any version incorporating the improved treatment of microbial sulfate reduction.

Notation	Species	Species Name
c_A	$O_2(g)$	Gaseous oxygen
c_0	$O_2(aq)$	Dissolved oxygen
c_1	$CuCl_2^-$	Dissolved cuprous chloride complex ion
c_2	Cu_2O	Precipitated cuprous oxide
c_3	Cu^{2+}	Dissolved cupric ions
c_4	$CuCl_2 \cdot 3Cu(OH)_2$	Precipitated basic cupric chloride
c_5	Cu(II)(ads)	Adsorbed cupric species
c_6	Cl^-	Dissolved chloride ions
c_7	Fe(II)(aq)	Dissolved ferrous ions
c_8	FeS	Precipitated ferrous sulfide
c_9	HS^-	Dissolved sulfide ions
c_{10}	FeS_2	Pyrite
c_{11}	SO_4^{2-}	Sulfate ions
c_{12}	$H_2(aq)$	Dissolved H_2
c_{13}	$H_2(g)$	Gaseous H_2
c_{14}	$Cu_2S(s)$	Precipitated Cu_2S
c_{15}	$CaSO_4 \cdot 2H_2O$	Gypsum
c_{16}	$CH_3CO_2H(aq)$	Dissolved organic carbon (as acetic acid)
c_{17}	-	Solid organic carbon
c_{18}	-	Biotite
c_{19}	-	Siderite
B_1	SRB_1	Organotrophic SRB
B_2	SRB_2	Chemotrophic SRB
T	-	Temperature

Gypsum ($CaSO_4 \cdot 2H_2O$) is present as an accessory mineral in the bentonite and will act as a source of SO_4^{2-} that may then be reduced by SRB. Gypsum is assumed to dissolve subject to a saturation limit for sulfate (c_{11}^{sat}) based on an assumed solubility-determining phase. The dissolution reaction can be written as:

$$CaSO_4 \cdot 2H_2O \xrightarrow{k_{12}} Ca^{2+} + SO_4^{2-} + 2H_2O \quad (2\text{-}48)$$

The rate of dissolution, expressed as the rate of loss of gypsum or the rate of increase in SO_4^{2-} concentration, is given by:

$$-\frac{dc_{15}}{dt} = \frac{dc_{11}}{dt} = k_{12}[\theta(c_{15})\theta(c_{11}^{sat} - c_{11}) + \theta(c_{11} - c_{11}^{sat})](c_{11}^{sat} - c_{11}) \quad (2\text{-}49)$$

Thus, if gypsum is present ($c_{15} > 0$), it will dissolve at a rate determined by the degree of under-saturation of the solution ($c_{11}^{sat} - c_{11}$). If the solution is over-saturated with SO_4^{2-} (i.e., $c_{11} > c_{11}^{sat}$), then gypsum will precipitate. Such a situation could possibly arise as a result of a decrease in solubility as the temperature changes, but this mathematical construct is also included in the model to simulate the reversibility of gypsum dissolution/precipitation.

Gypsum is assumed to be the solubility-limiting calcium sulfate phase (as opposed to anhydrite or hemihydrate), with the solubility dependent on temperature based on the following polynomial derived from the fitting of experimental data in King et al. (2017a)

$$c_{11}^{sat} = 0.01290774 + 1.472958 \times 10^{-4}(T\text{-}273.15) - 2.384728 \times 10^{-6}(T\text{-}273.15)^2 + 8.292306 \times 10^{-9}(T\text{-}273.15)^3 \quad (2\text{-}50)$$

where c_{11}^{sat} is in units of $mol \cdot dm^{-3}$ and T is the temperature (in K).

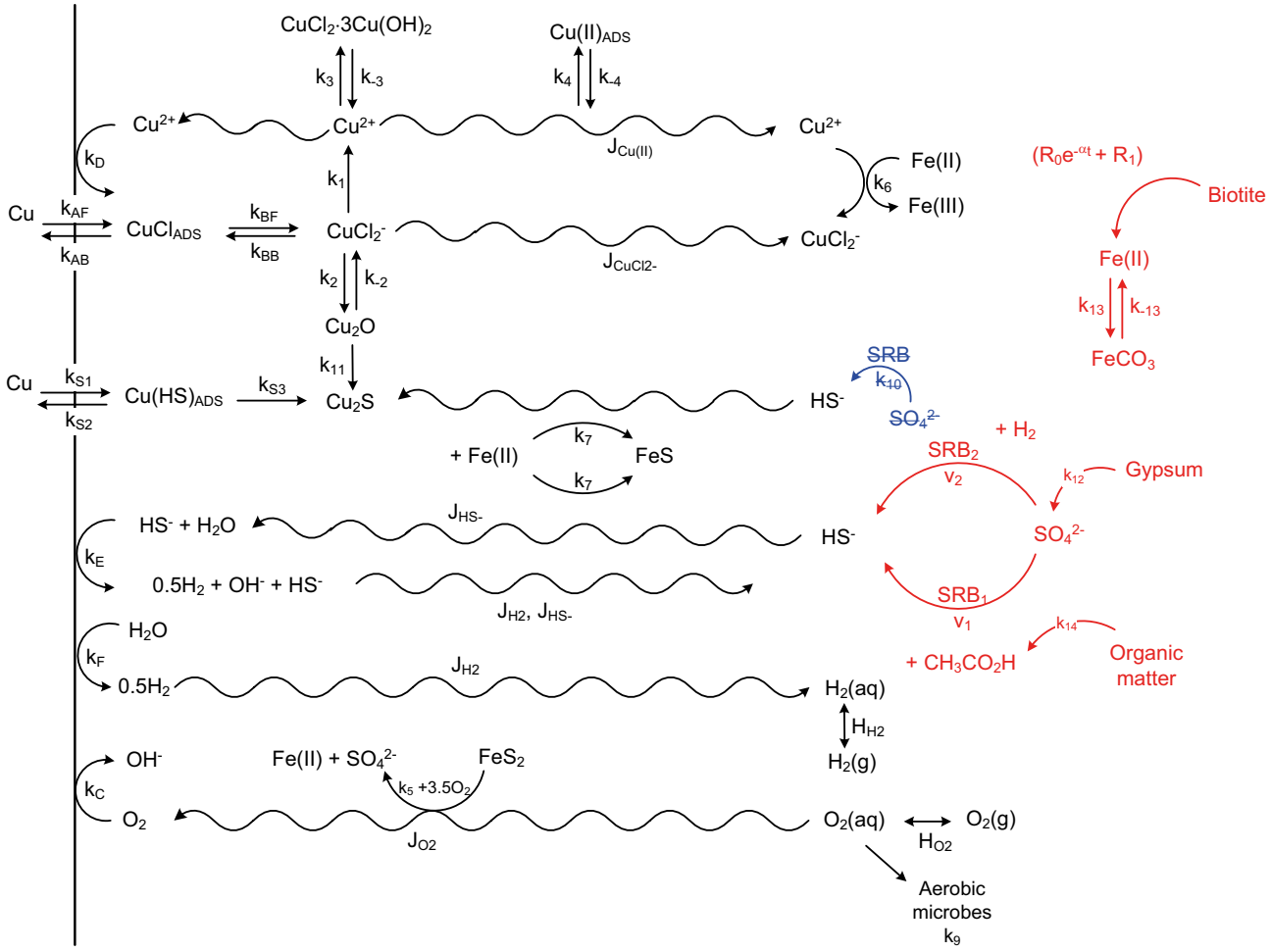

Figure 2-5. *Reaction scheme for CSM Version 1.2a-g. Additions to the reaction scheme used for Versions 1.2a to 1.2f inclusive are shown in red font and deletions shown in struck-through blue font.*

Above temperatures of approximately 40 °C, anhydrite is the solubility-limiting phase, with gypsum controlling the solubility at lower temperatures (King et al. 2017a). Therefore, the assumption that gypsum determines the solubility at all temperatures is conservative for T > 40 °C, as it results in higher $[SO_4^{2-}]$ and hence higher rates of sulfide formation, and realistic at lower temperatures.

Because of the importance of iron sulfides in controlling sulfide solubility and of Fe(II) in potentially acting as a sink for HS^-, two additional Fe(II)-bearing solids have been included in the reaction scheme for CSM V1.2g. One of these solid phases (typically taken to represent the biotite in the host rock) is assumed to dissolve via a shrinking-core mechanism

$$\text{Biotite} \xrightarrow{R_0 e^{-\alpha_F t} + R_1} \text{Fe(II)(aq)} \tag{2-51}$$

with the following kinetics

$$\frac{dc_7}{dt} = -\frac{dc_{18}}{dt} = \theta(c_{18}) A_F [R_0 e^{-\alpha_F t} + R_1] \tag{2-52}$$

where c_{18} is the concentration of biotite (expressed in terms of the number of equivalent moles of Fe(II) per unit volume of the system). Biotite is assumed to be present in a limited quantity, the amount of which is defined initially for each layer (material) in the model (c_{18}^{init}).

The other solid phase (typically taken to represent iron carbonate (siderite) $FeCO_3$ present in the host rock or the buffer and backfill materials) dissolves or precipitates based on the degree of under- or over-saturation of the solution, respectively:

$$\text{Fe(II)} + HCO_3^- \underset{k_{-13}}{\overset{k_{13}}{\rightleftarrows}} FeCO_3 + H^+ \tag{2-53}$$

Bicarbonate (HCO_3^-) is not tracked in the model and is assumed to be present in excess (from the dissolution of calcite).

The corresponding kinetic expression is given by:

$$-\frac{dc_7}{dt} = \frac{dc_{19}}{dt} = k_{13} \max(0, c_7 - c_7^{satFeCO3}) - k_{-13} c_{19} \quad (2\text{-}54)$$

where c_{19} is the concentration of siderite and $c_7^{satFeCO3}$ is the concentration of Fe(II)(aq) in equilibrium with $FeCO_3$. The value of $c_7^{satFeCO3}$ is defined based on a pore-water HCO_3^- concentration assumed to be controlled by the solubility of calcite.

Note, $c_7^{satFeCO3}$ is different from c_7^{sat}, which is the concentration of Fe(II) in equilibrium with FeS. Thus, Fe(II) can precipitate as either $FeCO_3$ (reversibly) or FeS (irreversibly). The fraction that precipitates as each phase will be determined by the relative degrees of under-saturation, the respective rate constants, and, for FeS, the HS^- concentration.

One of the two types of SRB (organotrophic SRB1) uses organic C as an energy source. Both types of SRB use organic C to build cell material. In addition, recycling of dead microbial cell material will produce organic C. Organic C is present initially as a solid in the buffer and backfill materials and could be present in the ground water as dissolved organic C. Only a fraction of the solid organic C is soluble and potentially available for microbial activity.

In the CSM V1.2g, all organic C (solid and dissolved) is assumed to be present in the form of acetic acid (CH_3CO_2H). Only dissolved organic C can participate in microbial processes. The solid organic carbon dissolves irreversibly (i.e., it does not form solid C if there is an excess in solution), but there is a maximum dissolved organic C concentration (c_{16}^{sat})

$$\text{Solid organic C} \xrightarrow{k_{14}} CH_3CO_2H \quad (2\text{-}55)$$

for which the rate expression is:

$$\frac{dc_{16}}{dt} = -\frac{dc_{17}}{dt} = \theta(c_{17}) k_{14} \max(0, c_{16}^{sat} - c_{16}) \quad (2\text{-}56)$$

where c_{16} and c_{17} are the concentrations of dissolved and solid organic C, respectively.

As in the MAM (King et al. 1999), two types of SRB are included in the CSM V1.2g; one that uses organic carbon (CH_3CO_2H) (organotrophic, SRB1) and one that uses H_2 (chemotrophic, SRB2) as the source of energy. Both types of microbe use CH_3CO_2H to build cell material. The various microbial characteristics incorporated into the CSM V1.2g include:

- Two types of SRB, one organotrophic (SRB1) and one chemotrophic (SRB2).
- Microbial growth occurs as a result of metabolism (using CH_3CO_2H as C source).
- Cell death occurs with recycling of a fraction of the dead cell material into dissolved organic C (Lovely and Klug 1986).
- The rate of microbial processes is described by Monod kinetic expressions, with an optimum temperature (usually 39 °C, but 25 °C for ISP inter-model comparison exercise) and lower rates at higher and lower temperatures subject to minimum (5 °C) and maximum (60 °C) temperatures below and above which the rate is zero.
- Microbial dormancy occurs as a result of low water activity (< 0.96 (Brown 1990)).
- No diffusion of microbes.

For the ISP inter-model comparison exercise (Section 5), the microbial population was treated as constant with neither the growth nor death of cells.

The two sulfate reduction reactions can be written as:

$$SO_4^{2-} + CH_3CO_2H + H^+ \xrightarrow{SRB1, v_1} 2CO_2 + HS^- + 2H_2O \quad (2\text{-}57)$$

$$SO_4^{2-} + 4H_2 + H^+ \xrightarrow{SRB2, v_2} HS^- + 4H_2O \quad (2\text{-}58)$$

where we do not track either H^+, CO_2, or H_2O in the code.

The corresponding rate expressions are

$$-\frac{dc_{11}}{dt} = -\frac{dc_{16}}{dt} = \frac{dc_9}{dt} = \theta(S - S_{MIC})v_1 \quad (2\text{-}59)$$

and

$$-\frac{dc_{11}}{dt} = -\frac{1}{4}\frac{dc_{12}}{dt} = \frac{dc_9}{dt} = \theta(S - S_{MIC})v_2 \quad (2\text{-}60)$$

where

$$v_1 = \frac{\mu_1^{max}}{Y_1} B_1 \left(\frac{c_{11}}{K_{111}+c_{11}}\right)\left(\frac{c_{16}}{K_{16}+c_{16}}\right) \exp\left[\frac{\Delta H_{B_1}^{T\le T_{opt1}}}{R}\left(\frac{1}{T} - \frac{1}{T_{opt1}}\right)\right] \quad (2\text{-}61)$$

for $T_{min1} < T \le T_{opt1}$

and

$$v_1 = \frac{\mu_1^{max}}{Y_1} B_1 \left(\frac{c_{11}}{K_{111}+c_{11}}\right)\left(\frac{c_{16}}{K_{16}+c_{16}}\right) \exp\left[\frac{\Delta H_{B_1}^{T>T_{opt1}}}{R}\left(\frac{1}{T} - \frac{1}{T_{opt1}}\right)\right] \quad (2\text{-}62)$$

for $T_{opt1} < T < T_{max1}$.

Similarly for SRB2

$$v_2 = \frac{\mu_2^{max}}{Y_2} B_2 \left(\frac{c_{11}}{K_{112}+c_{11}}\right)\left(\frac{c_{12}}{K_{12}+c_{12}}\right) \exp\left[\frac{\Delta H_{B_2}^{T\le T_{opt2}}}{R}\left(\frac{1}{T} - \frac{1}{T_{opt2}}\right)\right] \quad (2\text{-}63)$$

and

$$v_2 = \frac{\mu_2^{max}}{Y_2} B_2 \left(\frac{c_{11}}{K_{112}+c_{11}}\right)\left(\frac{c_{12}}{K_{12}+c_{12}}\right) \exp\left[\frac{\Delta H_{B_2}^{T>T_{opt2}}}{R}\left(\frac{1}{T} - \frac{1}{T_{opt2}}\right)\right] \quad (2\text{-}64)$$

where μ_i^{max} and Y_i are the respective maximum specific growth rate and biomass yield coefficient for the two reactions (i = 1,2). For ease of presentation, we define $v_1^{max} = \mu_1^{max}/Y_1$ and $v_2^{max} = \mu_2^{max}/Y_2$.

In addition to being consumed in the organotrophic sulfate reduction reaction, CH_3CO_2H is also used to build cell material. The amount of CH_3CO_2H used for cell growth depends on (i) how much energy is produced by the reaction and (ii) the source of N used to build cells (as the stoichiometry depends on whether N comes from, say, ammonia or nitrate). Here, we will assume that cells (assumed molecular formula $C_5H_7O_2N$) are produced from ammonium ions NH_4^+ according to

$$5/2\ CH_3CO_2H + NH_4^+ \rightarrow C_5H_7O_2N + H^+ + 3H_2O \quad (2\text{-}65)$$

The energy generated by each of the electron-transfer reactions (Equations (2-57) and (2-58)) is converted to an appropriate amount of ATP (adenosine 5'-triphosphate) and then to an equivalent number of grams of cell material, defined here by the corresponding coefficient a_{1B} and a_{2B}, respectively.

As well as being consumed in cell growth, a fraction of the dead cell material (K_{R1} and K_{R2}, for SRB1 and SRB2 respectively) is recycled back into CH_3CO_2H. The fractional death rate of cells is denoted by b_{1B} and b_{2B} for the organotrophic and chemotrophic SRB, respectively.

As a result of these changes, new or updated MBE are required for Fe(II)(aq) (species 7), HS^- (species 9), SO_4^{2-} (species 11), H_2(aq) (species 12), gypsum (species 15), CH_3CO_2H (species 16), solid organic C (species 17), biotite (species 18), $FeCO_3$ (species 19), and SRB1 (species B1) and SRB2 (species B2), as follows

$$\varepsilon_a \frac{\partial(Sc_7)}{\partial t} = \frac{\partial}{\partial x}\left(\tau_f \varepsilon_e S D_7 \frac{\partial c_7}{\partial x}\right) + \varepsilon_a S A_P [R_0 e^{-\alpha_P t} + R_1]\theta(c_{10}) + \varepsilon_a S A_F [R_0 e^{-\alpha_G t} + R_1]\theta(c_{18}) + k_{-13} c_{19} - \varepsilon_a S[k_6 c_3 c_7 + k_7 \max(0, c_7 - c_7^{sat}) c_9 + k_{13} \max(0, c_7 - c_7^{satFeCO3})] \quad (2\text{-}66)$$

$$\varepsilon_a \frac{\partial(Sc_9)}{\partial t} = \frac{\partial}{\partial x}\left(\tau_f \varepsilon_e S D_9 \frac{\partial c_9}{\partial x}\right) + \varepsilon_a S\left[1.5 A_P (R_0 e^{-\alpha_P t} + R_1)\theta(c_{10}) - k_7 \max(0, c_7 - c_7^{sat}) c_9 + \theta(S - S_{MIC})v_1 + \theta(S - S_{MIC})v_2\right] \quad (2\text{-}67)$$

$$\varepsilon_a S\frac{\partial c_{11}}{\partial t}=\frac{\partial}{\partial x}\left(\tau_f\varepsilon_e SD_{11}\frac{\partial c_{11}}{\partial x}\right)+\varepsilon_a S\begin{bmatrix}2A_P k_5 c_0^{1/2}\theta(c_{10})-\theta(S-S_{MIC})v_1-\theta(S-S_{MIC})v_2\\+k_{12}[\theta(c_{15})\theta(c_{11}^{sat}-c_{11})+\theta(c_{11}-c_{11}^{sat})](c_{11}^{sat}-c_{11})\end{bmatrix} \quad (2\text{-}68)$$

$$\frac{\partial}{\partial t}\left(\varepsilon_a\left[S+(1-S)\widetilde{H}_H\right]c_{12}\right)=\frac{\partial}{\partial x}\left(\tau_f\varepsilon_e\left[SD_{12}+(1-S)^3D_{13}\widetilde{H}_H\right]\frac{\partial c_{12}}{\partial x}\right)-4\varepsilon_a S\theta(S-S_{MIC})v_2 \quad (2\text{-}69)$$

$$-\frac{\partial c_{15}}{\partial t}=\varepsilon_a Sk_{12}[\theta(c_{15})\theta(c_{11}^{sat}-c_{11})+\theta(c_{11}-c_{11}^{sat})](c_{11}^{sat}-c_{11}) \quad (2\text{-}70)$$

$$\varepsilon_a\frac{\partial(Sc_{16})}{\partial t}=\frac{\partial}{\partial x}\left(\tau_f\varepsilon_e SD_{16}\frac{\partial c_{16}}{\partial t}\right)+\varepsilon_a S\begin{bmatrix}\theta(c_{17})k_{14}\max(0,c_{16}^{sat}-c_{16})-\theta(S-S_{MIC})v_1\\-\frac{5}{2}F_G\theta(S-S_{MIC})(a_{1B}v_1+a_{2B}v_2)\\+F_R(K_{R1}b_{1B}B_1+K_{R2}b_{2B}B_2)\end{bmatrix} \quad (2\text{-}71)$$

$$\frac{\partial c_{17}}{\partial t}=-\varepsilon_a S\theta(c_{17})k_{14}\max(0,c_{16}^{sat}-c_{16}) \quad (2\text{-}72)$$

$$\frac{\partial c_{18}}{\partial t}=-\varepsilon_a S\theta(c_{18})A_F[R_0e^{-\alpha_G t}+R_1] \quad (2\text{-}73)$$

$$\frac{\partial c_{19}}{\partial t}=\varepsilon_a Sk_{13}\max(0,c_7-c_7^{satFeCO3})-k_{-13}c_{19} \quad (2\text{-}74)$$

$$\varepsilon_a\frac{\partial B_1}{\partial t}=\varepsilon_a\theta(S-S_{MIC})a_{1B}v_1-\varepsilon_a b_{1B}B_1 \quad (2\text{-}75)$$

$$\varepsilon_a\frac{\partial B_2}{\partial t}=\varepsilon_a\theta(S-S_{MIC})a_{2B}v_2-\varepsilon_a b_{2B}B_2 \quad (2\text{-}76)$$

The boundary conditions for c_7, c_9, and c_{11} are unchanged, but a constant concentration RHS boundary condition is used for c_{12} rather than zero-flux condition used for V1.2e. Dissolved organic C CH_3CO_2H (c_{16}) is assigned the following boundary conditions:

- LHS boundary – zero flux.
- RHS boundary – constant concentration.

Gypsum (c_{15}), solid organic C (c_{17}), biotite (c_{18}), $FeCO_3$ (c_{19}), SRB1 (B_1), and SRB2 (B_2) do not require boundary conditions as they do not diffuse.

The initial conditions for the additional species included in CSM V1.2g are listed in Table 2-7. Initial conditions for c_7, c_9, c_{11}, and c_{12} are unchanged.

Table 2-7. Initial conditions for additional species in CSM V1.2g.

Species	Initial condition	Comment
Gypsum	c_{15}^{init}	Layer-dependent
Dissolved organic C	c_{16}^{init}	Layer-dependent
Solid organic C	c_{17}^{init}	Layer-dependent
Biotite	c_{18}^{init}	Layer-dependent
$FeCO_3$	0	Layer-dependent
SRB1	B_1^{init}	Layer-dependent
SRB2	B_2^{init}	Layer-dependent

Simulations with CSM Version 1.2g

Two runs were performed with Version 1.2g, in which microbial activity was either allowed or not allowed to occur in the bentonite (and Cu_2S film) (Table 2-4):

- Run 1.2g1: $S_{MIC} = 1$ (microbial activity not allowed in layers 1, 2, 3, and 4).
- Run 1.2g2: $S_{MIC} = 0$ (microbial activity allowed in layers 1, 2, 3, and 4).

2.3.8 Treatment of gaseous H_2S

The presence of gaseous H_2S can have two possible affects on the corrosion of copper canisters. First, partitioning of dissolved sulfide into the gas phase in unsaturated pores in the buffer and backfill material could result in more-rapid transport of H_2S to the canister surface. Second, gaseous H_2S is highly reactive towards copper and a number of other metals (Graedel et al. 1985) and could lead to sulfidation at RH values below those typically associated with aqueous corrosion processes.

The source of $H_2S(g)$ is the dissolved sulfide (or, more correctly, the dissolved $H_2S(aq)$ species) in the pore water. In aqueous solution, dissolved H_2S dissociates to produce bisulfide ions and protons

$$H_2S(aq) \rightleftarrows HS^- + H^+ \tag{2-77}$$

for which the dissociation constant is given by

$$K_1 = \frac{[HS^-][H^+]}{[H_2S(aq)]} \tag{2-78}$$

where $\log_{10}K = 782.43945 + 0.361261T\text{-}(1.6722 \times 10^{-4})T^2 - (20565.7315/T)\text{-}(142.741722 \ln T)$ (Suleimenov and Seward 1997), which gives a value of −6.98 at 25 °C.

Dissolved H_2S is assumed to be in equilibrium, with gaseous H_2S with the relative concentrations given by Henry's law

$$[H_2S(g)] = \widetilde{H}_{H2S}[H_2S(aq)] \tag{2-79}$$

where $\widetilde{H}_{H2S}$ is the inverse Henry's law constant for H_2S, which has a value of 10 atm·dm^3·mol^{-1} at 25 °C and an activation energy of −18 300 J/mol (Sander 1999). At 25 °C, 1 atm of an ideal gas is equivalent to a concentration of 0.040876 mol·dm^{-3}·atm^{-1}. Thus, the unitless inverse Henry's law constant for H_2S is 0.40876.

The MBE for gaseous H_2S (species 20, concentration c_{20}) is given by

$$\frac{\partial((1-S)\varepsilon_a c_{20})}{\partial t} = \frac{\partial}{\partial x}\left(\tau_f \varepsilon_e (1-S)^3 D_{20} \frac{\partial c_{20}}{\partial x}\right) - R_{H_2S} \tag{2-80}$$

where R_{H2S} is the rate of dissolution of $H_2S(g)$, i.e., the rate of formation of $H_2S(aq)$, and is given by

$$R_{H_2S} = \varepsilon_a S k_{15}(c_9^{sat} - c_9)(1-S)c_{20} \tag{2-81}$$

where

$$c_9^{sat} = \frac{K_1}{[H^+]}\frac{c_{20}}{\widetilde{H}_{H2S}} \tag{2-82}$$

and

$k_{15} = 0.0122$ s^{-1} at 25 °C

where k_{15} is the dissolution rate constant for gaseous H_2S, which is assumed to be equivalent to a half-life of approximately 1 min. Dissolution (and exsolution, if c_9 exceeds the saturated value) is, therefore, considered to be rapid. An activation energy for k_{15} of 60 000 J/mol is assumed.

For the Version 1.2h model, the modified MBE for HS^- is

$$\begin{aligned}\varepsilon_a \frac{\partial(Sc_9)}{\partial t} = {} & \frac{\partial}{\partial x}\left(\tau_f \varepsilon_e S D_9 \frac{\partial c_9}{\partial x}\right) + \varepsilon_a S[k_{10}\theta(c_{11})\theta(S - S_{MIC}) + 1.5A_P(R_0 e^{-\alpha_P t} + R_1)\theta(c_{10}) \\ & - k_7\, max(0, c_7 - c_7^{sat})c_9] + \frac{[H^+]}{K_1} R_{H_2S}\widetilde{H}_{H2S}\end{aligned} \tag{2-83}$$

and, for the complete Version 1.2a-h incorporating all of the changes to the reaction mechanism described in this section, the modified MBE for HS^- is

$$\begin{aligned}\varepsilon_a \frac{\partial(Sc_9)}{\partial t} = {} & \frac{\partial}{\partial x}\left(\tau_f \varepsilon_e S D_9 \frac{\partial c_9}{\partial x}\right) + \varepsilon_a S[\theta(S - S_{MIC})v_1 + \theta(S - S_{MIC})v_2 \\ & - k_7\, max(0, c_7 - c_7^{sat})c_9 - k_{11}c_9 c_2] + \frac{[H^+]}{K_1} R_{H_2S}\widetilde{H}_{H2S}\end{aligned} \tag{2-84}$$

Two mechanisms have been proposed for the sulfidation of copper by gaseous H_2S. At low RH (approaching 0 % RH), the reaction is a gas-phase process involving the dissociative adsorption of H_2S and the evolution of H_2 (Graedel et al. 1985):

$$2Cu + H_2S(g) \rightleftarrows Cu_2S + H_2 \quad (2\text{-}85)$$

At higher RH, the reaction is believed to be electrochemical in nature involving the anodic dissolution of Cu coupled to the cathodic reduction of O_2, with Cu_2S formed by the precipitation of Cu^+ by HS^- (Tran et al. 2003, 2005):

$$2Cu \rightleftarrows 2Cu^+ + 2e^- \quad (2\text{-}86)$$

$$½O_2 + H_2O + 2e^- \rightarrow 2OH^- \quad (2\text{-}87)$$

$$H_2S(aq) + OH^- \rightleftarrows HS^- + H_2O \quad (2\text{-}88)$$

$$2Cu^+ + HS^- \rightarrow Cu_2S + H^+ \quad (2\text{-}89)$$

for the overall reaction

$$2Cu + H_2S(aq) + ½O_2 \rightarrow Cu_2S + H_2O \quad (2\text{-}90)$$

While there is general agreement that this electrochemical route occurs at high RH (> 75 %), Barbour et al. (2002) suggests that this mechanism applies at all RH. Even at low RH (< 5 %), it is suggested that the little water on the surface is present in the form of microdroplets capable of sustaining aqueous-based electrochemical reactions.

However, because the extent of gas-phase sulfidation of the canisters would be limited for this mechanism because of the limited amount of available O_2, it is assumed here that the surface reaction follows the dissociative adsorption mechanism of Graedel et al. (1985). Unlike the interfacial electrochemical reactions included in the CSM, Reaction (2-85) occurs at all RH values. Once complete saturation occurs, gaseous H_2S is no longer present and this surface reaction ceases.

Figure 2-6 shows the reaction scheme for CSM Version 1.2a-h which incorporates all of the updates and improvements to the code discussed in this section. Although $H_2S(g)$ reacts on the surface to produce Cu_2S, in the same way that the reaction of dissolved HS^- does, the gas-phase reaction is not electrochemical in nature and is not coupled to the other interfacial electrochemical processes. Consequently, the gas-phase formation of Cu_2S does not affect the time-dependence of E_{CORR}. Apart from dissolution as dissolved HS^-, gaseous H_2S is not involved in any other chemical process. Thus, unlike dissolved sulfide, gaseous H_2S is assumed not to react with Cu_2O or to precipitate as FeS.

Various kinetic expressions have been proposed for the interfacial reaction (Barbour et al. 2002, Graedel et al. 1985, Tran et al. 2003, 2005). Both linear and parabolic kinetics have been reported, with a transition from a constant growth rate consistent with transport control to parabolic kinetics at a film thickness of 150 nm to 1 μm. Tran et al. (2005) observed 3-stage film-growth kinetics involving sequential linear, parabolic, and a second linear growth phase, the latter observed for Cu_2S film thickness of greater than 0.4–0.7 μm.

Given the differences in the literature regarding the mechanism and kinetics of copper sulfidation by gaseous H_2S, a conservative approach is taken to the treatment of the rate of the interfacial reaction in the CSM Versions 1.2h and 1.2a-h. The overall stoichiometry of the reaction is assumed to be given by Equation (2-85), which is further assumed to occur at all RH values, as noted above. Thus, the extent of corrosion by gaseous H_2S is not limited by the availability of O_2 (as is the case for the reactions in Equation (2-90)), which could otherwise limit the extent of the gas-phase process.

There are reports of H_2S formation from the reduction of pyrite to pyrrhotite by hydrogen (Truche et al. 2010) or by the thermal reduction of SO_4^{2-} by H_2 (Truche et al. 2009). However, the kinetics of both processes are slow under repository conditions, even over the extended timescales of interest. In particular, there will be limited sources of H_2 in the repository and that hydrogen that is produced would likely be consumed by the chemotrophic reduction of SO_4^{2-} by SRB rather than by the thermally activated, non-catalysed reduction of either pyrite or sulfate. Therefore, abiotic reduction of pyrite and sulfate are not considered to be significant sources of gaseous H_2S.

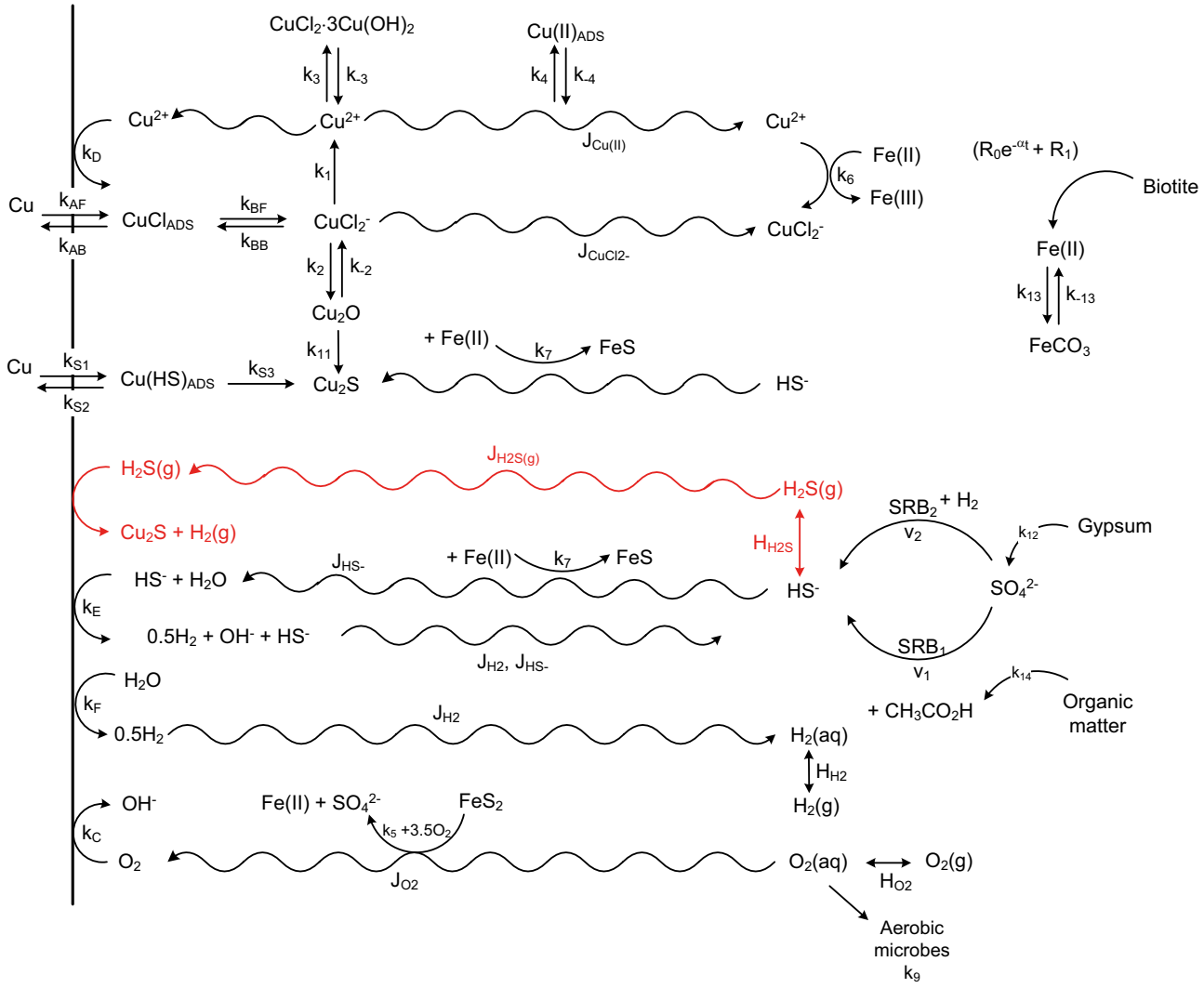

Figure 2-6. *Reaction scheme for CSM Version 1.2a-h. Additions to the reaction scheme used for Version 1.2a-g are shown in red font.*

Boundary conditions

The LHS boundary condition for c_{20} is based on the assumption of a period of linear film growth followed by parabolic kinetics, for which the expression for the time-dependent film thickness D(t) is given by:

$$D(t) = \theta(1-S_1)[\alpha t\theta(t_L-t) + \theta(t-t_L)(D_L + A(t-t_L)^n)] \quad (2\text{-}91)$$

where A is a fitting parameter, n is the time exponent, and

$$t_L = D_L/\alpha \quad (2\text{-}92)$$

where D_L is the film thickness corresponding to the transition from linear to parabolic growth and has a value of approximately 500 nm.

For $D_L \approx 500$ nm and $\alpha = 6.4 \times 10^{-11}$ dm/s (from Barbour et al. 2002), $t_L = 78\,125$ s $\approx$ 22 hours at room temperature. As a is temperature dependent (activation energy 33 000 J/mol), $t_L \approx$ 1 month for the initial canister temperatures of 45 °C. The film growth rate is given by

$$dD/dt = \theta(1-S_1)[\alpha\theta(t_L-t) + nA(t-t_L)^{n-1}\theta(t-t_L)] \quad (2\text{-}93)$$

where n = 0.826 and $A = 4.09 \times 10^{-10}$ dm/s$^{0.826}$.

The LHS boundary condition is given by

$$\tau_f \varepsilon_e (1 - S_1)^3 D_{20} \left.\frac{\partial c_{20}}{\partial x}\right|_{x=0} = \frac{\rho_1 (1-\varepsilon_{total})}{M_{Cu2S}} \frac{dD}{dt} \tag{2-94}$$

Because the number of moles of gaseous H_2 (c_{13}) produced at the surface is the same as the number of moles of c_{20} consumed at the surface, we also have:

$$\tau_f \varepsilon_e (1 - S_1)^3 D_{13} \left.\frac{\partial c_{13}}{\partial x}\right|_{x=0} = -\frac{\rho_1 (1-\varepsilon_{total})}{M_{Cu2S}} \frac{dD}{dt} \tag{2-95}$$

Gaseous H_2 is in equilibrium with dissolved H_2 (c_{12}), for which the modified boundary condition is

$$\tau_f \varepsilon_e \left[S_1 D_{12} + (1 - S_1)^3 D_{13} \widetilde{H_H}\right] \left.\frac{\partial c_{12}}{\partial x}\right|_{x=0} = \frac{1}{2}\left(\frac{i_E}{n_E} + \frac{i_F}{n_F}\right) - \frac{\rho_1 (1-\varepsilon_{total})}{M_{Cu2S}} \frac{dD}{dt} \tag{2-96}$$

The total film growth rate by both gaseous and aqueous routes is given by

$$\frac{dX_{film}}{dt} = \frac{dD}{dt} + \frac{M_{Cu2S}}{\rho_1 (1-\varepsilon_{total})} \frac{i_S}{F} \tag{2-97}$$

where X_{film} is the total film thickness.

Since the rock is assumed to be saturated at all times, c_{20} does not exist at the RHS boundary, so we can simply define a zero-concentration boundary condition.

Initial conditions

Gaseous H_2S is initially present in those layers that contain dissolved HS^- (c_9) and which are initially unsaturated. Of the various layers in the 9-layer best-estimate simulation (see Section 4), the buffer and backfill layers (layers 2-6) are assumed to be initially free of dissolved HS^- and the host rock (layer 9) is fully saturated at all times. Therefore, gaseous H_2S (c_{20}) is only initially present in the EDZ (layer 7) and EdZ (layer 8), which have non-zero c_{20}^{init} values given by

$$c_{20}^{init} = \widetilde{H}_{H2S} c_9^{init} \frac{[H^+]}{K_1} \tag{2-98}$$

where $[H^+] = 10^{-8}$ mol·dm^{-3}, $c_9^{init} = 10^{-5}$ mol·dm^{-3} in the default input parameters (Section 4), and K_1 is a function of temperature.

Simulation with CSM Version 1.2a-h

A single simulation was performed using Version 1.2a-h. Although a separate Version 1.2h was developed based on Version 1.1eq plus the treatment of gaseous H_2S, no simulations were performed with this version of the code as it neither includes H_2 nor the sophisticated treatment of microbial sulfate reduction of Version 1.2g, which was subsequently found to be the major source of gaseous H_2S.

Because the Version 1.2a-h simulation was performed after the other simulations described here, the input data were based on the best-estimate simulation input data listed in Table 4-1 to Table 4-4, inclusive. The additional input data required for Version 1.2a-h are listed in Table 2-8.

Table 2-8. Additional input data for CSM Version 1.2h and 1.2a-h.

Parameter	Description	Value	Comment	Reference
K_1	First dissociation constant for H_2S	$Log_{10}K_1 = 782.43945 + 0.361261T - (1.6722\times10^{-4})T^2 - (20565.7315/T) - (142.741722 \ln T)$	T is the temperature in K	Suleimenov and Seward (1997)
$\tilde{H}_{H2S}$	Inverse Henry's law constant for H_2S	0.40876	Unitless inverse Henry's law constant	Sander (1999)
ΔE_{HH2S}	Activation energy for $\tilde{H}_{H2S}$	−18 300 J/mol	-	Sander (1999)
D_{20}	Diffusion coefficient of gaseous H_2S	0.00165 dm^2/s	Taken to be the same as O_2 in air	-
ΔE_{D20}	Activation energy for D_{20}	−2 060 J/mol	Taken to be the same as O_2 in air	-
$[H^+]$	Hydrogen ion concentration	10^{-8} mol dm^{-3}	Based on the assumption of a pore-water pH of 8	-

2.4 Spatial separation of anodic and cathodic processes

There is experimental evidence to indicate that the cathodic reaction may occur on the surface of the Cu_2S film (Chen J 2015, private communication). In the current versions of the model, both anodic and cathodic reactions are assumed to be limited to the exposed metal surface at the base of the pores in the film. Certainly, Cu_2S can be semi-conducting and may be expected to support electrochemical reactions.

We make the following assumptions for the simulation of spatially separated anodic and cathodic reactions for the CSM Version 1.3 (Table 2-1):

- Prior to the formation of the Cu_2S film, all anodic and cathodic reactions occur over the entire surface area.
- Once a Cu_2S film forms,
  - The anodic reaction occurs at the copper/film interface at the base of pores, with an effective fractional surface area of ε_{film}.
  - The cathodic reaction(s) will occur on the surface of the Cu_2S at the film/bentonite interface, with an effective fractional surface area of $(1-\varepsilon_{film})$ (Version 1.3a) OR
  - The cathodic reaction(s) will occur on the surface of the Cu_2S at the film/bentonite interface AND on the sides of the pores within the growing film (Version 1.3b), with an effective fractional surface area of $(1-\varepsilon_{film}) + F_{pore}\frac{\varepsilon_{film}}{\bar{d}}L(t)$, where $\bar{d}$ is the mean pore width and L(t) is the time-dependent film thickness. For perfectly cylindrical or spherical pores (a geometry for which an analytical mathematical solution can be derived), F_{pore} has a value of 4 or 6, respectively. For real pores, the value of F_{pore} is somewhat lower. See Appendix B for the derivation of the surface area factor $F_{pore}\frac{\varepsilon_{film}}{\bar{d}}L(t)$.

The following changes were made to the full CSM Version 1.2a-f.

Cathodic reaction on surface of Cu_2S film (Version 1.3a)

The various interfacial electrochemical reactions and the corresponding Butler–Volmer expressions for Version 1.3a are:

$$Cu + Cl^- \underset{k_{AB}}{\overset{k_{AF}}{\rightleftarrows}} CuCl_{ADS} + e^- \tag{2-99}$$

$$CuCl_{ADS} + Cl^- \underset{k_{BB}}{\overset{k_{BF}}{\rightleftarrows}} CuCl_2^- \tag{2-100}$$

and

$$i_A(t) = n_A \varepsilon_{film} F \left(\frac{k_{AF} k_{BF}}{k_{AB}} (c_6(0,t))^2 \exp\left\{ \frac{F}{RT} (E - E_A^0) \right\} - k_{BB} c_1(0,t) \right) \tag{2-101}$$

for the anodic dissolution of Cu in Cl^- solution;

$$Cu + HS^- \underset{k_{S2}}{\overset{k_{S1}}{\rightleftarrows}} Cu(HS)_{ADS} + e^- \tag{2-102}$$

$$Cu + Cu(HS)_{ADS} + HS^- \xrightarrow{k_{S3}} Cu_2S + HS^- + H^+ + e^- \tag{2-103}$$

and

$$i_S(t) = n_S \varepsilon_{film} F k_S (c_9(0,t))^2 \exp\left\{ \frac{(1+\alpha_S)F}{RT} E \right\} \exp\left\{ -\frac{F}{RT} (E_{S12}^0 + \alpha_{S3} E_{S3}^0) \right\} \tag{2-104}$$

for the anodic dissolution of Cu in the presence of HS^- and the formation of a Cu_2S film;

$$O_2 + 2H_2O + 4e^- \xrightarrow{k_C} 4OH^- \tag{2-105}$$

and

$$i_C(t) = -n_0 (1 - \varepsilon_{film}) F k_C c_0(0,t) \exp\left\{ -\frac{\alpha_C F}{RT} (E - E_C^0) \right\} \tag{2-106}$$

for the cathodic reduction of O_2;

$$Cu^{2+} + 2Cl^- + e^- \xrightarrow{k_D} CuCl_2^- \tag{2-107}$$

and

$$i_D(t) = -n_D (1 - \varepsilon_{film}) F k_D c_3(0,t) \exp\left\{ -\frac{\alpha_D F}{RT} (E - E_D^0) \right\} \tag{2-108}$$

for the cathodic reduction of Cu^{2+};

$$HS^- + H_2O + e^- \xrightarrow{k_E} \frac{1}{2} H_2 + HS^- + OH^- \tag{2-109}$$

and

$$i_E(t) = -n_E (1 - \varepsilon_{film}) F k_E (c_9(0,t))^m \exp\left\{ -\frac{\alpha_E F}{RT} (E - E_E^0) \right\} \tag{2-110}$$

for the cathodic reduction of HS^-, and;

$$H_2O + e^- \xrightarrow{k_F} \frac{1}{2} H_2 + OH^- \tag{2-111}$$

and

$$\frac{i_F}{F} = -n_F F (1 - \varepsilon_{film}) k_F \exp\left\{ -\frac{\alpha_F F}{RT} (E - E_F^0) \right\} \tag{2-112}$$

for the cathodic reduction of H_2O.

Since, HS^- is not consumed in the newly re-written expression for Reaction (2-109) (Version 1.2f), we are not subject to the inconsistency of equating the currents for the consumption of HS^- to interfacial fluxes at two different locations (i.e., at the copper/film interface for Reactions (2-102) and (2-103) and at the film/bentonite interface for Reaction (2-109)) as we would have been if we had not modified the reaction.

Cathodic reaction on surface and within pores of Cu_2S film (Version 1.3b)

The Butler–Volmer expressions for the two anodic reactions are the same as above (Equations (2-101) and (2-104)).

The Butler–Volmer expressions for the four cathodic reactions are:

$$i_C(t) = -n_0\left((1-\varepsilon_{film}) + F_{pore}\frac{\varepsilon_{film}}{\bar{d}}L(t)\right)Fk_C c_0(0,t)\exp\left\{-\frac{\alpha_C F}{RT}(E-E_C^0)\right\} \quad (2\text{-}113)$$

$$i_D(t) = -n_D\left((1-\varepsilon_{film}) + F_{pore}\frac{\varepsilon_{film}}{\bar{d}}L(t)\right)Fk_D c_3(0,t)\exp\left\{-\frac{\alpha_D F}{RT}(E-E_D^0)\right\} \quad (2\text{-}114)$$

$$i_E(t) = -n_E\left((1-\varepsilon_{film}) + F_{pore}\frac{\varepsilon_{film}}{\bar{d}}L(t)\right)Fk_E(c_9(0,t))^m\exp\left\{-\frac{\alpha_E F}{RT}(E-E_E^0)\right\} \quad (2\text{-}115)$$

and

$$\frac{i_F}{F} = -n_F F\left((1-\varepsilon_{film}) + F_{pore}\frac{\varepsilon_{film}}{\bar{d}}L(t)\right)k_F\exp\left\{-\frac{\alpha_F F}{RT}(E-E_F^0)\right\} \quad (2\text{-}116)$$

where $\left((1-\varepsilon_{film}) + F\frac{\varepsilon_{film}}{\bar{d}}L(t)\right)$ is the fractional surface area for the cathodic reaction as a function of the film thickness L.

For the current simulations, we will assume a value of F_{pore} of 5 as a mean between perfect cylinders (F_{pore} = 4) and perfect spheres (F_{pore} = 6) and for $\bar{d}$ a value of 2×10^{-7} m, as characteristic of the pore diameter of P1-type films as reported by Chen et al. (2014a).

Simulations with CSM Version 1.3

Two simulations were performed for Version 1.3 (Table 2-4):

- Run 1.3a: Version 1.3a, S_{MIC} = 1 (no microbial activity in layers 1, 2, 3, and 4).
- Run 1.3b: Version 1.3b, S_{MIC} = 1 (no microbial activity in layers 1, 2, 3, and 4).

For both runs, F_{pore} = 5 and $\bar{d} = 2\times10^{-7}$ m.

2.5 Alternative film formation process

For the existing versions of the CSM, film growth is assumed to occur at the film/bentonite interface with a constant (in space and time) user-defined porosity. An alternative treatment of film-growth is to treat the film porosity as a parameter that is calculated directly within the code. This alternative treatment of the film-growth process has been previously used for predicting the corrosion behaviour of C-steel canisters (King and Kolář 2012) and of the precipitation of mineral phases in coatings on cathodically protected underground pipelines (King et al. 2004a).

In our previous attempts at treating the porosity as a parameter, the solid corrosion product was formed by the precipitation of a dissolved species produced by the interfacial anodic dissolution process. In the CSM, however, the major source of Cu_2S is the conversion of the surface intermediate species $Cu(HS)_{ADS}$ to directly produce the solid Cu_2S. Thus, unlike the previous cases where the dissolved precursor Fe^{2+} ion could diffuse away from the surface before precipitating as a solid, there is no equivalent process for the formation of Cu_2S. Thus, the decision was taken not to implement this alternative film treatment in the CSM.

Subsequently, it has become apparent that soluble copper sulfide species do play a role in the Cu_2S film formation process (Chen et al. 2018). Species such as Cu_3S_3 are soluble and there is evidence for their transport in solution prior to precipitation as Cu_2S. Such species have also been long known in the environmental literature (Luther et al. 2002). Therefore, it may be appropriate to re-visit the idea of an alternative film formation mechanism for Cu_2S in a future modification of the CSM.

2.6 Alternative bentonite model

2.6.1 Background

Various models have been developed to describe the structure and pore-water properties of highly compacted bentonite. A common type of model is the so-called multi-porosity approach in which the total pore volume is divided into different types of pore associated with, for example, open pores, dead-end pores, interlayer water, etc (Figure 2-7(a)). An alternative model is based on a single type of inter-layer water and the assumption of Donnan equilibrium between so-called "internal" and "external" solutions (Figure 2-7(b), Birgersson and Karnland 2009). All water is assumed to be associated with the surfaces of the montmorillonite clay particles (so-called interlayer water), with the properties largely influenced by the electrical double-layer that exists adjacent to the clay surface.

The existing CSM (and CCM) models are essentially based on a multi-porosity model. For example, we distinguish accessible (ε_a) and non-accessible (ε_{na}) pores and further sub-divide the accessible porosity into through pores that contribute to mass transport (ε_e) and dead-end pores (storage porosity ε_s). The pore-water composition is largely determined using a "mixing" approach, in which the concentrations of different solutes at a particular time and location are determined by the initial amount and the amounts gained or lost by mass transport and/or by reaction.

A single inter-layer porosity model was implemented in the CSM to determine whether the type of bentonite pore-water model has any affect on the predicted corrosion behaviour of the canister. Briefly, the single inter-layer porosity model states that:

- There is only one type of pore water in HCB, namely interlayer water closely associated with the clay surfaces.
- All of the porosity is accessible to all solutes, i.e., there is no exclusion of anions from the interlayer water (due to the negative surface charge on the clay particles), as sometimes assumed in multi-porosity models.
- *At equilibrium*, the ratio between the activity of species i inside the clay $(a_i)_{int}$ to that in the external solution $(a_i)_{ext}$ is given by

$$\Xi^{-z_i} = \frac{(a_i)_{int}}{(a_i)_{ext}} \qquad (2\text{-}117)$$

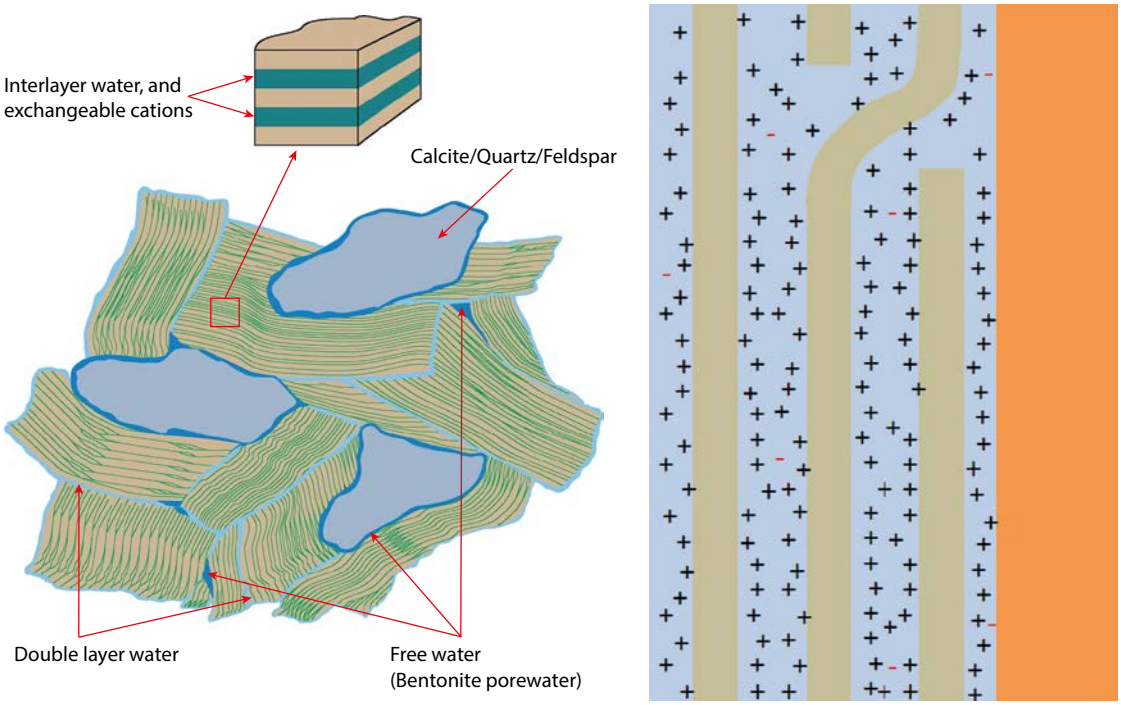

(a) Multi-porosity model

(b) Interlayer-only or Donnan equilibrium model

Figure 2-7. *Schematic representations of the pore structure for alternative bentonite models. Figure 2-7a from Bradbury and Baeyens (2003).*

where Ξ is the ion equilibrium coefficient and z is the charge for species i (e.g., −1 for Cl^-, −2 for SO_4^{2-}, +1 for Na^+). The parameter Ξ has the same value for all ions and depends on the clay density, ionic strength, and cation-exchange capacity (CEC). Since Ξ has a value of between 0 and 1, the implication is that the concentration of anions in the pore solution is lower than that in the external solution (ground water), whereas the concentrations of cations are higher. For the current purposes, the activity coefficients of a given species in the external and external solutions are assumed to be the same so that Equation (2-117) can be re-written in terms of concentrations.

The CSM Version 2.0 is based on the single inter-layer bentonite pore-water model. The starting point for Version 2.0 is a six-layer implementation of the Version 1.2a-f model.

2.6.2 Changes to CSM for the single inter-layer model

Conceptually, the single inter-layer model is explained in terms of a layer of bentonite separated from an external solution by a porous filter (see Birgersson and Karnland 2009, Figure 6). The corrosion behaviour is largely impacted by the composition of the pore fluid in contact with the canister surface. Since there is no bulk aqueous phase in contact with the canister surface, the question is whether this fluid is represented by the internal or external solutions in the conceptual single porosity model.

Following discussions with SKB personnel, the consensus is that the porous Cu_2S corrosion product will act as the filter on one side of the bentonite, so that the canister surface is in contact with the *external* electrolyte. On the other side of the bentonite, it is unclear whether the bentonite content of the backfill is sufficiently high that the pore structure in the backfill will also be determined by the single porosity model. Therefore, to avoid such uncertainty, we have implemented the single porosity model using the six-layer geometry, with the layers representing the growing Cu_2S film, three sub-layers of HCB, EDZ, and a layer of intact rock. It is believed that the EDZ will also fulfil the role of the conceptual filter constraining the right-hand side of the HCB.

As noted above, in the single porosity model, the distribution of solutes between the internal and external solutions is only defined at equilibrium. It may take many thousands/tens of thousands of years to achieve equilibrium, and the question then is how to treat the transient pore-water composition in the single porosity model. For CSM Version 2.0, we impose the local Donnan equilibrium at the interfaces between the left-hand filter/HCB and at the HCB/right-hand filter for t > 0. The initial pore-water composition is given as it is currently, based on a mixing model.

The change in the bentonite model requires several changes to the code, including:

- Treatment of the porosity in the MBE for all species.
- Time-dependent composition of the pore water within the HCB and at the boundaries between the corrosion product/HCB and the HCB/EDZ.
- Choice of the number and nature of the layers in the model.

Diffusive Mass Transport and Reaction Terms in MBE

For Version 2.0, the entire porosity is treated as accessible and available for mass transport. Therefore, for all species, the existing MBE of the type

$$\varepsilon_a \frac{\partial(Sc_i)}{\partial t} = \frac{\partial}{\partial x}\left(\tau_f \varepsilon_e S D_i \frac{\partial c_i}{\partial x}\right) + \varepsilon_a S \sum_j R_j + R_j^{`} \qquad (2\text{-}118)$$

are replaced by expressions of the type

$$\varepsilon \frac{\partial(Sc_i)}{\partial t} = \frac{\partial}{\partial x}\left(\tau_f \varepsilon S D_i \frac{\partial c_i}{\partial x}\right) + \varepsilon S \sum_j R_j + R_j^{`} \qquad (2\text{-}119)$$

where ε is the total porosity.

Because we use the same MBE for all layers, we are effectively implementing a single-pore model for all layers.

Transient Pore-water Composition

The *initial* pore-water composition is determined as now using a mixing model based on the initial degree of saturation and the content of soluble mineral impurities in the bentonite.

For times t > 0, we assume that filters are present at both the left-hand and right-hand boundaries of the bentonite (Figure 2-8). These filters are represented by the porous corrosion product (layer 1, L1) (which only forms after some time, but which is assumed to be present at all times) and the EDZ (layer 5, L5).

Thus:

- For t > 0, we impose the Donnan equilibrium (Equation (2-117)) at both the L1/L2 and L4/L5 interfaces.
- The value of Ξ is dependent on ionic strength, so may be different at the two interfaces and will change with time as the ionic strength increases.
- As time proceeds, the concentration of the species within the HCB sub-layers but away from the interfaces will increase as solute diffuses into the HCB.
- The Donnan principle is applied only to the charged ground water species included in the model, i.e., Cl^- (species 6), HS^- (species 9), and SO_4^{2-} (species 11).

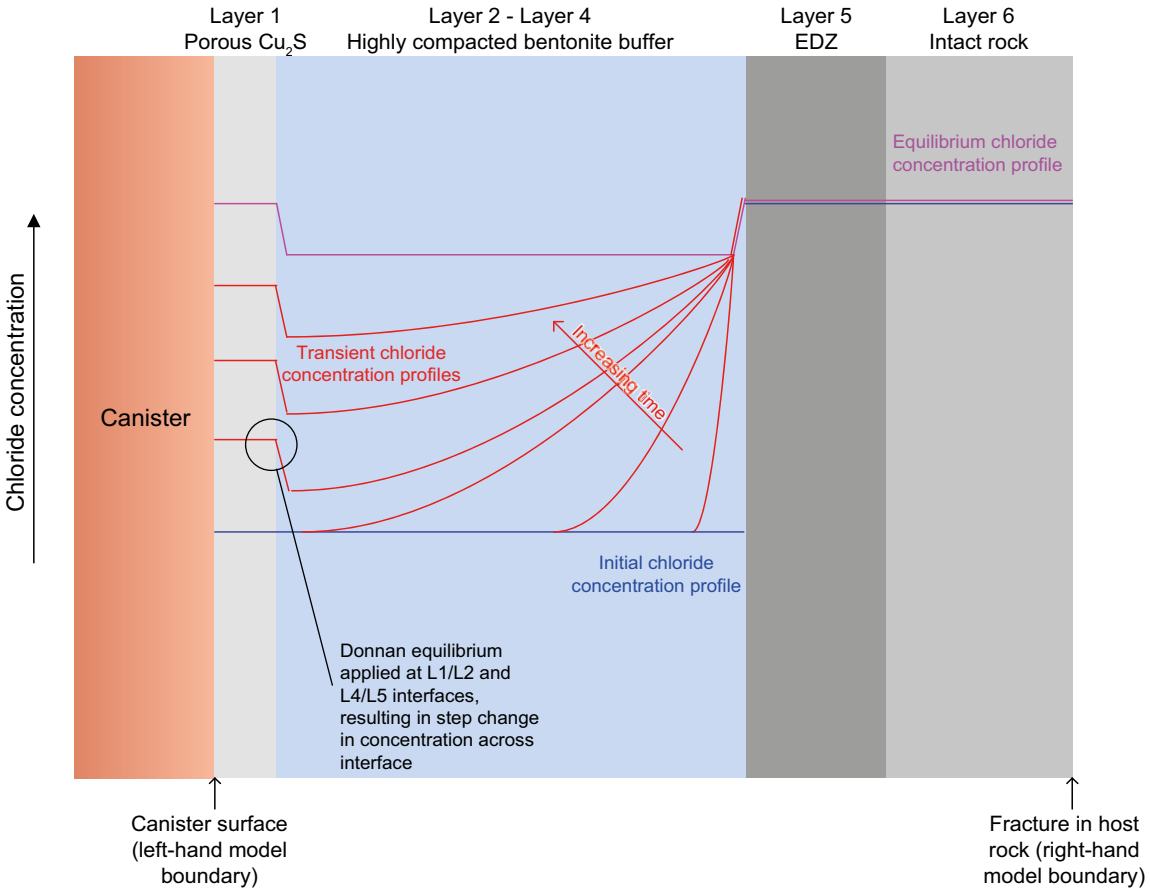

Figure 2-8. *Illustration of the conceptual treatment of the transient pore-water composition in the Donnan model for CSM Version 2.0.*

Equilibrium Pore-water Composition

At equilibrium, the composition of the "external solution" in Layer 1 (for Cl^-, HS^-, and SO_4^{2-}) is the same as that in the EDZ (Layer 5).

Input Data for CSM Version 2.0

A single run was performed with the CSM Version 2.0 (Table 2-4).

The additional input data required for CSM Version 2.0 are the value for the ion equilibrium coefficient Ξ and for the total porosity ε_{tot} for each of the layers. Idiart and Pękala (2016) give values for Ξ ranging from 0.31 to 0.64 derived by fitting the Donnan equilibrium model to the results of various large-scale tests with compacted bentonite. Internal and external solution compositions were corrected for calculated activity coefficients to estimate values of Ξ. The highest values were from bentonites with low CEC and are, perhaps, not representative of that to be used in the repository. Values for MX-80 bentonite ranged from 0.31 to 0.39 and decreased with increasing dry density. The most suitable value for the current study is $\Xi = 0.31$ for a dry density of 1 600 kg/m^3.

The total porosity ε_{tot} is simply the sum of the accessible and non-accessible porosities for each of the layers in the model and is given by:

- Cu_2S film (layer 1) $\varepsilon_{tot} = 0.1$
- Bentonite (layers 2–4) $\varepsilon_{tot} = 0.40$
- EDZ, the excavation damaged zone representing the layer of damaged rock closest to the surface of the opening (layer 5) $\varepsilon_{tot} = 0.006$
- Rock (layer 6) $\varepsilon_{tot} = 0.003$

The threshold degree of saturation for microbial activity S_{MIC} was assumed to be 1 for layers 1, 2, 3, and 4 (equivalent to no microbial activity in the bentonite).

3 Results of simulations with updated versions of the CSM

3.1 Reference simulation with CSM Version 1.1eq

The reference against which the effects of the various improvements and changes to the model will be compared is based on the CSM Version 1.1eq code. Two reference simulations were run using the input parameters in Appendix C, one with nine layers and the other with six layers (for comparison with the six-layer model used to simulate the single inter-layer porosity model in Version 2.0). The layers included in the 9-layer simulation were:

- Layer 1 Cu_2S film
- Layer 2 HCB (inner sub-layer)
- Layer 3 HCB (middle sub-layer)
- Layer 4 HCB (outer sub-layer)
- Layer 5 Backfill (inner sub-layer)
- Layer 6 Backfill (outer sub-layer)
- Layer 7 EDZ
- Layer 8 EdZ
- Layer 9 Host rock

Layer-dependent input parameters are summarized in Table 3-1. The basis for each of the values, as well as those of other input parameters, are defined in Appendix C. Parameters that were subsequently found to be important are highlighted in bold font.

Table 3-1a. Input data for the layer-specific parameters for the CSM Version 1.1eq reference simulations. Layers 1–3.

Parameter	Layer 1	Layer 2	Layer 3
Layer name	Cu_2S film	HCB inner	HCB middle
Length (dm)	Variable	2	2
Effective porosity for mass transport ε_e	0.1	0.05	0.05
Storage porosity ε_s	0	0.05	0.05
Non-accessible porosity ε_{na}	0	0.3	0.3
Tortuosity factor τ_f	0.1	0.1	0.1
Threshold saturation for microbial activity S_{MIC}	**1**	**1**	**1**
Maximum Cu^{2+} adsorption capacity c_5^{max} (mol/kg)	0	0.09375	0.09375
Pyrite specific surface area A_p (dm^{-1})	0	0.139	0.139
Initial concentration of dissolved O_2 $(c_0)_{init}$ (mol/dm^3)	n.d.*	0.000361	0.000256
Initial concentration of Cl^- ions $(c_6)_{init}$ (mol/dm^3)	n.d.	0.096	0.096
Initial concentration of dissolved Fe(II) $(c_7)_{init}$ (mol/dm^3)	n.d.	0	0
Initial concentration of sulfide ions $(c_9)_{init}$ (mol/dm^3)	n.d.	0	0
Initial concentration of pyrite $(c_{10})_{init}$ (mol/dm^3)	n.d.	0.00963	0.00963
Initial concentration of SO_4^{2-} ions $(c_{11})_{init}$ (mol/dm^3)	n.d.	**0.149**	**0.149**
Time-dependent saturation S(t)	External input	External input	External input
Particle density ρ (kg/dm^3)	5.6	2.7	2.7
Saturation-dependent thermal conductivity K(S) ($W \cdot dm^{-1} \cdot K^{-1}$)	External input	External input	External input
Heat capacity C ($J \cdot kg^{-1} \cdot K^{-1}$)	845	845	845

* n.d. not defined.

Table 3-1b. Layers 4–6.

Parameter	Layer 4	Layer 5	Layer 6
Layer name	HCB outer	Backfill inner	Backfill outer
Length (dm)	2.93	40	47
Effective porosity for mass transport ε_e	0.05	0.22	0.22
Storage porosity ε_s	0.05	0	0
Non-accessible porosity ε_{na}	0.3	0	0
Tortuosity factor τ_f	0.1	0.1	0.1
Threshold saturation for microbial activity S_{MIC}	**1**	**0.75**	**0.75**
Maximum Cu^{2+} adsorption capacity c_5^{max} (mol/kg)	0.09375	0.113	0.113
Specific surface area of pyrite A_p (dm^{-1})	0.139	0.382	0.382
Initial concentration of dissolved O_2 $(c_0)_{init}$ (mol/dm^3)	0.000223	0.000213	0.000205
Initial concentration of Cl^- ions $(c_6)_{init}$ (mol/dm^3)	0.096	0.036	0.036
Initial concentration of dissolved Fe(II) $(c_7)_{init}$ (mol/dm^3)	0	0	0
Initial concentration of sulfide ions $(c_9)_{init}$ (mol/dm^3)	0	0	0
Initial concentration of pyrite $(c_{10})_{init}$ (mol/dm^3)	0.00963	0.0265	0.0265
Initial concentration of SO_4^{2-} ions $(c_{11})_{init}$ (mol/dm^3)	**0.149**	**0.479**	**0.479**
Time-dependent saturation S(t)	External input	External input	External input
Particle density ρ (kg/dm^3)	2.7	2.7	2.7
Saturation-dependent thermal conductivity K(S) ($W \cdot dm^{-1} \cdot K^{-1}$)	External input	External input	External input
Heat capacity C ($J \cdot kg^{-1} \cdot K^{-1}$)	845	845	845

Table 3-1c. Layers 7–9.

Parameter	Layer 7	Layer 8	Layer 9
Layer name	EDZ	EdZ	Host rock
Length (dm)	5	20	20
Effective porosity for mass transport ε_e	0.006	0.003	0.003
Storage porosity ε_s	0	0	0
Non-accessible porosity ε_{na}	0	0	0
Tortuosity factor τ_f	0.1	0.1	0.1
Threshold saturation for microbial activity S_{MIC}	**0**	**0**	**0**
Maximum Cu^{2+} adsorption capacity c_5^{max} (mol/kg)	0	0	0
Specific surface area of pyrite A_p (dm^{-1})	**0**	50	5
Initial concentration of dissolved O_2 $(c_0)_{init}$ (mol/dm^3)	0.000204	0.000204	0
Initial concentration of Cl^- ions $(c_6)_{init}$ (mol/dm^3)	0.1	0.1	0.1
Initial concentration of dissolved Fe(II) $(c_7)_{init}$ (mol/dm^3)	0	0	10^{-5}
Initial concentration of sulfide ions $(c_9)_{init}$ (mol/dm^3)	10^{-5}	10^{-5}	10^{-5}
Initial concentration of pyrite $(c_{10})_{init}$ (mol/dm^3)	**0**	21	2.1
Initial concentration of SO_4^{2-} ions $(c_{11})_{init}$ (mol/dm^3)	**0.0094**	**0.0094**	**0.0094**
Time-dependent saturation S(t)	External input	External input	External input
Particle density ρ (kg/dm^3)	2.7	2.7	2.7
Saturation-dependent thermal conductivity K(S) ($W \cdot dm^{-1} \cdot K^{-1}$)	External input	External input	External input
Heat capacity C ($J \cdot kg^{-1} \cdot K^{-1}$)	845	845	845

As is shown below, the behaviour of the system is dominated by the production, transport, and consumption of sulfide ions HS^-. An important source of sulfide is the microbial reduction of sulfate. The rate of this process depends on (i) the viability of microbial activity and (ii) either the presence (Version 1.1eq and interim versions of Version 1.2 other than Versions 1.2c and 1.2g) or the concentration (Versions 1.2c and 1.2g) of SO_4^{2-}. Microbes are assumed to be viable if the (time-dependent) degree of saturation exceeds the threshold value S_{MIC}. Based on the values of S_{MIC}, microbial activity is not viable in the Cu_2S film or HCB, is possible in the backfill if the saturation exceeds a value of 0.75, and is assumed to be possible in the EDZ and host rock at all times (on the assumption that these layers never dry out). (In a number of simulations, microbial activity is permitted in the HCB in order to determine the effect of this microbial activity close to the canister surface. See Table 2-4).

The other important parameter is the availability of sulfate. For Version 1.1eq (and for intermediate versions of 1.2 except for Versions 1.2c and 1.2g), the rate of sulfate reduction is independent of the SO_4^{2-} concentration but requires that sulfate is present (Section 2.1). For Version 1.2c and the full Version 1.2a-f (and any subsequent version developed from Version 1.2a-f), the rate of sulfate reduction is assumed to be proportional to the SO_4^{2-} concentration (Section 2.3.3). An important source of SO_4^{2-} is the dissolution of gypsum, present as an accessory mineral in the HCB and backfill. The dissolution of gypsum is not included in Versions 1.2a to 1.2f or 1.2h, but is explicitly treated in Version 1.2g. In order not to under-estimate the contribution from the dissolution of gypsum for versions other than Version 1.2g, the initial pore-water SO_4^{2-} concentration in the backfill is estimated on the assumption that the total gypsum inventory is initially dissolved. This then produces a very high initial [SO_4^{2-}] in the backfill (Table 3-1(b)). The initial sulfate concentrations in the HCB and rock layers are based on a modelled pore-water composition (Pastina and Hellä 2006) and a baseline ground water composition given by King et al. (2010).

The results of the reference simulation using the 9-layer Version 1.1eq are presented here in some detail. Figure 3-1 shows the predicted time dependence of the corrosion potential (E_{CORR}) and the depth of corrosion for the total simulation period of 10^6 years. These results are consistent with the results of simulations using Version 1.1 (King et al. 2011b). The value of E_{CORR} is initially quite high as the environmental conditions are aerobic due to the O_2 initially present and the Cu(II) formed by the oxidation of $CuCl_2^-$ by O_2. The break in the E_{CORR} curve indicates the period during which the surface of the canister is assumed to dry out to such an extent that aqueous interfacial processes cease and the canister stops corroding. Eventually, however, the canister surface re-wets sufficiently for corrosion to resume (after 116 a for the assumed re-saturation behaviour for the reference case) and E_{CORR} slowly decreases as remaining Cu(II) is consumed by corrosion of the canister. As the repository becomes more anaerobic, however, processes involving sulfide start to dominate and the E_{CORR} eventually drops precipitously (after 4 500 years) as the interfacial reactions become dominated by the formation of Cu_2S supported by the cathodic reduction of HS^-. The total depth of corrosion predicted for the reference case is 0.48 mm after 10^6 years (Figure 3-1). Of this total amount of corrosion, > 99.9 % is due to the formation of Cu_2S.

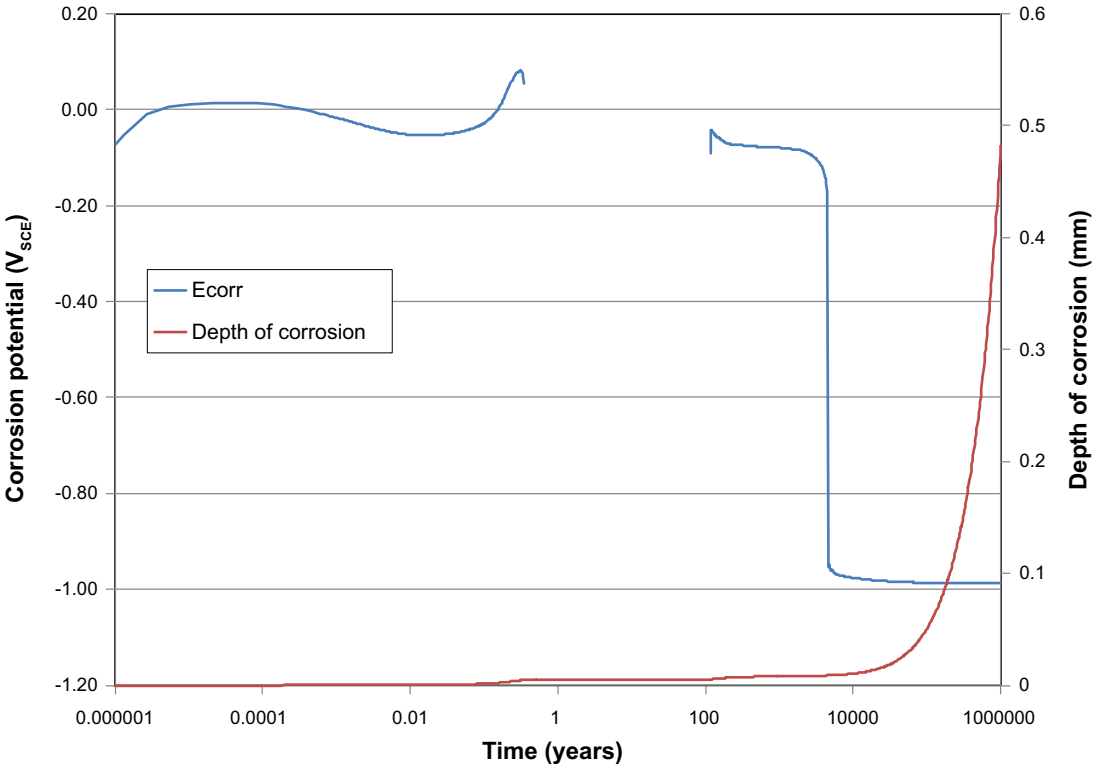

Figure 3-1. *Time-dependence of the corrosion potential (E_{CORR}) and the depth of corrosion for the reference simulation using the 9-layer CSM Version 1.1eq.*

Figure 3-2 shows the time-dependence of the Cu_2S film thickness and the depth of corrosion, expressed on a linear time scale. Apart from the very early period (shown in Figure 3-3), the rate of corrosion and film growth are constant, consistent with a transport-limited corrosion reaction. (In Figure 3-2, the step-like pattern of film growth is an artefact of how growth is modelled in the code. The amount of Cu_2S that precipitates is accumulated in an auxiliary register until such time that there is sufficient material to grow the film by an exact number of grid intervals. Any excess Cu_2S is retained in the register until such time that sufficient material is available to once again extend the film to the next grid point.)

In addition to indicating the initial period of non-linear corrosion, Figure 3-3 also highlights the period between 0.35 years and 116 years when corrosion ceases because the surface of the canister is too dry to support aqueous electrochemical processes. The figure also indicates that the Cu_2S film first starts to form after the canister surface re-wets after 116 years, long before the precipitous drop predicted in E_{CORR}. During this intervening period, the formation of Cu_2S is supported by the cathodic reduction of Cu^{2+} and $CuCl_2^-$, both of which occur at more positive equilibrium potentials than the reduction of HS^- that dominates at long times. Therefore, the value of E_{CORR} is predicted to be relatively positive at a time when a Cu_2S film is present. The extent of the electrochemical coupling of $CuCl_2^-$ reduction to the anodic formation of Cu_2S could be limited by the homogeneous reaction between the dissolved Cu(I) species and HS^- in solution, a reaction not currently included in the CSM. Such a homogeneous reaction would reduce the period of relatively positive E_{CORR} values.

The simultaneous reduction of $CuCl_2^-$ and sulfidation of copper can also been seen in Figure 3-4, which illustrates the time-dependence of the charge density (i.e., the extent of the electrochemical reaction) for each of the five electrochemical processes included in Version 1.1eq. Although the sulfidation of copper supported by the reduction of HS^- dominates the system, there is some overlap between the formation of Cu_2S and the "formation" of $CuCl_2^-$. As indicated by the decrease in charge density for the latter reaction, copper dissolution as $CuCl_2^-$ initially proceeds in the forward direction as an anodic process, but later becomes the cathodic reaction supporting the formation of Cu_2S. Overall, however, the extent of this coupling of $CuCl_2^-$ reduction and Cu_2S formation is small compared to the overwhelming extent to which the sulfidation reaction is supported by the reduction of HS^-. The reduction of O_2 is not a significant cathodic reaction during the aerobic phase, as the reduction of Cu^{2+} (produced by the homogeneous oxidation of $CuCl_2^-$ by O_2) is kinetically favoured.

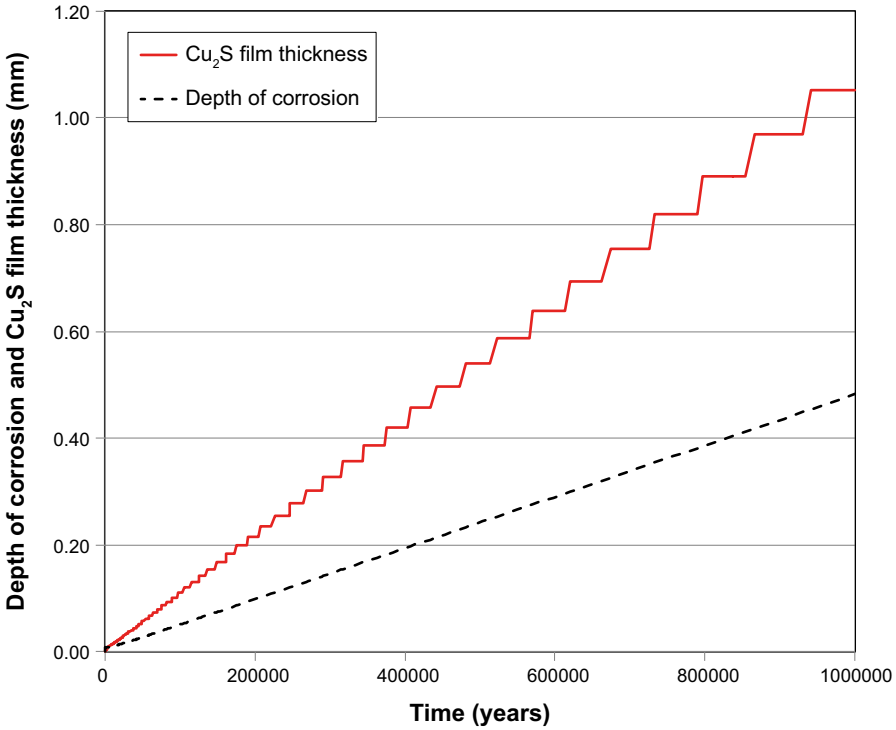

Figure 3-2. *Time-dependence of the Cu_2S film thickness and the depth of corrosion for the reference simulation using the 9-layer CSM Version 1.1eq. The step-like pattern for the Cu_2S film thickness is an artefact of the code and corresponds to the positions of the finite-difference spatial grid.*

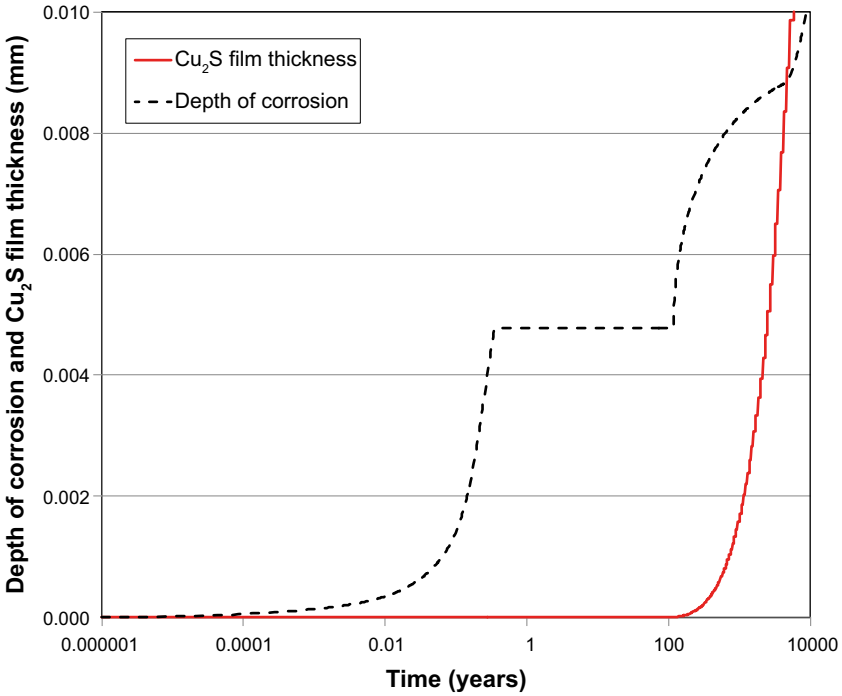

Figure 3-3. *Time-dependence of the Cu_2S film thickness and the depth of corrosion from Figure 3-2 for the initial period showing the cessation of corrosion during the initial dry-out phase and the onset of Cu_2S formation after approximately 100 years.*

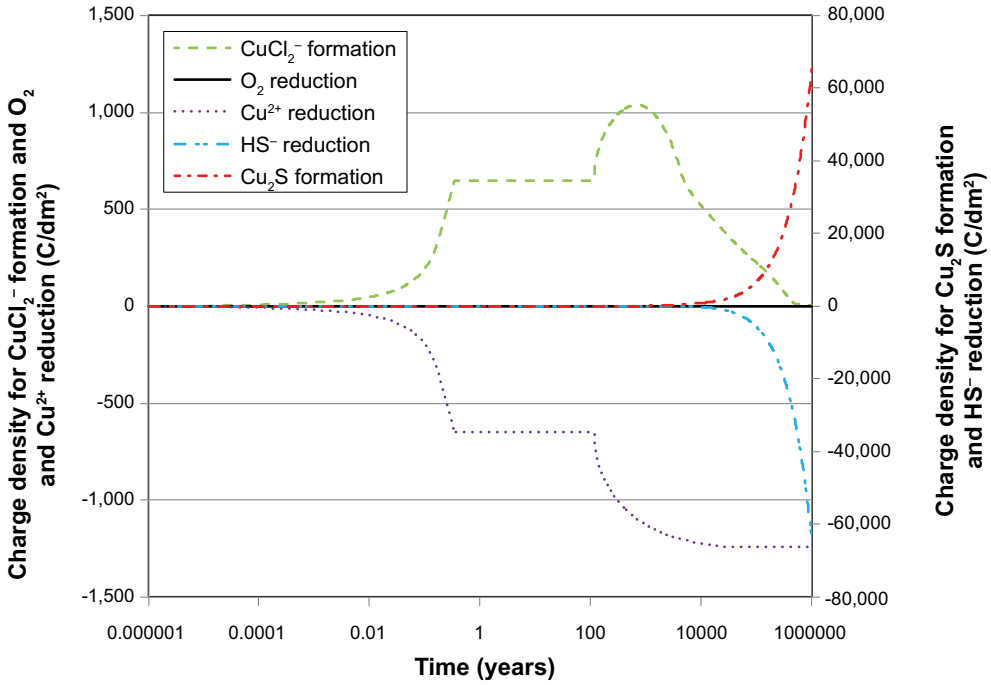

Figure 3-4. *Time-integrated charge density for each of the interfacial electrochemical reactions highlighting the contribution of each process to the total corrosion for the reference simulation using the 9-layer CSM Version 1.1eq.*

As might be expected, the repository system is predicted to be dominated by reactions involving sulfide for the majority of the simulation period of 10^6 years. Figure 3-5 shows the total amount of microbial sulfate reduction, anaerobic pyrite dissolution, and FeS precipitation as a function of time over the entire simulation period. The extents of the latter two processes are identical and, as confirmed by later simulations, it appears that the assumed products of the anaerobic dissolution of FeS_2 (namely HS^- and Fe(II)) simply re-precipitate as FeS. In essence, the thermodynamically more-stable FeS_2 phase is converted to the less-stable and more-soluble FeS. This behaviour is counter-intuitive and is a consequence of assuming that pyrite irreversibly dissolves anaerobically at a significant rate, contrary to the conclusions from King (2013).

Figure 3-5 also shows that significant microbial sulfate reduction is predicted to occur. As noted above, microbial activity is assumed to be suppressed in the HCB in the Version 1.1eq reference simulation and instead sulfate reduction is predicted to occur primarily in the backfill material (Figure 3-6). The rate of sulfate reduction is higher closer to the canister as the reaction is treated as being thermally activated. In comparison, there is very little sulfate reduction in either the EDZ or host rock, both because of the lower assumed sulfate concentration and because of the lower porosity of these layers (Table 3-1).

Because the sulfate reduction reaction is limited only by the availability of SO_4^{2-} (and sufficient saturation to allow microbial activity), large amounts of sulfide are predicted to be produced and to accumulate in the repository. Figure 3-7 shows the predicted distributions of HS^-, SO_4^{2-}, and precipitated FeS after a simulation time of 10^6 years. Sulfide concentrations as high as approximately 5×10^{-3} mol·dm^{-3} are predicted, which is unreasonable for a system containing Fe(II) but is a modelling consequence of assuming that all of the gypsum present in the system is initially dissolved. Indeed, despite this assumption, there is predicted to be significant dissolved SO_4^{2-} still present in the system after 10^6 years, with a concentration of approximately 0.18 mol·dm^{-3} predicted in the HCB and backfill (Figure 3-7).

Interestingly, Figure 3-7 indicates that no FeS precipitates in the EDZ (between 93.93 dm and 98.93 dm). It is assumed that all of the pyrite in this layer has been oxidized during the operational phase (Table 3-1(c)), so that neither pyrite oxidation nor anaerobic dissolution occur. The fact that no FeS subsequently precipitates confirms that, in the model, the formation of FeS is a direct consequence of the anaerobic dissolution of FeS_2.

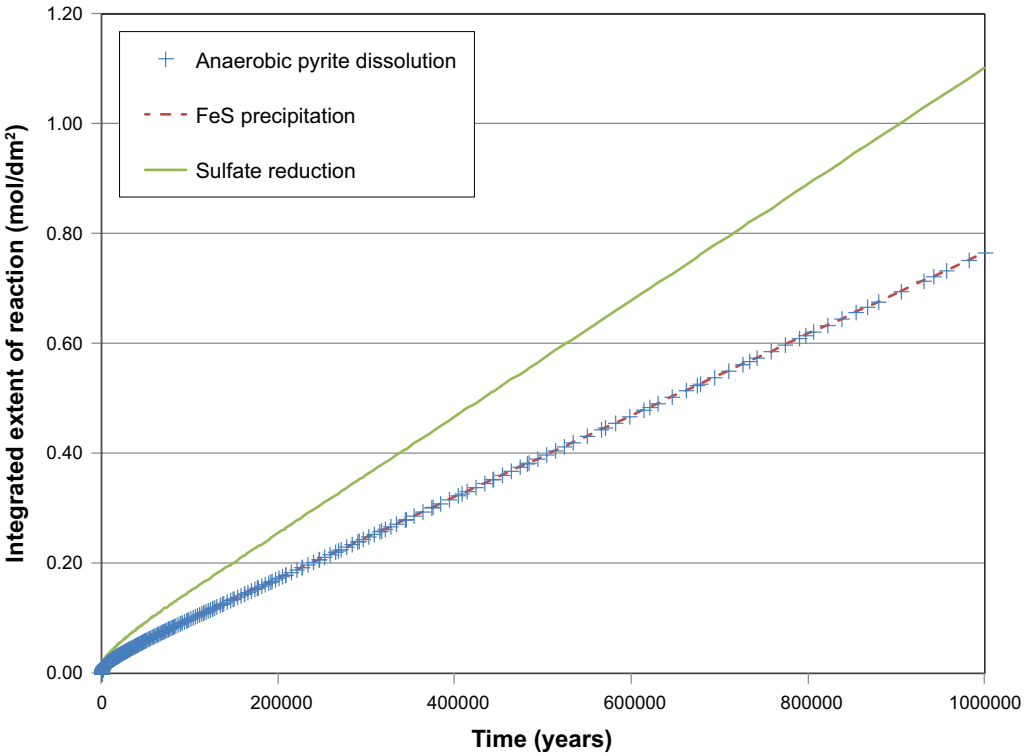

Figure 3-5. *Time dependence of the total extent of sulfate reduction, anaerobic pyrite dissolution, and FeS precipitation for the reference simulation using the 9-layer CSM Version 1.1eq.*

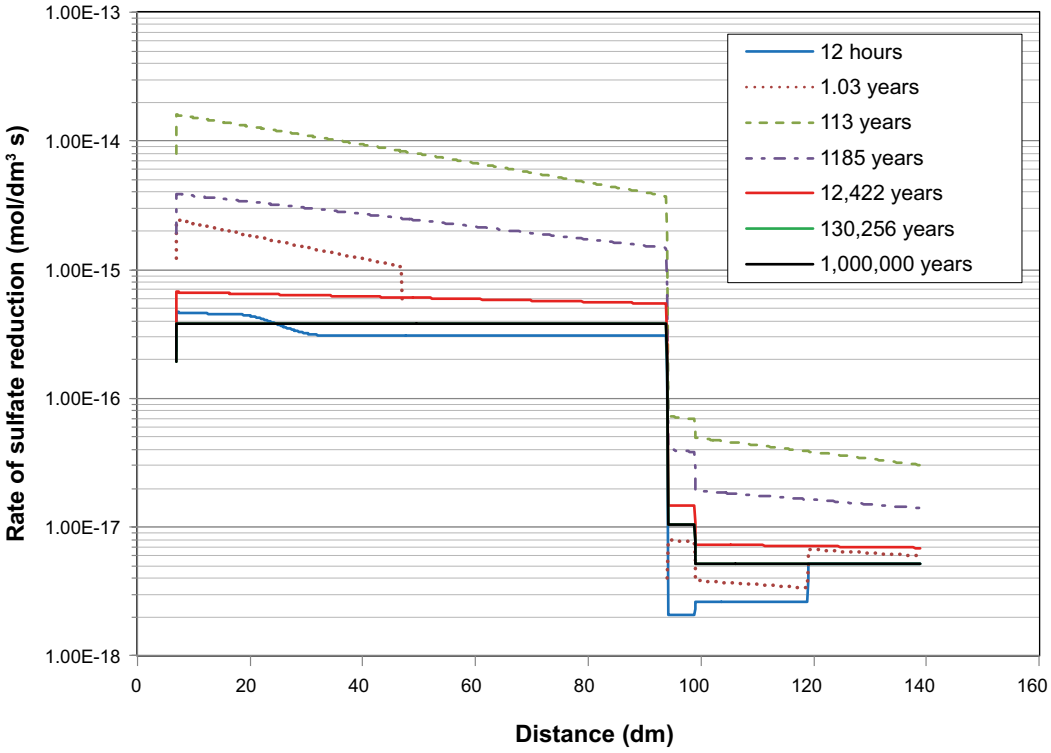

Figure 3-6. *Spatial dependence of the rate of sulfate reduction for selected times for the reference simulation using the 9-layer CSM Version 1.1eq. The backfill layer occupies the region between 6.93 dm and 93.93 dm, with the EDZ and EdZ in the region 94 dm to 119 dm.*

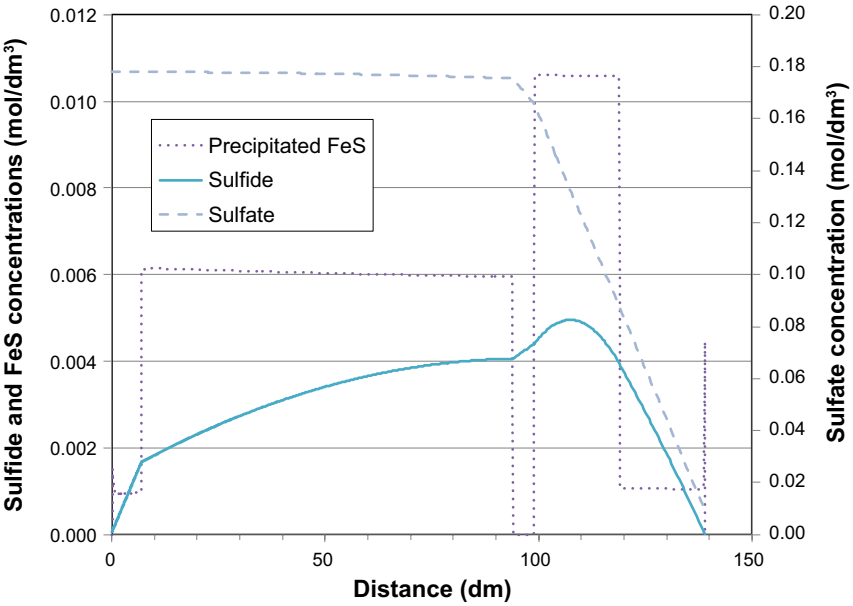

Figure 3-7. *Spatial distribution of the concentrations of sulfate, sulfide, and FeS after 10^6 years for the reference simulation using the 9-layer CSM Version 1.1eq.*

Despite the high concentrations of HS^- formed, the corrosion of the canister is predicted to be transport limited. Figure 3-8 shows the concentration profile of HS^- across the HCB (and part of the inner backfill layer) after a period of 10^6 years. The HS^- concentration at the HCB/backfill boundary is predicted to be 1.65×10^{-3} mol·dm^{-3}, which would produce a maximum steady-state flux to the canister surface of 1.2×10^{-15} mol·cm^{-2}·s^{-1}. This value is a factor of 25–1 700 times lower than the estimated threshold flux for transport control based on experimental measurements (King et al. 2017b). Thus, the CSM prediction of transport control is consistent with that predicted on the basis of the experimentally determined threshold flux for transport control.

The significance of sulfate reduction in the backfill and, more importantly, of the assumptions made here to model that process, can be seen by comparing the results of the reference simulations for the 9-layer and 6-layer Version 1.1eq. These two simulations differ only in the exclusion of the backfill layers and the inclusion of a single EDZ layer for the 6-layer model. The difference in the predicted corrosion behaviour can be seen from the data in Table 3-2. If the backfill, especially, is excluded, the initial sulfate inventory drops by a factor of 90 and the extent of SO_4^{2-} reduction decreases by a factor of over 200. The predicted depth of corrosion after 10^6 years is only 7.1 µm, of which 1.6 µm can be attributed to the presence of O_2 and 5.5 µm to the presence of HS^-. The predicted time dependence of the depth of corrosion and of the Cu_2S film thickness for the 9-layer and 6-layer runs with Version 1.1eq are compared in Figure 3-9 and Figure 3-10, respectively (along with the results of the simulations for the various runs with Versions 1.2a to 1.2f). The reduced extent of sulfide production also delays the time at which E_{CORR} decreases precipitously (Figure 3-11).

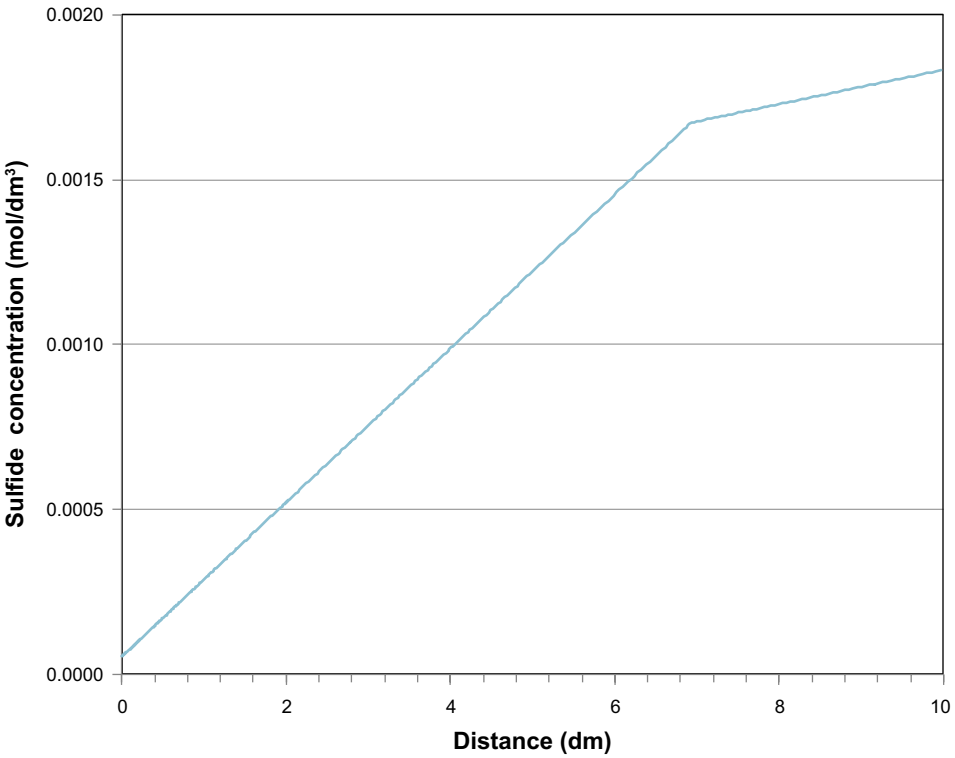

Figure 3-8. *Predicted sulfide concentration profile in the HCB layer after 10^6 years for the reference simulation using the 9-layer CSM Version 1.1eq. The HCB layer thickness is 6.93 dm.*

3.2 Improvements to reaction scheme CSM Versions 1.2a–1.2h

3.2.1 Modification to the reaction scheme CSM Versions 1.2a to 1.2f

The results of the various runs with Versions 1.2a to 1.2f, as well as for the overall Version 1.2a-f are summarized in Figure 3-9 to Figure 3-11 and Table 3-2 and Table 3-3.

The major effects of excluding the anaerobic dissolution of pyrite from the reaction scheme (Version 1.2a) are to suppress the formation of FeS and a decrease in the extent of corrosion. Very little FeS is predicted to form if there is no anaerobic dissolution of FeS_2 (Table 3-2), confirming the conclusion above that, in the model, FeS primarily forms from the dissolution of pyrite and re-precipitation of the dissolution products. The extent of corrosion is approximately 22 % lower than the Version 1.1eq reference case, although the extent of sulfate reduction is the same. Thus, the small fraction of pyrite that is predicted to dissolve in the reference case (only 0.2 % of the inventory) may be a significant contributor to the amount of corrosion in the model. However, there is no evidence that pyrite does dissolve anaerobically (King 2013) and, for the model, we used dissolution rates derived from a study of the dissolution of biotite in the absence of specific measurements for pyrite. There is no effect of excluding the anaerobic dissolution of pyrite on the predicted time dependence of E_{CORR} (Figure 3-11).

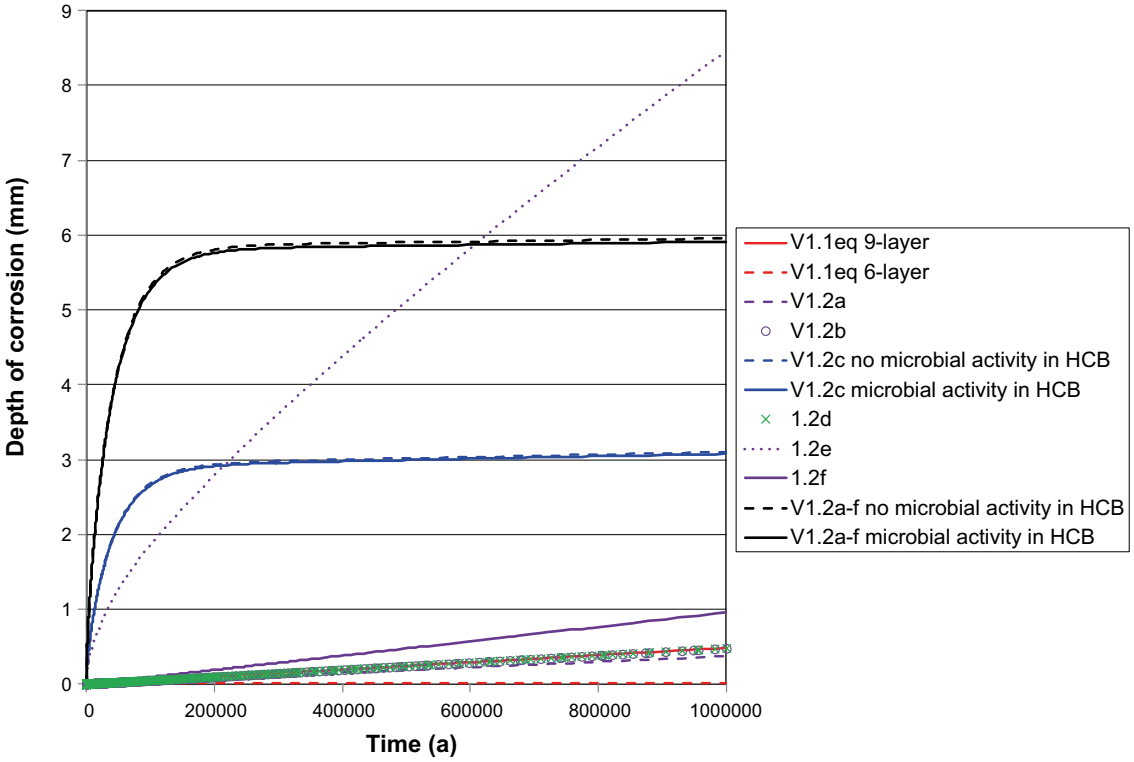

Figure 3-9. *Predicted time dependence of the depth of corrosion for the CSM Version 1.1eq, individual Versions 1.2a to 1.2f, and full Version 1.2a-f.*

Table 3-2. Results of simulations using CSM Version 1.1eq, individual Versions 1.2a to 1.2f, and full Version 1.2a-f for a period of 10^6 years for processes related to the extent of corrosion and sulfide production and consumption.

Run	Net charge density for $CuCl_2^-$ formation		Charge density for Cu_2S formation		Cu_2S film thickness	Extent of SO_4^{2-} reduction	Inventories ($mol \cdot dm^{-2}$)							
							SO_4^{2-}		HS^-		FeS_2		FeS	
	($C \cdot dm^{-2}$)	(mm)	($C \cdot dm^{-2}$)	(mm)	(mm)	($mol \cdot dm^{-2}$)	Initial	Final	Initial	Final	Initial	Final	Initial	Final
V1.1eq 9-layer	7.89	6×10^{-5}	6.6×10^{4}	0.48	1.05	1.10	7.42	3.53	10^{-6}	0.063	464.4	463.6	0	0.77
V1.1eq 6 layer	212	1.6×10^{-3}	752	5.5×10^{-3}	0.013	0.0051	0.081	0.0073	10^{-6}	1.2×10^{-5}	42.1	42.0	0	0.23
V1.2a	25.2	2×10^{-4}	5.0×10^{4}	0.37	0.82	1.10	7.42	3.53	10^{-6}	0.047	464.4	464.4	0	0.00018
V1.2b	6.13	5×10^{-5}	6.5×10^{4}	0.48	1.05	1.10	7.42	3.53	10^{-6}	0.063	464.4	463.6	0	0.78
V1.2c1	0.45	3×10^{-6}	4.2×10^{5}	3.1	7.16	8.78	7.42	6×10^{-4}	10^{-6}	0.024	464.4	463.6	0	0.77
V1.2c2	−14.7	-	4.2×10^{5}	3.1	6.59	8.72	7.42	6×10^{-4}	10^{-6}	0.024	464.4	463.6	0	0.77
V1.2d	1.1×10^{3}	0.008	6.5×10^{4}	0.48	1.05	1.10	7.42	3.53	10^{-6}	0.063	464.4	463.6	0	0.77
V1.2e	1.0×10^{6}	7.5	1.3×10^{5}	0.96	2.05	1.10	7.42	3.53	10^{-6}	0.062	464.4	463.6	0	0.77
V1.2f	7.19	5×10^{-5}	1.3×10^{5}	0.96	2.05	1.10	7.42	3.53	10^{-6}	0.064	464.4	463.6	0	0.77
V1.2a-f.1	19.3	1.4×10^{-4}	8.1×10^{5}	5.95	13.2	8.79	7.42	6×10^{-4}	10^{-6}	0.0087	464.4	464.4	0	0.011
V1.2a-f.2	20.7	1.5×10^{-4}	8.0×10^{5}	5.91	13.2	8.72	7.42	6×10^{-4}	10^{-6}	0.0087	464.4	464.4	0	0.011

Table 3-3. Results of simulations using CSM Version 1.1eq, individual Versions 1.2a to 1.2f, and full Version 1.2a-f for a period of 10^6 years for processes related to the consumption of the initial oxygen inventory.

Run	O_2 inventory	Charge density for O_2 reduction		Extent of $CuCl_2^-$ oxidation		Extent of pyrite oxidation		Extent of aerobic respiration	
	($mol \cdot dm^{-2}$)	($C \cdot dm^{-2}$)	(%)	($mol \cdot dm^{-2}$)	(%)	($mol \cdot dm^{-2}$)	(%)	($mol \cdot dm^{-2}$)	(%)
V1.1eq 9-layer	0.0378	2.6×10^{-3}	0	3.36×10^{-3}	8.9	9.21×10^{-3}	91	7.1×10^{-5}	0.19
V1.1eq 6 layer	0.00161	2.6×10^{-3}	0	1.61×10^{-3}	99.9	6.0×10^{-7}	0.14	1.5×10^{-9}	0
V1.2a	0.0378	2.6×10^{-3}	0	3.36×10^{-3}	8.9	9.21×10^{-3}	91	7.1×10^{-5}	0.19
V1.2b	0.0378	2.6×10^{-3}	0	3.37×10^{-3}	8.9	9.87×10^{-3}	91	7.3×10^{-5}	0.19
V1.2c1	0.0378	2.6×10^{-3}	0	3.36×10^{-3}	8.9	9.21×10^{-3}	91	7.1×10^{-5}	0.19
V1.2c2	0.0378	2.2×10^{-3}	0	3.26×10^{-3}	8.6	9.24×10^{-3}	91	8.9×10^{-5}	0.23
V1.2d	0.0378	2.6×10^{-3}	0	3.36×10^{-3}	8.9	9.21×10^{-3}	91	7.1×10^{-5}	0.19
V1.2e	0.0378	2.0×10^{-3}	0	3.39×10^{-3}	9.0	9.21×10^{-3}	91	7.1×10^{-5}	0.19
V1.2f	0.0378	2.6×10^{-3}	0	3.36×10^{-3}	8.9	9.21×10^{-3}	91	7.1×10^{-5}	0.19
V1.2a-f.1	0.0378	2.6×10^{-3}	0	3.37×10^{-3}	8.9	9.87×10^{-3}	91	7.3×10^{-5}	0.19
V1.2a-f.2	0.0378	2.6×10^{-3}	0	3.37×10^{-3}	8.9	9.87×10^{-3}	91	9.2×10^{-5}	0.24

Updating the stoichiometry for the oxidative dissolution of pyrite (from 3.75 mol O_2 to 3.5 mol O_2) had no effect on the predicted results (Version 1.2b). There was no effect on the predicted time dependence of the depth of corrosion, Cu_2S film thickness, or behaviour of E_{CORR} (Figure 3-9 to Figure 3-11). There was no effect either on the contribution of the various O_2-consumption processes to the consumption of the initial O_2 inventory (Table 3-3). It is interesting to note from Table 3-3 that when there is backfill present in the repository with a significant content of pyrite, the oxidative dissolution of FeS_2 is predicted to account for consumption of approximately 90 % of the O_2 inventory.

In Version 1.2c, the mechanism of sulfate reduction by SRB was updated (to make it first order with respect to the sulfate concentration) and a new value of the rate constant was derived from the study of Bengtsson et al. (2017). Two simulations were performed; one in which there was no microbial activity in the HCB (run V1.2c1) and one in which microbial activity was allowed in the buffer (run V1.2c2). There was not much difference in the results for the two runs, but there was a very significant difference between Version 1.2c and Version 1.1eq. The extent (Table 3-2) and rate (compare the initial slopes of the plots in Figure 3-9 and Figure 3-10) of sulfate reduction were far higher for the updated Version 1.2c. The total extent of sulfate reduction was approximately seven times higher and virtually all of the available sulfate was reduced, compared with only approximately 50 % for the reference case (Table 3-2). Higher rates of sulfate reduction also caused an earlier transition in E_{CORR} (Figure 3-11).

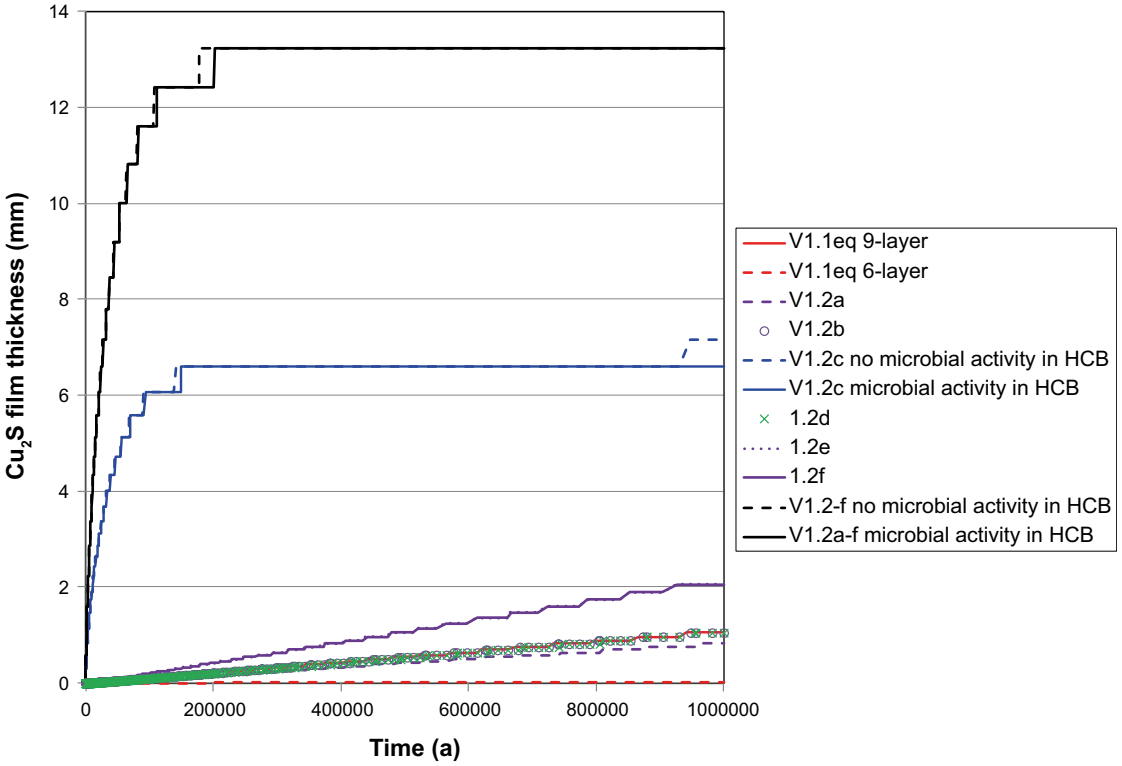

Figure 3-10. *Predicted time dependence of the Cu_2S film thickness for the CSM Version 1.1eq, individual Versions 1.2a to 1.2f, and full Version 1.2a-f.*

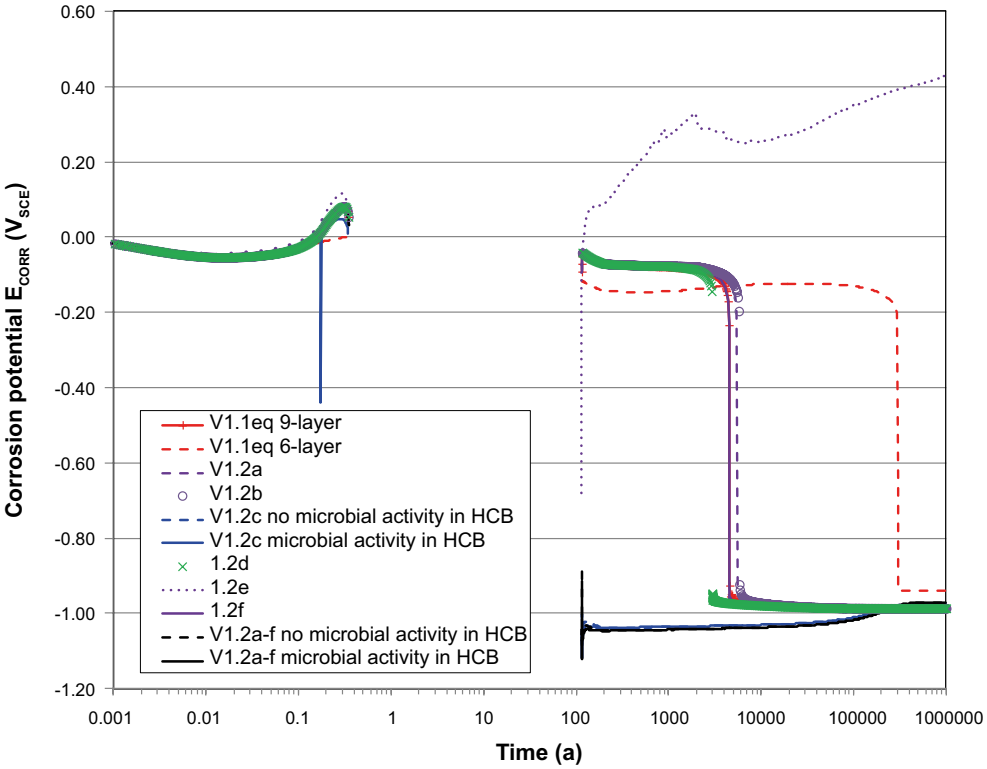

Figure 3-11. *Predicted time dependence of the corrosion potential E_{CORR} for the CSM Version 1.1eq, individual Versions 1.2a to 1.2f, and full Version 1.2a-f.*

However, although we have updated the sulfate reduction mechanism in Version 1.2c, there are still a number of artefacts in the predicted results. The large amount of sulfide formed is partly a consequence of the fact that we have chosen to initially dissolve the entire gypsum inventory in the backfill in order to account for all possible sources of sulfate. Thus, the rate of sulfate reduction is artificially high as it is assumed to be proportional to the SO_4^{2-} concentration and is not limited by the availability of SO_4^{2-} until such time that virtually the entire inventory has been consumed. It is possible, however, that the rate of sulfate reduction will be limited by the low solubility of gypsum (which will result in a lower pore-water [SO_4^{2-}] than that assumed here) and/or by the gypsum dissolution rate. In addition, the rate of the microbially mediated process may be limited by the availability of energy sources and electron donors. These shortcomings in the treatment of microbial sulfate reduction were addressed in Version 1.2g, the results of which are described in Section 3.2.2.

For the current purposes, it is sufficient to note that sulfate reduction appears to be a significant source of HS^- for canister corrosion. It is necessary, therefore, to ensure that we properly simulate this process, including all of the possible limiting processes, in the CSM.

The only apparent differences of including the conversion of Cu_2O to Cu_2S (Version 1.2d) were:

- A slightly greater contribution to the overall extent of corrosion by copper oxidation to Cu(I) (Table 3-2) due to the fact that the Cu_2O layer was chemically converted to Cu_2S before it could dissolve as $CuCl_2^-$ and be subsequently reduced to Cu(0) in support of copper sulfidation.
- Earlier onset of the precipitous decrease in E_{CORR} (Figure 3-11), again because the Cu(I) species in the Cu_2O film were *chemically* converted to Cu_2S rather than being *electrochemically* reduced.

The inclusion of the reduction of H_2O as an additional cathodic process (Version 1.2e) had significant effects on the predicted corrosion behaviour. First, a greater depth of corrosion was predicted after 10^6 a than for any other simulation (Figure 3-9), with approximately 90 % of that corrosion resulting from the anodic dissolution as $CuCl_2^-$ rather than the formation of Cu_2S (Table 3-2). Furthermore, very positive E_{CORR} values were predicted during the period when the repository environment would be expected to be dominated by sulfide (Figure 3-11). (The E_{CORR} values in Figure 3-11 are more positive than those indicated in the Evans diagram in Figure 3-12 because the latter refers to relatively high rates of mass transport in stagnant bulk solution. For the restrictive mass transport conditions in the repository, E_{CORR}

shifts to more-positive values, as predicted). As shown in Figure 3-13, corrosion is primarily the result of the coupling of the anodic dissolution of copper as $CuCl_2^-$ to the evolution of H_2 from the cathodic reduction of H_2O. The evolution of H_2 from the cathodic reduction of HS^- is insignificant, which results in a doubling of the thickness of the Cu_2S film (Table 3-2, Figure 3-10) since all sulfide reaching the canister surface is consumed by the anodic reaction instead of being divided between the sulfidation and HS^- reduction processes.

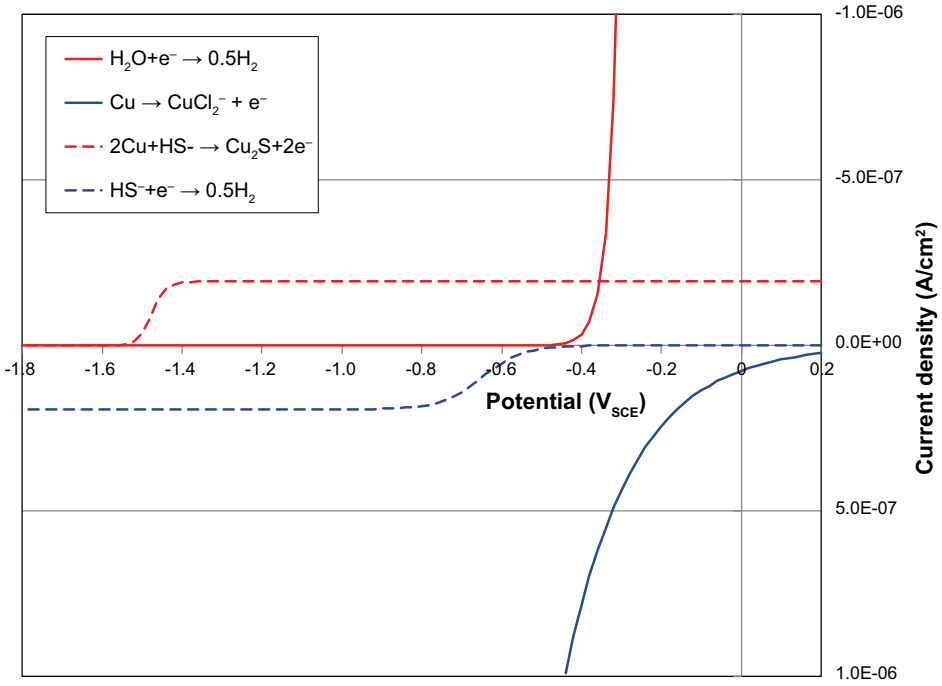

Figure 3-12. *Current density (i) versus potential (E) diagram for the principal anodic (in red) and cathodic (in blue) reactions for CSM Version 1.2e. The i-E curves for the anodic sulfidation reaction (dashed red line) and the evolution of H_2 due to the cathodic reduction of HS^- (dashed blue curve) are shown as net transport-limited processes assuming a steady-state mass-transfer coefficient of 2×10^{-4} cm/s (equivalent to that in stagnant bulk solution). Non-transport-limited i-E curves are shown for the anodic dissolution as $CuCl_2^-$ (solid red curve) and for the cathodic reduction of H_2O (solid blue curve). In reality, the anodic process is both reversible and likely to be transport limited, which would result in a lower current density.*

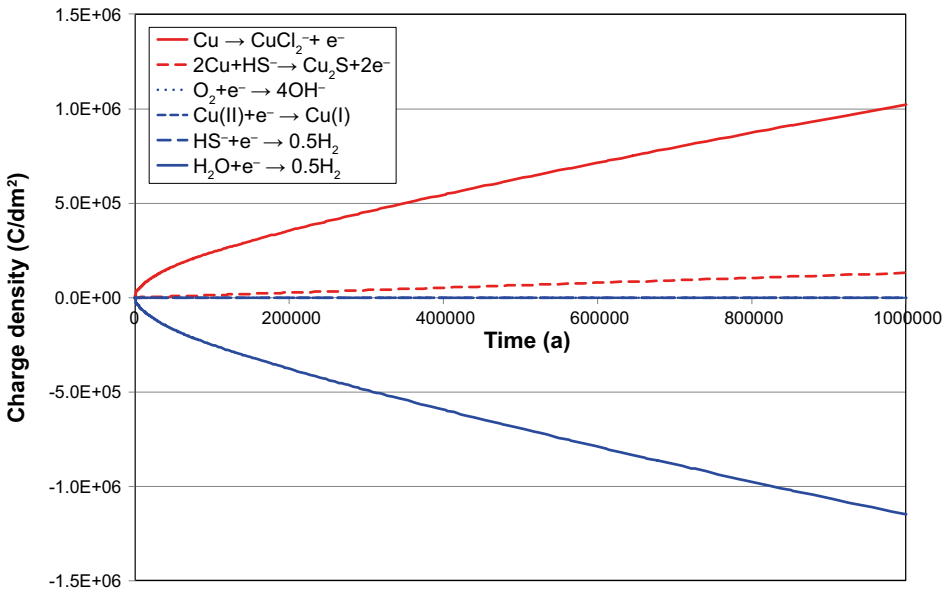

Figure 3-13. *Predicted time dependence of the charge density for each anodic (in red) and cathodic (in blue) reactions for CSM Version 1.2e.*

Figure 3-12 shows a current density (i) versus potential (E) diagram for the principal anodic and cathodic processes for Version 1.2e. Because the equilibrium potential for the cathodic reduction of H_2O (Appendix A) is more-positive than that for the evolution of H_2 from the reduction of HS^-, the former reaction can couple to the anodic dissolution of $CuCl_2^-$ at relatively positive potentials. However, this coupling does not occur in practise, as indicated by E_{CORR} values of the order of −0.9 V_{SCE} measured in sulfide-containing Cl^- solutions (King et al. 2011a, Smith et al. 2007b). Instead, such negative potentials are consistent with the coupling of the formation of Cu_2S and the cathodic reduction of HS^- (Figure 3-12). Although H_2O is present at a much higher concentration than HS^-, it appears that the cathodic reduction of H_2O is kinetically hindered in this system. It is concluded, therefore that the values for the kinetic parameters derived from Cu/H_2O system (Appendix A) do not properly describe the kinetics of H_2O reduction on copper in sulfide environments.

The correct accounting of sulfide for the cathodic reduction of HS^- (Version 1.2f) has a significant effect on the depth of corrosion. As discussed in Section 2.3.6, we have previously not correctly accounted for the sulfide in the HS^- species assumed to be undergoing cathodic reduction. Because the product of this reaction (nominally the sulfide species S^{2-}) is not included in the model, this sulfide is effectively lost from the system. In reality, any S^{2-} species would rapidly protonate to re-form the HS^- species from which it was produced. The results of the simulation with Version 1.2f demonstrates that we were indeed previously mis-accounting for all of the sulfide reaching the canister surface. As expected, the depth of corrosion and of the thickness of the Cu_2S film for Version 1.2f is double that for the reference case with Version 1.1eq (Table 3-2, Figure 3-9 and Figure 3-10). In addition, the precipitous decrease in E_{CORR} occurs slightly earlier than in the reference case, although the final value of the potential is similar (Figure 3-11).

Lastly, two simulations were performed using a version of the code that incorporated all of the individual changes described above (Version 1.2a-f). (For these calculations, the rate constant for the interfacial reduction of H_2O (k_F) was set to zero based on the conclusion that this process either does not occur or the derived input parameter values in Appendix A are incorrect). The resulting corrosion behaviour was similar to that for Version 1.2c (improved treatment of microbial sulfate reduction), except that the predicted depth of corrosion (Figure 3-9) and Cu_2S film thickness (Figure 3-10) were doubled because of the correction to the accounting for sulfide produced by the cathodic reduction of HS^- (Version 1.2f). As for the results from Version 1.2c (Figure 3-11), the predicted E_{CORR} exhibits the precipitous decrease to values of approximately −1.0 V_{SCE} as soon as the surface re-wets following the period of dry out because of the high concentration of sulfide predicted based on the change in the treatment of the microbial sulfate reduction process.

3.2.2 Improved treatment of microbial sulfate reduction CSM Version 1.2g

In comparison with Version 1.1eq, the changes introduced for Version 1.2g were as follows:

- Replacement of zero-order kinetics for the reduction of sulfate with a Monod expression for both organotrophic and chemotrophic SRB.
- Dissolution of gypsum and temperature-dependent sulfate solubility.
- Possible limitation by the availability of organic carbon.
- Siderite and biotite dissolution as sources of dissolved Fe(II) instead of anaerobic pyrite dissolution.

In common with the stepwise development of the code for Versions 1.2a through 1.2f, none of the other incremental changes were included in Version 1.2g. For example, the treatment of pyrite oxidation or the accounting for S^{2-} ions produced by the reduction of HS^- in Version 1.2g was the same as that for Version 1.1eq, which is used here as a reference for the two runs carried out with Version 1.2g. As described in Table 2-4, these two simulations differed in whether microbial activity was excluded (run 1.2g1) or permitted (run 1.2g2) in the HCB layers.

Figure 3-14 shows the predicted time dependence of the depth of corrosion for the two runs using the improved treatment of microbial sulfate reduction as well as for the reference calculation using Version 1.1eq. The introduction of the revised microbial kinetics and additional sources of dissolved Fe(II) to act as a sink for HS^- in Version 1.2g results in less corrosion than for Version 1.1eq (of the order of 12 μm and 9 μm after 10^6 a for 1.2g1 and 1.2g2, respectively). There is a corresponding difference between the predicted Cu_2S film thickness for the runs using Version 1.2g and Version 1.1eq (Figure 3-15). Thus, the alternative kinetic treatment for microbial sulfate reduction results in less

damage to the canister. This difference is due partly to a decrease in the extent of sulfate reduction (1.1 mol dm^{-2} for V1.1eq after 10^6 a compared with 0.57 mol dm^{-2} for both V1.2g runs after the same period) and partly due to the increased precipitation of FeS (0.77 mol dm^{-2} for V1.1eq after 10^6 a compared with 1.96 mol dm^{-2} for both V1.2g runs after the same period). Thus, FeS precipitation accounts for at most 70 % of the microbially produced sulfide for V1.1eq, but potentially a greater fraction for V1.2g. (In the latter case, the cumulative amount of FeS exceeds the amount of sulfide produced by microbial activity because of the greater contribution from the precipitation of HS^- from the ground water). The impact of FeS as a sink for microbially produced sulfide is discussed in more detail for the best-estimate calculations in Section 4 and the benchmarking runs in Section 5.

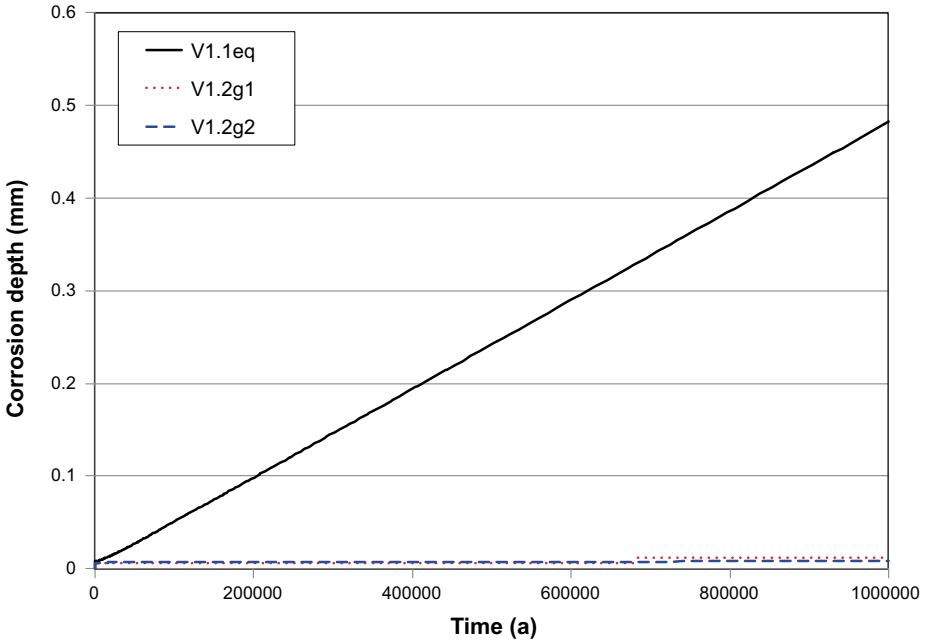

Figure 3-14. *Predicted time-dependence of the depth of corrosion for two simulations carried out with Version 1.2g and that for Version 1.1eq for comparison. For runs 1.2g1 and 1.2g2, microbial activity was excluded and permitted in the HCB, respectively.*

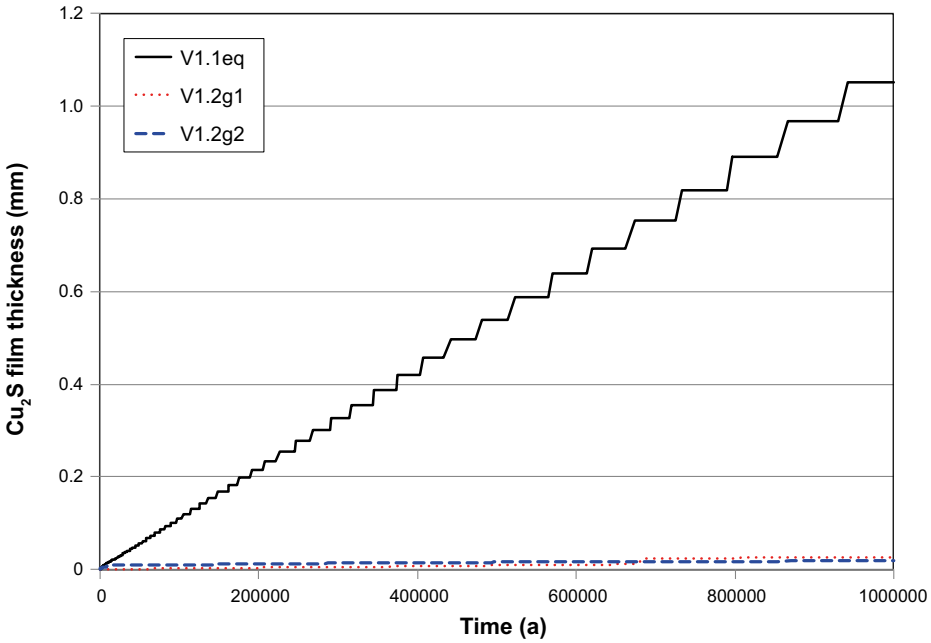

Figure 3-15. *Predicted time-dependence of the Cu_2S film thickness for two simulations carried out with Version 1.2g and that for Version 1.1eq for comparison. For runs 1.2g1 and 1.2g2, microbial activity was excluded and permitted in the HCB, respectively.*

Interestingly, there is little difference in the predicted extent of corrosion for Version 1.2g depending on whether microbial activity is (1.2g2) or is not (1.2g1) permitted in the HCB layers. For the improved microbial treatment, the extent of sulfate reduction is limited by the amount of organic carbon, which is predicted to be totally consumed after 18 000 a or 185 000 a with and without microbial activity in the buffer, respectively.

Figure 3-16 shows the predicted time dependence of E_{CORR} for the three runs. In so far as the time at which the potential drops precipitously to negative values is an indication of the relative extent of sulfide production, the trends observed in E_{CORR} are consistent with the trends in the predicted corrosion damage discussed above. Thus, the higher rate of sulfide production for Version 1.1eq results in faster transport of HS^- to the canister surface and an earlier decrease in E_{CORR} than the slower microbial kinetics in the improved Version 1.2g. In the latter case, if microbial activity is allowed to occur in the HCB, the decrease in E_{CORR} occurs earlier as the sulfide is produced closer to the canister surface. If microbial activity is restricted to the backfill and EDZ/EdZ layers only (run 1.2g1, red dotted curve in Figure 3-16), the decrease in E_{CORR} is not predicted to occur until approximately 650 000 a postclosure because of a combination of (i) the slower and more-limited sulfate reduction, (ii) the longer diffusion distance to the canister surface, and (iii) the greater potential for precipitation of sulfide as FeS prior to reaching the canister.

If microbial activity is assumed to occur in the HCB (blue dashed curve in Figure 3-16), E_{CORR} exhibits an unusual "double-dip". The first decrease in E_{CORR} results from the transport of HS^- produced primarily in the buffer to the canister surface. Of the two sulfate reduction pathways, the extent of organotrophic activity far exceeds the chemotrophic pathway, accounting for > 99.9 % of the total sulfide production after 10^6 a. The organotrophic pathway ceases once all of the organic carbon is consumed after 18 000 a and, in the absence of a continued flux of HS^- to the canister surface, the value of E_{CORR} increases. However, there is a subsequent period of chemotrophic sulfate reduction predicted to occur at times later than 10^5 a, presumably corresponding to the time it takes the H_2 produced by corrosion due to the prior organotrophic production of HS^- to reach the EDZ/EdZ layers where there is a remaining microbial population. The extent of chemotrophic sulfate reduction is small compared with that produced organotrophically, but E_{CORR} responds to the **relative** rates of the anodic and cathodic reactions not to the absolute rate. Thus, in the absence of other electrochemical processes occurring at this time, even small amounts of chemotrophically produced sulfide can cause a decrease in E_{CORR}.

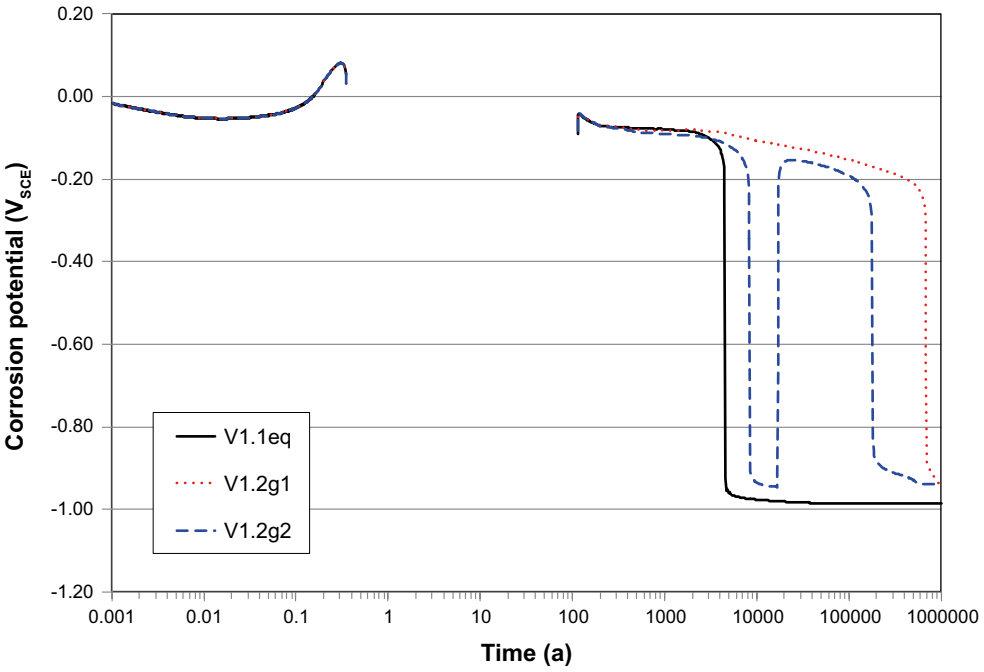

Figure 3-16. *Predicted time dependence of the corrosion potential E_{CORR} for two simulations using CSM Version 1.2g and for Version 1.1eq for comparison. For runs 1.2g1 and 1.2g2, microbial activity was excluded and permitted in the HCB, respectively.*

The results from a series of simulations using a version of the code incorporating all changes in Versions 1.2a to 1.2g included (denoted Version 1.2a-g) are described in Section 4.

3.2.3 Treatment of gaseous H_2S CSM Version 1.2a-h

Figure 3-17 compares the time dependence of the Cu_2S film thickness for the Version 1.2a-h simulation with that for the best-estimate simulation with Version 1.2a-g (see Section 4). For the Version 1.2a-h simulation, both the total film thickness and the contribution from the gaseous sulfidation reaction are shown. The gaseous pathway leads to an approximate doubling of the film thickness after 10^6 a, but the reaction involving $H_2S(g)$ ceases after approximately 5.2 a at a thickness of 23.4 µm.

Gaseous H_2S is initially present in the EDZ and EdZ layers only, with dissolved HS^- being present in these layers as well as the intact rock (Figure 3-18). However, the total amount of gas-phase Cu_2S formation (7.5×10^{-3} mol/dm^2, equivalent to the film thickness of 23.4 mm) is approximately four orders of magnitude greater than the amounts of gaseous H_2S (5.3×10^{-7} mol/dm^2) and dissolved HS^- (9.6×10^{-7} mol/dm^2) initially present. Volatilisation of dissolved sulfide in the host rock does not appear to be a significant source of gaseous H_2S because the low porosity limits the amount of sulfide that can be released to the gas phase.

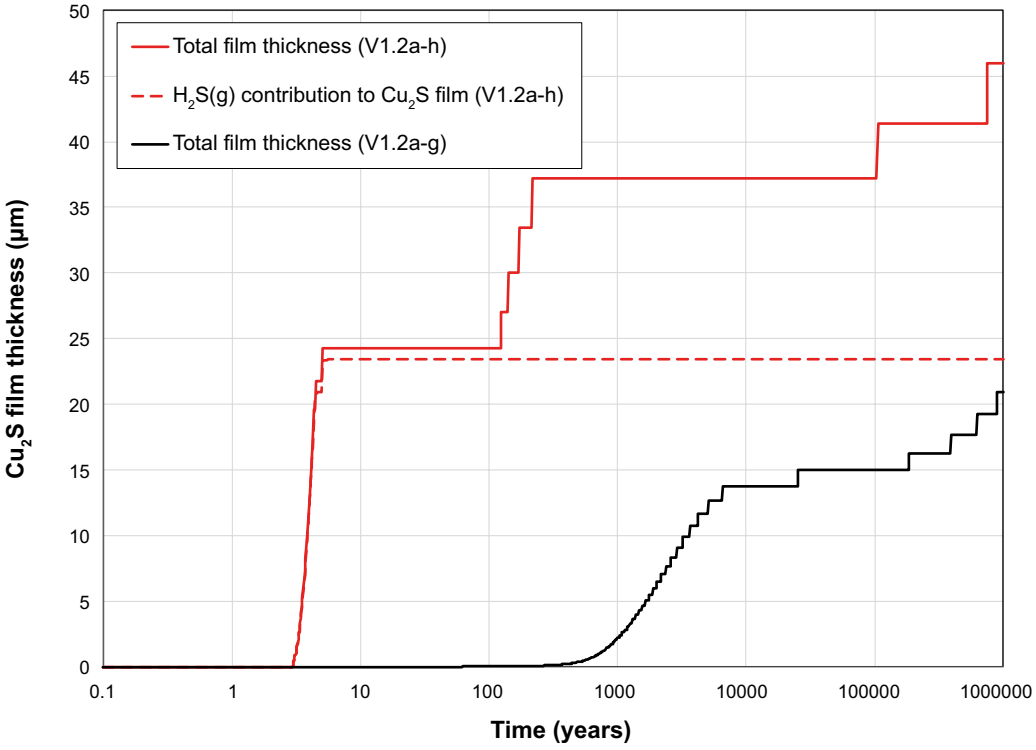

Figure 3-17. *Comparison of the time-dependent thickness of the Cu_2S film for the best-estimate simulations using CSM Version 1.2a-g (black) and Version 1.2a-h (red). For Version 1.2a-h, the contribution to film growth via the gas-phase sulfidation reaction is also shown. The stepwise nature of the growth curves is an artefact of how film growth is treated in the model, in which growth only occurs once sufficient Cu_2S has formed to extend the film to the next grid point.*

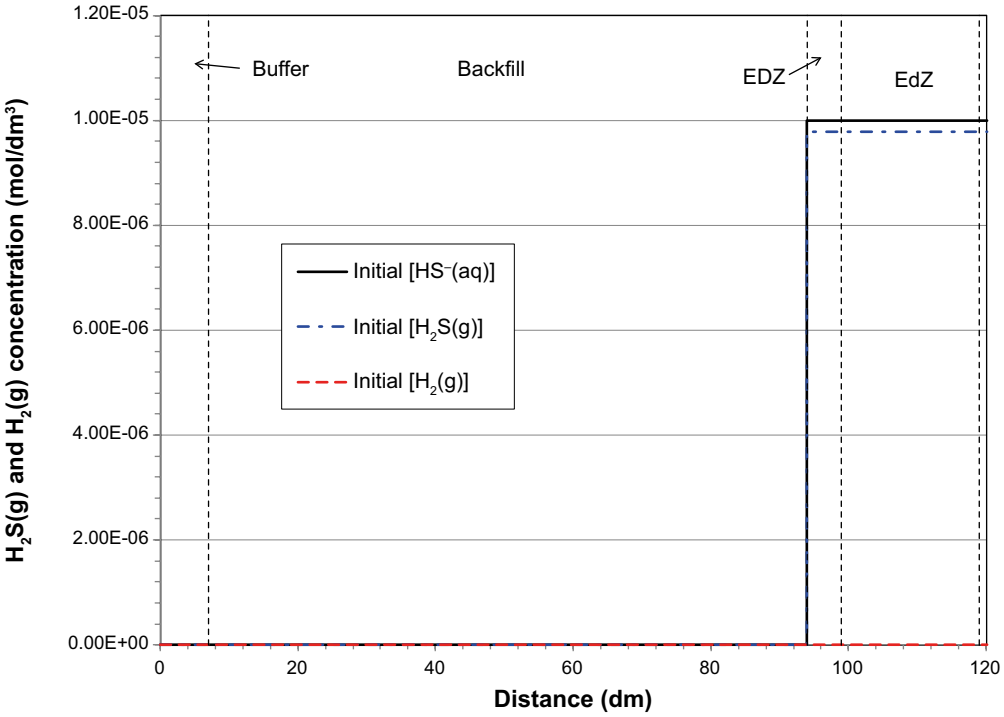

Figure 3-18. *Initial distributions of dissolved sulfide and of gaseous H_2S and hydrogen for the Version 1.2a-h simulation.*

The majority of the gas-phase Cu_2S film results from sulfide produced by microbial activity, primarily just inside the backfill layer closest to the buffer/backfill interface. Figure 3-19 shows the distributions of dissolved HS^- and of gaseous H_2S and H_2 for various times between approximately 1 month and 11 years. The source of gaseous H_2S is clearly the EDZ and EdZ where microbial activity is possible at all times (Figure 3-20) and just inside the backfill layer where microbial activity is possible for the first 4.5 a (based on the assumed threshold degree of saturation for microbial activity (Table 4-1) and the assumed saturation profiles for the best-estimate case (Table 4-2)).

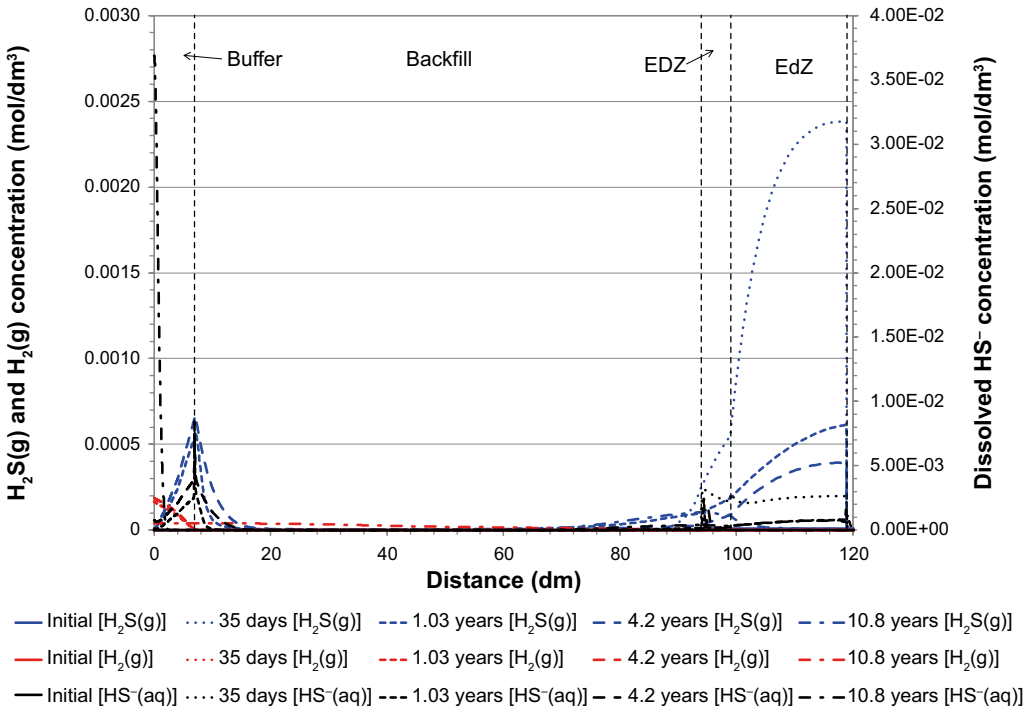

Figure 3-19. *Concentration profiles for dissolved sulfide and of gaseous H_2S and hydrogen for times up to 10.8 years for the Version 1.2a-h simulation.*

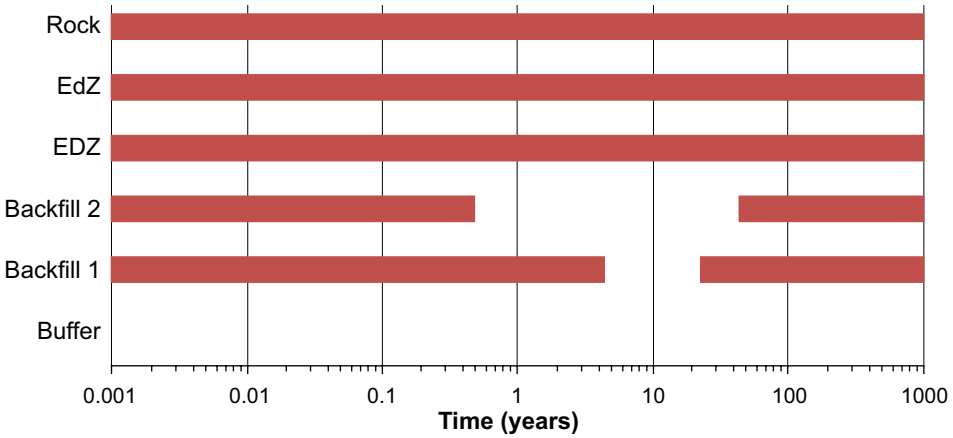

Figure 3-20. *Bar graph illustrating the times at which microbial activity is possible in the various layers for the Version 1.2a-h simulation. Microbial activity does not occur in the buffer at any time and ceases in the two backfill layers during the gap between the bars.*

The peak in $H_2S(g)$ concentration at the buffer/backfill interface is a clue to the process responsible for the early production of dissolved sulfide, which then leads to the formation of gaseous H_2S and the sulfidation of the copper. Although the buffer is a source of organic carbon for organotrophic sulfate reduction, the canister surface is also a source of H_2 for chemotrophic sulfate reduction. Figure 3-21 shows that the chemotropic pathway initially outpaces the organotrophic route. In fact, the extent of chemotrophic sulfate reduction up to the point of inflection in the curve at approximately 4 a exactly equals the extent of gas-phase sulfidation of the copper (7.5×10^{-3} mol/dm^2, equivalent to a film thickness of 23.4 mm). Thus, 100 % of the early chemotrophically produced dissolved HS^- is predicted to eventually partition into the gas phase and lead to the formation of Cu_2S. As noted in Section 2.3.8, unlike dissolved HS^-, gaseous H_2S is assumed not to react with any other species in the system and is free to (rapidly) diffuse to the canister surface. It should be noted that this is occurring at a time at which the other interfacial reactions have ceased because the canister surface is deemed to have dried out sufficiently to prevent aqueous-based electrochemical processes.

Figure 3-19 also shows the gaseous H_2 profiles, with the canister surface as the source. The gas-phase sulfidation of copper produces H_2 (Reaction (2-85)), which then diffuses towards the backfill where it is consumed by the chemotrophic reduction of sulfate to produce more sulfide. It is important to remember, however, that this process is not autocatalytic as 4 mol H_2 are required to produce 1 mol HS^- (Reaction (2-58)). This fact, along with the cessation of microbial activity in the backfill after 4.2 a, contributes to the temporary cessation of sulfate production. As the repository saturates and the gas-phase diffusion of H_2S towards, and of H_2 away from, the canister surface slows down, the reaction between $H_2S(g)$ and the canister stops. Thereafter, the organotrophic reduction of sulfate becomes the dominant pathway, eventually accounting for over 90 % of the total sulfate reduction (Figure 3-21).

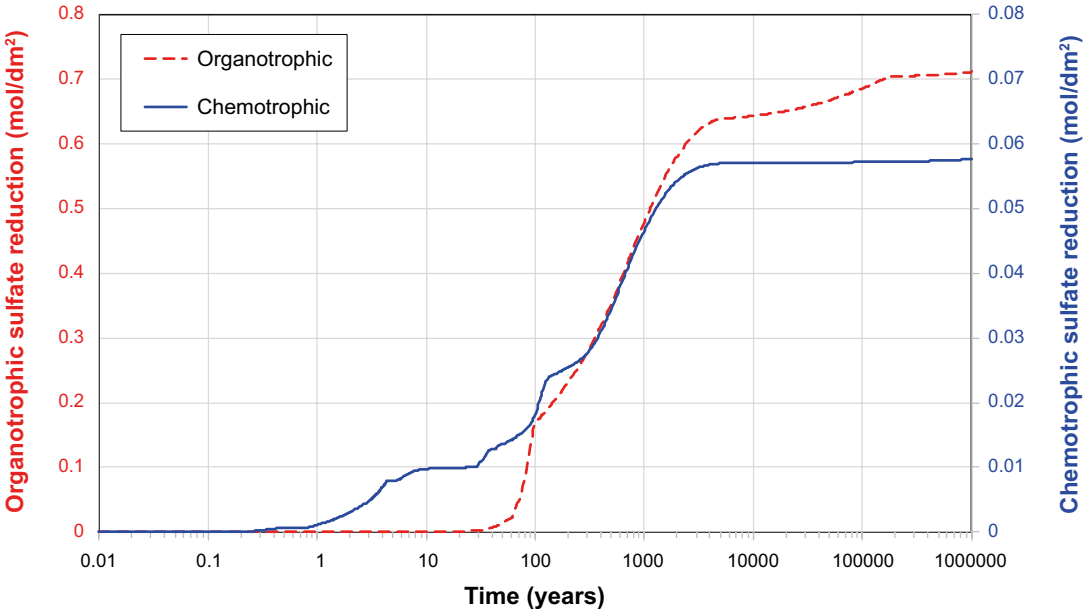

Figure 3-21. *Time dependence of the cumulative extents of organotrophic (in red) and chemotrophic (in blue) sulfate reduction for the Version 1.2a-h simulation. Note the difference in scales for the two axes.*

3.3 Spatial separation of anodic and cathodic processes CSM Version 1.3

Following the treatment described in Section 2.4, two runs were performed to assess one aspect of the spatial separation of anodic and cathodic reactions, specifically the effect of anodes and cathodes of different surface area. Other consequences of the spatial separation of anodic and cathodic processes, such as localised corrosion of the surface or different rates of mass transport of sulfide to the anodes and cathodes can not be simulated using the 1-D CSM. Version 1.3 of the code was developed from the prior Version 1.2a-f, which is used here as a reference. Because H_2O is not believed to be the species undergoing cathodic reduction for the reasons stated earlier, the corresponding interfacial rate constant k_F was set to zero for the following runs.

Two simulations were performed with Version 1.3, one in which the cathodic reaction was assumed to occur on the surface of the Cu_2S film (run 1.3a) and the other in which the cathode included both the exposed surface of the film and the internal surfaces of the pores (run 1.3b). In both cases the anode was limited to the copper surface at the base of the pores in the film. Thus, for run 1.3a, the cathode:anode surface area ratio was equal to $(1-\varepsilon_{film})$: ε_{film}, equivalent to a value of 9 for the assumed film porosity of 0.1 for the period when a film was present on the surface. For run 1.3b, the cathode:anode surface area ratio increased with time as the film thickened, starting from a value of 9 and increasing (based on the results of the simulation) to a value of 3.2×10^5 after 10^6 a.

Figure 3-22 and Figure 3-23 show the predicted time dependence of the depth of corrosion and Cu_2S film thickness, respectively, for runs 1.3a and 1.3b compared with that for the reference simulation using Version 1.2a-f. Since the majority of corrosion results from the formation of Cu_2S and since the corrosion rate is transport limited, there is no effect of the cathode:anode surface area ratio on the predicted corrosion damage.

In contrast to the extent of corrosion, the distribution of the anodic and cathodic reactions does have some effect on the value of E_{CORR} during the long-term anaerobic phase (Figure 3-24). If both anodic and cathodic reactions were under complete transport control then the relative surface areas would have no effect on E_{CORR} as the rate of supply of sulfide is determined by the *geometric* surface area. The fact that E_{CORR} exhibits more-positive values with increasing cathode:anode surface area ratio suggests that the cathodic reaction is under (partial) kinetic control due to the rate of the interfacial reaction. See Section 6 for further discussion of this issue.

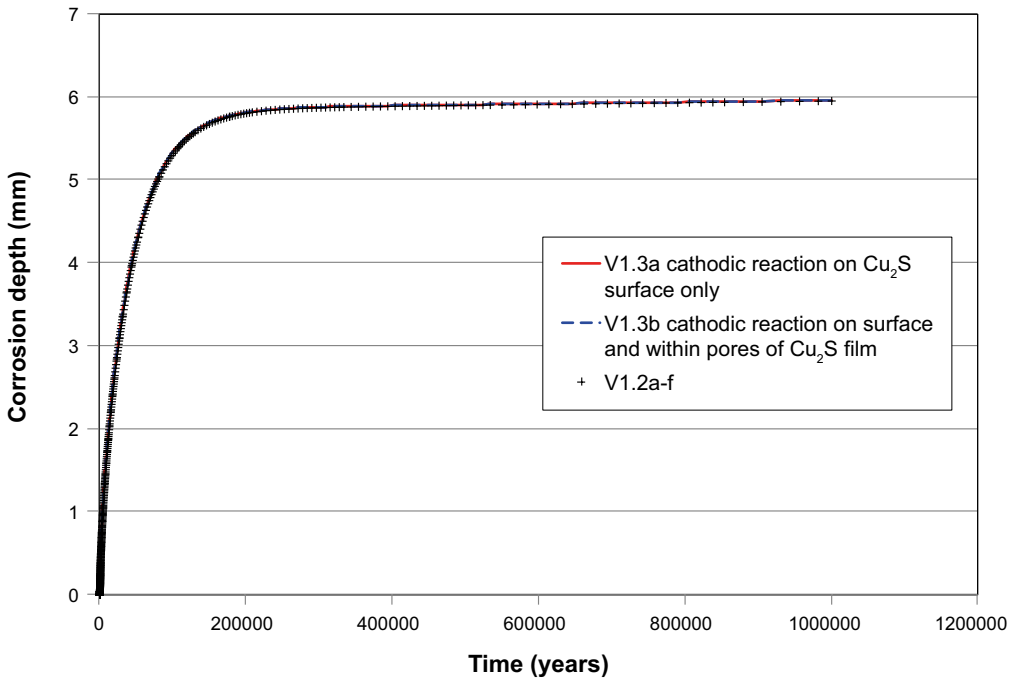

Figure 3-22. *Effect of the location of the cathode on the predicted depth of corrosion compared with co-located anodes and cathodes (V1.2a-f).*

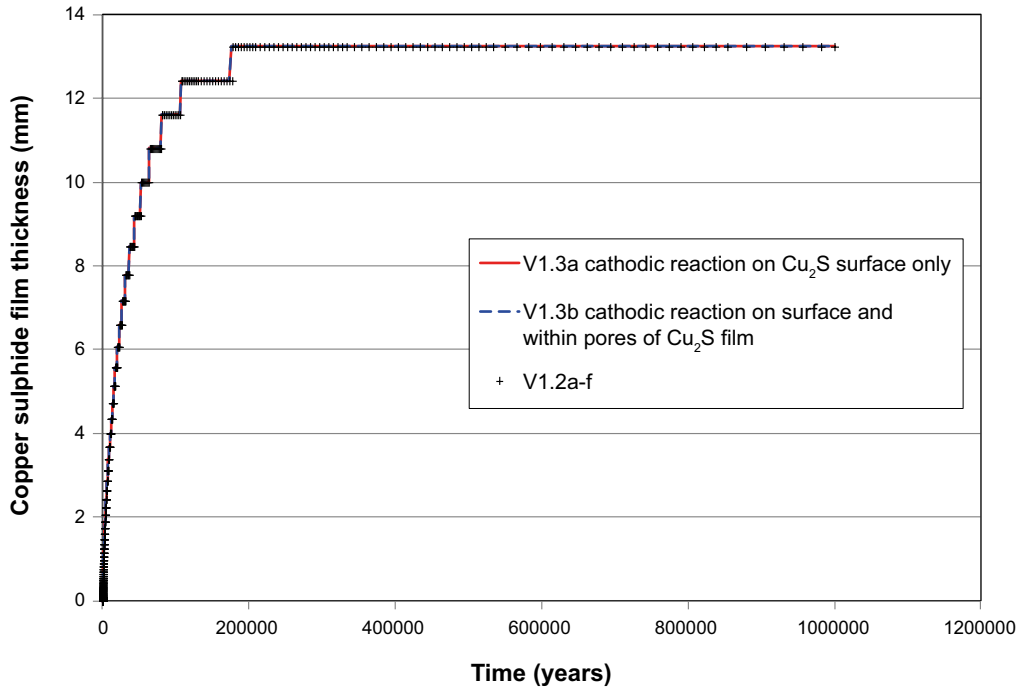

Figure 3-23. *Effect of the location of the cathode on the predicted Cu_2S film thickness compared with co-located anodes and cathodes (V1.2a-f).*

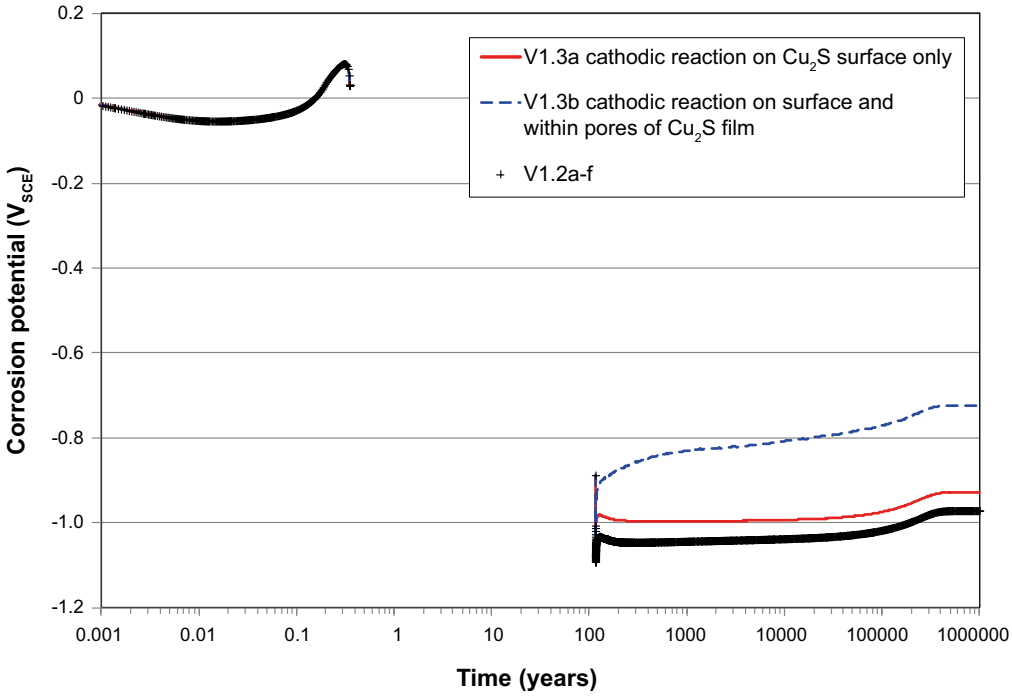

Figure 3-24. *Effect of the location of the cathode on the predicted time dependence of E_{CORR} compared with co-located anodes and cathodes (V1.2a-f).*

3.4 Alternative film formation process CSM Version 1.4

As discussed in Section 2.5, an alternative treatment of film formation involving the spatial distribution of the precipitation of Cu_2S was not implemented in the CSM. Therefore, no simulations were performed with Version 1.4.

3.5 Alternative bentonite model CSM Version 2.0

An attempt was made to implement certain aspects of the single interlayer porosity (Donnan equilibrium) bentonite model in the CSM. As described in Section 2.6, the specific feature simulated was the Donnan equilibrium between the concentrations of ions between "internal" and "external" solutions at interfaces. Two interfaces were considered, represented by the Cu_2S film/HCB and HCB/EDZ. The focus here is on the behaviour of anions, particularly Cl^- and HS^-, both of which impact the corrosion behaviour.

A six-layer version of the CSM was used in the simulations. The Donnan equilibrium was implemented in Version 1.2a-f (again, with k_F set to zero to exclude the cathodic reduction of H_2O) and was denoted Version 2.0. Since no simulations were performed with a six-layer Version 1.2a-f, a six-layer implementation of Version 1.1eq is used here as a reference.

Figure 3-25 and Figure 3-26 show the predicted time dependence of the depth of corrosion and Cu_2S film thickness, respectively, for Version 2.0. Considerably deeper corrosion and a thicker Cu_2S film were predicted for the version including the Donnan equilibrium than for the "reference" six-layer V1.1eq (see also Table 3-4). To what degree this enhanced corrosion was due to the introduction of the Donnan treatment and to what degree it was due to the other updates to the code is difficult to determine. Based on the results for the nine-layer code with and without the various updates described in Sections 2.3.1 to 2.3.6 (but without H_2O as an additional oxidant), these updates resulted in an approximately ten-fold increase in the extent of corrosion (Table 3-4). That Version 2.0 produced an approximately 50-fold increase in corrosion compared with the non-updated six-layer code perhaps indicate an additional enhancement in corrosion due to the implementation of the Donnan equilibrium.

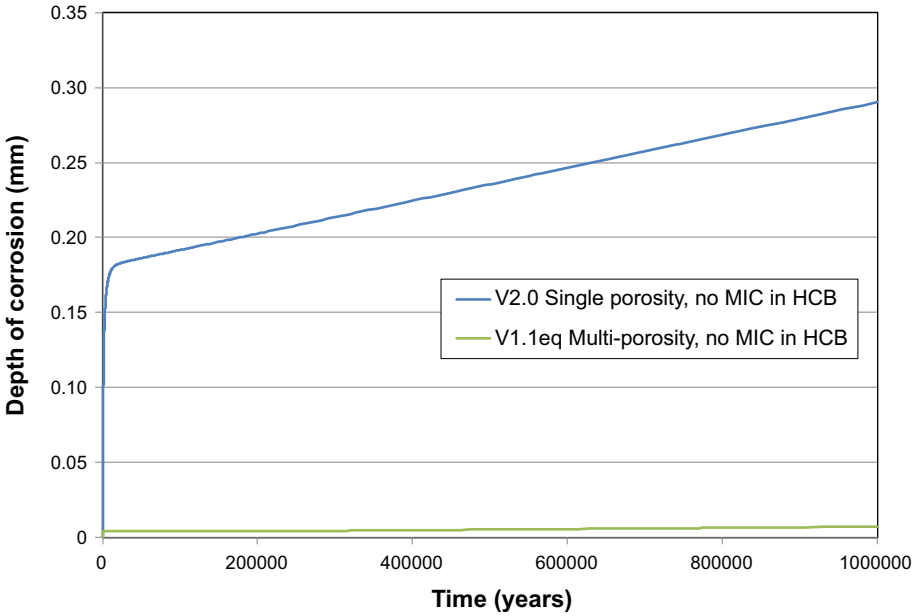

Figure 3-25. *Predicted time dependence of the depth of corrosion for the implementation of a single-layer (Donnan equilibrium) bentonite model (CSM Version 2.0).*

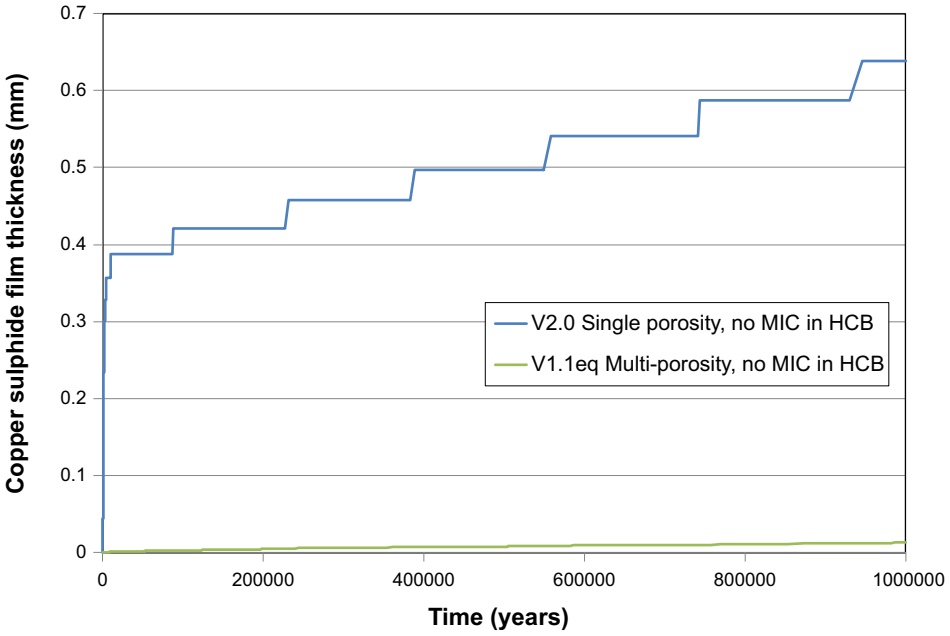

Figure 3-26. *Predicted time dependence of the Cu_2S film thickness for the implementation of a single-layer (Donnan equilibrium) bentonite model (CSM Version 2.0).*

The predicted time-dependence of the E_{CORR} for V2.0 is consistent with an enhanced effect of sulfide (Figure 3-27). The precipitous decrease in E_{CORR} occurred much earlier for V2.0 than for the "reference" case using V1.1eq.

Further development of V2.0 to better implement the single interlayer porosity model and additional simulations are necessary to better understand whether the "Donnan bentonite model" predicts more corrosion than the traditional multi-porosity approach.

Table 3-4. Comparison of predicted depth of corrosion and Cu_2S film thickness after 10^6 a for Version 2.0 and for simulations with various six-layer and nine-layer versions of the CSM code.

CSM Version	Depth of corrosion after 10^6 a (mm)	Cu_2S film thickness after 10^6 a (mm)	Comment
V2.0	0.29	0.64	Six-layer code based on V1.2a-f (k_F = 0), plus Donnan equilibrium at Cu_2S/HCB and HCB/EDZ interfaces
V1.1eq, six-layer	0.0071	0.013	Six-layer code without any of the updates described in Sections 2.31 to 2.3.6
V1.2a-f, nine-layer	5.95	13.2	Nine-layer code with updates described in Sections 2.3.1 to 2.3.6 (k_F = 0)
V1.1eq, nine-layer	0.48	1.05	Nine-layer code without updates

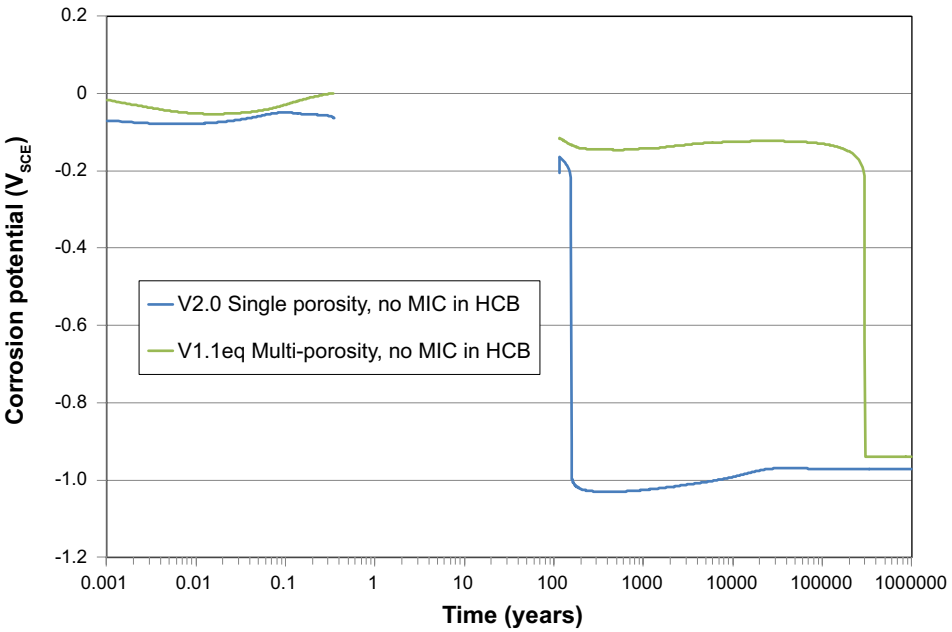

Figure 3-27. *Predicted time dependence of the corrosion potential for the implementation of a single-layer (Donnan equilibrium) bentonite model (CSM Version 2.0).*

4 Default or “best-estimate” CSM simulation and sensitivity analyses

4.1 Definition of “best-estimate” scenario

The “best-estimate” scenario represents our best current understanding of how we expect the canister corrosion behaviour and near-field environment to evolve with time. These analyses were performed using CSM Version 1.2a-g. This best estimate scenario is based on the following conditions:

- As for the reference simulation with CSM V1.1eq (Table 3-1), a 9-layer version of the CSM V1.2a-g was used with the following layers (from the canister surface outwards):
  1. Porous Cu_2S of varying thickness.
  2. Inner layer of buffer material.
  3. Middle layer of buffer material.
  4. Outer layer of buffer material.
  5. Inner layer of backfill material.
  6. Outer layer of backfill material.
  7. Excavation damaged zone (EDZ) (the layer of damaged rock closest to the surface of the opening).
  8. Excavation disturbed zone (EdZ) (a layer of disturbed rock beyond the EDZ).
  9. Intact host rock.
- Microbial activity (both sulfate reduction and aerobic respiration) are permitted subject to a threshold degree of saturation corresponding to a water activity (a_w) of 0.96. This condition is not met in the buffer or Cu_2S film at any time.
- A fractional death rate is applied to the microbial population due to the requirements for cell maintenance, with a fraction of the dead cell material being recycled as dissolved organic material.
- SRB are initially present in all layers with the numbers equally divided between organotrophs and chemotrophs.
- Gypsum is assumed to be present in the buffer and backfill materials, but not in the rock layers.
- Solid organic matter is present initially in the buffer and backfill materials, but not in the rock layers. There is no dissolved organic matter present initially.
- Iron carbonate is present in the buffer and backfill, but not in the rock layers.
- Biotite, another potential source of Fe(II), is present in the backfill and rock layers, but not in the buffer.
- The system is initially aerobic and becomes anaerobic as a consequence of corrosion of the canister and other redox processes.
- The temperature within the repository is spatially and temporally dependent as a result of heat output from the canister. The temperature profiles are calculated within the code by solving a heat-conduction equation subject to time-dependent temperatures at the canister surface and the edge of the rock layer representing the right-hand boundary of the model, along with saturation-dependent thermal properties of the different layers.
- The degree of saturation of the different layers in the model is temporally dependent as a result of moisture first being driven away from the canister during the early part of the thermal transient, followed by re-wetting as the ground water saturates the rock and buffer and backfill. The degree of saturation is not calculated within the code but is inputted as a time series for each of the nine layers. The degree of saturation is assumed to be spatially uniform within each layer.

The corresponding reaction scheme for CSM V1.2a-g is illustrated in Figure 2-5. The layer-dependent input parameters used for the best-estimate simulations are listed in Table 4-1, with any exceptions for particular simulations specifically noted in the text. Table 4-2 summarises the assumed time-dependent degree of saturation of the different layers and Table 4-3 lists the saturation-dependent thermal conductivity for the four materials considered in the model. The time-dependent temperatures at the canister surface and at the far-field boundary of the model are listed in Table 4-4, along with the initial spatial temperature distribution. The non-layer-dependent input data are summarised in Appendix C, again except where specifically noted in the text.

A number of sensitivity analyses were performed to determine the impact of:

- Permitting microbial activity in the buffer material.
- Assuming no microbial death due to cell maintenance requirements.
- The time to saturate the buffer and backfill materials.
- A transport path vertically through the deposition hole and tunnel backfill versus an horizontal transport path only through the buffer in the deposition hole.

Table 4-1a. Input data for the layer-specific parameters for the best-estimate CSM Version 1.2a-g simulations. Layers 1–3.

Parameter	Layer 1	Layer 2	Layer 3
Layer name	Cu_2S film	HCB inner	HCB middle
Length (dm)	Variable	2	2
Effective porosity for mass transport ε_e	0.1	0.05	0.05
Storage porosity ε_s	0	0.05	0.05
Non-accessible porosity ε_{na}	0	0.3	0.3
Tortuosity factor τ_f	0.1	0.1	0.1
Threshold saturation for microbial activity S_{MIC}	1	1	1
Maximum Cu^{2+} adsorption capacity c_5^{max} (mol/kg)	0	0.09375	0.09375
Specific surface area of pyrite A_P (dm^{-1})	0	0.139	0.139
Specific surface area of biotite A_F (dm^{-1})	n.d.*	0	0
Initial concentration of dissolved O_2 $(c_0)_{init}$ (mol/dm^3)	n.d.	0.000361	0.000256
Initial concentration of Cl^- ions $(c_6)_{init}$ (mol/dm^3)	n.d.	0.096	0.096
Initial concentration of dissolved Fe(II) $(c_7)_{init}$ (mol/dm^3)	n.d.	0	0
Initial concentration of sulfide ions $(c_9)_{init}$ (mol/dm^3)	n.d.	0	0
Initial concentration of pyrite $(c_{10})_{init}$ (mol/dm^3)	n.d.	0.00963	0.00963
Initial concentration of SO_4^{2-} ions $(c_{11})_{init}$ (mol/dm^3)	n.d.	0.01546	0.01497
Initial concentration of dissolved H_2 $(c_{12})_{init}$ (mol/dm^3)	n.d.	0	0
Initial concentration of gypsum $(c_{15})_{init}$ (mol/dm^3)	n.d.	0.0365	0.0365
Initial concentration of dissolved organic matter (DOM) $(c_{16})_{init}$ (mol/dm^3)	n.d.	0	0
Initial concentration of solid organic matter (SOM) $(c_{17})_{init}$ (mol/dm^3)	n.d.	0.0105	0.0105
Initial concentration of biotite $(c_{18})_{init}$ (mol/dm^3)	n.d.	0	0
Initial concentration of siderite $(c_{19})_{init}$ (mol/dm^3)	n.d.	0.0678	0.0678
Initial population of organotrophic SRB (g_{cells}/dm^3)	n.d.	9×10^{-8}	9×10^{-8}
Initial population of chemotrophic SRB (g_{cells}/dm^3)	n.d.	9×10^{-8}	9×10^{-8}
Time-dependent saturation S(t)	External input	External input	External input
Particle density ρ (kg/dm^3)	5.6	2.7	2.7
Saturation-dependent thermal conductivity K(S) ($W \cdot dm^{-1} \cdot K^{-1}$)	External input	External input	External input
Heat capacity C ($J \cdot kg^{-1} \cdot K^{-1}$)	845	845	845

* n.d. not defined.

Table 4-1b. Layers 4–6.

Parameter	Layer 4	Layer 5	Layer 6
Layer name	HCB outer	Backfill inner	Backfill outer
Length (dm)	2.93	40	47
Effective porosity for mass transport ε_e	0.05	0.22	0.22
Storage porosity ε_s	0.05	0	0

Table 4-1b. Continued.

Parameter	Layer 4	Layer 5	Layer 6
Non-accessible porosity ε_{na}	0.3	0	0
Tortuosity factor τ_f	0.1	0.1	0.1
Threshold saturation for microbial activity S_{MIC}	1	0.75	0.75
Maximum Cu^{2+} adsorption capacity c_5^{max} (mol/kg)	0.09375	0.113	0.113
Specific surface area of pyrite A_p (dm^{-1})	0.139	0.382	0.382
Specific surface area of biotite A_F (dm^{-1})	0	7.89	7.89
Initial concentration of dissolved O_2 $(c_0)_{init}$ (mol/dm^3)	0.000223	0.000213	0.000205
Initial concentration of Cl^- ions $(c_6)_{init}$ (mol/dm^3)	0.096	0.036	0.036
Initial concentration of dissolved Fe(II) $(c_7)_{init}$ (mol/dm^3)	0	0	0
Initial concentration of sulfide ions $(c_9)_{init}$ (mol/dm^3)	0	0	0
Initial concentration of pyrite $(c_{10})_{init}$ (mol/dm^3)	0.00963	0.0265	0.0265
Initial concentration of SO_4^{2-} ions $(c_{11})_{init}$ (mol/dm^3)	0.01461	0.0142	0.0142
Initial concentration of dissolved H_2 $(c_{12})_{init}$ (mol/dm^3)	0	0	0
Initial concentration of gypsum $(c_{15})_{init}$ (mol/dm^3)	0.0365	0.19	0.19
Initial concentration of dissolved organic matter (DOM) $(c_{16})_{init}$ (mol/dm^3)	0	0	0
Initial concentration of solid organic matter (SOM) $(c_{17})_{init}$ (mol/dm^3)	0.0105	0.00573	0.00573
Initial concentration of biotite $(c_{18})_{init}$ (mol/dm^3)	0	0.3	0.3
Initial concentration of siderite $(c_{19})_{init}$ (mol/dm^3)	0.0678	0.163	0.163
Initial population of organotrophic SRB (g_{cells}/dm^3)	9×10^{-8}	1×10^{-6}	1×10^{-6}
Initial population of chemotrophic SRB (g_{cells}/dm^3)	9×10^{-8}	1×10^{-6}	1×10^{-6}
Time-dependent saturation S(t)	External input	External input	External input
Particle density ρ (kg/dm^3)	2.7	2.7	2.7
Saturation-dependent thermal conductivity K(S) ($W\cdot dm^{-1}\cdot K^{-1}$)	External input	External input	External input
Heat capacity C ($J\cdot kg^{-1}\cdot K^{-1}$)	845	845	845

Table 4-1c. Layers 7–9.

Parameter	Layer 7	Layer 8	Layer 9
Layer name	EDZ	EdZ	Host rock
Length (dm)	5	20	20
Effective porosity for mass transport ε_e	0.006	0.003	0.003
Storage porosity ε_s	0	0	0
Non-accessible porosity ε_{na}	0	0	0
Tortuosity factor τ_f	0.1	0.1	0.1
Threshold saturation for microbial activity S_{MIC}	0	0	0
Maximum Cu^{2+} adsorption capacity c_5^{max} (mol/kg)	0	0	0
Specific surface area of pyrite A_p (dm^{-1})	0	50	5
Specific surface area of biotite A_F (dm^{-1})	50	50	0.5
Initial concentration of dissolved O_2 $(c_0)_{init}$ (mol/dm^3)	0.000204	0.000204	0
Initial concentration of Cl^- ions $(c_6)_{init}$ (mol/dm^3)	0.1	0.1	0.1
Initial concentration of dissolved Fe(II) $(c_7)_{init}$ (mol/dm^3)	0	0	1×10^{-5}
Initial concentration of sulfide ions $(c_9)_{init}$ (mol/dm^3)	1×10^{-5}	1×10^{-5}	1×10^{-5}
Initial concentration of pyrite $(c_{10})_{init}$ (mol/dm^3)	0	21	2.1
Initial concentration of SO_4^{2-} ions $(c_{11})_{init}$ (mol/dm^3)	0.0094	0.0094	0.0094
Initial concentration of dissolved H_2 $(c_{12})_{init}$ (mol/dm^3)	0	0	0
Initial concentration of gypsum $(c_{15})_{init}$ (mol/dm^3)	0	0	0
Initial concentration of dissolved organic matter (DOM) $(c_{16})_{init}$ (mol/dm^3)	0	0	0
Initial concentration of solid organic matter (SOM) $(c_{17})_{init}$ (mol/dm^3)	0	0	0
Initial concentration of biotite $(c_{18})_{init}$ (mol/dm^3)	0.4	0.4	0.4
Initial concentration of siderite $(c_{19})_{init}$ (mol/dm^3)	0	0	0
Initial population of organotrophic SRB (g_{cells}/dm^3)	0.5	0.5	3×10^{-8}
Initial population of chemotrophic SRB (g_{cells}/dm^3)	0.5	0.5	3×10^{-8}
Time-dependent saturation S(t)	External input	External input	External input
Particle density ρ (kg/dm^3)	2.7	2.7	2.7
Saturation-dependent thermal conductivity K(S) ($W\cdot dm^{-1}\cdot K^{-1}$)	External input	External input	External input
Heat capacity C ($J\cdot kg^{-1}\cdot K^{-1}$)	845	845	845

Table 4-2a. Time-dependent degree of saturation for the various layers used for the best-estimate simulations. Layers 1–5.

Layers 1 and 2		Layer 3		Layer 4		Layer 5	
Time (a)	Saturation	Time (a)	Saturation	Time (a)	Saturation	Time (a)	Saturation
0	0.78	0	0.78	0	0.78	0	0.8
0.01	0.77	0.01	0.77	0.01	0.77	0.9	0.8
0.2	0.5	0.2	0.52	0.2	0.54	1.25	0.799
0.4	0.4	0.4	0.44	0.4	0.48	1.6	0.795
0.6	0.3	0.6	0.36	0.6	0.42	3	0.77
0.8	0.2	0.8	0.28	0.8	0.36	5	0.74
0.9	0.15	0.93	0.235	0.93	0.335	8	0.709
1	0.12	1.05	0.208	1.05	0.308	9	0.702
1.122	0.107	1.2	0.2	1.2	0.3	10	0.7
1.5	0.1	2	0.192	2	0.292	11.5	0.701
2	0.098	4	0.19	4	0.29	13	0.706
4	0.095	7	0.192	7	0.292	20	0.74
7	0.098	10	0.2	10	0.3	30	0.8
10	0.1	15	0.222	15	0.322	45	0.8805
25	0.118	25	0.27	28	0.39	51	0.902
50	0.166	50	0.4	50	0.5	60	0.913
73	0.225	77	0.56	77	0.66	100	0.95
95	0.29	100	0.7	100	0.8	110	0.96
105	0.335	110	0.76	110	0.84	120	0.97
110	0.38	120	0.82	120	0.88	130	0.98
120	0.46	130	0.88	130	0.92	140	0.99
130	0.54	140	0.94	140	0.96	150	1
140	0.62	148	0.99	148	0.992	1 000 000	1
150	0.7	150	0.996	150	0.997		
190	0.95	155	0.998	155	0.999		
198	0.99	160	1	160	1		
200.5	0.997	1 000 000	1	1 000 000	1		
205	0.999						
210	1						
1 000 000	1						

Table 4-2b. Layers 6–9.

Layer 6		Layer 7		Layer 8		Layer 9	
Time (a)	Saturation	Time (a)	Saturation	Time (a)	Saturation	Time (a)	Saturation
0	0.8	0	0.197	0	0.5	0	1
0.009	0.8	0.01	0.2	0.9	0.5	1 000 000	1
0.0125	0.79995	0.2	0.26	1	0.501		
0.019	0.79945	0.4	0.32	1.2	0.503		
0.03	0.7983	0.6	0.38	2	0.518		
0.05	0.796	0.8	0.44	3	0.54		
0.2	0.78	0.9	0.475	6	0.625		
0.4	0.76	0.98	0.495	8	0.675		
0.6	0.74	1.1	0.499	10	0.7		
0.8	0.72	1.4	0.5	15	0.72		
1	0.7	50	0.5	40	0.773		
1.4	0.689	64	0.515	50	0.8		
2	0.677	75	0.535	92	0.97		
5	0.637	89	0.568	99	0.995		
8	0.609	100	0.6	110	1		
9	0.602	105	0.628	1 000 000	1		

Table 4-2b. Continued.

Layer 6		Layer 7		Layer 8		Layer 9	
Time (a)	**Saturation**	**Time (a)**	**Saturation**	**Time (a)**	**Saturation**	**Time (a)**	**Saturation**
10	0.6	110	0.668				
11.5	0.601	120	0.76				
13	0.606	130	0.84				
20	0.646	140	0.92				
30	0.725	147	0.979				
45	0.8705	150	0.998				
47.6	0.889	154	1				
51	0.902	1 000 000	1				
60	0.913						
100	0.95						
110	0.96						
120	0.97						
130	0.98						
140	0.99						
147	0.9976						
150	0.9994						
154	1						
1 000 000	1						

Table 4-3. Saturation dependence of the thermal conductivity K for the Cu_2S, bentonite, backfill, and rock layers used for the best-estimate simulations using CSM V1.2a-g.

Cu_2S		Bentonite		Backfill		Rock	
Saturation	**K***	**Saturation**	**K**	**Saturation**	**K**	**Saturation**	**K**
0	0.1	0	0.03	0	0.1	0	0.3
0.2	0.1	0.2	0.03	0.2	0.1	0.2	0.3
0.8	0.2	0.8	0.12	0.8	0.2	0.8	0.3
1	0.2	1	0.13	1	0.2	1	0.3

* K in units of $W \cdot dm^{-1} \cdot K^{-1}$.

Table 4-4. Time dependence of the canister surface and far-field rock temperatures and the initial spatial temperature distribution used for the best-estimate simulations using CSM V1.2a-g.

Time-dependent temperatures at canister surface and at right-hand far-field rock boundary			Initial temperature distribution	
Time (a)	**Far-field rock temperature (°C)**	**Canister surface temperature (°C)**	**Distance from canister surface (dm)**	**T (°C)**
0	10.5	45	0	45
20	40.5	75.5	1	45
30	39	74.5	1.5	44
40	38	72.5	2	40
50	36.5	71	2.5	30
60	35	69	3	20
70	34	67.5	3.5	16
80	33	66.5	4	15
90	32.5	65	20	15
100	32	64	30	10.5
200	28.5	59	10 000	10.5
300	26.5	56.4		
400	26	54		
500	25	52		
600	24.5	50		

Table 4-4. Continued.

Time-dependent temperatures at canister surface and at right-hand far-field rock boundary			Initial temperature distribution	
Time (a)	**Far-field rock temperature (°C)**	**Canister surface temperature (°C)**	**Distance from canister surface (dm)**	**T (°C)**
700	24	47.5		
800	23.5	46		
900	23	43.5		
1 000	22.5	42.5		
2 000	19.5	31		
3 000	17	26.5		
4 000	16.5	23		
5 000	16	21.5		
6 000	15	20.5		
7 000	14.5	20		
8 000	14.5	19		
9 000	14	18.5		
10 000	14	18		
20 000	12.5	14.5		
30 000	12	13.5		
40 000	11.5	13		
50 000	11	12.5		
60 000	11	12		
70 000	11	11.5		
80 000	10.5	11		
90 000	10.5	11		
100 000	10.5	10.5		
1 000 000	10.5	10.5		

4.2 Results of “best-estimate” simulation

The CSM predicts a wide range of behaviours apart from the evolution of the corrosion performance over time. Analysis of the fate of the initially trapped O_2, of the generation and consumption of sulfide, and of the fate of the Fe(II) in the system provides insight into how the repository environment evolves with time as well as providing a useful quality check on the computations. In addition, various aspects of the treatment of microbial sulfate reduction can be used to determine the nature of the limiting process(es).

4.2.1 Corrosion

The evolution of the corrosion behaviour of the canister is characterised by the time-dependence of the corrosion potential, corrosion rate, depth of corrosion, and of the individual anodic and cathodic current densities.

Figure 4-1 shows the predicted time dependence of the corrosion potential (E_{CORR}) for the best-estimate simulation. In general, E_{CORR} shifts from relatively positive potentials during the early aerobic phase to more-negative values as the repository environment becomes anaerobic and dominated by the presence of sulfide. The time dependence of the corrosion rate and of the depth of corrosion are shown in Figure 4-2, along with the predicted thickness of the interfacial Cu_2S film. The total depth of corrosion after 10^6 a of approximately 9.3 µm is further sub-divided in the figure into contributions from aerobic and anaerobic corrosion. Of the total corrosion, 6.4 µm (or approximately 70 %) results from aerobic corrosion processes supported by the cathodic reduction of O_2 and Cu(II) and

only 2.9 µm from corrosion in the presence of sulfide. Thus, after 10^6 a, the Cu_2S film thickness is predicted to be only 20.9 µm, the majority due to the chemical conversion of Cu_2O to Cu_2S. As will be discussed in more detail below, the extent of "anaerobic corrosion" is minimal because much of the sulfide is precipitated as mackinawite before reaching the canister surface.

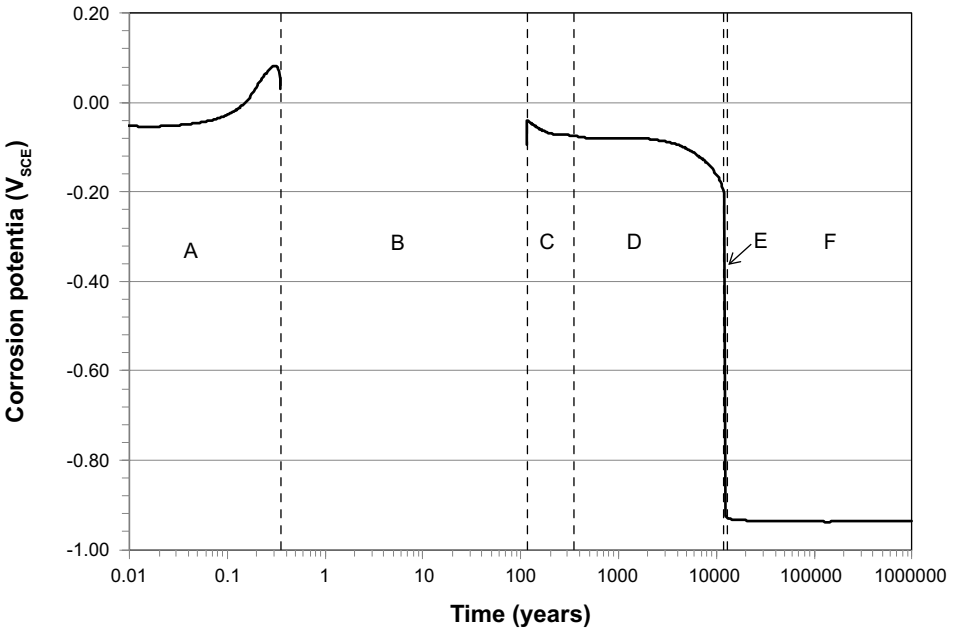

Figure 4-1. *Predicted time-dependence of the corrosion potential for the best-estimate scenario.*

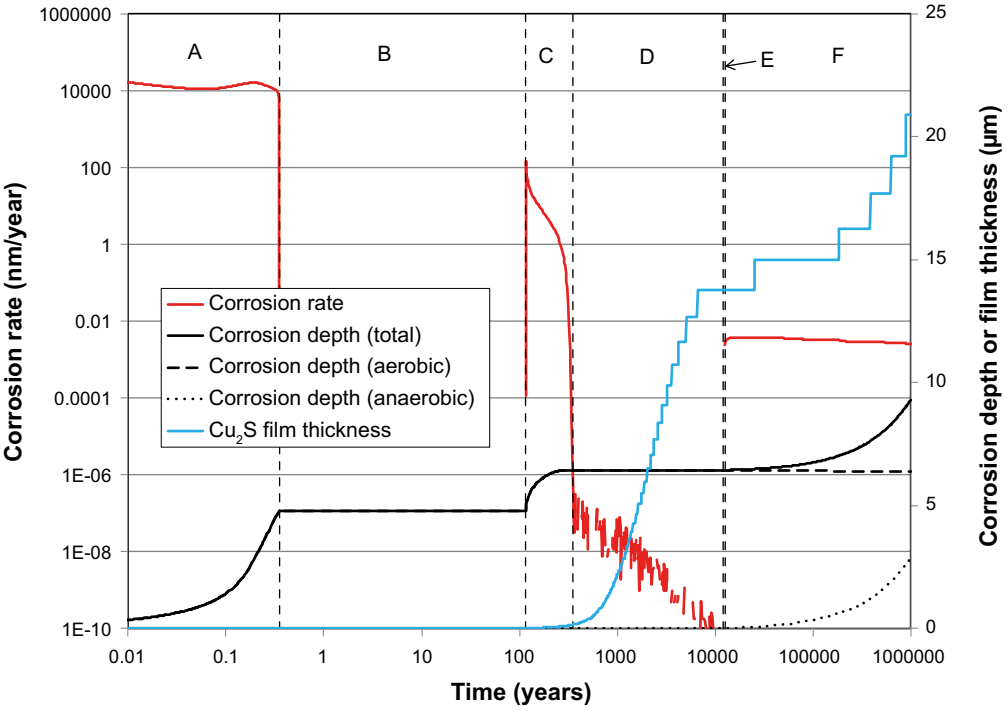

Figure 4-2. *Time dependence of the corrosion rate, the copper sulfide film thickness, and the depth of corrosion for the best-estimate scenario. The aerobic and anaerobic contributions to the total depth of corrosion are also shown. The computational noise in the corrosion rate in period D is due to the extremely low rates.*

The evolution of the corrosion behaviour in Figure 4-1 and Figure 4-2 is divided into different time periods based on the corresponding predominant processes. Figure 4-3 shows the individual anodic and cathodic processes for each of the six phases, which can be characterised as follows:

- Phase A – during the early part of the aerobic period, the anodic dissolution of copper as $CuCl_2^-$ is supported by the cathodic reduction of Cu^{2+}, with the interfacial reduction of O_2 being a minor contributor to the overall cathodic current.
- Phase B – during this period, the canister surface is presumed to be too dry to support interfacial electrochemical reactions and corrosion ceases. The timing and duration of this period depends on the assumed time-dependent saturation of the buffer closest to the canister (Table 4-2). Although no corrosion occurs during this period, species continue to diffuse and react in other regions of the repository away from the canister surface.
- Phase C – once the canister surface re-wets, aerobic corrosion continues with Cu dissolution supported by the reduction of Cu^{2+} (formed by reaction between $CuCl_2^-$ by O_2). By this time, all of the initially trapped O_2 has been consumed (see below) so that the cathodic reduction of oxygen no longer occurs. Phase C continues until such time that all of the Cu(II) in the system has been consumed by electrochemical reduction on the canister surface. For the best-estimate simulation, this period lasts until approximately 350 a, at which point all dissolved Cu^{2+}, adsorbed Cu(II), and precipitated $CuCl_2 \cdot 3Cu(OH)_2$ is predicted to have been consumed.
- Phase D – following the consumption of all of the O_2 and Cu(II) in the system and prior to the arrival of HS^- at the canister surface, there is an extended period of time during which essentially no corrosion occurs, despite the fact that the surface is wet and could sustain electrochemical processes. The duration of this period depends on the sources of sulfide and their location and of the availability of sinks for HS^- in the system. For the best-estimate scenario, this phase spans the period from approximately 350 a to 12 000 a post-closure.
- Phase E – starting at approximately 12 000 a post-closure, HS^- reaches the canister surface and supports corrosion to produce Cu_2S supported by the cathodic reduction of Cu(I). Thus, the previously corroded copper from the aerobic phase now becomes an oxidant in the presence of sulfide. The previously precipitated Cu_2O is converted to Cu_2S via a chemical process, but the dissolved $CuCl_2^-$ species are cathodically reduced (to Cu metal) in support of copper sulfidation, although the extent of this coupling would be decreased by the homogeneous reaction between $CuCl_2^-$ and HS^- (not currently included in the CSM reaction scheme). Corrosion is also supported by the evolution of H_2 from the interfacial reduction of the proton in the HS^- ion, which becomes the predominant cathodic process.
- Phase F – finally, for periods beyond 12 800 a, the sulfidation of Cu is supported by the cathodic reduction of HS^-.

It has been shown that the rate of corrosion of copper canisters under anaerobic conditions is controlled by the rate of supply of HS^- to the surface (King et al. 2017b). Figure 4-4 shows the predicted HS^- concentration profiles through the buffer material as sulfide diffuses to the canister from the backfill material in which it is produced by the microbial reduction of SO_4^{2-}. Consistent with the presumption of transport control, the interfacial $[HS^-]$ is close to zero, although the CSM predicts a small but finite concentration (of the order of 10^{-6} mol·dm^{-3}) at the canister surface. The non-zero interfacial sulfide concentration suggests a certain degree of joint kinetic-transport control, possibly because the anodic and cathodic reactions are assumed to only occur on a fraction of the entire surface area equal to the interfacial porosity of the Cu_2S film. The sensitivity of the predicted interfacial sulfide concentration to this assumption should be investigated.

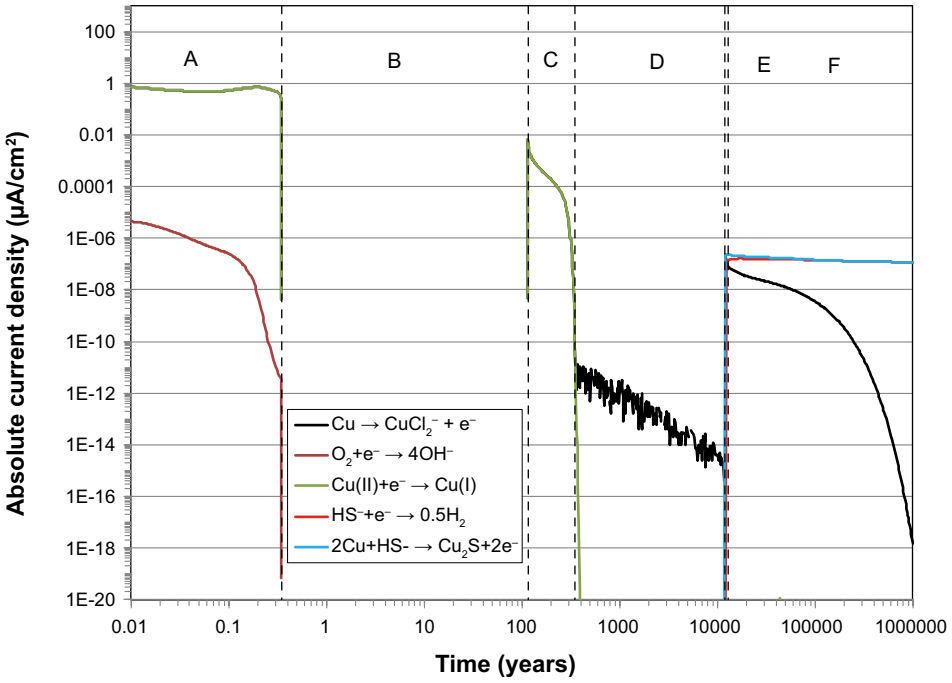

Figure 4-3. *The evolution of the dominant anodic and cathodic processes for the best-estimate scenario. The computational noise in the anodic current density in period D is due to the extremely low values.*

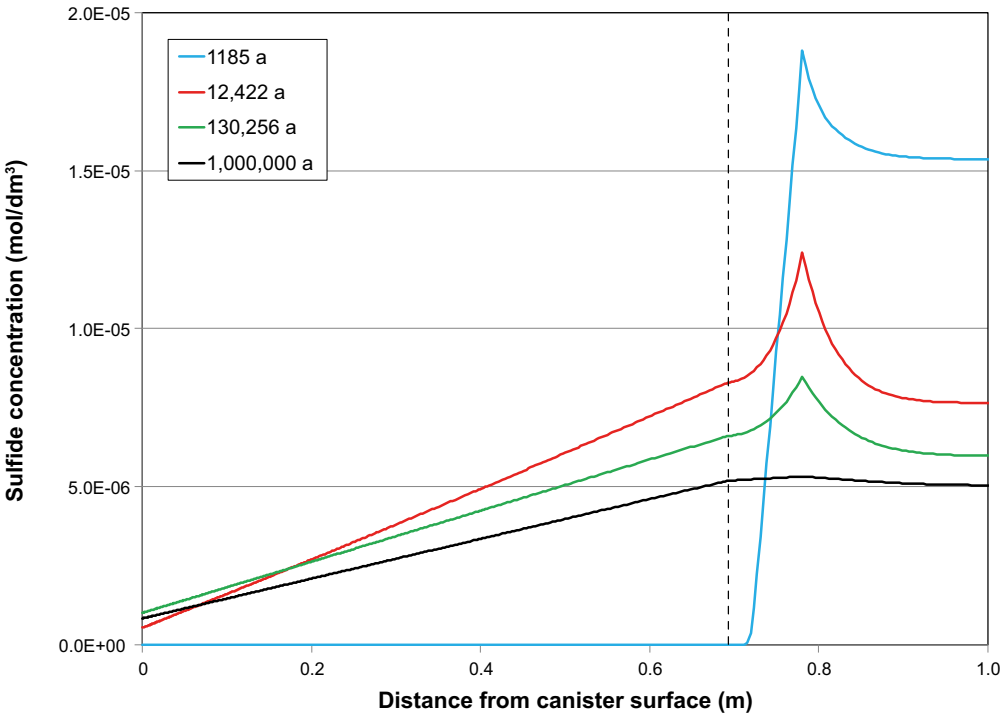

Figure 4-4. *Sulfide concentration profiles within the buffer material as a result of microbial sulfate reduction in the backfill. The interface between the buffer and backfill is at a distance of 0.693 m from the canister surface. The peak in the sulfide concentration in the backfill corresponds to the location of maximum microbial activity.*

4.2.2 Oxygen balance

The duration of the aerobic phase and the fate of the initially trapped O_2 is of interest because this period represents the time at which rapid localised corrosion and SCC processes are most likely to occur. Figure 4-5 shows the predicted inventories (i.e., the sum in all of the buffer, backfill, and rock layers represented in the model) of dissolved and gaseous O_2 as a function of time. Under unsaturated conditions, the gas phase represents a greater source of O_2 than the saturated pore space, but as dissolved O_2 reacts gaseous oxygen dissolves to maintain the equilibrium between the two species. For the best-estimate simulation, all of the initial O_2 is consumed within 26 a of the closure of the repository. This time does not represent the end of the aerobic phase as Cu(II) persists up to approximately 350 a post-closure.

Four O_2 consumption processes are included in the CSM V1.2a-g (Figure 2-5), with the corresponding fractions of the initial oxygen consumed by each as follows:

- Interfacial cathodic reduction; ~10^{-5} %.
- Homogeneous oxidation of Cu(I) to Cu(II); 9.0 %.
- Oxidation of pyrite; 90.8 %.
- Aerobic microbial respiration; 0.2 %.

Therefore, of these various O_2-consumption processes, the oxidation of pyrite and, to a lesser extent, the oxidation of Cu(I), account for virtually all of the initially trapped oxygen.

It should be noted, however, that the consumption of O_2 has been observed to occur much more rapidly (within a period of days to weeks) in the FE-G experiment currently in progress at the Mont Terri URL (Giroud et al. 2018, Müller et al. 2017). Although all of the processes responsible for O_2 consumption in this full-scale test are not currently understood, it is apparent that oxygen is lost from the system at a time at which the buffer material is too dry to support conventional aqueous-based processes. It is believed that O_2 may be adsorbed by the bentonite, although the reversibility of this process is currently unclear. Whatever the process responsible for the rapid decrease in O_2 concentration in the FE-G experiment, it may be necessary to add another O_2 consumption process in a future development of the CSM.

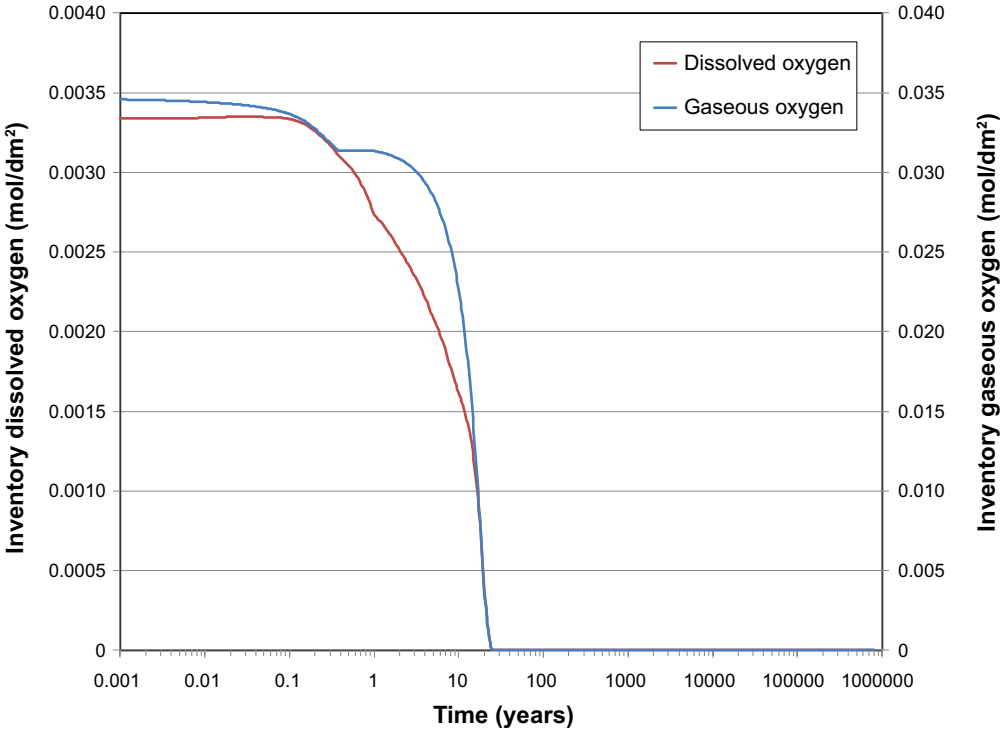

Figure 4-5. *Predicted time dependence of the consumption of oxygen for the best-estimate scenario.*

4.2.3 Sulfide balance

There are two sources and three sinks for sulfide in the reaction scheme for the CSM V1.2a-g (Figure 2-5). Sulfide is produced by either organotrophic or chemotrophic reduction of sulfate and is present initially in the excavation-damaged and -disturbed zones (EDZ and EdZ, respectively), and rock layers and at all times in the ground water (representing the right-hand boundary of the model). The three sinks for sulfide are dissolved HS^- in the pore water of the different layers or as precipitated mackinawite FeS or Cu_2S.

The relative importance of the various sinks varies as the repository environment evolves (Figure 4-6). Initially, the sulfide is present primarily in dissolved form but as Fe(II) accumulates within the system (driven by the temperature-dependent dissolution of $FeCO_3$ and biotite), the precipitation of mackinawite becomes the major sink for sulfide. Between approximately 200 a and 12 000 a, Cu_2S accumulates due to the chemical conversion of Cu_2O to Cu_2S. Beyond that time, Cu_2S film growth is the result of interfacial electrochemical reactions. By the end of the 10^6-a simulation period, the vast majority (98.5 %) of the sulfide in the system is present as FeS.

The time dependence of the ratio of the sulfide sinks to sulfide sources is shown in Figure 4-7. This ratio also takes into account the HS^- crossing the right-hand boundary of the model, either entering from the ground water or diffusing in the opposite direction out of the rock layer if the concentration of microbially produced HS^- exceeds that assumed to be present in the ground water. This figure serves as a quality check on the code output, with the ratio very close to one indicating accurate accounting for all of the sulfide produced and consumed during the simulation. (The ratio exceeding one at short times may result from an integration error as the total amount of sulfide in the system initially is very small).

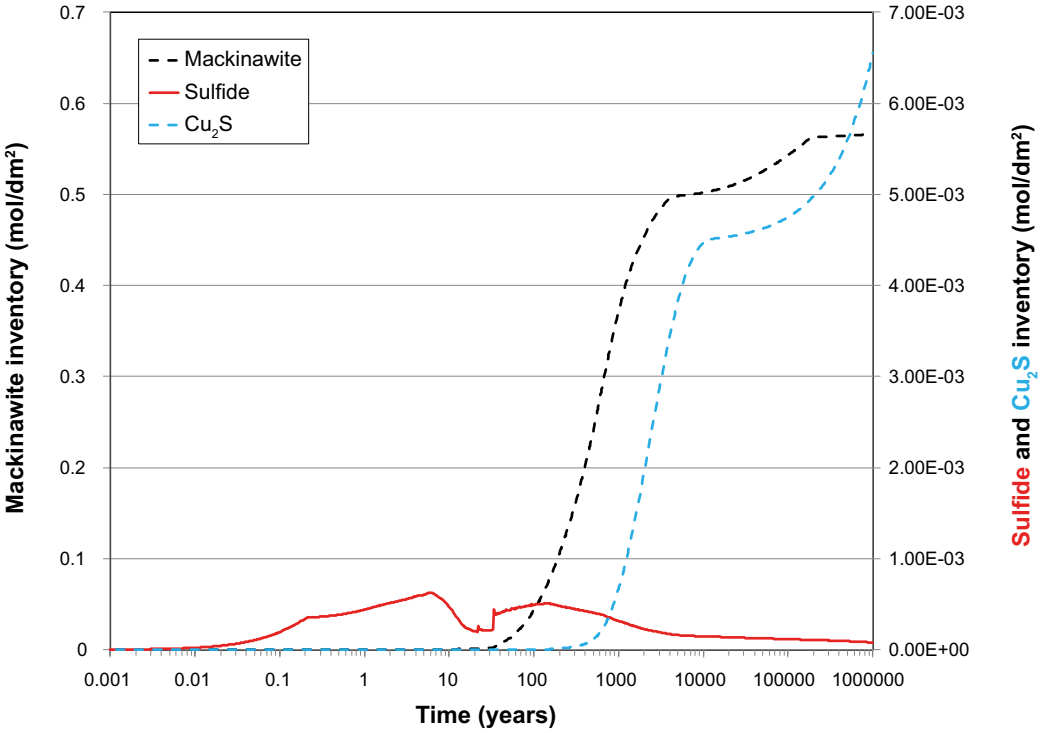

Figure 4-6. *The total amounts of different forms of sulfide as a function of time.*

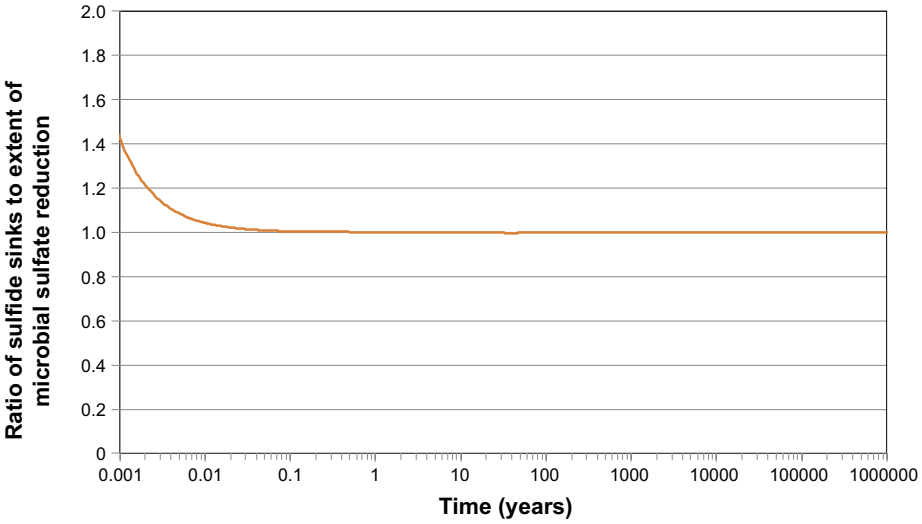

Figure 4-7. *The ratio of the inventories of sulfide species from Figure 4-6 to the total extent of microbial sulfate reduction as a function of time. This ratio also takes into account the sulfide from the groundwater, assumed to be present at a constant concentration of 10^{-5} mol·dm^{-3} for the best-estimate simulation.*

4.2.4 Fe(II) balance

It is apparent from Figure 4-6 that the precipitation of FeS is a significant sink for sulfide. There are four Fe(II) solid phases included in the reaction scheme for CSM V1.2a-g, namely:

- Biotite, assumed to be present initially in the backfill and rock layers, and which undergoes temperature-dependent dissolution releasing Fe(II).
- Pyrite (FeS_2), present initially in all buffer, backfill, and rock layers (except for the EDZ, for which it is assumed that prolonged exposure to aerobic conditions during the operational phase results in the oxidation of all pyrite present as fracture-filling minerals). Pyrite oxidatively dissolves, releasing Fe(II), but does not dissolve under anaerobic conditions (and, therefore, is a source of neither Fe(II) nor HS^-).
- Iron carbonate ($FeCO_3$), assumed to be present initially in both the buffer and backfill materials, precipitates reversibly in the presence of excess Fe(II) (as produced, for example, by the irreversible dissolution of biotite).
- Mackinawite (FeS) is not present initially in the system but irreversibly precipitates if the dissolved Fe(II) and HS^- concentrations exceed the value of the solubility product.

Figure 4-8 shows the time-dependent inventories of each of these four solid phases. Initially, there is a large inventory of ferrous minerals in the form of pyrite, biotite, and iron carbonate, amounting to a total of approximately 520 mol/dm^2 Fe(II). These ferrous-containing minerals represent not only a potentially large redox buffer, but also a large source of Fe(II) for the precipitation of sulfide in the system. Thus, the inventory of mackinawite increases significantly during the evolution of the repository environment but, even after 10^6 a, represents just a small fraction of the total amount of Fe(II) in the system.

Figure 4-9 shows the distribution of mackinawite in the system at four different times over the course of the 10^6-a simulation. Because there is a large excess of Fe(II) present, the FeS accumulates at the locations where sulfide is produced by microbial activity. (Although FeS is also produced in the rock layers due to incoming HS^- from the ground water, the "concentration" of FeS expressed per unit volume of the system is low as the porosity of the rock layers is small). Mackinawite tends to precipitate in the backfill closer to the buffer material as this is where the rate of microbial sulfate reduction is highest. The rate of microbial activity increases with temperature up to the optimum temperature of 39 °C. Thus, for much of the simulation period, the rate of sulfate reduction tends to increase the closer the distance to the canister. However, microbial activity is suppressed in the buffer due to the low water activity, even though the buffer is a source of both organic carbon and sulfate. The consequence is that the rate of microbial sulfate reduction is highest just inside the backfill (in which microbial activity is possible subject to a threshold degree of saturation) and close to the source of nutrients and electron acceptors from the buffer.

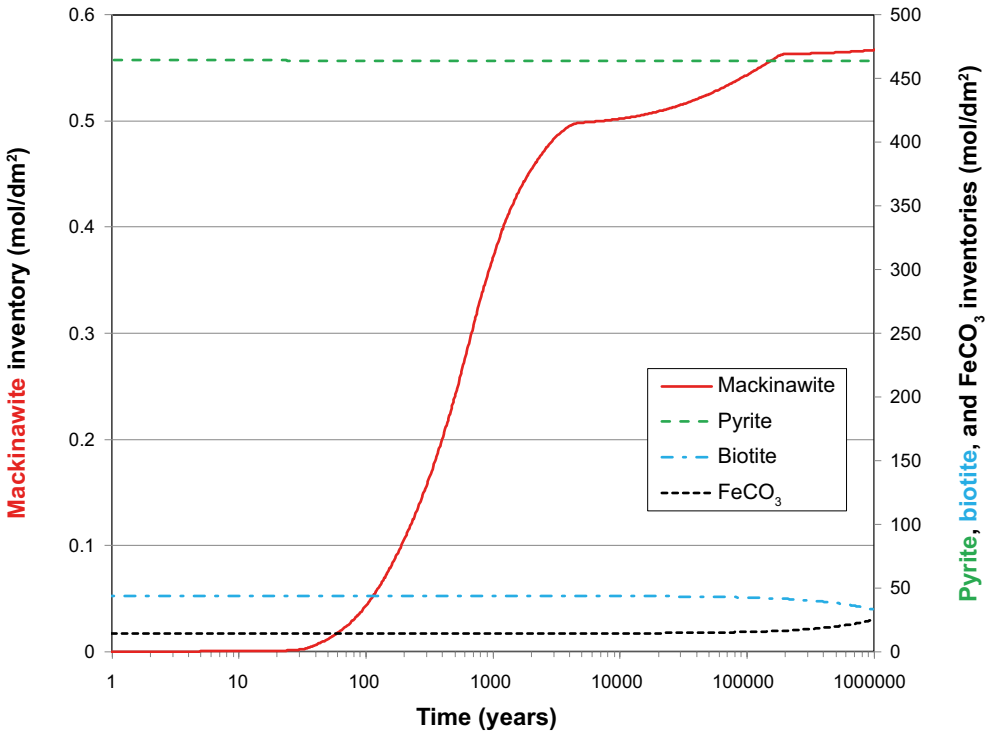

Figure 4-8. *Time dependence of the inventories of various Fe(II) mineral phases.*

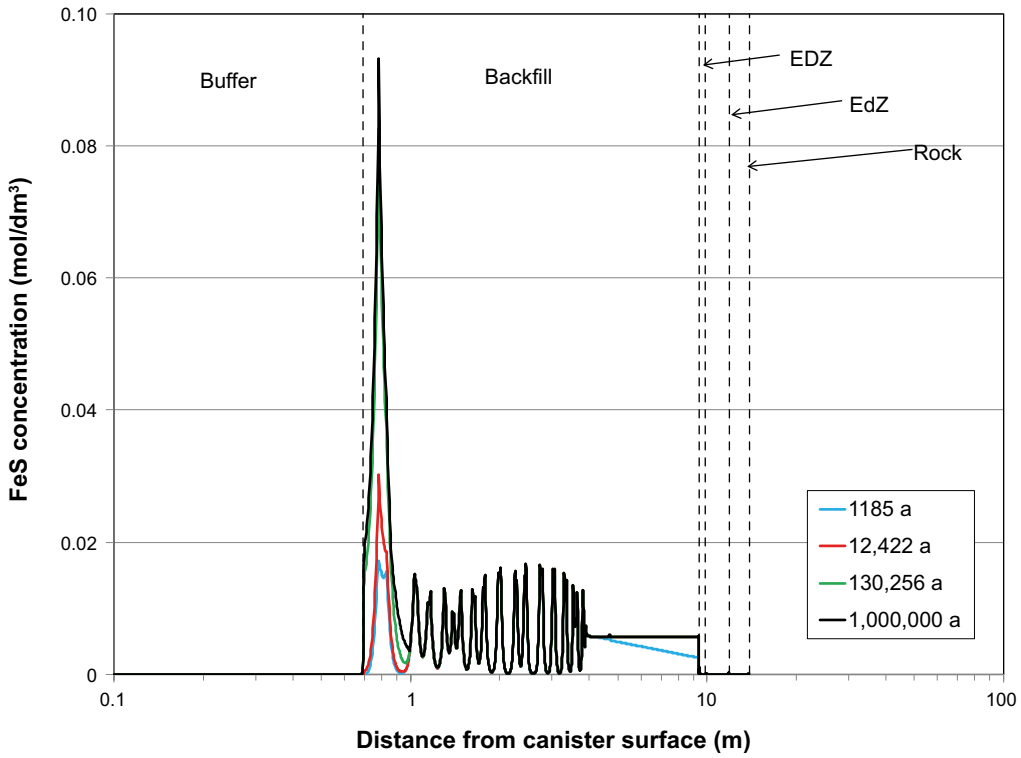

Figure 4-9. *Concentration profiles for precipitated mackinawite (expressed in terms of moles per unit volume of the system) for four different times. The vertical dashed lines indicate the interfaces between the various buffer, backfill, and rock layers assumed for the best-estimate simulation. The fluctuations in the FeS profiles are due to integration artefacts associated with the discretisation of the spatial grid.*

4.2.5 Microbial aspects

4.2.5.1 Distribution of microbial activity

As noted above, microbial activity in the backfill and rock layers is the most important source of sulfide. Figure 4-10 and Figure 4-11 show the predicted spatial distribution of the rate of organotrophic sulfate reduction at early and later times during the course of the simulation, respectively. No significant chemotrophic sulfate reduction was predicted to occur at any time during the simulation.

In the CSM V1.2a-g, microbial activity occurs provided nutrients (organic material and/or H_2) and electron acceptors (i.e., sulfate ions) are present, subject to a threshold degree of saturation. The threshold saturation represents a water activity (a_W) of 0.96, which is deemed to be the threshold below which microbial activity does not occur (Brown 1990). This threshold a_W is never achieved in the buffer, even at full saturation, so microbial activity (either sulfate reduction or aerobic respiration) does not occur close to the canister. Since the backfill is also assumed to partially dry out based on the assumed saturation behaviour (Table 4-2), microbial activity in the backfill layers is also limited at certain times until it has sufficiently saturated. Thus, microbial activity occurs throughout the backfill and EDZ and EdZ layers initially (see the 3-month profile in Figure 4-10). The outer part of the backfill is assumed to dry out first but the inner backfill remains relatively wet due to water entering from the buffer. Thus, microbial activity is maintained in the inner portion of the backfill after 2.6 a but not further out in the backfill. Eventually the entire backfill dries out sufficiently to stop microbial activity, but when it does resaturate, microbial activity occurs throughout the backfill and especially close to the buffer/backfill interface, as described above (profile for 181 a in Figure 4-10 and all profiles in Figure 4-11).

The total amount of organotrophic sulfate reduction is shown as a function of time in Figure 4-12. After 10^6 a, the chemotrophic pathway accounts for less than 10^{-30} mol/dm^2 of sufide production. Because the system is assumed to be initially free of dissolved H_2, chemotrophic sulfate reduction is only possible after a period of anaerobic corrosion of the canister and the resulting production of hydrogen. However, corrosion is delayed because much of the organotrophically produced sulfide precipitates as mackinawite before reaching the canister.

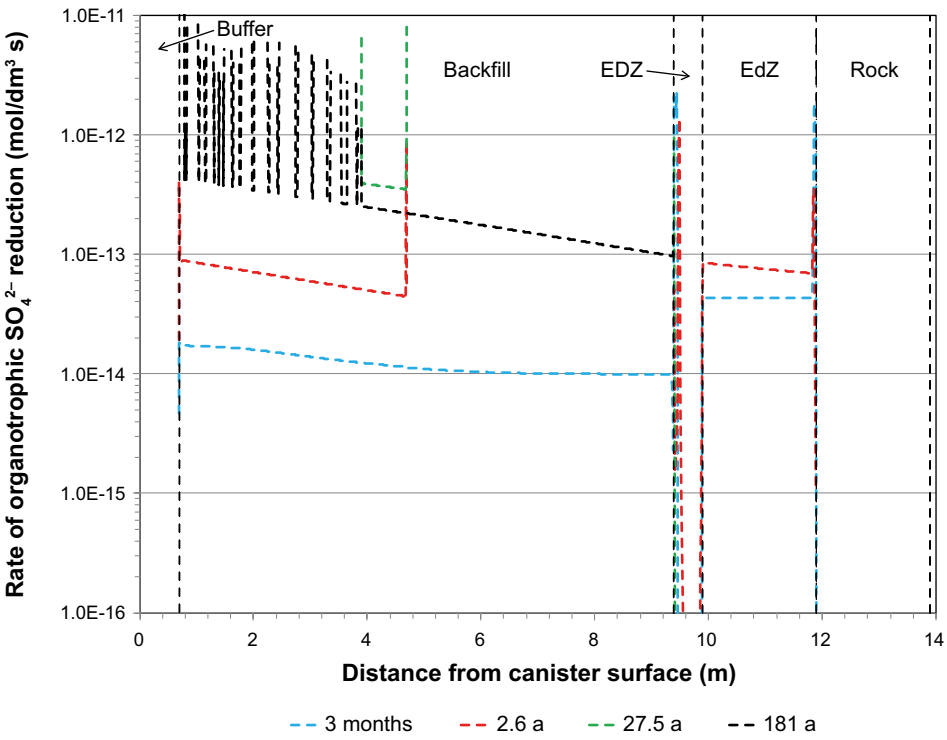

Figure 4-10. *Predicted spatial distribution of the rate of organotrophic sulfate reduction at early times up to 181 a.*

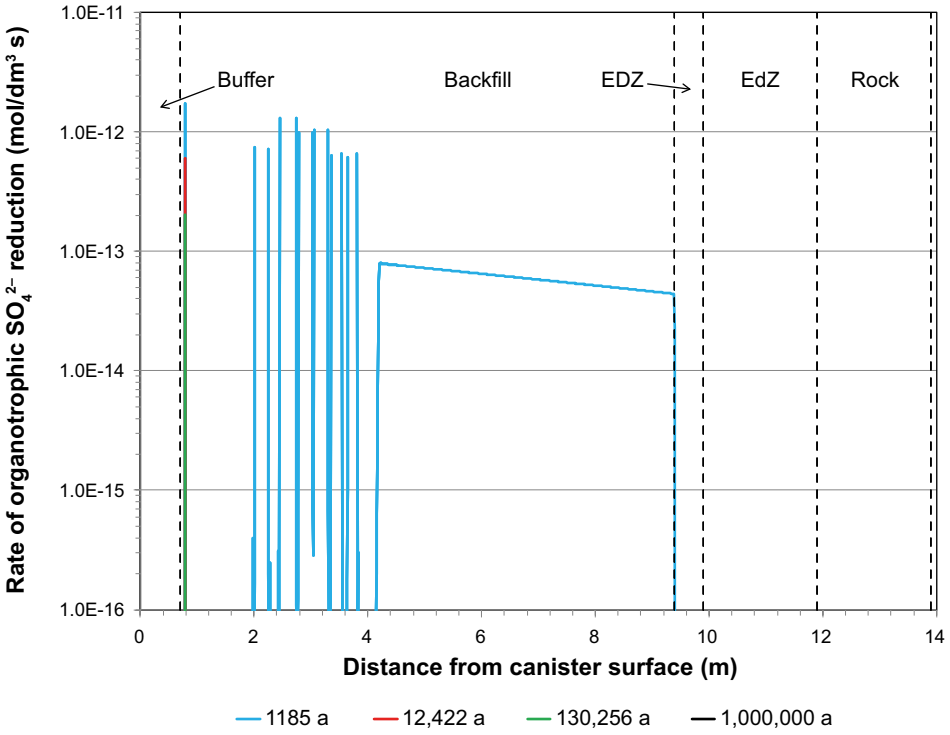

Figure 4-11. *Predicted spatial distribution of the rate of organotrophic sulfate reduction at later times between 1 185 a and 1 000 000 a.*

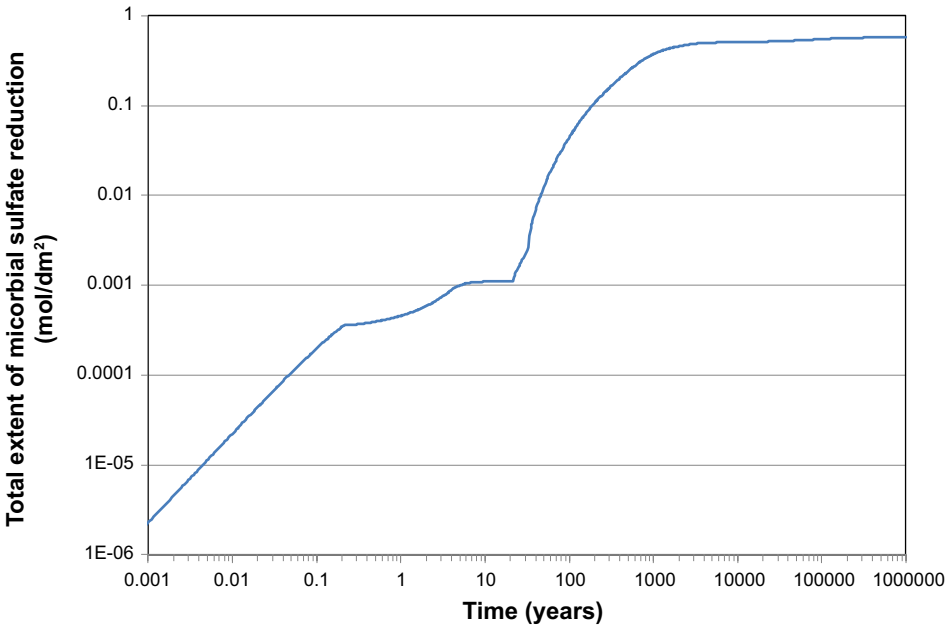

Figure 4-12. *Total extent of organotrophic microbial sulfate reduction as a function of time.*

The result of this microbial activity is a pore water dissolved maximum HS^- concentration of approximately 10^{-5} mol·dm^{-3} (Figure 4-13). Locally higher concentrations (up to approximately 3×10^{-5} mol·dm^{-3}) occur within the backfill layer where the microbial sulfate reduction is focussed.

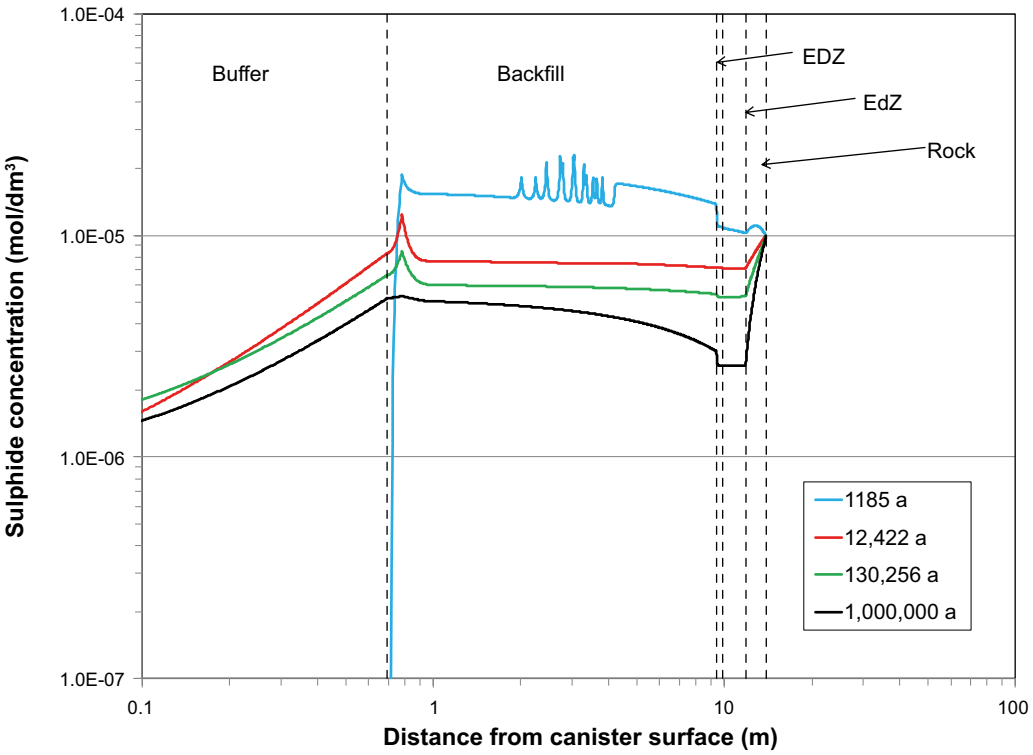

Figure 4-13. *Predicted spatial distributions of dissolved sulfide at four different times.*

4.2.5.2 Microbial population

Equal populations of organotrophic and chemotrophic SRB are assumed to be present initially in all layers of the model, with the highest populations in the EDZ and EdZ. The population increases as a result of metabolic activity and, for the best-estimate simulation, microbes are assumed to die as a result of cell maintenance requirements (the need for energy to sustain cell functions other than production generation, van Bodegom 2007). A fraction of the dead cell material (90 %) is assumed to be recycled as dissolved organic material to support further organotrophic sulfate reduction and the growth of both organotrophs and chemotrophs.

Figure 4-14 shows the predicted populations of the two strains of SRB as a function of time. The original population of chemotrophs quickly dies off due to cell maintenance requirements but a stable population is established once chemotrophic sulfate production becomes possible with the generation of H_2 from canister corrosion. On the other hand, organotrophic sulfate production occurs for much of the simulation period and the population of organotrophs fluctuates in response to the opposing effects of death due to cell maintenance and growth due to metabolic activity.

4.2.5.3 Organic matter

Organic matter persists for approximately 200 000 a (Figure 4-15). Solid organic material (SOM) is assumed to be present initially in the buffer and backfill materials, but not in the rock layers or ground water. Although dissolved organic material (represented in the model by acetate) is not present initially, the SOM is assumed to dissolve via a temperature-dependent first order process with a rate constant at 25 °C of 2.2×10^{-9} s^{-1} (equivalent to a half-life of 10 a). This relatively slow dissolution process was chosen to represent the recalcitrant nature of the solid organic material in bentonite, although the dissolution rate will be accelerated due to the increase in the near-field temperature (assumed activation energy 60 000 J/mol).

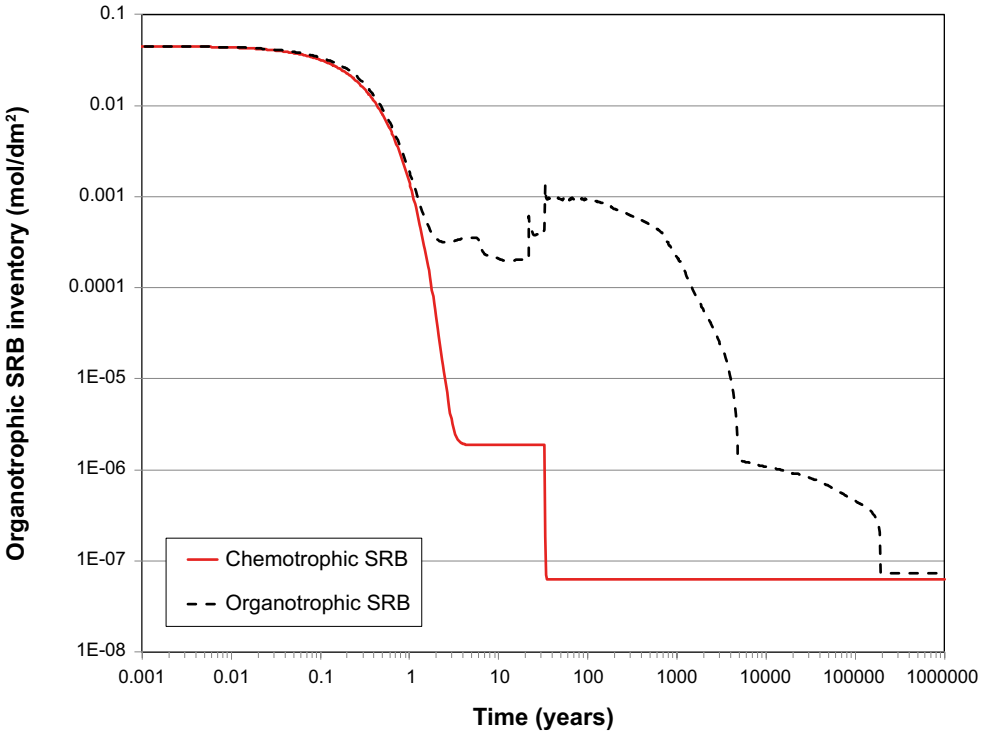

Figure 4-14. *Predicted time-dependent microbial populations in the entire system.*

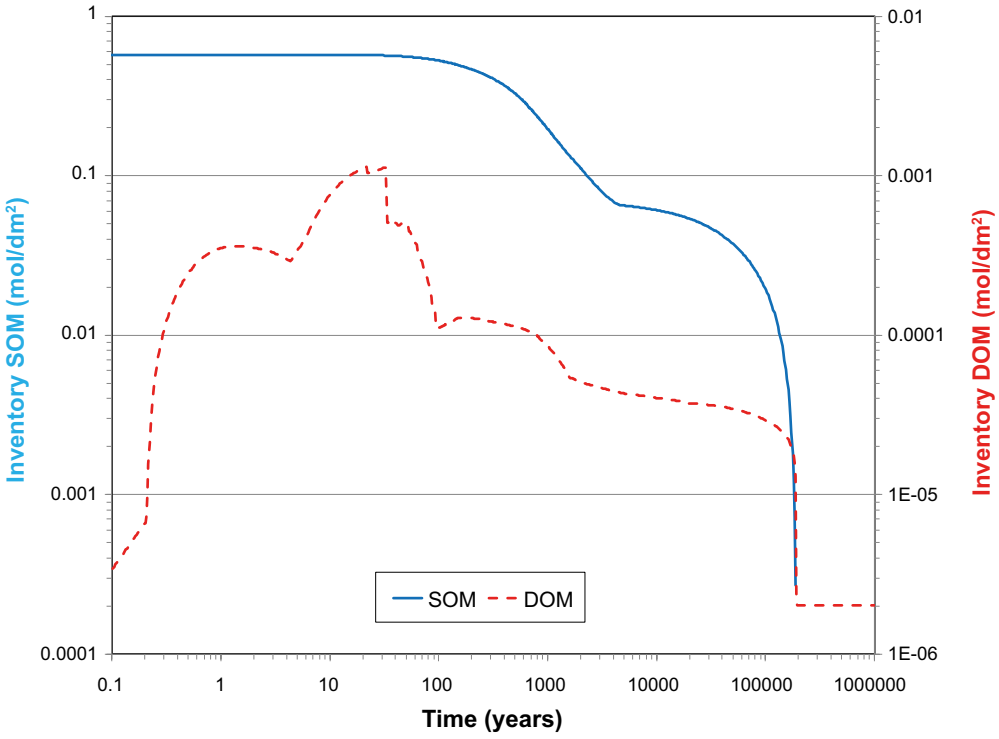

Figure 4-15. *Inventories of solid (SOM) and dissolved organic material (DOM) as a function of time.*

As shown in Figure 4-16, the organic material in the backfill is consumed faster than that in the buffer and becomes locally depleted at the location of greatest microbial activity close to the buffer/backfill interface. In contrast, microbial activity does not occur in the buffer at any time and the dissolved organic matter must diffuse into the backfill layer to react. Some DOM also diffuses into the EDZ and EdZ layers accounting for the microbial activity observed at these locations at short times (Figure 4-10).

4.2.5.4 Sulfate

Gypsum is assumed to be present as an accessory mineral in both the buffer and backfill. In comparison to the amount of organic material present, the inventory of sulfate is virtually unlimited and ~3 % of the initial gypsum content is predicted to be consumed over the 10^6-a simulation period (Figure 4-17).

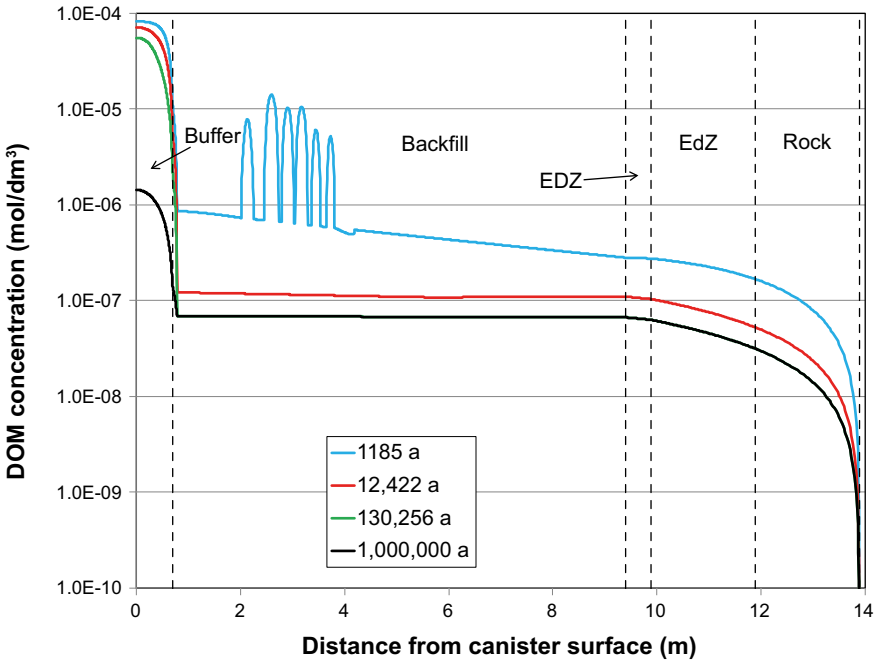

Figure 4-16. *Predicted concentration profiles for dissolved organic material for four different simulation times.*

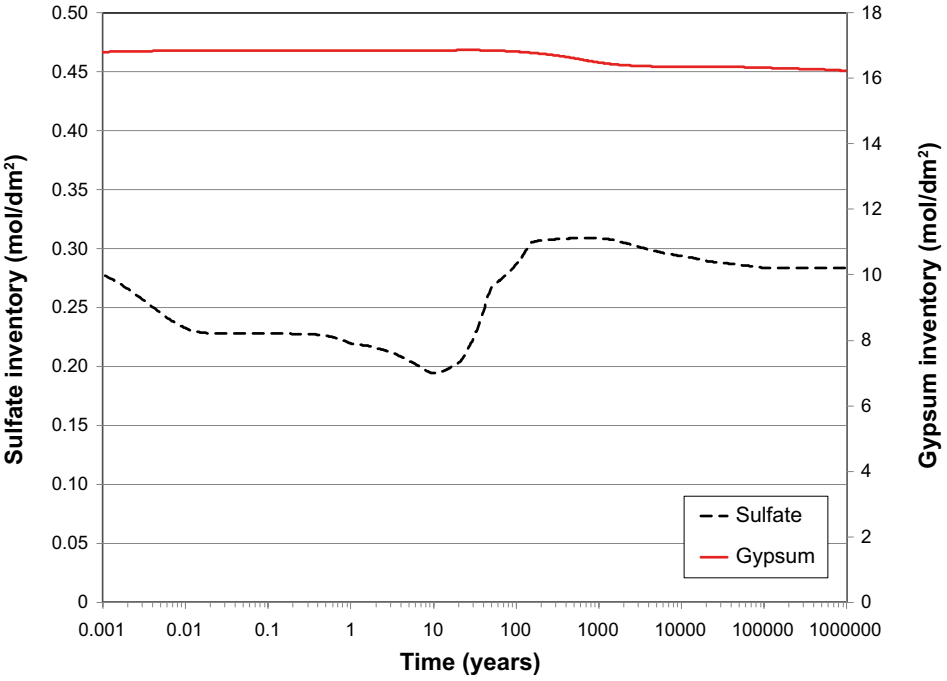

Figure 4-17. *Time dependent inventories of dissolved sulfate and gypsum.*

4.3 Sensitivity analyses

The best-estimate simulation was based on the assumption that microbial activity was not permitted at any time in the buffer material and that the microbial population was subject to death due to cell maintenance requirements. Separate sensitivity analyses were performed to assess the impact of these assumptions. The sensitivity of the predicted results to variation in the saturation time and to the modelled orientation of the diffusion path (horizontal as opposed to vertical) was also investigated, the latter in order to assess the impact of excluding backfill from the analysis.

Table 4-5 summarises the different sensitivity analyses that were performed to investigate the effects of:

- The assumption of microbial death and the recycling of dead cell material due to metabolic activity (runs 1.2a-g1 (death) and 1.2a-g2 (death)) versus no death of microbes (runs 1.2a-g1 (no death) and 1.2a-g2 (no death)).
- Allowing microbial activity to occur in the buffer material (runs 1.2a-g2 (death and no death)) versus the usual assumption of no microbial activity in the buffer (runs 1.2a-g1 (death and no death)).
- Repository saturation times of 20 a, 200 a, and 2 000 a (runs 1.2a-gSat20, 1.2a-gSat200, and 1.2a-gSat2000, respectively). The effect of saturation time was investigated only for the default conditions of microbial death due to cell maintenance requirements, the absence of microbial activity in the buffer, and backfill included in the diffusion path.
- Horizontal diffusion towards and away from the canister (runs 1.2a-gHorTr1 and 1.2a-gHorTr2, without and with microbial activity in the buffer, respectively) versus the usual assumption of a vertical diffusion path that includes a layer of backfill material.

Table 4-5. Summary of sensitivity analyses performed investigating the effects of microbial mortality, microbial activity in the buffer, the saturation time, and the exclusion of backfill (horizontal diffusion path).

Run	Microbial death/ no death	Microbial activity in buffer (Y/N)	Backfill included (Y/N)	Saturation time (a)	Comments
1.2a-g1 (death)	Death	N	Y	200	Best estimate (vertical transport pathway)
1.2a-g1 (no death)	No death	N	Y	200	
1.2a-g2 (death)	Death	Y	Y	200	
1.2a-g2 (no death)	No Death	Y	Y	200	
1.2a-gSat20	Death	N	Y	20	Saturation profile in Figure 4-24(a)
1.2a-gSat200	Death	N	Y	200	Saturation profile in Figure 4-24(b)
1.2a-gSat2000	Death	N	Y	2 000	Saturation profile in Figure 4-24(c)
1.2a-gHorTr1	Death	N	N	200	Best estimate (horizontal transport pathway)
1.2a-gHorTr2	Death	Y	N	200	

Table 4-6 and Table 4-7 summarise some of the results of the various sensitivity analyses in terms of processes related to the extent of corrosion and sulfide production and consumption (Table 4-6) and consumption of the initial oxygen (Table 4-7).

Table 4-6. Results of best-estimate simulations using CSM Version 1.2a-g and sensitivity analyses for a period of 10^6 years for processes related to the extent of corrosion and sulfide production and consumption.

Run	Net charge density for $CuCl_2^-$ formation		Charge density for Cu_2S formation		Cu_2S film thickness	Extent of SO_4^{2-} reduction	Inventories (mol dm^{-2})							
							SO_4^{2-}		HS^-		FeS_2		FeS	
	(C dm^{-2})	(µm)	(C dm^{-2})	(µm)	(µm)	(mol dm^{-2})	Initial	Final	Initial	Final	Initial	Final	Initial	Final
1.2a-g1 (death)	871	6.4	394	2.9	20.9	0.575	16.8	16.5	9.6×10^{-7}	8.1×10^{-5}	464	464	0	0.56
1.2a-g1 (no death)	871	6.4	111	0.8	16.3	0.519	16.8	16.5	9.6×10^{-7}	3.2×10^{-6}	464	464	0	0.513
1.2a-g2 (death)	874	6.4	347	2.6	19.2	0.568	16.8	16.5	9.6×10^{-7}	3.1×10^{-6}	464	464	0	0.560
1.2a-g2 (no death)	874	6.4	333	2.5	19.2	0.519	16.8	16.5	9.6×10^{-7}	3.2×10^{-6}	464	464	0	0.511
1.2a-gSat20	355	2.6	415	3.1	12.7	0.579	16.8	16.5	9.6×10^{-7}	8.1×10^{-5}	464	464	0	0.572
1.2a-gSat200	267	2.0	422	3.1	11.7	0.577	16.8	16.5	9.6×10^{-7}	8.1×10^{-5}	464	464	0	0.571
1.2a-gSat2000	257	1.9	423	3.1	10.7	0.577	16.8	16.5	9.6×10^{-7}	8.1×10^{-5}	464	464	0	0.571
1.2a-gHorTr1	238	1.8	502	3.7	11.7	0.0414	0.13	0.044	9.6×10^{-7}	1.3×10^{-6}	462	462	0	0.0352
1.2a-gHorTr2	186	1.4	434	3.2	10.7	0.0376	0.13	0.048	9.6×10^{-7}	4.9×10^{-7}	462	462	0	0.0326

Table 4-7. Results of best-estimate simulations using CSM Version 1.2a-g and sensitivity analyses for a period of 10^6 years for processes related to the consumption of the initial oxygen inventory.

Run	O_2 inventory	Charge density for O_2 reduction		Extent of $CuCl_2^-$ oxidation		Extent of pyrite oxidation		Extent of aerobic respiration	
	(mol dm^{-2})	(C dm^{-2})	(%)	(mol dm^{-2})	(%)	(mol dm^{-2})	(%)	(mol dm^{-2})	(%)
1.2a-g1 (death)	0.0380	0.0025	< 0.001	0.00342	9.0	0.0345	90.8	7.3×10^{-5}	0.2
1.2a-g1 (no death)	0.0380	0.0025	< 0.001	0.00342	9.0	0.0345	90.8	7.3×10^{-5}	0.2
1.2a-g2 (death)	0.0380	0.0025	< 0.001	0.00342	9.0	0.0345	90.7	9.2×10^{-5}	0.2
1.2a-g2 (no death)	0.0380	0.0025	< 0.001	0.00342	9.0	0.0345	90.8	9.2×10^{-5}	0.2
1.2a-gSat20	0.0380	0.0026	< 0.001	0.0011	2.9	0.0357	94.0	1.5×10^{-3}	3.9
1.2a-gSat200	0.0380	0.0026	< 0.001	0.0011	2.9	0.0357	94.0	1.1×10^{-3}	2.9
1.2a-gSat2000	0.0380	0.0026	< 0.001	0.0011	2.9	0.0357	94.0	1.1×10^{-3}	2.9
1.2a-gHorTr1	0.00104	0.0026	0.001	0.00099	95.2	0.00005	5.0	1.0×10^{-8}	0.001
1.2a-gHorTr2	0.00104	0.0022	0.001	0.00099	95.0	0.00005	5.0	5.5×10^{-8}	0.005

4.3.1 Impact of allowing microbial activity in the buffer

To assess the impact of microbial activity in the bentonite, the threshold degree of saturation was set to zero, thus permitting sulfate reduction to occur in the buffer at all times.

Figure 4-18 shows the impact of microbial activity in the buffer on the predicted corrosion potential of the canister for the assumptions of both the death and "no death" of cells. Allowing microbial activity to occur in the buffer results in a faster transition in E_{CORR} to relatively negative values, regardless of whether cells are assumed to die or not as a result of cell maintenance requirements. There is relatively little difference in the timing of the precipitous drop in E_{CORR} depending upon whether microbes are, or are not, assumed to die due to cell maintenance requirements.

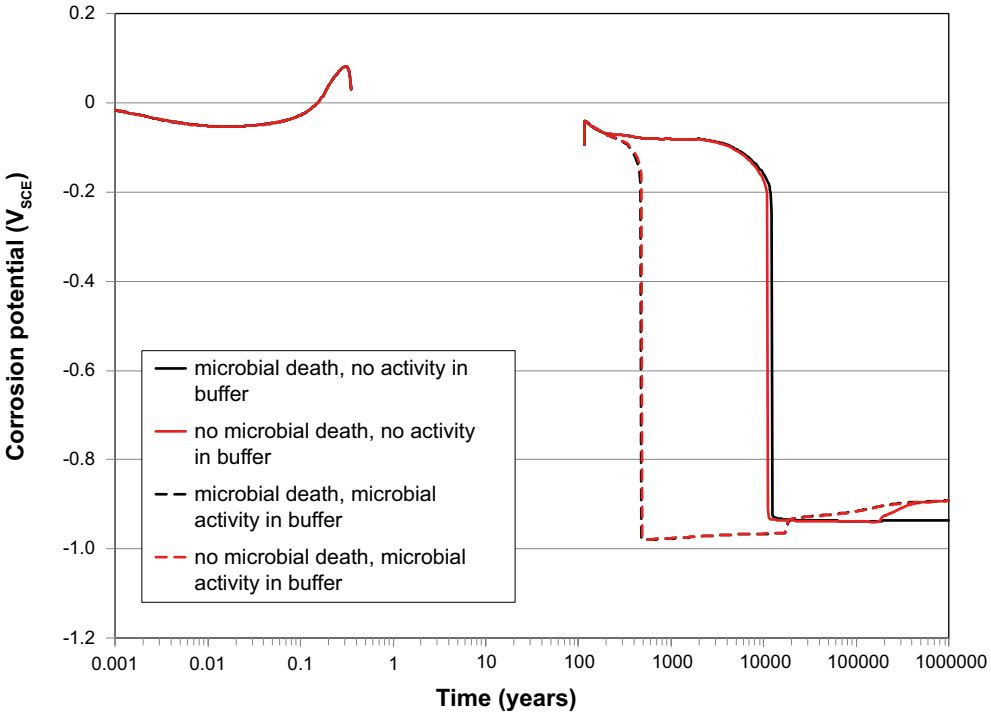

Figure 4-18. *The impact of permitting microbial activity in the buffer material on the evolution of the corrosion potential. Solid lines indicate no microbial activity in the buffer, dashed lines indicate microbial activity is allowed. Black lines indicate microbial death, red lines indicate no death of microbes due to cell maintenance requirements.*

Allowing microbial activity to occur in the buffer has some effect on the total depth of corrosion (Figure 4-19). The impact of the earlier transport of sulfide to the cansiter surface if microbial activity is allowed in the buffer can be seen from the figure. In addition, in a system that is organic-carbon limited, assuming microbial death *and recycling of dead cell material* results in more corrosion as the recycled cell material acts as a continuing source of carbon.

This earlier transport of sulfide to the canister is apparent from the time dependence of the depth of anaerobic corrosion, i.e., that part of the total corrosion due to the formation of Cu_2S. Figure 4-20 and Figure 4-21 show the time dependence of the depth of anaerobic corrosion on logarithmic and linear scales, respectively. It is apparent from Figure 4-20 that the transport of HS^- occurs relatively soon after the establishement of anaerobic conditions if microbial activity occurs in the buffer, consistent with the earlier decrease in E_{CORR} in Figure 4-18.

Although the rate of corrosion due to microbial sulfate reduction is higher initially if activity occurs in the buffer, the available organic carbon is consumed faster and the rate of sulfide production and of anaerobic corrosion eventually slows. In the case of microbial death, all of the *solid* organic material is consumed after a period of 19 000 a if activity is allowed in the buffer, whereas it persists for 190 000 a if activity is limited to the backfill and EDZ. If cells are assumed not to die, then the solid organic material is consumed slightly earlier (18 000 a and 190 000 a with and without microbial activity in the buffer). More importantly, however, microbial death and recycling is sufficient to maintain the *dissolved* organic carbon concentration (see the DOM content in Figure 4-15). This persistent DOM allows microbial activity to continue throughout the 10^6-a simulation period, resulting in more corrosion.

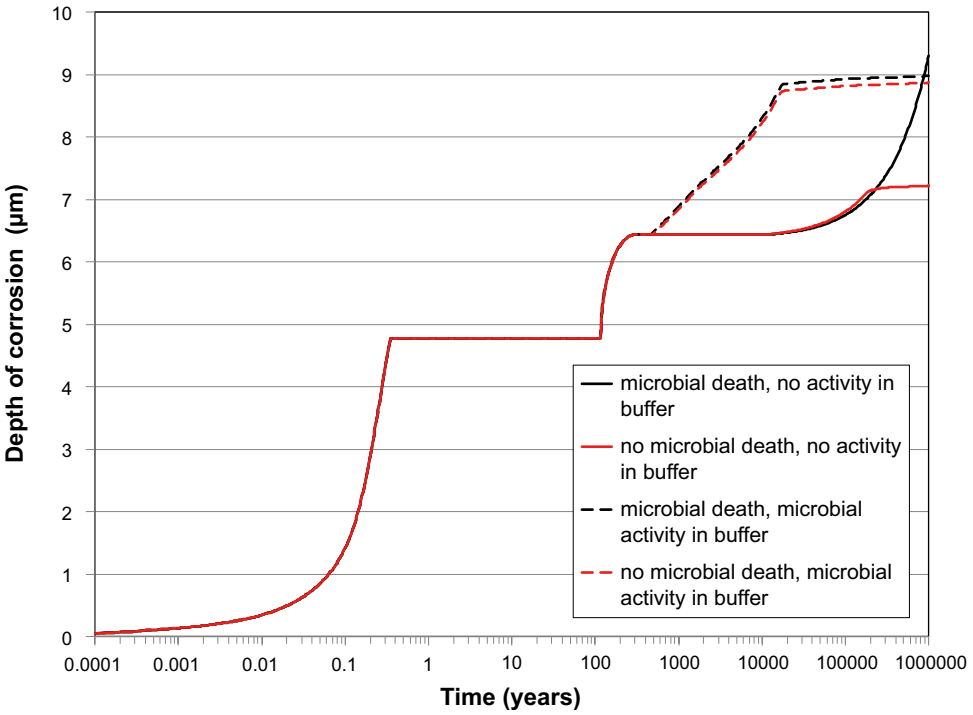

Figure 4-19. *The impact of microbial activity in the buffer material on the overall depth of corrosion of the canister. Solid lines indicate no microbial activity in the buffer, dashed lines indicate microbial activity is allowed. Black lines indicate microbial death, red lines indicate no death of microbes due to cell maintenance requirements.*

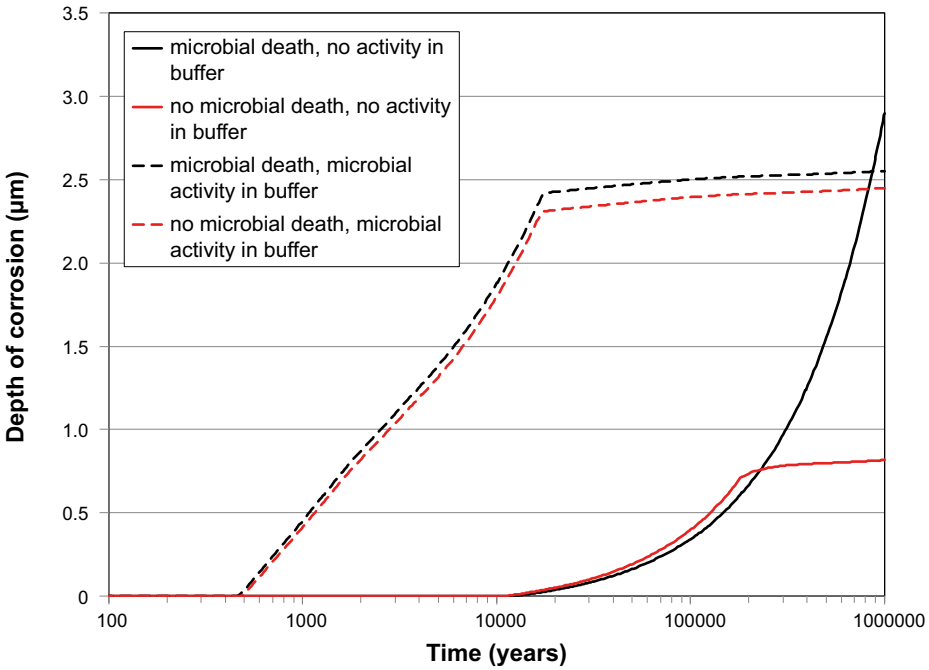

Figure 4-20. *Time dependence of the depth of corrosion due to the formation of Cu_2S (log time scale). Solid lines indicate no microbial activity in the buffer, dashed lines indicate microbial activity is allowed. Black lines indicate microbial death, red lines indicate no death of microbes due to cell maintenance requirements.*

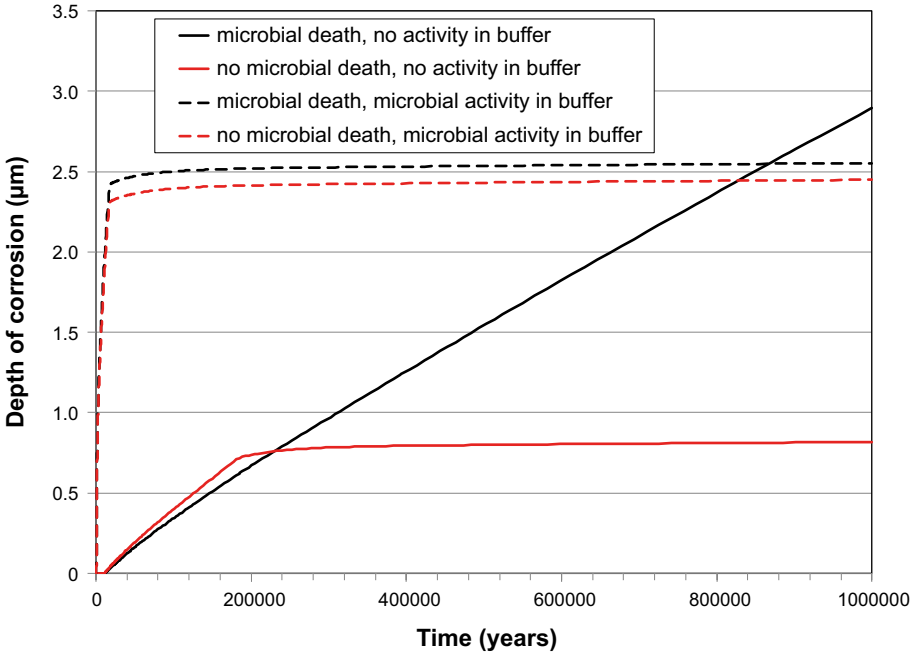

Figure 4-21. *Time dependence of the depth of corrosion due to the formation of Cu_2S (linear time scale). Solid lines indicate no microbial activity in the buffer, dashed lines indicate microbial activity is allowed. Black lines indicate microbial death, red lines indicate no death of microbes due to cell maintenance requirements.*

4.3.2 Impact of assumption of microbial death

Somewhat counter-intuitively, more microbial activity occurs if a fraction of the microbes are assumed to die due to cell maintenance (Figure 4-22). However, in a system that is organic-carbon limited, the recycling of dead cell material represents an additional source of organic carbon resulting in additional microbial activity. After 10^6 a, recycling of dead cell material results in approximately 10 % more sulfate reduction than in the absence of cell death.

Another consequence of the assumption regarding microbial mortality is the difference in the relative importance of organotrophic and chemotrophic sulfate reduction. In all cases, the organotrophic route is by far the more important, accounting for > 99.9 % of all sulfate reduction. However, in the case of no microbial death, approximately 0.03–0.09 % of the sulfide formed is produced by chemotrophic bacteria (Figure 4-23). If cells are allowed to die, the initial population of chemotrophic bacteria has become vanishingly small by the time that H_2 is produced by corrosion. Conversely, if the population is maintained, there are sufficient chemotrophic bacteria present in the system that some activity is predicted to occur. More chemotrophic sulfate reduction is predicted if microbial activity is allowed in the buffer, as these active microbes are closer to the source of H_2 (i.e., the canister surface).

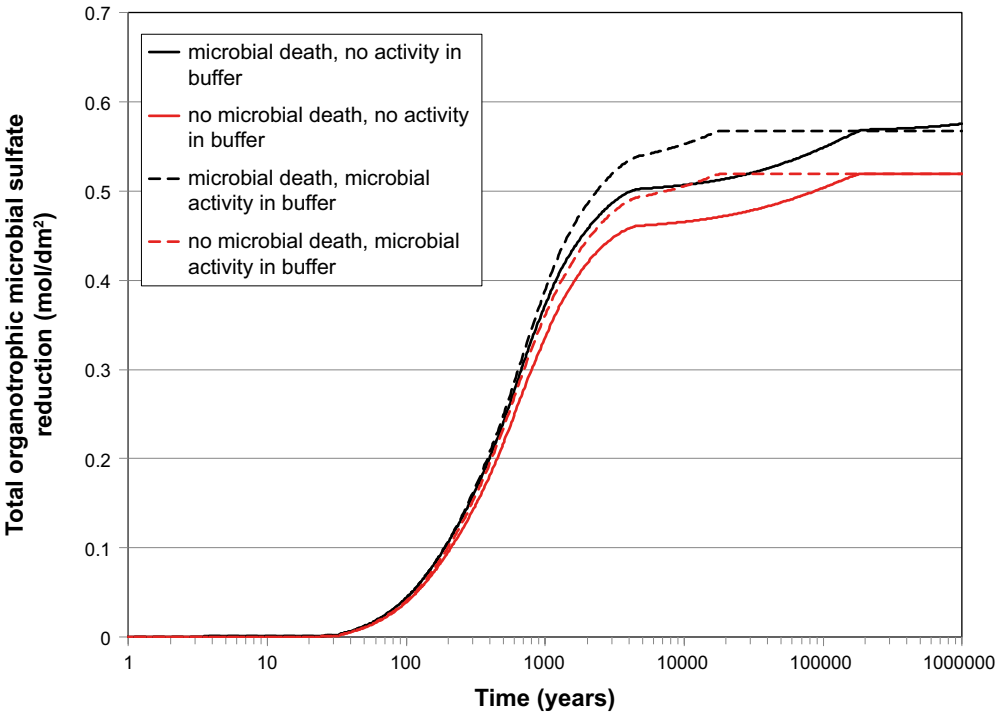

Figure 4-22. *Impact of different assumptions regarding microbial death due to cell maintenance on the total extent of sulfate reduction. Solid lines indicate no microbial activity in the buffer, dashed lines indicate microbial activity is allowed. Black lines indicate microbial death, red lines indicate no death of microbes due to cell maintenance requirements.*

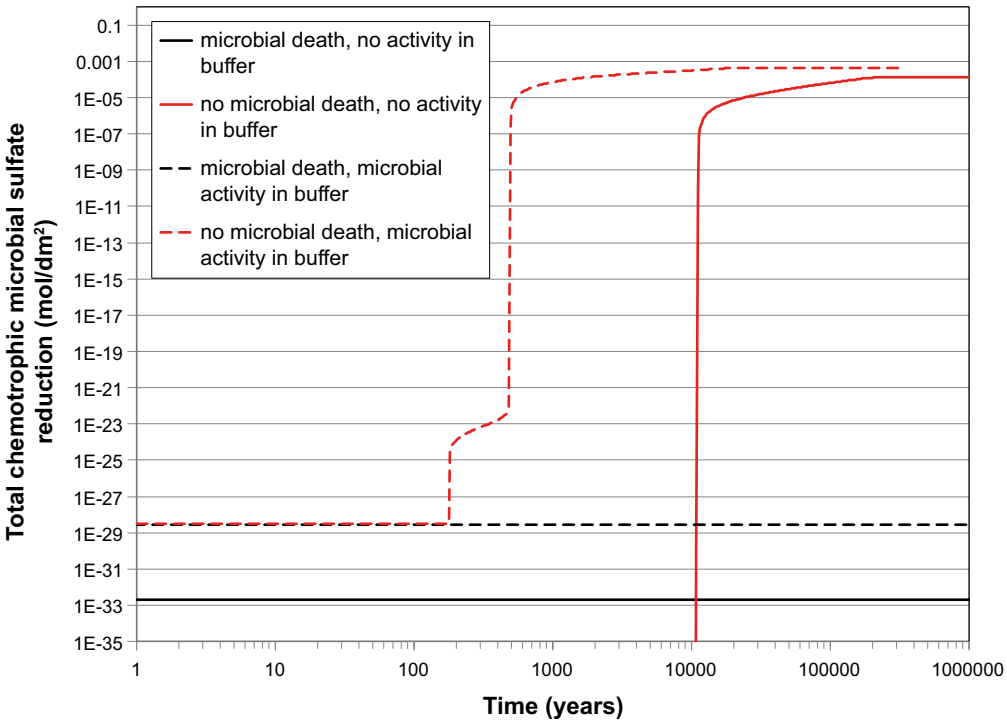

Figure 4-23. *Impact of different assumptions regarding microbial death due to cell maintenance on the extent of chemotrophic sulfate reduction. Solid lines indicate no microbial activity in the buffer, dashed lines indicate microbial activity is allowed. Black lines indicate microbial death, red lines indicate no death of microbes due to cell maintenance requirements.*

4.3.3 Buffer and backfill saturation time

These simulations were performed using the CSM Version 1.2a-g. For this version of the model, the effects of unsaturated conditions include (i) drying of the canister surface and the cessation of surface electrochemical reactions, (ii) suppression of microbial activity in the backfill material below a threshold moisture content, (iii) increased diffusivity of O_2 and H_2 (but not of gaseous H_2S, which is not included in V1.2a-g), and (iv) the concentration and subsequent dilution of dissolved solutes due to the loss and gain of H_2O.

Figure 4-24 shows the time dependence of the degree of saturation for each of the eight layers considered in the model for assumed saturation times of 20 a (Figure 4-24(a)), 200 a (Figure 4-24(b)), and 2 000 a (Figure 4-24(c)). From the canister surface outwards, these layers are: Bent1, Bent2, Bent3, Back1, Back2, EDZ, EdZ, and Rock. The saturation period is defined as the time at which all of the layers are fully saturated. These saturation profiles are based on the THM modelling of Åkesson et al. (2010) for a KBS-3 style repository and, in particular, were designed to capture the following concepts: (i) moisture is not lost from the deposition hole as a result of the initial drying but is instead re-distributed within the buffer, (ii) the extent to which the buffer closest to the canister dries out is a function of the heat output from the fuel and is independent of the properties of the host rock, (iii) at the canister surface, the degree of saturation of the buffer may drop to as low as 0.2, (iv) the last region of the repository to saturate is the central part of the backfill, represented in the model by layer Back1, and (v) the time for complete saturation is a function of the host-rock properties and is expected to vary between approximately a decade and a few thousand years. These saturation profiles are different from those (Table 4-2) used for the interim versions of the CSM described in Section 3, for the best-estimate analyses in Sections 4.2, 4.3.1, and 4.3.2, and for the study of the impact of diffusion orientation (Section 4.3.4). For these other analyses, a saturation time of 200 a was assumed but moisture was lost from the buffer layers upon initial dry-out, as would be expected for an in-room disposal repository design for which the profiles in Table 4-2 were developed.

The saturation in layer Bent1 is taken to be that at the canister surface, with interfacial electrochemical reactions considered to cease below a relative humidity of 60 %, corresponding to a degree of saturation of 0.42 based on the soil-water characteristic curve for compacted bentonite (Man and Martino 2009). For the default saturation time of 200 a, therefore, interfacial electrochemical reactions cease after 0.35 a and resume again after 116 a (Figure 4-24(d)). For shorter or longer saturation times, the time to dry out was kept the same (as this time is a function of the fuel properties), but the time to full saturation was increased proportionately. Thus, for saturation times of 20 a and 2 000 a, electrochemical interfacial reactions resume after 11.6 a and 1 160 a, respectively.

In addition to interfacial electrochemical reactions, the other process that is suppressed completely by the drying out of different layers is microbial activity in the backfill. Based on a threshold water activity for microbial activity of 0.96 (Brown 1990), microbial activity in the backfill would cease below a degree of saturation of 0.75 (Man and Martino 2009). However, based on the saturation profiles in Figure 4-24, the degree of saturation does not drop below 0.8 at any time and microbial activity is not suppressed in the backfill for these particular analyses. That was not the case in the other studies described above in which, based on the saturation profiles in Table 4-2, microbial sulfate reduction was suppressed in the two layers of backfill for times of approximately 5 a to 25 a for layer Back1 and 0.7 a to 35 a for layer Back2.

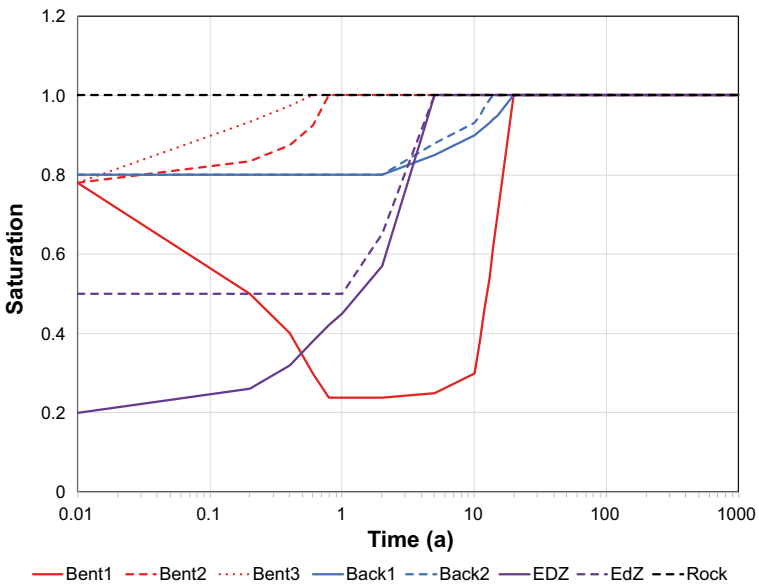

(a) Saturation time of 20 a.

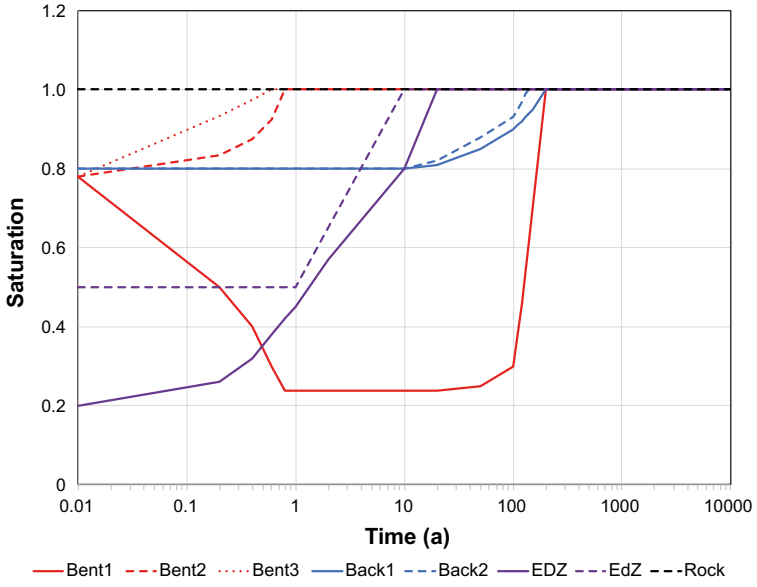

(b) Saturation time of 200 a.

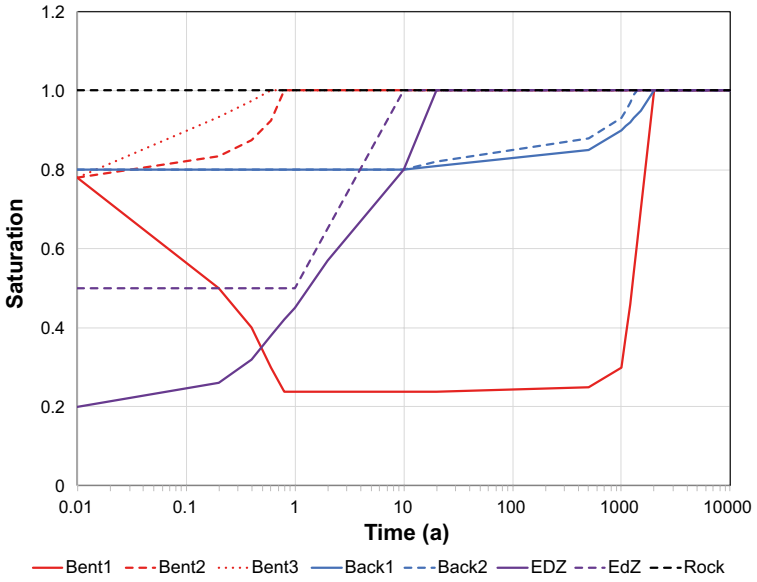

(c) Saturation time of 2,000 a.

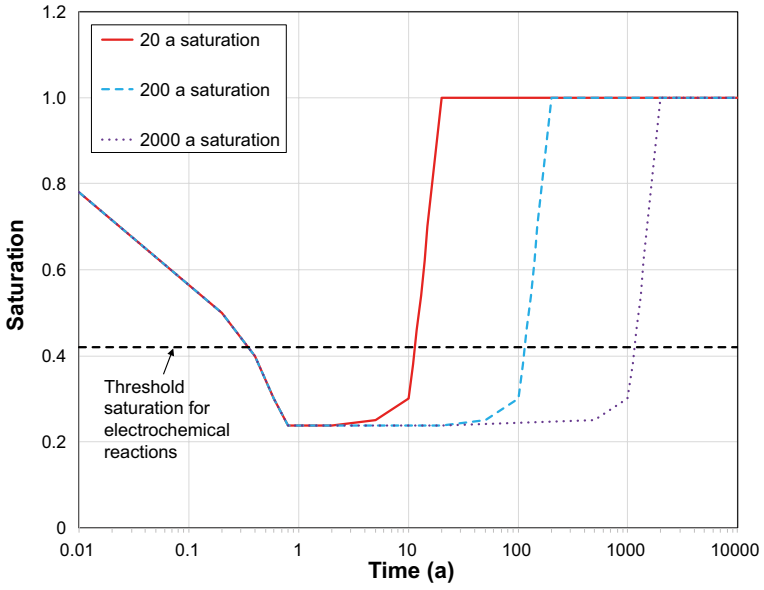

(d) Time dependence of the saturation at the canister surface. The dashed horizontal line indicates the threshold saturation for interfacial electrochemical reactions.

Figure 4-24. *Time-dependent degree of saturation for the for the eight layers considered in the model for various saturation times and the time dependence of the interfacial degree of saturation.*

Figure 4-25 and Figure 4-26 show the predicted dependence of the evolution of E_{CORR} and of the total depth of corrosion on the repository saturation time, respectively. A similar evolution is followed in each case, except that the time at which the precipitous drop in E_{CORR} occurs shifts to slightly earlier times with increasing saturation period. The time dependence of the total depth of corrosion is shown in Figure 4-26, from which it can be seen that more corrosion is predicted for the shortest saturation time. This is a consequence of a greater degree of aerobic corrosion (Figure 4-27(a)), since there is still O_2 present (which is required to produce the actual oxidant Cu^{2+}) in the repository at the time the canister surface wets sufficiently for corrosion to re-start upon re-saturation. There is no predicted effect of saturation time on the extent of anaerobic corrosion due to the formation of Cu_2S (Figure 4-27(b)). However, it should be emphasised that the version of the model used for these analyses (CSM Version 1.2a-g) does not include any effect due to gaseous H_2S.

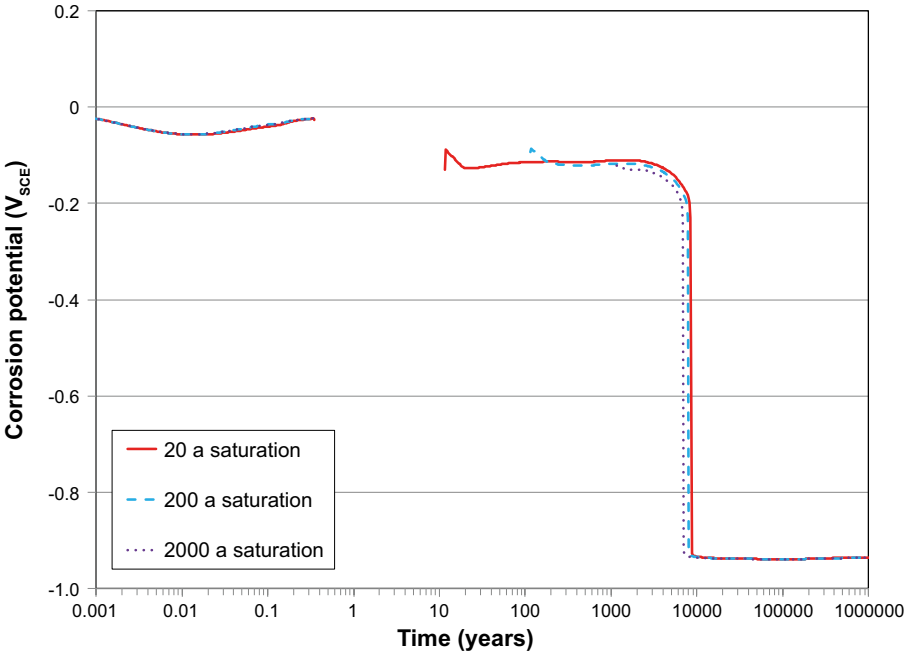

Figure 4-25. *Effect of repository saturation time on the evolution of the canister corrosion potential.*

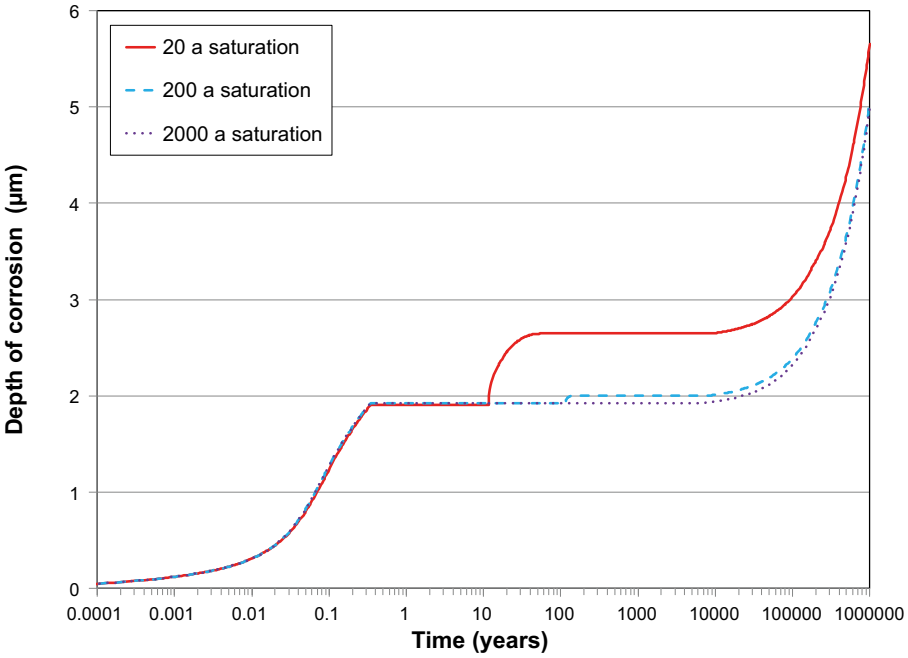

Figure 4-26. *Effect of repository saturation on the time dependence of the total depth of corrosion.*

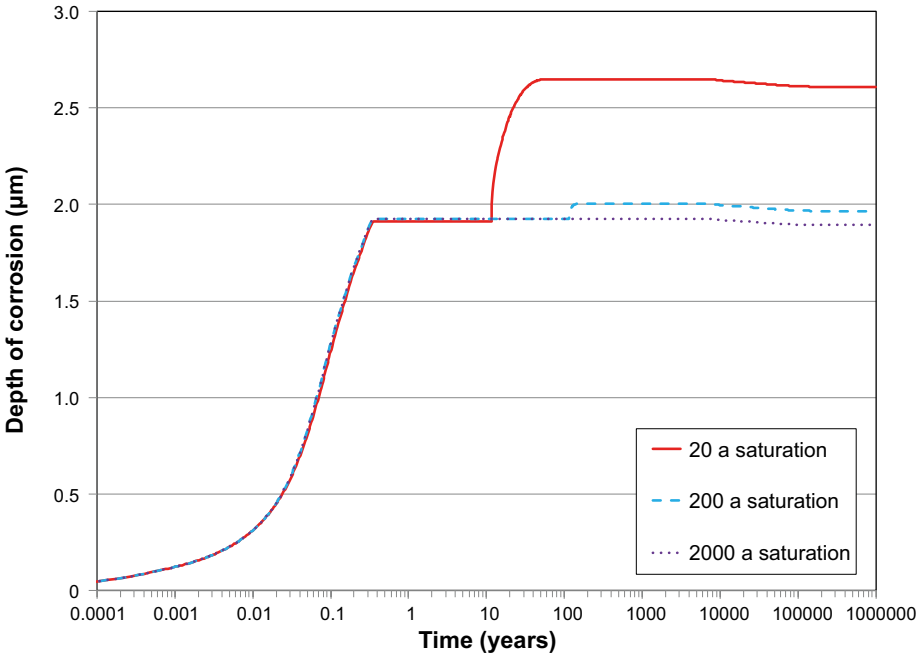

(a) Corrosion due to oxygen and Cu(II)

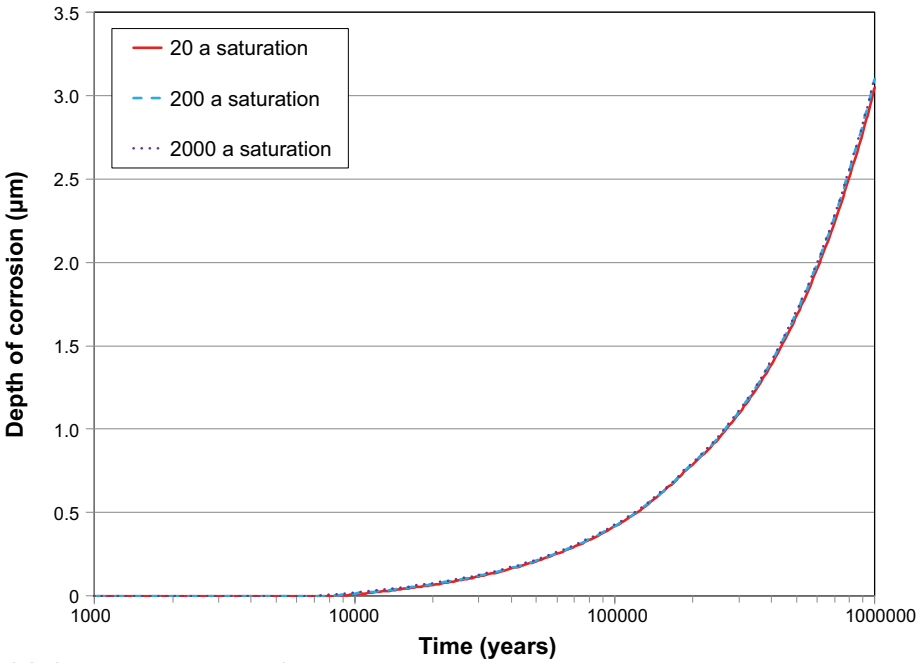

(b) Corrosion due to sulfide

Figure 4-27. *Effect of repository saturation on the time dependence of the depth of corrosion due to (a) oxygen and Cu(II) and (b) sulfide.*

4.3.4 Horizontal versus vertical diffusion

Two effects were considered in these sensitivity analyses; first simulation of the horizontal orientation across the deposition hole which effectively excludes the backfill from the diffusion path and, second, excluding or allowing microbial activity in the buffer. In all cases, microbes were assumed to die as a result of metabolic activity. The two runs representing the vertical orientation are 1.2a-g1 (death) (no microbial activity in buffer) and 1.2a-g2 (death) (microbial activity in buffer) (Table 4-5). The corresponding runs for the horizontal orientation are 1.2a-gHorTr1 (no microbial activity) and 1.2a-gHorTr2 (microbial activity in buffer) (Table 4-5). For the two horizontal orientation simulations, the thickness of the buffer layer was taken to be equal to that in the deposition hole (0.35 m), rather than the thickness of 0.693 m based on the buffer volume:canister surface area ratio used for the vertical orientation simulations.

Figure 4-28 and Figure 4-29 show the predicted time dependence of the corrosion potential and of the total depth of corrosion, respectively, for the two different orientations, with and without microbial activity in the buffer. The E_{CORR} drops precipitously as the interfacial reactions change from the dissolution of Cu as $CuCl_2^-$ supported by the reduction of Cu(II) (or O_2) to the sulfidation of copper supported by the evolution of H_2. Thus, E_{CORR} decreases sooner if microbial activity is allowed in the buffer for both transport orientations. However, regardless of whether microbial activity occurs in the buffer or not, E_{CORR} falls earlier for the horizontal orientation as microbially produced sulfide in the EDZ/EdZ has a shorter distance to diffuse to reach the canister surface.

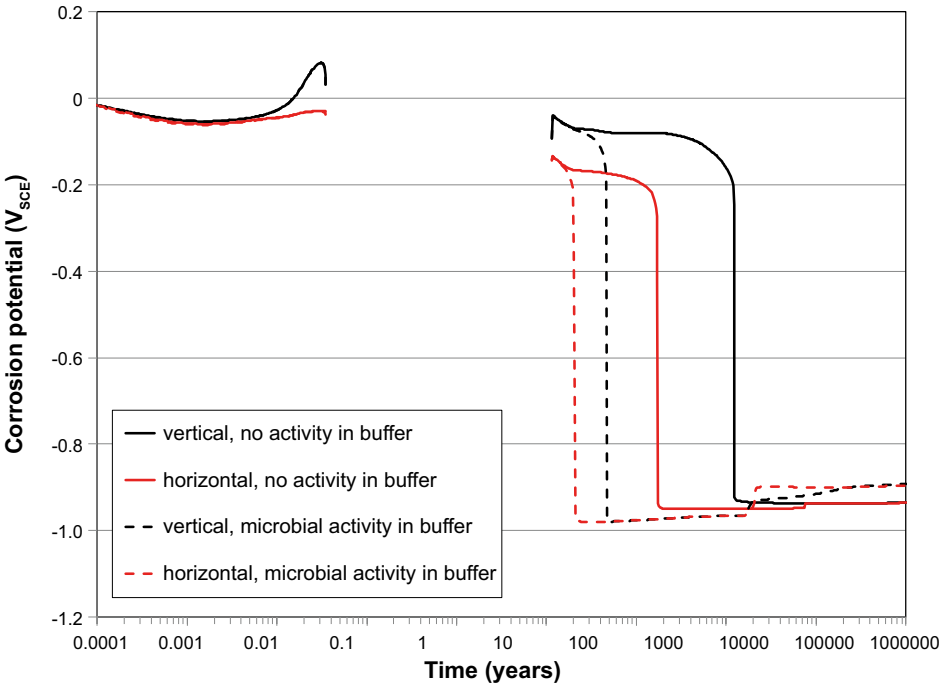

Figure 4-28. *Effect of the orientation of the assumed diffusion path and of the extent of microbial activity in the buffer on the evolution of the corrosion potential.*

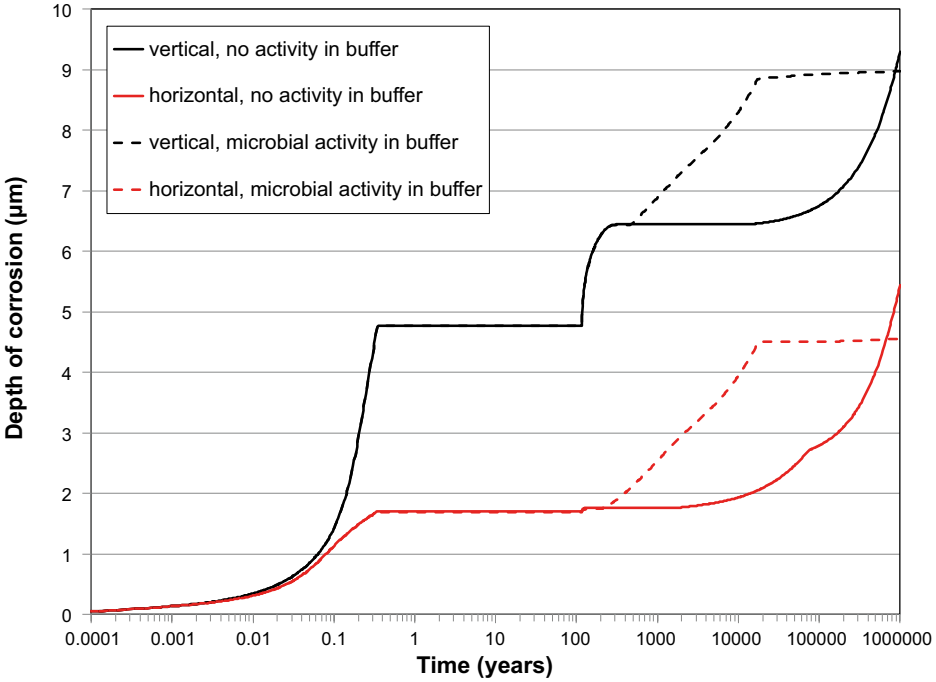

Figure 4-29. *Effect of the orientation of the assumed diffusion path and of the extent of microbial activity in the buffer on the time dependence of the total depth of corrosion.*

However, more corrosion is predicted to occur for the vertical orientation (Figure 4-29) as the presence of a large volume of backfill represents a major reservoir of O_2 (and the resulting Cu(II)) to support corrosion during the aerobic phase (Figure 4-30(a)). In terms of anaerobic corrosion (Figure 4-30(b)), sulfidation occurs earlier the closer the source of microbial activity is to the canister surface, although the total extent of corrosion after 10^6 a is similar in all cases as the system is largely limited by the amount of available organic carbon.

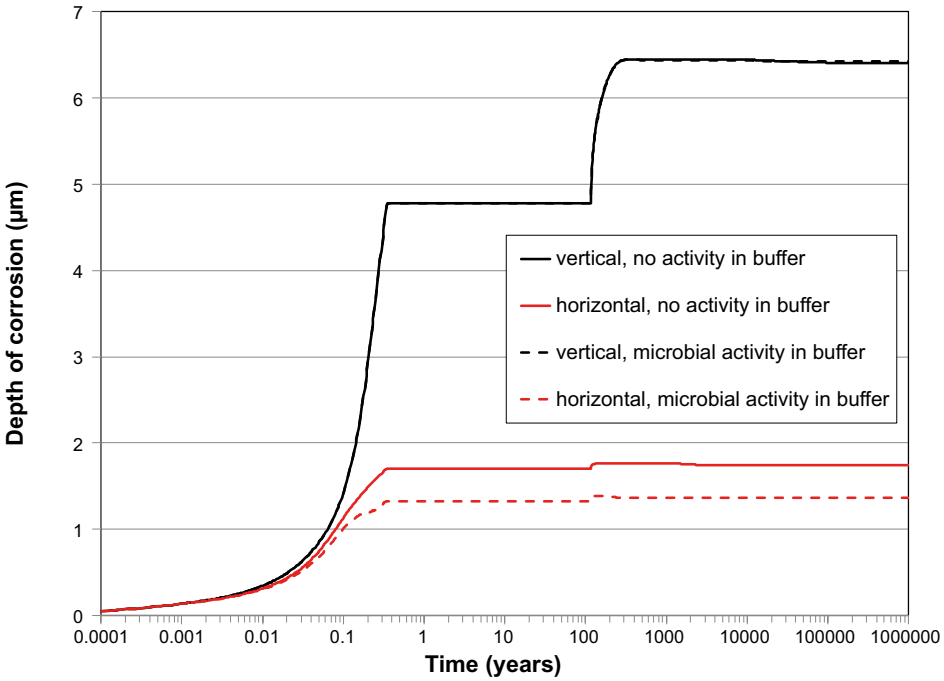

(a) Corrosion due to oxygen and Cu(II).

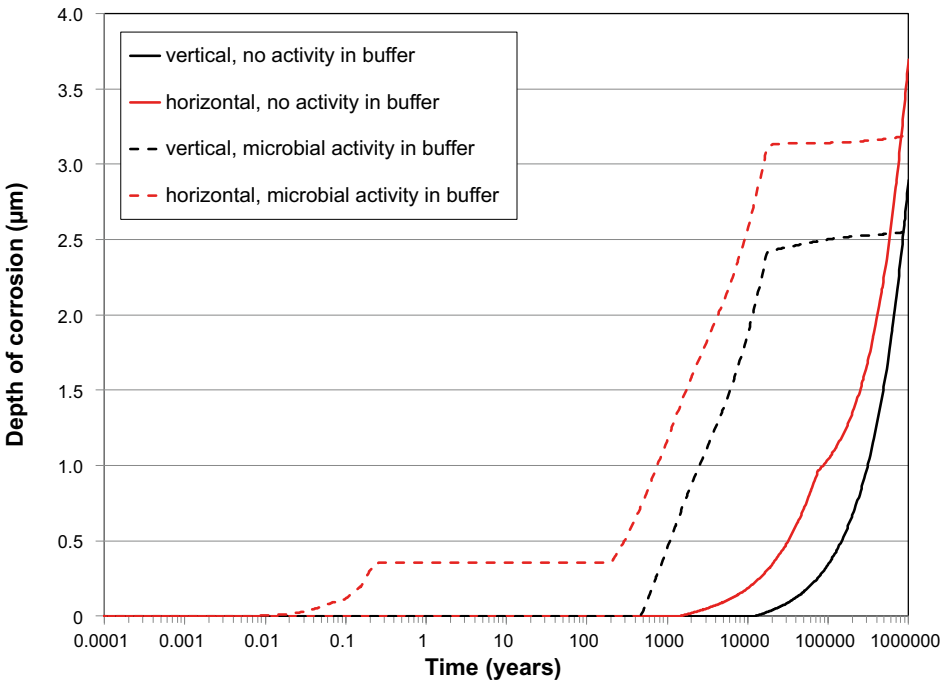

(b) Corrosion due to sulfide.

Figure 4-30. *Effect of the orientation of the assumed diffusion path and of the extent of microbial activity in the buffer on the time dependence of the depth of corrosion due to (a) oxygen and Cu(II) and (b) sulfide.*

5 Integrated Sulfide Project benchmarking exercise

5.1 Background

The CSM was used in a comparison exercise with two other reactive-transport models as part of the SKB-Posiva Integrated Sulfide Project. The two other modelling groups participating in the exercise were those from the University of Bern (Pękala et al. 2019), Switzerland and from a partnership between Amphos 21 and Clay Technology (Idiart et al. 2019). These latter groups have developed 1-D and 3-D reactive-transport models for the production, transport, and consumption of sulfide in a deep geological repository that incorporate detailed thermodynamic speciation codes. The version of the CSM used for the inter-model comparison ("benchmarking") exercise was the CSM Version 1.2a-g. Further background to the benchmarking exercise and the definition of the conditions for the Base Case and variant simulations are given in Appendix D.

The aims of the inter-model comparison exercise are as follows:

- To compare the predictions of three different kinetically and/or thermodynamically based reactive-transport models using a series of well-defined hypothetical base case and variant case scenarios.
- To determine the sensitivity of the extent of microbial sulfate reduction and the resulting corrosion to variability in different input parameters, conceptual model uncertainties, and to various repository design characteristics.
- To improve confidence in our understanding of, and our ability to predict, the generation and fate of sulfide in a KBS-3 style repository.

The CSM shares certain similarities with the UniBern and A-21/CT models but also differs in a number of significant respects. It is important to understand the nature of these similarities and differences when comparing the simulations from the different models. The relevant characteristics of the CSM can be summarised as follows:

- 1-D geometry.
- Arbitrary number of mass-transport layers, bounded on the left-hand side (LHS) by the canister surface and the right-hand side (RHS) by a water-bearing fracture in the host rock that maintains constant geochemical conditions.
- A total of 23 chemical and microbial species, plus temperature, are treated in the CSM Version 1.2a-g, although a number of these species were not relevant in the benchmarking exercise. Table 5-1 lists the various species and defines the corresponding notations for the respective concentrations used in the discussion below.
- Reaction scheme based on the processes considered to be most important in determining the corrosion behaviour of the canister, but which does not represent a complete mass- and charge-balance for all species present in the repository. For example, species such as calcite are not included in the model, whereas pyrite (which may react with initially trapped O_2 in the repository) is included. The near-field is considered to be buffered at a constant pH of 8. The CSM reaction scheme was not developed specifically for the ISP inter-model comparison exercise, but has been modified to the extent possible to conform with the specified input data in Appendix D.
- Mass-balance equations solved using finite-difference methods subject to various boundary conditions.
- Reactions are generally described by kinetic expressions rather than using equilibrium thermodynamics.
- Mass transport through the layers occurs by diffusion only, with the layers treated as equivalent porous media characterised by the porosity and tortuosity. Although multiple types of pore can be specified, each with an associated porosity, a single pore type was used for the benchmarking exercise. The value of the tortuosity factor was adjusted to provide the specified effective diffusivity. Diffusion coefficients are generally treated as species-specific in the CSM, but the same diffusion coefficient was used for all species as specified for the benchmarking exercise.

- Spatial and temporal variation in temperature with corresponding spatial and temporal variation in temperature-dependent parameter values. For the benchmarking exercise, a uniform temperature of 25 °C was assumed except for the two variant cases denoted Therm1 and Therm2.
- For the Base Case simulation, a total of five layers were specified corresponding to (i) a layer of precipitated Cu_2S that varies in size according to the time-dependent corrosion of the canister, (ii) a layer of compacted bentonite buffer, (iii) a layer of backfill material, (iv) a layer representing the thermally spalled rock volume around the tunnel (rock-tunnel interface RTI) or deposition hole (rock-deposition hole interface RDI), and (v) the host rock (Figure 5-1). A four-layer model was used in variant cases in which the backfill was excluded (denoted Buff0, Buff1, Buff2, IDe3, and IDe4).
- Electrochemical kinetic expressions are used as LHS boundary conditions for species participating in corrosion reactions with the imposition of a zero net-current condition to simulate a freely corroding system. These boundary conditions permit the prediction of the corrosion potential (E_{CORR}) and the corrosion rate (as a corrosion current density i_{CORR}).
- The CSM code runs rather rapidly with a typical execution time of 10–30 minutes for a simulation period of 10^6 a using a 4-core, 2.6 GHz CPU.

Table 5-1. Summary of the various species considered in the CSM Version 1.2a-g and the corresponding notation for the respective concentrations.

Notation*	Species	Species Name
c_A	$O_2(g)$	Gaseous oxygen
c_0	$O_2(aq)$	Dissolved oxygen
c_1	$CuCl_2^-(aq)$	Dissolved cuprous chloride complex ion
c_2	$Cu_2O(s)$	Precipitated cuprous oxide
c_3	$Cu^{2+}(aq)$	Dissolved cupric ions
c_4	$CuCl_2{\cdot}3Cu(OH)_2(s)$	Precipitated basic cupric chloride
c_5	Cu(II)(ads)	Adsorbed cupric species
c_6	$Cl^-(aq)$	Dissolved chloride ions
c_7	Fe(II)(aq)	Dissolved ferrous ions
c_8	FeS(s)	Precipitated ferrous sulfide
c_9	$HS^-(aq)$	Dissolved sulfide ions
c_{10}	$FeS_2(s)$	Pyrite
c_{11}	$SO_4^{2-}(aq)$	Sulfate ions
c_{12}	$H_2(aq)$	Dissolved H_2
c_{13}	$H_2(g)$	Gaseous H_2
c_{14}	$Cu_2S(s)$	Precipitated Cu_2S
c_{15}	$CaSO_4{\cdot}2H_2O$	Gypsum
c_{16}	-	Dissolved organic matter (DOM)**
c_{17}	-	Solid organic matter (SOM)
c_{18}	-	Biotite
c_{19}	$FeCO_3(s)$	Iron carbonate
B_1	SRB_1	Organotrophic SRB
B_2	SRB_2	Chemotrophic SRB
T	-	Temperature

* In the CSM, the concentrations of dissolved and solid species are referred to unit volume of either the pore water or of the entire system (pores plus solids), respectively. The concentration of adsorbed Cu(II) (c_5) is defined per unit mass of adsorbent. The SRB populations (B_1 and B_2) are expressed in terms of g_{cells} per unit volume of pore water. Although not relevant for the ISP benchmarking exercise, the concentration of gaseous species is referred to unit volume of unsaturated pores.

** For mass-balance purposes, the DOM is assumed to be represented by acetate.

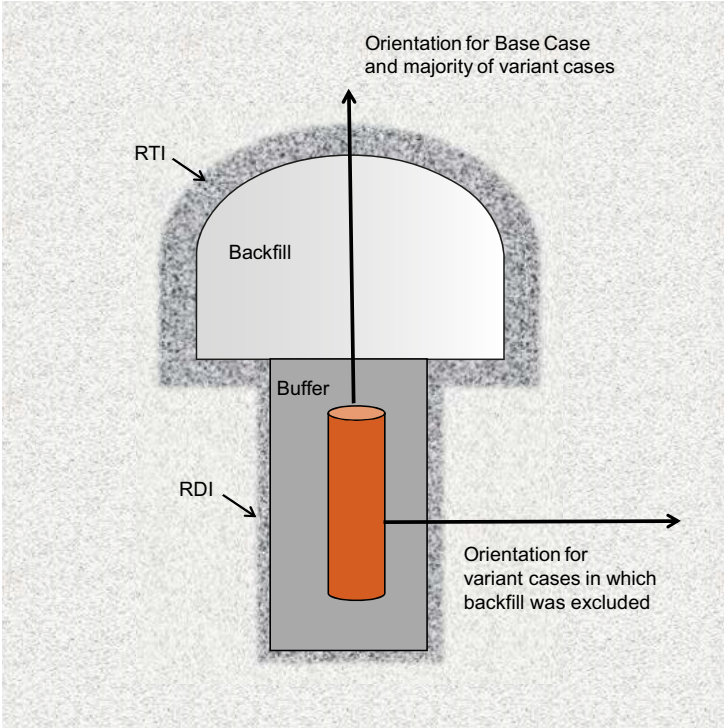

Figure 5-1. *Figure illustrating the orientations assumed for the CSM 1-D simulations for the Base Case and the majority of variant cases and, alternatively, for the variant cases in which the backfill was excluded.*

5.2 Definition of Base Case and variants

It is important to bear in mind that the Base Case and variant analyses represent hypothetical scenarios that have been defined primarily to determine the sensitivity of the system to various factors and to allow inter-model comparison.

The Base Case and variant cases specified in Appendices D1 and D2, respectively, were implemented using a set of constant and a set of layer-dependent input parameters. The set of constant input parameter values were used for all simulations, except where specifically noted in the text, and are listed in Appendix D3. The different variants were primarily simulated by changing values of various layer-dependent input parameters, as described in more detail below.

5.2.1 Definition of Base Case

The Base Case simulation for the benchmarking exercise differs from the conditions used for the best-estimate analysis described in Section 4 in a number of ways, including:

- No initial aerobic phase.
- Constant temperature of 25 °C.
- Fully saturated conditions at all times.
- Constant microbial population.

In addition to the constant input parameters defined in Appendix D3, a number of layer-dependent parameters are defined for the Base Case and variants. Table 5-2 summarises the layer-dependent parameters for the Base Case simulation, their values, and a brief definition for each parameter. Many of these values are defined in the specifications for the Base Case in Appendix D1, while a number of others are derived, including:

- The thickness of the buffer and backfill materials is defined by the ratio of the buffer or backfill volume to the surface area of the canister (Appendix D1). Generally, the volume:surface area ratio is used to conserve the correct initial O_2 inventory when considering aerobic conditions (not included in the benchmarking exercise). One consequence of using the volume:surface area ratio, however, is that the effective lengths of the buffer and backfill layers used here differ from the geometric dimensions used by A-21/CT for their 1-D simulations. For example, for the Base Case simulation, the thickness of the buffer and backfill layers used for the CSM calculations were 0.83 m and 6.0 m, respectively. In comparison, the corresponding thicknesses for the 1-D model used by A-21/CT were 2.5 m and 4.4 m, respectively. Thus, the distance between the canister surface and the source of sulfide (the RTI) is approximately the same for both models.
- All porosity is assumed to be accessible and to contribute to diffusive mass transport (i.e., there are no isolated or dead-end pores).
- Microbial activity is only allowed in the rock-tunnel interface region (layer 7).
- The values of the tortuosity factor "tau" were adjusted to give the effective diffusivities defined in Appendix D1.
- Input files related to the spatial and temporal variation in temperature and saturation were not defined for the Base Case simulation.

5.2.2 Definition of variant cases

A number of variant cases were defined for each modelling group, as summarised in Appendix D2. Table 5-3 gives the nomenclature for each of the variant cases run using the CSM V1.2a-g and provides a brief description of each case.

5.2.2.1 Buffer density

Three variant cases were run to examine the effects of excluding the backfill material and modifying the properties of the buffer to permit microbial activity. For a 1-D model, these variants can also be used to represent a mass-transport path horizontal to the deposition hole, compared with the vertical path implicit in the Base Case simulation.

The three buffer variants were (Table 5-3):

- Buff0 – essentially a reference case for the horizontal transport path. As for the Base Case, no microbial activity is allowed in the buffer material. Removal of the backfill layer has the effect of reducing the amount of available organic material to support microbial activity and removes all siderite from the system. The location of microbial activity (in this case, the rock-deposition hole interface) is also moved closer to the canister. The population of both organotrophic and chemotrophic SRB is assumed to be 6.01×10^{-3} $g_{cells} \cdot dm^{-3}$ (based on 2.4×10^{8} cells/dm^3 sessile plus 3×10^{5} cells/dm^3 planktonic, for a total of 2.403×10^{8} cells/dm^3 of rock or 1.20×10^{10} cells/dm^3 of pore water based on 2 % porosity of the RDI. A cell mass of 5×10^{-13} g/cell is assumed).
- Buff1 – microbial activity is permitted in the buffer and an SRB population is assumed (B1 = B2 = 1×10^{-4} g_{cells} dm^{-3}). This variant simulates the effect of the loss of buffer density on microbial activity, but no changes were made to the mass-transport properties or compostion of the buffer.
- Buff2 – buffer is assumed to be absent (as well as the backfill), with the layer properties identical to those of the ground water. Thus, microbial activity is possible ($S_{MIC} = 0$) but, although SRB are assumed to be present in the deposition hole (B1 = B2 = 1×10^{-5} g_{cells} dm^{-3}, based on 20 % of the total planktonic microbial population of 10^{-8} cells dm^{-3} and a cell mass of 5×10^{-13} g/cell), there is no source of organic material in the model. The porosity and tortuosity factor were both set to 1. This extreme variant essentially simulates the unlikely situation of missing buffer.

For these three buffer variants, the thickness of the interface zone in which microbial activity is possible (RDI) is 0.1 m, rather than 0.3 m used for the RTI. The buffer thickness of 0.83 m used in the Base Case (determined from the buffer volume:canister surface area ratio) was also used for the various Buff variant cases.

5.2.2.2 Backfill density

Two backfill variant cases were used to simulate the effect of allowing microbial activity in the backfill with different initial microbial populations. The two backfill variants are:

- Back1 – microbial activity is allowed in the backfill (by setting $S_{MIC} = 0$ for the backfill layer). For this first variant case, a relatively high backfill SRB population was assumed (B1 = B2 = 1×10^{-4} g_{cells} dm^{-3}).
- Back2 – identical to Back1, except for a lower SRB population, arbitrarily taken to be one tenth of that in Back1 (B1 = B2 = 1×10^{-5} g_{cells} dm^{-3}).

For a 1-D model, permitting microbial activity in the backfill as well as the RTI shortens the distance between the source of sulfide and the canister.

Table 5-2. Definition of the layer-dependent input parameters for the Base Case simulation.

Parameter	Layer 1	Layer 2	Layer 3	Layer 4	Layer 5	Units	Definition
	Cu_2S film	Bent	Back	RTI	Rock		Name of medium
L	variable	8.31	59.8	3	50	dm	Thickness of layer
epsE	0.1	0.43	0.43	0.01	0.005	unitless	Effective porosity of medium
epsS	0	0	0	0	0	unitless	Storage porosity of medium
epsN	0	0	0	0	0	unitless	Porosity inaccessible to diffusant in medium
rho	5.6	2.7	2.7	2.7	2.7	$kg \cdot dm^{-3}$	Particle density of medium
S_MIC	1	1	1	0	1	unitless	Threshold saturation above which microbial activity is permitted in the medium
c5max	0	0.395	0.235	0	0	mol/kg	Maximum value of Cu(II)(ads) in medium
AP	0	0.564	1.65	0	0	dm^{-1}	Surface area of exposed pyrite per unit volume in medium
tau	0.1	0.05	0.05	0.05	0.04	unitless	Tortuosity factor of medium
k9room	0	0	0	0	0	s^{-1}	Aerobic microbial activity rate in medium
c6init	-	0.2223	0.17601	0.1131	0.1131	$mol \cdot dm^{-3}$	Initial pore-water concentration of Cl^- in medium
c7init	-	1.10×10^{-05}	1.80×10^{-05}	5.70×10^{-06}	5.70×10^{-06}	$mol \cdot dm^{-3}$	Initial pore-water concentration of Fe(II) in medium
c9init	-	1.2×10^{-06}	6×10^{-07}	0	0	$mol \cdot dm^{-3}$	Initial pore-water concentration of HS^- in medium
cPinit	-	0.0393	0.115	0	0	$mol \cdot dm^{-3}$	Initial concentration of pyrite in medium
cSinit	-	0.0094	0.0185	0	0	$mol \cdot dm^{-3}$	Initial pore-water concentration of sulfate in medium
c12init		0	0	0	0	$mol \cdot dm^{-3}$	Initial pore-water concentration of dissolved H_2 in medium
AF	0	0	0	0	0	dm^{-1}	Surface area of exposed biotite per unit volume in medium
c15init	-	0.0365	0.19	0	0	$mol \cdot dm^{-3}$	Initial concentration of gypsum in medium
c16init	-	8.33×10^{-05}	8.33×10^{-05}	0	0	$mol \cdot dm^{-3}$	Initial pore-water concentration of DOM in medium
c17init	-	0.0654	0.0717	0	0	$mol \cdot dm^{-3}$	Initial concentration of SOM in medium
c18init	-	0	0	0	0	$mol \cdot dm^{-3}$	Initial concentration of biotite in medium
c19init		0	0.163	0	0	$mol \cdot dm^{-3}$	Initial concentration of $FeCO_3$ in medium
B1	-	0	0	4.01×10^{-03}*	0	$g_{cells}\ dm^{-3}$	Pore-water concentration of organotrophic SRB in medium
B2	-	0	0	4.01×10^{-03}*	0	$g_{cells}\ dm^{-3}$	Pore-water concentration of chemotropic SRB in medium
S_in	Not defined	Not defined	Not defined	Not defined	Not defined	Not defined	Name of file with degree of saturation of medium as function of time
K_in	K1_in	Kbent_in	Kback_in	Krock_in	Krock_in		Name of file with thermal conductivity ($W \cdot dm^{-1}\ K^{-1}$) of medium as function of S
Cp	845	830	845	728	728	$J\ K^{-1}\ kg^{-1}$	Particle specific heat of medium

* Based on 8×10^7 cells/dm^3 sessile plus 1×10^5 cells/dm^3 planktonic, for a total of 8.01×10^7 cells/dm^3 of rock or 8.01×10^9 cells/dm^3 of pore water based on 1 % porosity of the RTI. In turn, this is equivalent to 4.01×10^{-3} g_{cells} dm^{-3} for a cell mass of 5×10^{-13} g/cell. The populations of organotrophs and chemotrophs are assumed to be the same.

Table 5-3. Summary of Base Case and variant simulations run using the CSM Version 1.2a-g.

Run	Comment
Base Case	Base Case simulation
Buff0	No backfill, no microbial activity in buffer
Buff1	No backfill, microbial activity allowed in buffer
Buff2	No backfill, buffer replaced initially by groundwater
Back1	Microbial activity allowed in backfill, high initial biomass
Back2	Microbial activity allowed in backfill, low initial biomass
IDe1	10 x higher RTI* diffusivity
IDe2	100 x higher RTI diffusivity
IDe3	No backfill, 10 x higher RDI* diffusivity
IDe4	No backfill, 100 x higher RDI diffusivity
ORG1	Decrease SOM** content of buffer and backfill by 10 x
ORG2	Decrease half-life of SOM by 10 x
ORG3	Decrease half-life of SOM by 100 x
Fe1	Siderite added to buffer
Fe2	Double the siderite content in backfill
Fe3	Siderite added to buffer and double content in backfill
Fe4	Siderite absent from all layers
Therm1	Spatial and temporal variation in temperature, maximum canister temperature 75 °C
Therm2	Spatial and temporal variation in temperature, maximum canister temperature 97 °C
GW1	Sulfate added to groundwater and (initially) to the RTI and rock layers
GW2	DOM*** added to groundwater and (initially) to the RTI and rock layers
GW3	Sulfide added to groundwater and (initially) to the RTI and rock layers
K1	10 x faster organotrophic sulfate reduction
K2	10 x faster chemotrophic sulfate reduction
K3	10 x faster organotrophic and chemotrophic sulfate reduction
Fine RTI	Fine spatial grid in RTI
Finer RTI	Finer spatial grid in RTI

* RTI rock-tunnel interface, RDI rock-deposition hole interface.

** SOM solid (undissolved) organic matter.

*** DOM dissolved organic matter.

5.2.2.3 Interface diffusivity

The rock-tunnel (RTI) and rock-deposition hole (RDI) interfaces represent the only locations where microbial sulfate reduction is assumed to occur in the Base Case simulation. An increased diffusivity in the interface regions would allow faster supply of electron acceptors and nutrients, as well as faster removal of sulfide ions. The variant cases considered effective diffusivities either 10 times or 100 times higher than for the Base Case. Separate simulations were performed for increased diffusivity in the RTI and in the RDI (in which case the backfill was also removed and a reduced number of layers was used, Figure 5-1). Because the same bulk-solution diffusion coefficient is used for all layers in the CSM (and then modified by the porosity and tortuosity factor to derive an effective diffusivity), the effective diffusivity in the interface was increased by artificially increasing the tortuosity factor for the interface layer. In this way, neither the porosity of the interface layer nor the diffusivity in other layers was affected.

The four variant cases involving increased diffusivity in the interface regions were as follows:

- IDe1 – effective diffusivity in the RTI of 5×10^{-12} m^2 s^{-1}, a factor of ten higher than for the Base Case.
- IDe2 – effective diffusivity in the RTI of 5×10^{-11} m^2 s^{-1}, a factor of 100 higher than for the Base Case.
- IDe3 – effective diffusivity in the RDI of 1.5×10^{-11} m^2 s^{-1}, a factor of ten higher than for variant Buff0. The RDI thickness was defined as 0.1 m. In addition, the backfill layer was removed from the model.
- IDe4 – effective diffusivity in the RDI of 1.5×10^{-10} m^2 s^{-1}, a factor of 100 higher than for for variant Buff0. The RDI thickness was defined as 0.1 m. In addition, the backfill layer was removed from the model.

5.2.2.4 Organic matter

Various factors impact the availability of the organic material required to support organotrophic sulfate reduction. For the Base Case, both dissolved and solid organic material is assumed to be present initially in the buffer and backfill materials. The dissolved organic material (assumed for mass-balance purposes to be in the form of acetate), is consumed by microbial activity and is replaced by dissolution of the solid organic material. Dissolution of SOM is assumed to follow first-order kinetics with a rate constant (for the Base Case) equivalent to a half-life of 10 a. The organic material present in the buffer and backfill is clearly poorly-soluble (otherwise it would already have been consumed by microbial activity), but the extent of its availability is uncertain. The assumed half-life of 10 a was chosen to not only represent the recalcitrant nature of the organics but also to reflect the fact that both elevated temperature and irradiation increase the bioavailability of organic material in bentonite (Stroes-Gascoyne et al. 1997, Vilks et al. 1998). The assumed half-life was varied in a series of sensitivity analyses.

Three variant cases were carried out related to the amount and availability of SOM:

- ORG1 – the initial amount of SOM in the buffer and backfill was reduced by a factor of ten from that in the Base Case.
- ORG2 – the rate of dissolution of SOM was reduced by a factor of ten compared with the Base Case by setting $k_{14} = 2.2 \times 10^{-10}$ s^{-1}, leading to an SOM "half-life" of 100 a.
- ORG3 – the rate of dissolution of SOM was reduced by a factor of 100 compared with the Base Case by setting $k_{14} = 2.2 \times 10^{-11}$ s^{-1}, leading to an SOM "half-life" of 1 000 a.

5.2.2.5 Fe(II) minerals

As shown by the results of the best-estimate simulation in Section 4, the presence of Fe(II) in the system acts as an effective sink for sulfide in the form of mackinawite precipitation. The major source of Fe(II) in the Base Case simulation is siderite ($FeCO_3$) present in the backfill, with the buffer assumed to contain no siderite.

Four variant cases were performed to assess the impact of various concentrations and distributions of siderite within the buffer and backfill materials, as follows:

- Fe1 – siderite was added to the buffer at a concentration equivalent to 0.5 wt%.
- Fe2 – the amount of siderite in the backfill was doubled compared with the Base Case to a concentration equivalent to 2.2 wt%.
- Fe3 – siderite was added to the buffer (0.5 wt%) and the amount in the backfill doubled to 2.2 wt%.
- Fe4 – siderite was removed from the backfill, so that the only source of Fe(II) in the system is that initially present in the pore water and that in the ground water.

5.2.2.6 Thermal effects

The Base Case simulation was run assuming isothermal conditions of 25 °C. In reality, the decay heat from the spent fuel inside the canister will result in elevated temperatures in the near-field for a period of approximately 20 000 a post-closure. The CSM was developed from the outset to account for the effects of spatial and temporal variations in temperature and, therefore, incorporates a heat-conduction equation which is solved within the code to predict the evolution of temperature subject to user-defined time-dependent temperatures at the left-hand (i.e., the canister surface) and right-hand (i.e., the host rock) boundaries of the model. The thermal conductivity of the various materials in the repository are generally dependent on the degree of saturation, but values for fully saturated conditions were used here for the benchmarking variant cases. By taking into account the spatial and temporal variation in temperature, the values for all of the temperature-dependent parameters (such as diffusion coefficients, rate constants, solubilities, electrochemical potentials, etc) also become spatially and temporally variable. The temperature dependence of these parameters is typically described by an Arrhenius-type expression and an associated activation energy (Appendix C), although standard electrochemical potentials exhibit a linear dependence on temperature.

The general shape of the evolution of the canister surface temperature is well-established from various international nuclear waste management programmes (Åkesson et al. 2010, King et al. 2017a, Pastina and Hellä 2006).

Two variant cases were considered, as follows:

- Therm1 – maximum canister temperature of 75 °C.
- Therm2 – maximum canister surface temperature of 97 °C.

The time dependence of the canister temperatures for these two variant cases are shown in Figure 5-2. A similar time dependence was used for the temperature of the rock at the right-hand boundary of the model, but with a peak value of 40.5 °C for both cases falling to a long-term background temperature of 10.5 °C. These bounding values are used to solve a heat-conduction equation (Equation (2-14)), with the precise time- and spatial-dependence of the temperature dependent upon the thermal properties of the different media.

5.2.2.7 Groundwater composition

In the CSM, the ground water composition defines the concentration of various species at the RHS boundary and the initial concentrations in the interface and rock layers. Three different variant cases were performed to examine the impact of adding different species to the ground water, as follows:

- GW1 – 0.0048 mol·dm^{-3} (460 mg/L) sulfate ions were added to the ground water (and initially to the interface and rock layers).
- GW2 – 0.000417 mol·dm^{-3} (25 mg/L) DOM (as acetate) was added to the ground water (and initially to the interface and rock layers).
- GW3 – 6.3×10^{-7} mol·dm^{-3} (0.02 mg/L) sulfide ions were added to the ground water (and initially to the interface and rock layers). This variant was performed to determine the effect of an additional source of sulfide, with the [HS^-] given by the composition of the reference brackish groundwater in Table 6-3 of Hellä et al. (2014).

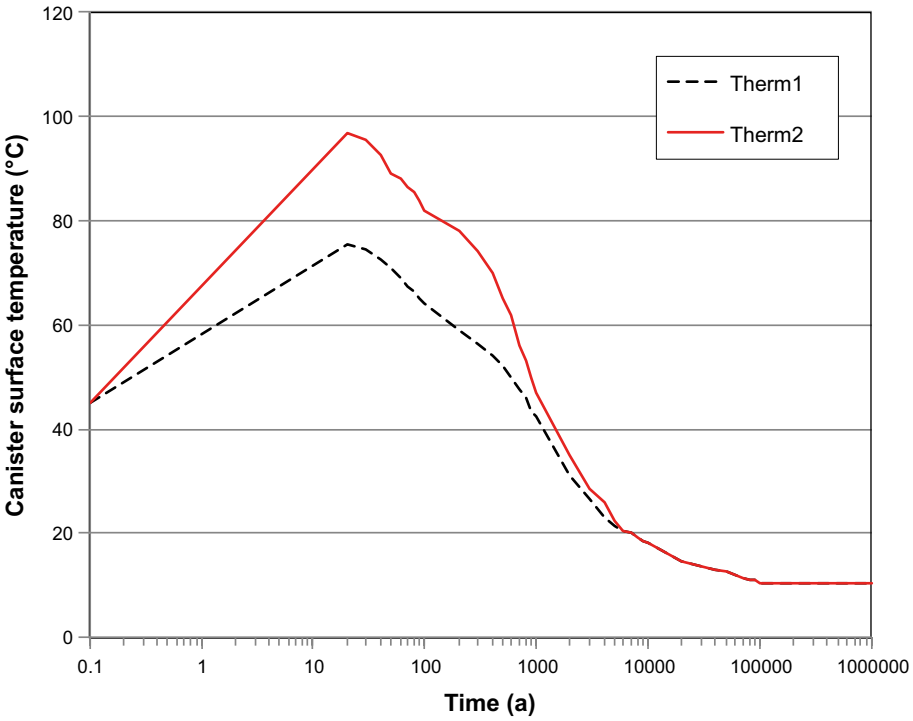

Figure 5-2. *Canister surface temperature profiles used for variant cases Therm1 and Therm2.*

5.2.2.8 Kinetic rates

To examine the sensitivity towards the value of the specific Monod reaction rate constants for organotrophic and chemotrophic sulfate reduction (v1max and v2max, respectively, Appendix D3), three variant cases were run, as follows:

- K1 – increase the rate constant for organotrophic sulfate reduction by a factor of ten (v1max = 1.3×10^{-5} mol g_{cells}^{-1} s^{-1}).
- K2 – increase the rate constant for chemotrophic sulfate reduction by a factor of ten (v2max = 5.7×10^{-6} mol g_{cells}^{-1} s^{-1}).
- K3 – increase the rate constants for both the organotrophic and chemotrophic reduction of sulfate by a factor of ten (v1max = 1.3×10^{-5} mol g_{cells}^{-1} s^{-1}, v2max = 5.7×10^{-6} mol g_{cells}^{-1} s^{-1}).

5.2.2.9 Fineness of the interface grid spacing

For the Base Case, microbial activity is restricted to the rock-tunnel interface zone. The CSM uses a geometrical progression to define the spacing between grid points on the basis that concentration gradients are steepest closest to the canister and decrease with increasing distance. Therefore, to avoid computational penalties from using a uniformly spaced grid, the distance between grid points is increased the further away from the canister. However, since the rock-tunnel interface is located some distance form the canister, this may result in the interface zone being represented by a relatively small number of grid points. Because of concerns with mesh size effects for the A-21/CT model (Andrés Idiart, private communication, October 2017), it was decided to examine the sensitivity of the results to the grid spacing in the interface region.

For the Base Case simulation, the interface region is defined by 33 intervals with an average spacing of 0.0091 m (total thickness of rock-tunnel interface zone 0.3 m). Two variant cases were run with the following characteristics:

- Fine RTI – 48 intervals, average spacing 0.0063 m.
- Finer RTI – 104 intervals, average spacing 0.0029 m.

5.3 Results of simulations

Selected results from the Base Case and variant simulations are summarised in Table 5-4 and Table 5-5. Table 5-4 summarises the depth of corrosion, the percentage of sulfide precipitated as mackinawite, and the fraction of remaining organic material and gypsum after simulation times of 10^5 a and 10^6 a. Table 5-5 lists the amount of different species present in the model system after a simulation time of 10^5 a. Because the CSM is 1-D, the inventories in Table 5-5 are given in units of mol dm^{-2} for chemical species and g_{cells} dm^{-2} for the two types of SRB.

5.3.1 Base Case

The Base Case took a total of 74 minutes 6 s of CPU time to run for a simulated period of 10^6 years. A total of 981 time steps were used for the solution, ranging in intervals from 10^{-5} s to 388 years. Time steps were incremented according to a geometric progression subject to maximum limits on the change of concentration of the different species in the model. The maximum change in concentration of any species in any time step was 5×10^{-4} mol/dm^3. Profiles were plotted at 43 time intervals from 12 hours to 10^6 years.

5.3.1.1 Corrosion

The predicted corrosion behaviour of the canister for the Base Case simulation is illustrated in Figure 5-3 to Figure 5-5. The predicted time-dependence of the corrosion potential is shown in Figure 5-3 for a simulation period of 10^6 a. The negative values of E_{CORR} in the range −0.90 to −0.95 V_{SCE} are consistent with the anodic sulfidation of the canister to form Cu_2S supported by the cathodic reduction of the proton in the HS^- ion. However, the corrosion rate is very low (of the order of 0.01 nm/a) as the flux of HS^- to the canister surface is small (Figure 5-5).

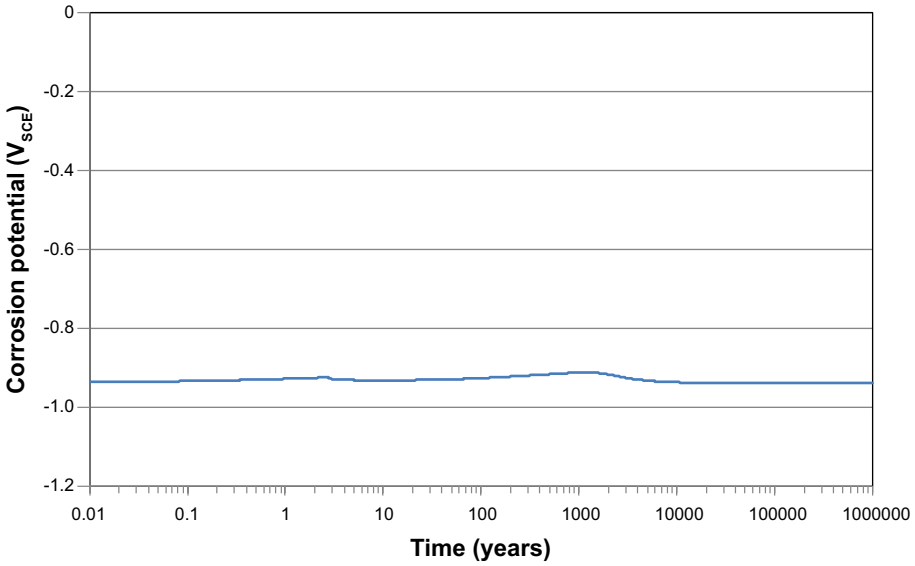

Figure 5-3. *Time dependence of the corrosion potential (E_{CORR}) of the canister for the Base Case simulation.*

Figure 5-4 shows the time dependence of the depth of corrosion and of the growth of the surface Cu_2S film. The linear dependence indicates a constant anaerobic corrosion rate (of the order of 0.008 nm a^{-1}) and is consistent with a transport-limited corrosion process. The flux of HS^- at the canister surface is small initially (Figure 5-5), but after 10 000 a reaches a constant value of approximately 10^{-6} mol m^{-2} a^{-1}. The sulfide flux up to 1 000 a is due to the HS^- initially in the pores of the buffer and backfill materials, with the subsequent increase due to the arrival of SRB-produced sulfide from the RTI.

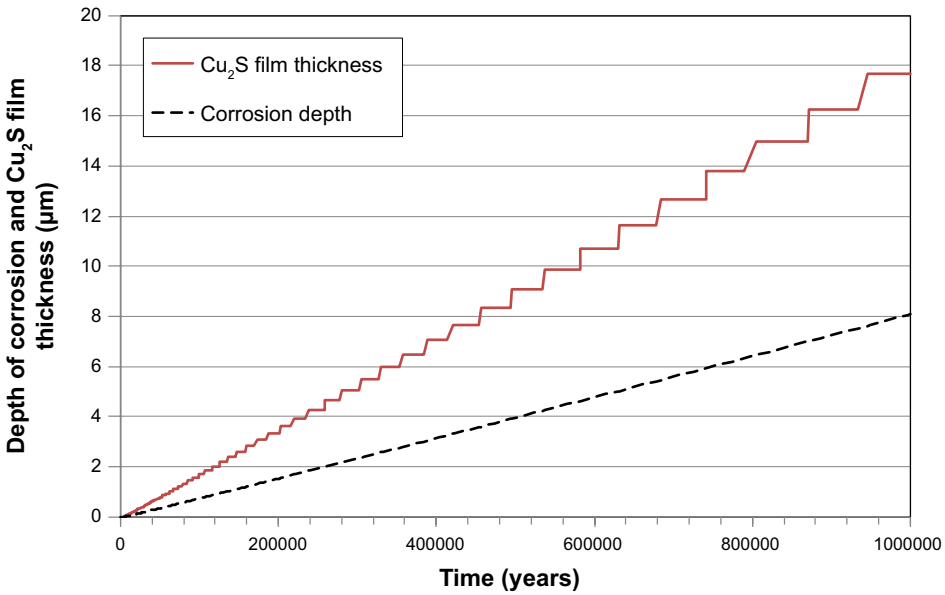

Figure 5-4. *Time dependence of the depth of corrosion and of the Cu_2S film thickness for the Base Case simulation. The stepwise nature of the film thickness is an artefact of the manner in which film growth is treated in the code.*

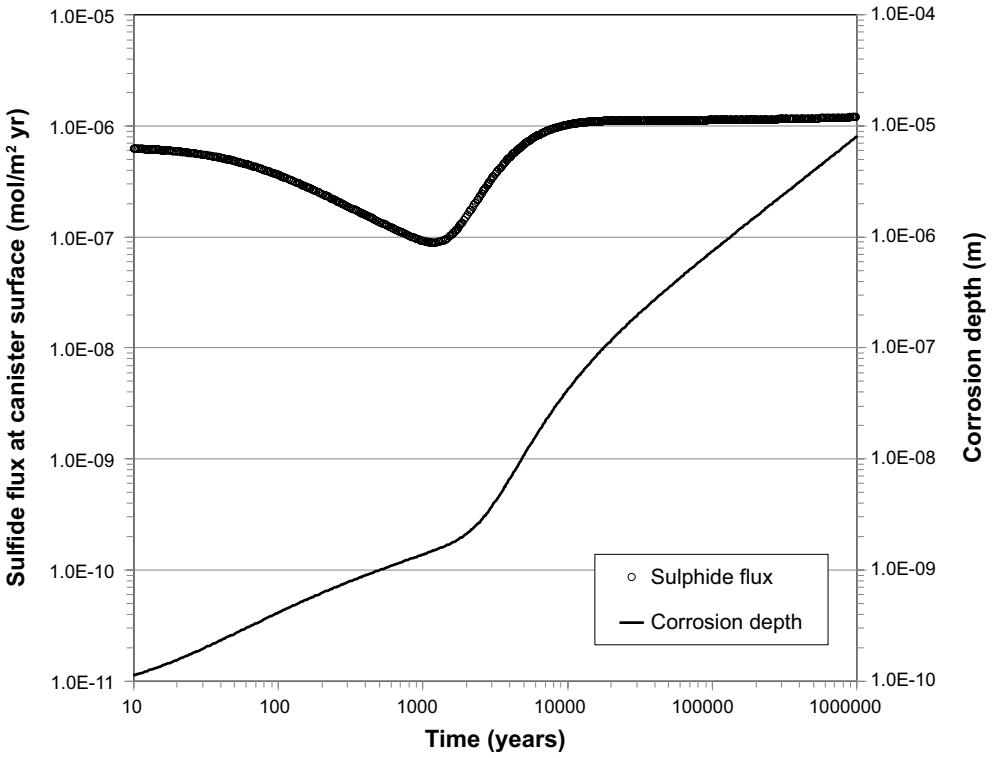

Figure 5-5. *Predicted time dependence of the sulfide flux to the canister surface and the depth of corrosion up to 1 000 000 a for the Base Case simulation.*

The source of HS^- is the microbial sulfate reduction in the RTI and Figure 5-6 shows the total extent of both organotrophic and chemotrophic pathways up to 10^6 a in terms of the amount of sulfide produced. Organotrophic sulfate reduction is the predominant pathway, producing > 99 % of the total HS^- after 10^6 a. Approximately 83 % of the initial inventory of organic material remains after 10^6 a (Figure 5-7, Table 5-4) suggesting that the availability of organics is not a limiting factor for the Base Case conditions. Neither does the availability of sulfate limit the extent of microbial sulfide production since the gypsum inventory is hardly diminished over the entire simulation period of 10^6 a (Figure 5-8, Table 5-5).

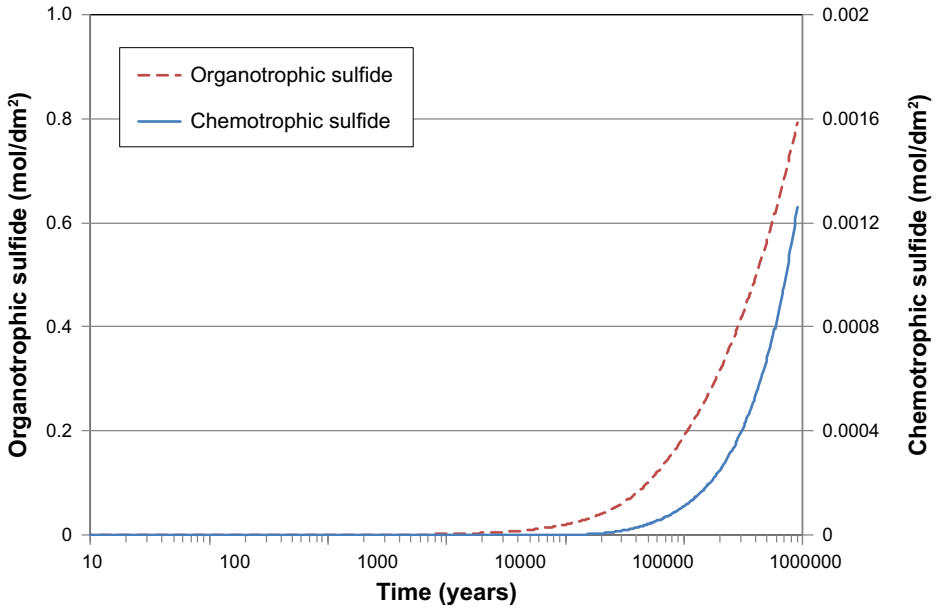

Figure 5-6. *Cumulative amount of organotrophic and chemotrophic sulfate reduction as a function of time for the Base Case simulation.*

Table 5-4. Summary of the depth of corrosion, fraction of sulfide precipitated as mackinawite, and percentage of remaining organic material and gypsum after 10^5 years and 10^6 years for the Base Case and variant cases.

Case	Comment	10^5 years				10^6 years			
		Corrosion depth (µm)	% sulfide as FeS	% total organics remaining	% gypsum remaining	Corrosion depth (µm)	% sulfide as FeS	% total organics remaining	% gypsum remaining
Base Case	Base Case simulation	0.75	99.5	96.0	98.7	8.09	99.0	82.6	91.7
Buff0	No backfill, no microbial activity in buffer	197	0.2	55.0	0	224	0.2	48.8	0
Buff1	No backfill, microbial activity allowed in buffer	237	0	46.1	0	237	0	45.9	0
Buff2	No backfill, buffer replaced initially by groundwater	0	0	0	0	0	0	0	0
Back1	Microbial activity allowed in backfill, high initial biomass	46	98.6	6.0	61.4	108	96.9	0	57.3
Back2	Microbial activity allowed in backfill, low initial biomass	44	98.7	6.1	61.4	106	96.9	0	57.3
IDe1	10 x higher RTI diffusivity	0.76	99.7	94.8	98.2	8.13	99.0	81.7	91.3
IDe2	100 x higher RTI diffusivity	0.76	99.7	94.6	98.1	8.14	99.0	81.5	91.2
IDe3	No backfill, 10x higher RDI diffusivity	205	0.6	53.3	0	225	0.9	48.7	0
IDe4	No backfill, 100x higher RDI diffusivity	205	0.7	53.2	0	225	1.0	48.6	0
ORG1	Decrease SOM content of buffer and backfill by 10 x	0.75	98.5	82.6	99.6	7.88	95.9	42.1	96.5
ORG2	Decrease half-life of SOM by 10 x	0.75	98.8	97.9	99.5	8.03	98.5	83.7	92.2
ORG3	Decrease half-life of SOM by 100 x	0.74	96.7	99.2	100.1	7.85	96.9	92.5	95.8
Fe1	Siderite added to buffer	0.75	99.3	96.0	98.7	8.09	98.5	82.6	91.7
Fe2	Double the siderite content in backfill	0.58	99.5	96.0	98.7	6.17	98.9	82.6	91.7
Fe3	Siderite added to buffer and double content in backfill	0.58	99.5	96.0	98.7	6.17	98.9	82.6	91.7
Fe4	Siderite absent from all layers	126	0.5	96.0	98.6	663	0.5	82.6	90.7
Therm1	T(x,t), maximum canister temperature 75 °C	0.37	99.6	96.4	99.2	3.36	100.2	84.6	93.4
Therm2	T(x,t), maximum canister temperature 97 °C	0.37	99.6	96.3	99.2	3.36	100.1	84.6	93.4
GW1	Sulfate added to groundwater and (initially) rock layers	0.75	99.3	96.0	98.8	8.09	98.5	82.6	92.2
GW2	DOM added to groundwater and (initially) rock layers	0.75	99.3	96.0	98.7	8.09	98.5	82.6	91.7
GW3	Sulfide added to groundwater and (initially) rock layers	0.75	99.5	96.0	98.7	8.09	99.3	82.6	91.7
K1	10 x faster organotrophic sulfate reduction	0.76	99.5	94.6	98.1	8.14	98.6	81.6	91.3
K2	10 x faster chemotrophic sulfate reduction	0.75	99.3	96.0	98.7	8.09	98.5	82.6	91.7
K3	10 x faster organotrophic and chemotrophic sulfate reduction	0.76	99.5	94.6	98.1	8.14	98.6	81.6	91.3
Fine RTI	Fine spatial grid in RTI	0.75	99.3	95.8	98.6	8.09	98.5	82.6	91.7
Finer RTI	Finer spatial grid in RTI	0.75	99.4	95.3	98.4	8.11	98.6	82.3	91.6

Table 5-5. Inventories* of various species remaining in the model system after 10^5 years.

Run	Fe(II)aq	FeS	HS^-	Pyrite	SO_4^{2-}	H_2	Gypsum	DOM	SOM	Siderite	Org. SRB	Chemo. SRB
Base Case	3.88E−06	0.190	0.00020	7.20	0.45	8.19E−05	11.52	0.00239	4.64	9.57	0.00012	0.00012
Buff0	4.02E−08	0.001	0.00053	0.33	0.04	1.86E−04	0.00	0.00022	0.30	0.01	0.00012	0.00012
Buff1	3.85E−07	0.000	0.00000	0.33	0.00	1.42E−03	0.00	0.00031	0.25	0.01	0.00048	0.00048
Buff2	8.59E−07	0.000	0.00000	0.00	0.00	0.00E+00	0.00	0.00000	0.00	0.01	0.00020	0.00020
Back1	3.24E−06	4.489	0.00043	7.20	0.45	2.88E−05	7.16	0.00022	0.29	5.27	0.00269	0.00269
Back2	3.25E−06	4.487	0.00043	7.20	0.45	2.85E−05	7.16	0.00022	0.29	5.27	0.00038	0.00038
IDe1	3.87E−06	0.252	0.00020	7.20	0.45	8.22E−05	11.45	0.00237	4.58	9.51	0.00012	0.00012
IDe2	3.86E−06	0.262	0.00020	7.20	0.45	8.21E−05	11.44	0.00236	4.57	9.50	0.00012	0.00012
IDe3	4.06E−08	0.002	0.00052	0.33	0.03	1.82E−04	0.00	0.00022	0.29	0.01	0.00012	0.00012
IDe4	4.04E−08	0.002	0.00052	0.33	0.03	1.82E−04	0.00	0.00022	0.29	0.01	0.00012	0.00012
ORG1	3.92E−06	0.083	0.00018	7.20	0.45	8.11E−05	11.62	0.00223	0.40	9.67	0.00012	0.00012
ORG2	3.91E−06	0.102	0.00019	7.20	0.45	8.12E−05	11.60	0.00229	4.73	9.66	0.00012	0.00012
ORG3	3.93E−06	0.036	0.00018	7.20	0.45	8.06E−05	11.67	0.00191	4.79	9.72	0.00012	0.00012
Fe1	3.94E−06	0.190	0.00020	7.20	0.45	8.19E−05	11.52	0.00239	4.64	10.13	0.00012	0.00012
Fe2	4.88E−06	0.190	0.00015	7.20	0.45	6.34E−05	11.52	0.00239	4.64	19.38	0.00012	0.00012
Fe3	4.93E−06	0.190	0.00015	7.20	0.45	6.34E−05	11.52	0.00239	4.64	19.94	0.00012	0.00012
Fe4	8.09E−08	0.001	0.02868	7.20	0.45	1.46E−02	11.50	0.00239	4.64	0.01	0.00012	0.00012
Therm1	3.84E−06	0.176	0.00015	7.20	0.42	4.68E−05	11.57	0.00236	4.65	9.58	0.00012	0.00012
Therm2	3.84E−06	0.176	0.00015	7.20	0.42	4.68E−05	11.57	0.00236	4.65	9.58	0.00012	0.00012
GW1	3.88E−06	0.190	0.00020	7.20	0.45	8.19E−05	11.52	0.00239	4.64	9.57	0.00012	0.00012
GW2	3.88E−06	0.190	0.00020	7.20	0.45	8.19E−05	11.52	0.00245	4.64	9.57	0.00012	0.00012
GW3	3.88E−06	0.190	0.00020	7.20	0.45	8.19E−05	11.52	0.00239	4.64	9.57	0.00012	0.00012
K1	3.86E−06	0.260	0.00020	7.20	0.45	8.25E−05	11.45	0.00236	4.57	9.50	0.00012	0.00012
K2	3.88E−06	0.190	0.00020	7.20	0.45	8.16E−05	11.52	0.00239	4.64	9.57	0.00012	0.00012
K3	3.86E−06	0.260	0.00020	7.20	0.45	8.21E−05	11.45	0.00236	4.57	9.50	0.00012	0.00012
Fine RTI	3.88E−06	0.200	0.00020	7.20	0.45	8.21E−05	11.51	0.00239	4.63	9.56	0.00012	0.00012
Finer RTI	3.87E−06	0.224	0.00020	7.20	0.45	8.25E−05	11.48	0.00238	4.61	9.53	0.00012	0.00012

* Inventories are in units of mol dm^{-2}, except for the two SRB species which are in units of $g_{cells}\ dm^{-2}$.

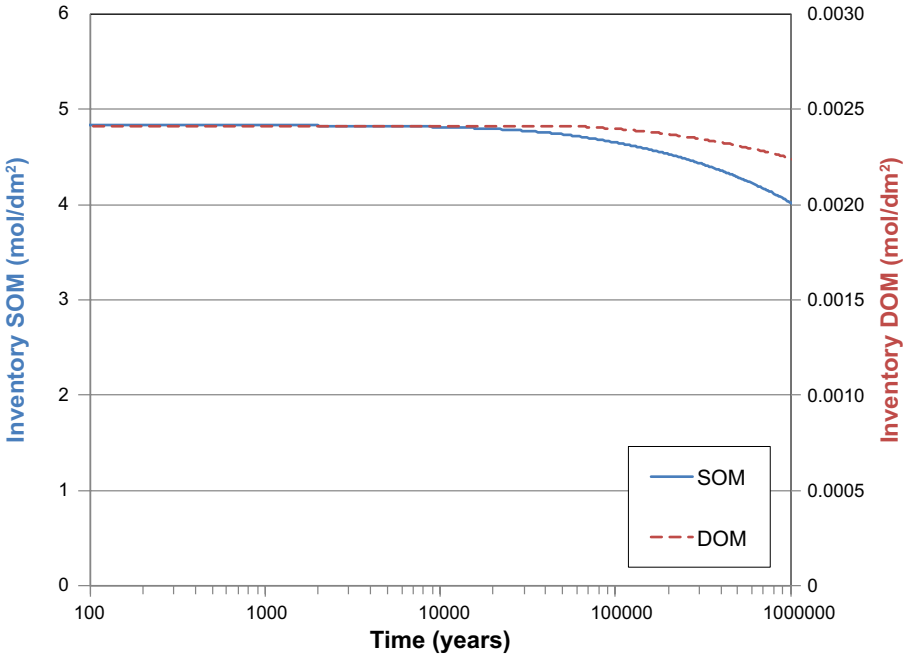

Figure 5-7. *Time dependence of the remaining inventory of solid (SOM) and dissolved (DOM) organic material for the Base Case simulation.*

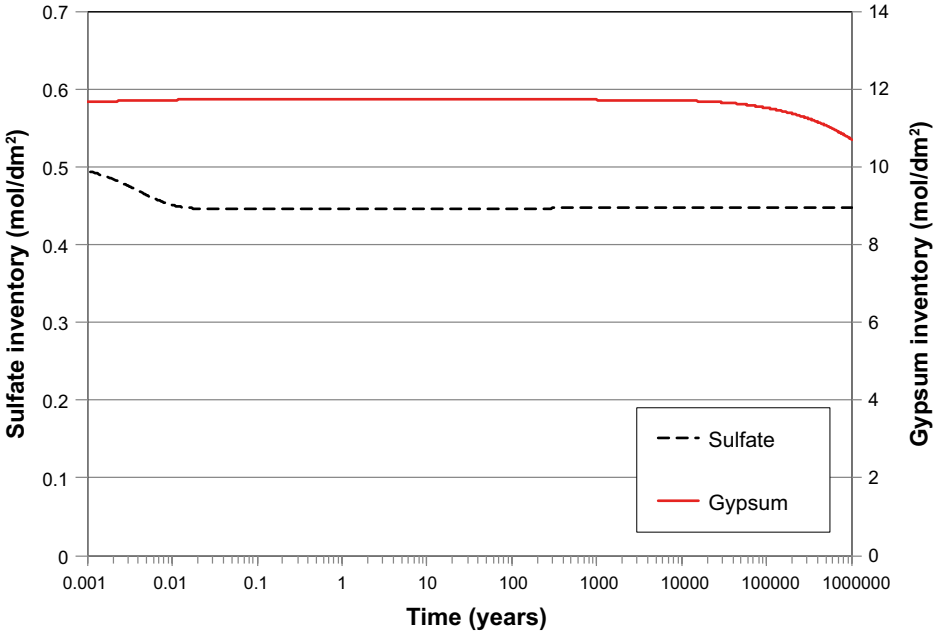

Figure 5-8. *Predicted time dependence of the inventories of dissolved sulfate ions and gypsum for the Base Case simulation.*

5.3.1.3 Sulfide species

Of the sulfide that is produced, the vast majority (> 99 %) is present as precipitated mackinawite (Figure 5-9, Table 5-4). As a quality check on the execution of the code, the predicted amount of sulfide present as FeS, Cu_2S, dissolved HS^-, and that which diffuses into the geosphere is equal to the amount produced by the two microbial sulfate reduction processes (Figure 5-10).

Precipitation of mackinawite primarily occurs at the backfill-RTI interface (Figure 5-11). For the chosen conditions for the Base Case simulation (Table 5-2), mackinawite precipitation is most likely to occur at this location since (i) microbial activity is only permitted in the RTI and (ii) the buffer and backfill are the only sources of SO_4^{2-} and organic material in the system. Thus, sulfate reduction occurs within the RTI but right at the interface with the backfill. Based on the shape of the FeS profile in Figure 5-11, the sulfide diffuses a small distance into the backfill before precipitating because the available Fe(II) becomes locally depleted in the backfill at the junction with the RTI.

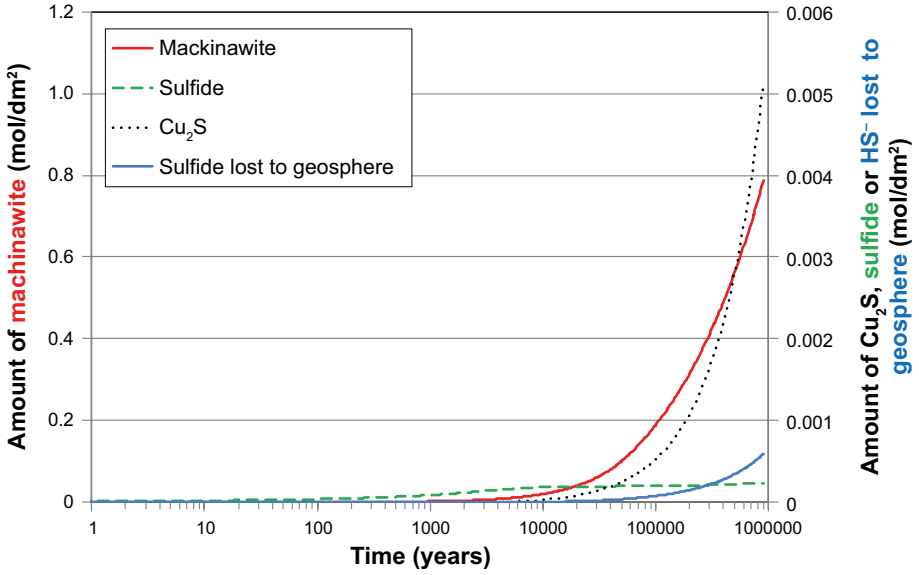

Figure 5-9. *Predicted time-dependent cumulative amount of sulfide species for the Base Case simulation.*

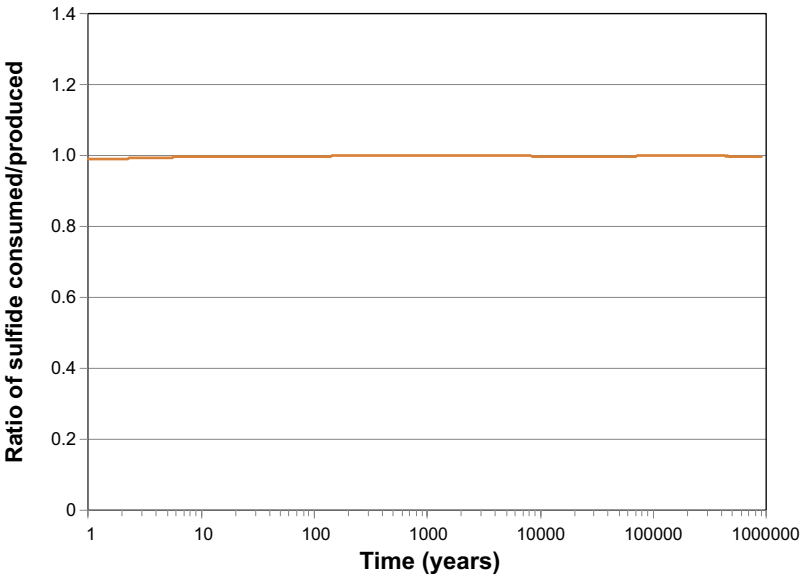

Figure 5-10. *Ratio of the amount of sulfide present as dissolved or precipitated species and that which diffuses into the geosphere to the amount produced by microbial sulfate reduction as a function of time for the Base Case simulation.*

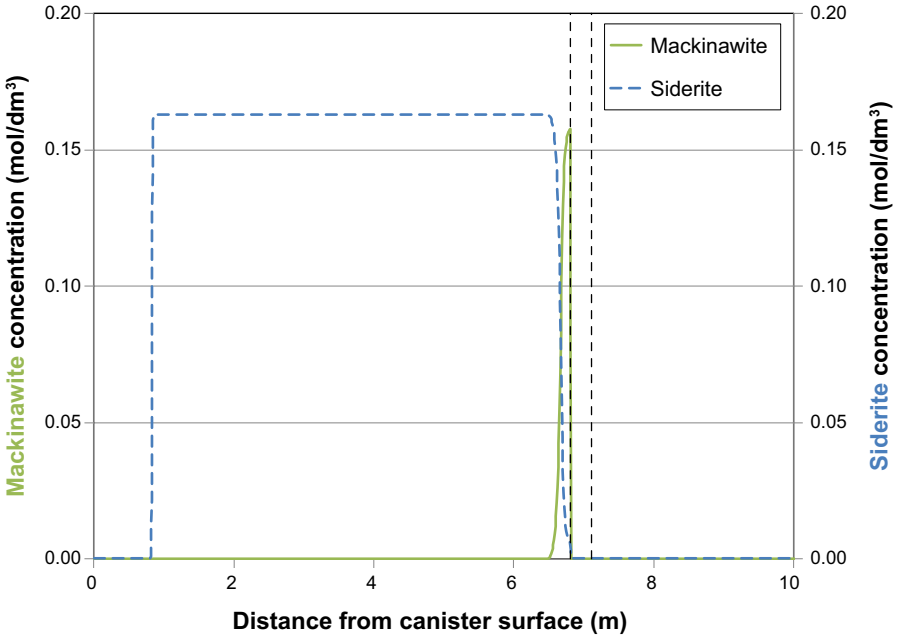

Figure 5-11. *Spatial distributions of mackinawite and siderite after a simulation time of 130 256 a for the Base Case simulation. The "concentration" of mackinawite and siderite are expressed as the number of moles per unit volume of the system. The location of the RTI is indicated by the vertical dashed lines.*

Figure 5-12 shows the sulfide concentration profiles in, and immediately adjacent to, the RTI for a range of times for the Base Case simulation. The highest sulfide concentration is observed at the backfill-RTI interface and gradually diminishes with time as HS^- diffuses both towards the canister and away through the RTI into the host rock. Although high concentrations of HS^- are observed in the host rock, the amount of sulfide that diffuses away from the RTI is relatively small as the porosity of the rock is much lower than that of the backfill and buffer materials.

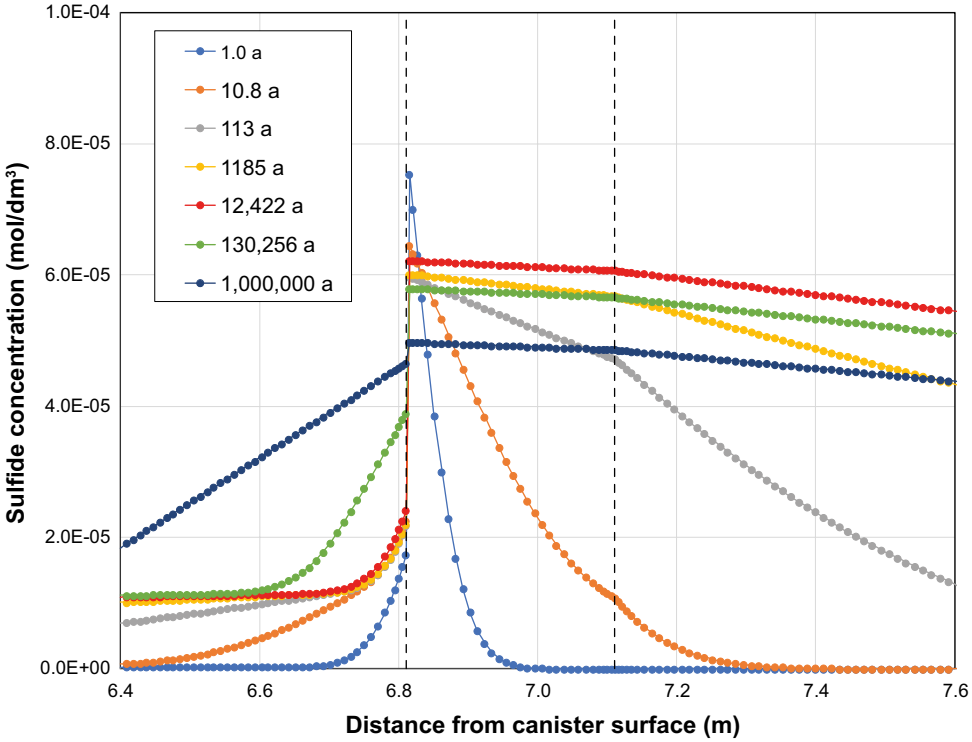

Figure 5-12. *Sulfide concentration profiles in the RTI and adjacent backfill (to the left) and rock layers (to the right) for various simulation times. The location of the RTI is indicated by the vertical dashed lines.*

5.3.1.4 Ferrous minerals

Precipitation of HS^- by Fe(II) is an important process in the overall evolution of the repository and is primarily responsible for limiting the extent of anaerobic corrosion of the canister. Even though the Fe(II) may become depleted at the backfill-RTI interface based on the profile in Figure 5-11, there is still a vast excess of ferrous minerals available in the repository near-field (Figure 5-13, Table 5-5).

Figure 5-14 shows the dissolved Fe(II) concentration profiles in and adjacent to the RTI for various times for the Base Case simulation. As would be expected, the [Fe(II)] profiles are the inverse of the sulfide concentration profiles, with lower dissolved iron concentrations at the locations of highest sulfide concentration.

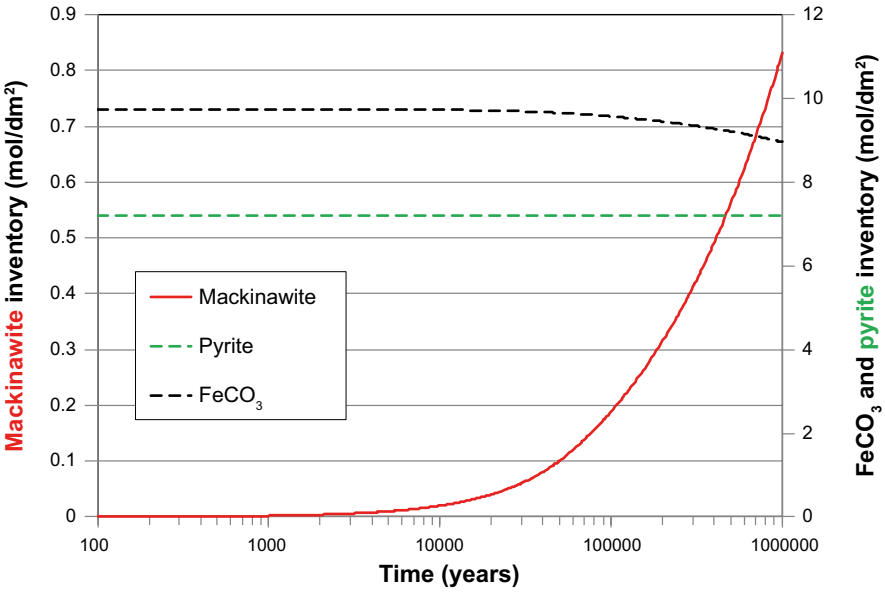

Figure 5-13. *Time-dependent inventories of ferrous minerals in the system for the Base Case simulation. In the absence of O_2 from the Base Case, pyrite is unreactive and plays no role during the simulation.*

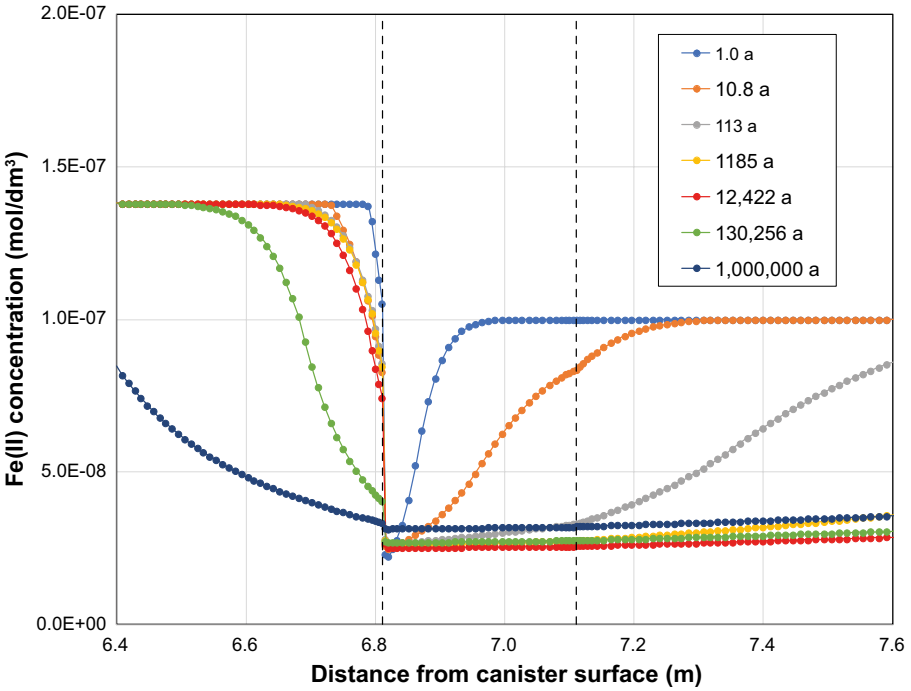

Figure 5-14. *Dissolved Fe(II) concentration profiles in the RTI and adjacent backfill (to the left) and rock layers (to the right) for various simulation times. The location of the RTI is indicated by the vertical dashed lines.*

5.3.2 Variant cases

In addition to the summaries of various results in Table 5-4 and Table 5-5, a comparison is provided here between the appropriate Base Case simulation and the time-dependent sulfide flux at the canister surface and the depth of corrosion for each of the variant cases discussed below.

5.3.2.1 Microbial activity in the RTI versus the RDI

One of the issues with a 1-D model is that it is difficult to properly simulate the complex 3-D geometry of the deposition hole and disposal tunnel. For the Base Case simulation, microbial sulfate reduction occurs in the RTI which is separated from the canister surface by layers of buffer and backfill material with a total combined thickness (in the model) of 6.81 m. The Base Case geometry, therefore, essentially represents transport in a vertical direction through the buffer and backfill materials.

In contrast, the variant case Buff0 represents transport in the horizontal direction through a layer of buffer directly in contact with the RDI in which microbial activity is assumed to occur. In addition to representing a shorter distance between the source of sulfide and the canister, the other major differences between the Base Case and Buff0 simulations are the absence of $FeCO_3$ (since the buffer is assumed to be free of siderite) and the lower inventory of organic material for Buff0.

These differences have a significant impact on the predicted corrosion behaviour of the canister (Figure 5-15, Table 5-4). The flux of sulfide to the canister surface is higher in the Buff0 simulation, both because the microbial activity occurs closer to the canister and because of the absence of siderite to act as a sink for HS^- through the precipitation of mackinawite. As a result, the predicted depth of corrosion after 10^5 a is 197 µm compared with only 0.75 µm for the Base Case simulation including backfill. Indeed, corrosion stops after 150 000 a with a depth of 224 µm, by which time all of the gypsum has been consumed and microbial sulfide production ceases. On a time-averaged basis, therefore, the corrosion rate of the canister prior to the consumption of all of the gypsum is approximately 1.5 nm/a for the Buff0 variant case, compared with a mean rate over the same time period of 0.008 nm/a for the Base Case simulation including backfill. Thus, the corrosion rate is predicted to be approximately two orders of magnitude higher for the Buff0 variant case.

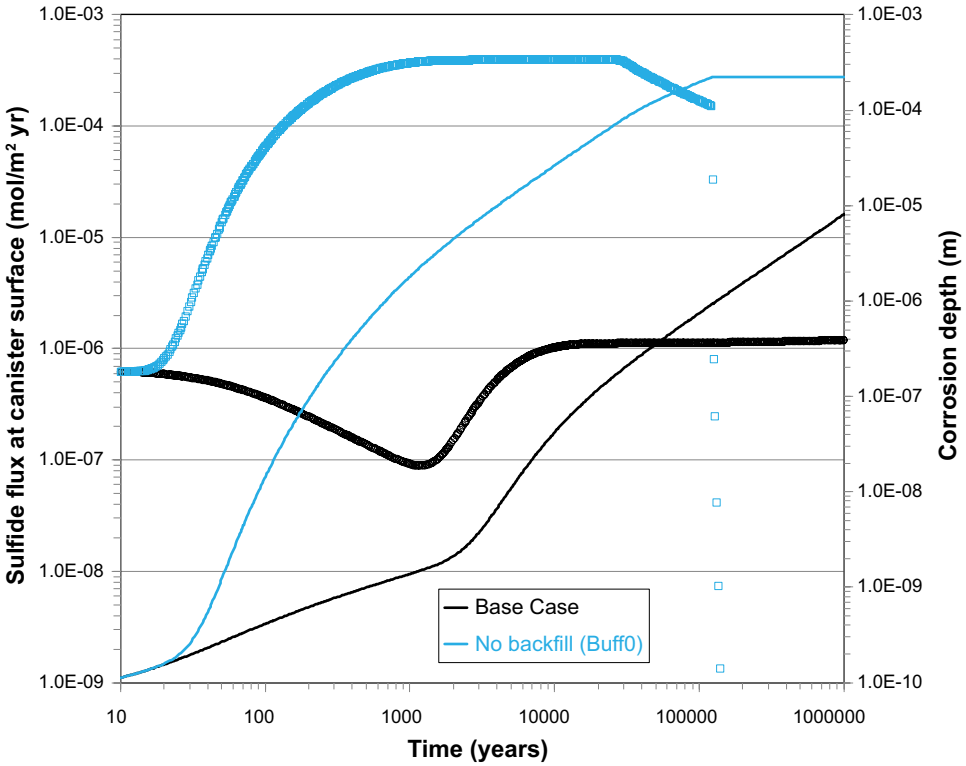

Figure 5-15. *Comparison of the sulfide flux (open squares) and depth of corrosion (solid lines) as a function of time for the Base Case simulation (black) and for variant case Buff0 (blue) for which the backfill layer is excluded from the model. The same colour is used for the symbols and lines for a given simulation.*

Figure 5-16 compares the amounts of sulfide produced by microbial activity to the amounts consumed as a function of time. In contrast to the Base Case where > 99 % of the sulfide was produced by organotrophic sulfate reduction, the chemotrophic pathway accounts for 12 % of the sulfate reduction for the Buff0 simulation because the location of microbial activity is closer to the source of H_2, i.e., the canister surface. It is apparent from Figure 5-16 that chemotrophic sulfate reduction only starts after the canister has begun to corrode (following transport of organotrophically produced sulfide to the surface).

On the consumption side, because of the absence of siderite in the buffer, only a small amount of mackinawite is predicted to form. The FeS that does form results from the precipitation of dissolved Fe(II) present in the ground water and initially in the pore water of the buffer and rock layers. Instead, corrosion of the canister accounts for 50 % of the amount of sulfide produced. Dissolved HS^- accumulates in the system during the period of microbial activity, but is then consumed after production ceases. The remaining sulfide is believed to be lost from the RHS boundary (essentially lost into the geosphere). (Although the numerical integration of the RHS flux suggests that only small amounts of sulfide are lost to the geosphere, Figure 5-16, there is no other sink for sulfide in the system that could account for the remaining approximately 50 % of the HS^- produced).

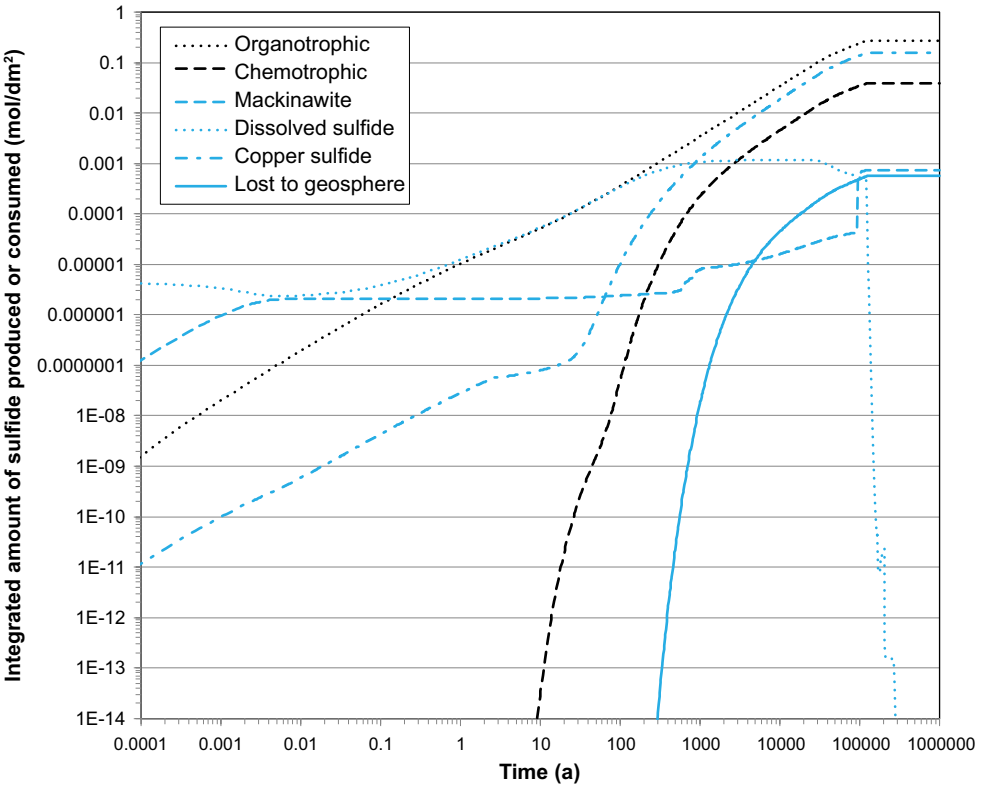

Figure 5-16. *Time dependence of the integrated amounts of sulfide produced (black) and consumed (blue) by various processes in the Buff0 simulation.*

5.3.2.2 Buffer density

As described in Section 5.2.2.1, two runs were carried out to determine the effect of buffer density using a version of the model without backfill. The results from run Buff1, in which microbial activity was allowed in the buffer, and Buff2, in which the buffer was replaced by ground water are compared with the results from the reference case Buff0 in Figure 5-17. Permitting microbial activity in the buffer (Buff1) resulted in a higher sulfide flux and faster corrosion initially than the case where sulfide reduction occurs in the RDI only (Buff0). The highest corrosion rate predicted was 33 nm/a. However, the faster sulfide reduction simply results in faster consumption of the gypsum (after 12 000 a, compared with 94 000 a for Buff0), and the depth of corrosion after 10^6 a is similar (Table 5-4).

Replacing the buffer by ground water (Buff2) resulted in no corrosion as there was no source of organic material (Table 5-4).

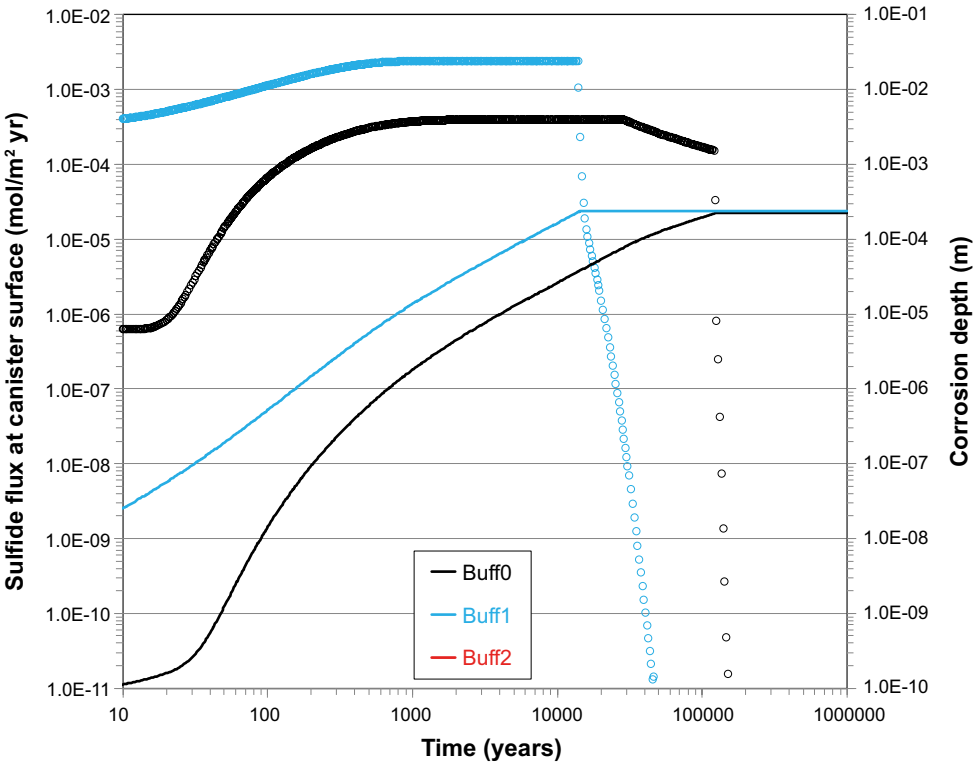

Figure 5-17. Effect of buffer density on the flux of sulfide to the canister (open circles) and the depth of corrosion (solid lines) for simulation times up to 10^6 a. The same colour is used for the symbols and lines for a given simulation. The curves for Buff2 do not appear in the figure as there is no sulfide production for that variant in the absence of organic material.

5.3.2.3 Backfill density

Two variant cases were carried out to determine the effect of permitting microbial activity in the backfill; the two cases being characterised by a relatively high initial biomass (Back1) and a lower initial biomass (Back2) (Section 5.2.2.2). As in the Base Case simulation, both the buffer and backfill materials are assumed to contain organic matter.

The effect of permitting microbial activity in the backfill on the sulfide flux and depth of corrosion is illustrated in Figure 5-18. For this 1-D simulation, allowing microbial sulfide production in the backfill has the effect of moving the source of HS^- closer to the canister, so that the sulfide reaches the canister earlier and at a higher rate than if microbial activity is restricted to the RTI only (as in the Base Case). This increased rate of sulfide production, however, results in faster consumption of the available organic material, which is predicted to be totally consumed after approximately 520 000 a (Back1). In the Base Case simulation, 83 % of the organic material remains after 10^6 a (Table 5-4). As a result of the higher rate of sulfide production and transport to the canister, the depth of corrosion after 10^5 a is predicted to be 46 µm compared with only 0.76 µm for the Base Case simulation (Table 5-4).

There is relatively little impact of the initial biomass in the backfill on the predicted sulfide flux (Figure 5-18). The vast majority (> 97 %) of the sulfide produced is predicted to precipitate as FeS prior to reaching the canister surface. Thus, the increased rate of sulfide production in variant case Back1 compared with that in Back2 has little impact on the rate at which HS^- reaches the canister.

The increase in sulfide flux to the canister for variants Back1 and Back2 up to 30 000 a is because of the progressive consumption of siderite in the backfill due to the large amount of HS^- produced for these variant cases. As a result, an increasing fraction of the HS^- produced is able to reach the canister surface. The peak in the flux of sulfide to the canister surface at approximately 30 000 a corresponds to the time at which all of organic material in the backfill has been consumed. After that time, DOM must diffuse from the buffer to support microbial activity in the backfill and the flux of sulfide drops accordingly. The decrease in sulfide flux at times beyond 500 000 a is due to the consumption of all of the organic material from the buffer and the cessation of microbial sulfate reduction.

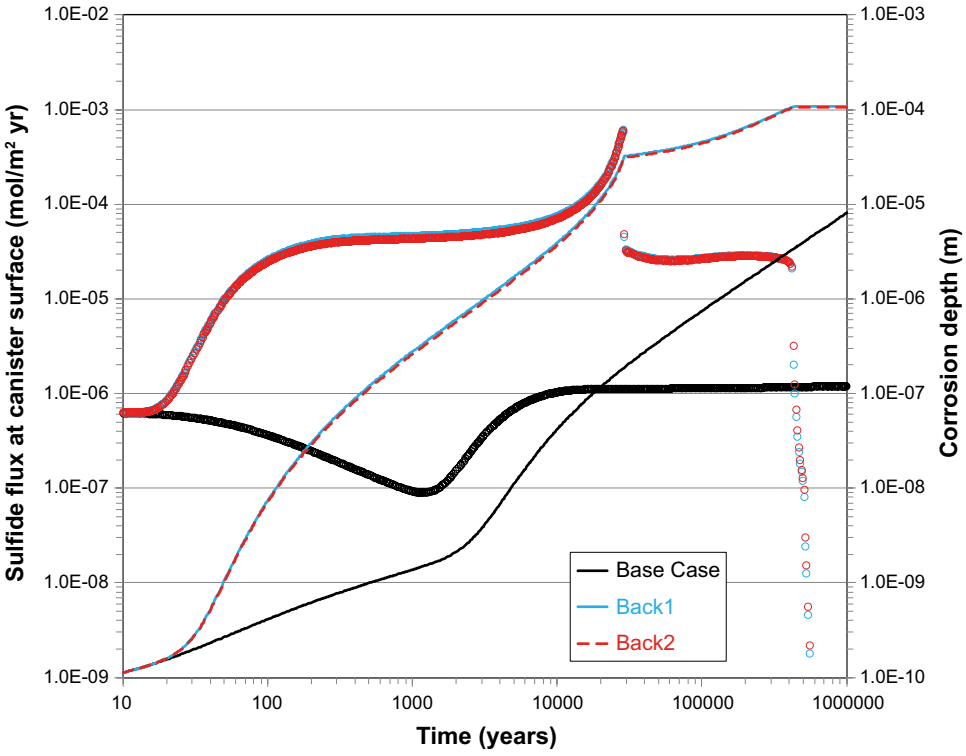

Figure 5-18. *Effect of permitting microbial activity in the backfill on the flux of sulfide to the canister (open circles) and the depth of corrosion (solid and dashed lines) for simulation times up to 10^6 a. The same colour is used for the symbols and lines for a given simulation. The sulfide fluxes for cases Back1 and Back2 overlap.*

5.3.2.4 Fe(II) minerals

It is clear from the Base Case simulation that the vast majority of sulfide produced by microbial activity in the RTI is precipitated as mackinawite before it reaches the canister. Thus, the concentration and distribution of soluble Fe(II) minerals (here simulated by siderite) may impact the predicted corrosion behaviour. Four variant cases were performed in which the amount of siderite in the buffer and backfill were varied. For reference, in the Base Case simulation the backfill was assumed to contain 1.1 wt% siderite but there was none in the buffer.

If all siderite is removed from the system the predicted flux of sulfide to the canister and the depth of corrosion are higher than for the Base Case (see variant Fe4, Figure 5-19). The maximum flux is approximately two and a half orders of magnitude higher than the Base Case and the depths of corrosion after 10^5 a are 0.75 µm with siderite in the backfill and 126 µm without siderite (Table 5-4). After 10^6 a, the corresponding corrosion depths are 8.09 µm and 663 µm, respectively. The highest sulfide flux corresponds to a corrosion rate of 3 nm/a.

In contrast to the large effect of removing siderite, there is no effect of adding siderite to the buffer as well as to the backfill (variant Fe1) and only a minor effect of doubling the siderite content of the backfill (Fe2) (Table 5-4 and Figure 5-19). These results suggest that, for the geometry assumed, Fe(II) in the backfill is the major sink for sulfide and that there is sufficient siderite present in the Base Case to precipitate the majority of the HS^-.

Adding siderite to the buffer and doubling the amount in the backfill (variant Fe3) produces no benefit over doubling the amount in the backfill alone.

5.3.2.5 Interface diffusivity

The interface regions around the tunnel (RTI) and deposition hole (RDI) are the locations where microbial activity is assumed to occur for the Base Case simulations. Therefore, increasing the diffusivity of these regions could affect the sulfide flux to the canister if (i) the rate of microbial activity was limited by the supply of electron acceptors (i.e., sulfate) or nutrients or (ii) diffusion of HS^- from the interface region was rate limiting.

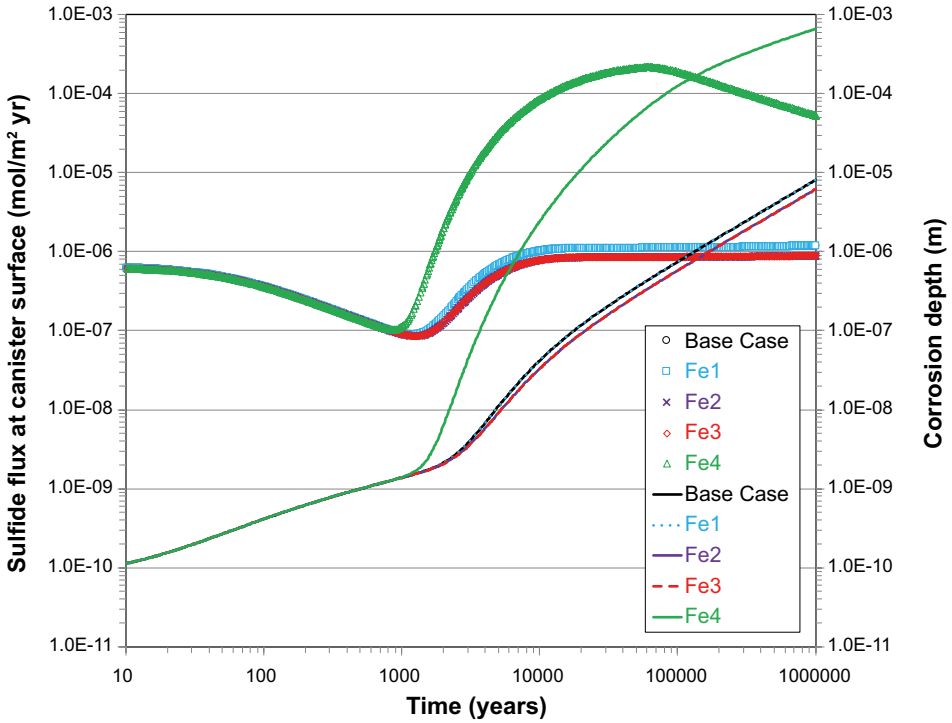

Figure 5-19. *Effect of different assumptions regarding the amount of siderite in the buffer and backfill on the flux of sulfide to the canister (open symbols) and the depth of corrosion (solid and dashed lines) for simulation times up to 10^6 a. The same colour is used for the symbols and lines for a given simulation.*

Increasing the diffusivity by a factor of 10 or 100 had no effect on the predicted sulfide flux to the canister or the depth of corrosion for microbial activity in either the RTI or RDI (Figure 5-20 and Figure 5-21, respectively). In all cases, the predicted flux and depth of corrosion are identical to those for the respective reference cases (the Base Case for the RTI and variant case Buff0 for the RDI). All other results in Table 5-4 and Table 5-5 are similar for the variant and respective reference cases.

The absence of an effect of the interface diffusivity may be because microbial activity in the RTI occurs primarily right at the RTI/backfill junction rather than through the entire interface region. Therefore, increasing the diffusivity of the entre RTI has little impact. This may be compounded by the fact that transport of sulfide to the canister is dominated not only by the relatively long diffusion path across the buffer and backfill but also by precipitation of HS^- as FeS prior to reaching the canister (which accounts for 99 % of the sulfide produced). The net effect is that the flux of sulfide at the canister surface is relatively insensitive to changes in the rate of microbial sulfate reduction in the RTI.

5.3.2.6 Organic matter

The amount of organic material in the buffer and backfill is not limiting for the Base Case simulation, with 96 % and 83 % remaining after 10^5 a and 10^6 a, respectively (Table 5-4). A number of variant cases were run in which either the amount of organic material was reduced by a factor of 10 (ORG1) or the rate of dissolution of the SOM was reduced by a factor of either 10 (ORG2) or 100 (ORG3) giving, in the latter two cases, "half-lives" for the SOM of 100 a and 1 000 a, respectively.

Reducing the amount of organic material by a factor of ten results in only a minor reduction in the extent of corrosion (Table 5-4 and Figure 5-22). For example, after 10^5 a the depths of corrosion are 0.75 µm for both the Base Case and variant ORG1, respectively (Table 5-4). After 10^6 a, the corresponding depths are 8.09 µm and 7.88 µm, respectively. The fractions of organic material remaining after 10^5 a and 10^6 a for the ORG1 variant case are 83 % and 42 %, respectively (Table 5-4). Greater depletion of the organics means that DOM must diffuse further in the case of the reduced amount of organics, which results in less total sulfate reduction. Thus, the "depletion front" of SOM in the backfill extends approximately 4 m away from the RTI after 10^6 a in the case of the ORG1 simulation compared with a distance of only 1 m for the Base Case simulation.

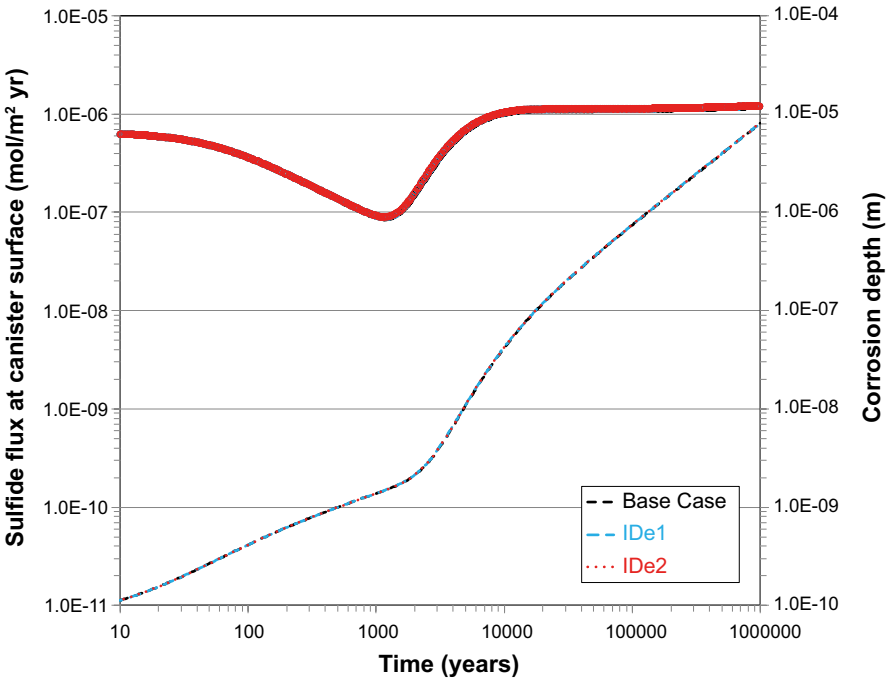

Figure 5-20. *Effect of increasing the diffusivity in the rock-tunnel interface by factors of 10 or 100 on the flux of sulfide to the canister (open circles) and the depth of corrosion (solid and dashed lines) for simulation times up to 10^6 a. The same colour is used for the symbols and lines for a given simulation.*

Slowing the rate of dissolution of SOM had similarly minimal effects on both the sulfide flux and the depth of corrosion (Table 5-4 and Figure 5-22), indicating that the rate of solubilisation of organic material is not limiting for the rates considered here.

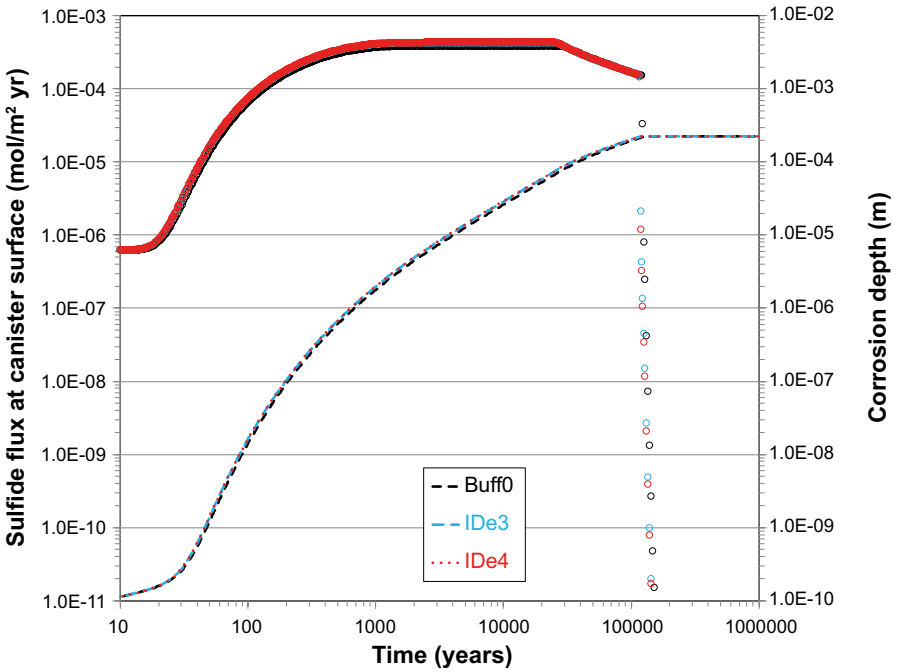

Figure 5-21. Effect of increasing the diffusivity in the deposition hole-tunnel interface by factors of 10 or 100 on the flux of sulfide to the canister (open circles) and the depth of corrosion (dashed lines) for simulation times up to 10^6 a. The reference case for the effect of RDI diffusivity is variant Buff0 rather than the Base Case simulation. The same colour is used for the symbols and lines for a given simulation.

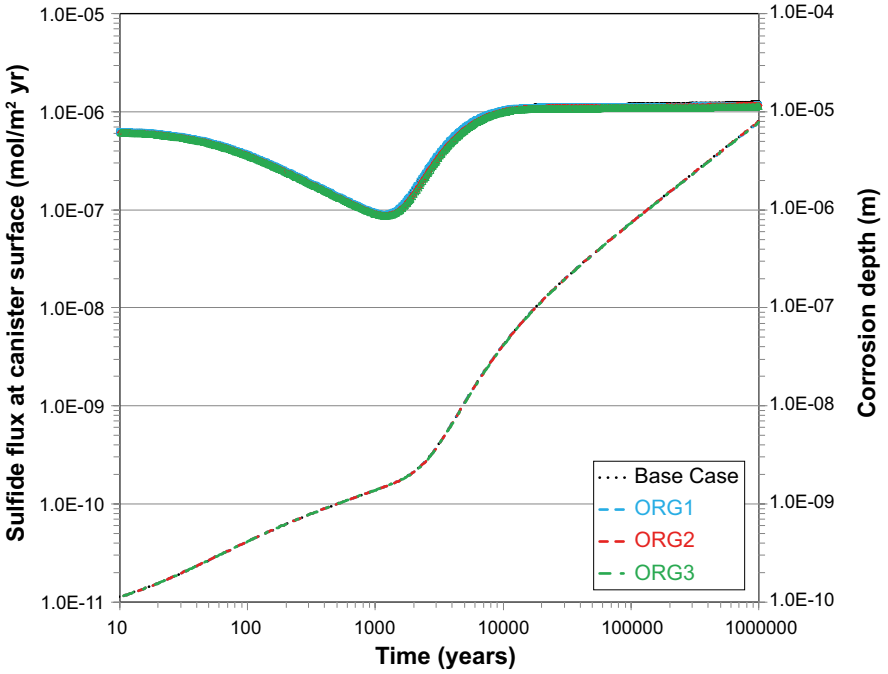

Figure 5-22. Effect of different assumptions regarding the amount or availability of organic material on the flux of sulfide to the canister (open symbols) and the depth of corrosion (solid and dashed lines) for simulations times up to 10^6 a. The same colour is used for the symbols and lines for a given simulation.

5.3.2.7 Thermal effects

The Base Case and other variant cases were run under isothermal conditions of 25 °C. In the CSM, many of the rate constants, diffusion coefficients, solubilities, and electrochemical parameters are temperature dependent. Therefore, two variant cases were run under conditions of spatially and temporally variable temperature, distinguished by maximum canister surface temperatures of 75 °C (Therm1) and 97 °C (Therm2). Of equal importance is the ambient temperature in the rock (assumed here to be 10.5 °C), which also defines the long-term temperature at the canister surface (Figure 5-2). The temperature elsewhere in the repository will lie between these two limits. In particular, the temperature in the RTI located 6.8 m from the canister surface (where the microbial activity is assumed to occur) varies between 10.5 °C and approximately 55 °C. Temperature profiles across the model domains are shown for various times in Figure 5-23. Figure 5-24 shows the effect of temperature on the relative rates of microbial reduction of sulfate for the assumed activation energies (Appendix D3) and the assumed minimum, optimum, and maximum temperatures for the inter-model comparison exercise of 5 °C, 25 °C, and 60 °C, respectively.

Increasing the system temperature increases the sulfide flux initially but leads to lower fluxes and less corrosion in the long term (Figure 5-25). There are a number of temperature-dependent parameters in the CSM that could account for these effects, including:

- Solubility of mackinawite, activation energy 24 000 J/mol.
- Siderite dissolution rate constant, assumed activation energy 60 000 J/mol.
- SOM dissolution rate constant, assumed activation energy 60 000 J/mol.
- Retrograde solubility of gypsum.
- Gypsum dissolution rate constant, assumed activation energy 60 000 J/mol.
- Minimum, optimum, and maximum temperatures for SRB of 5 °C, 25 °C, and 60 °C, respectively.

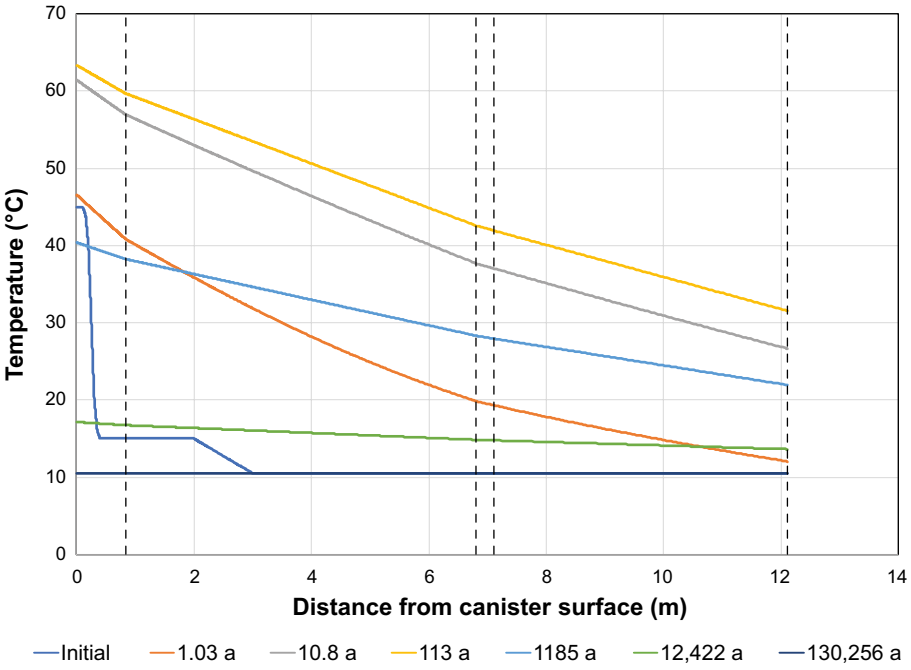

Figure 5-23. *Temperature profiles across the modelled domains for times ranging from zero to 130 256 a. The vertical dashed lines represent the junctions between the buffer and backfill (0.83 m), between the backfill and RTI (6.81 m), the RTI and host rock (7.11 m), and the far right-hand boundary of the model (12.11 m).*

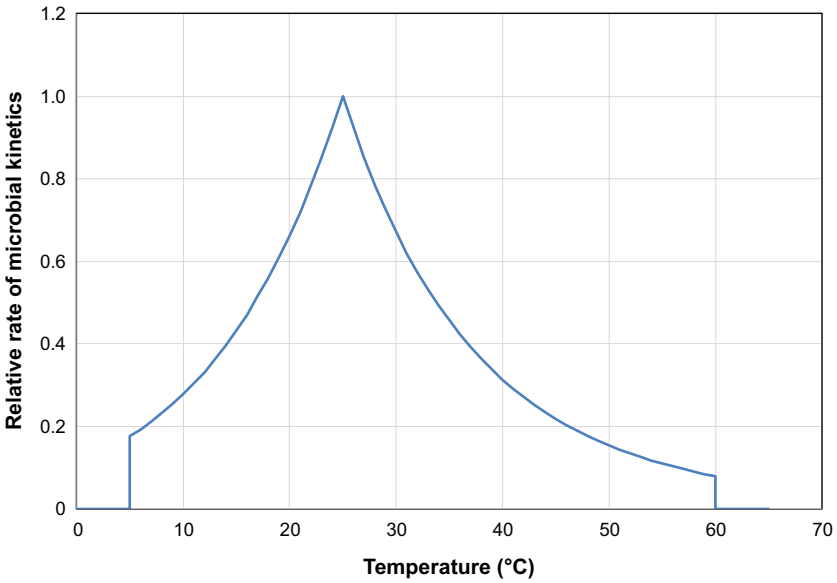

Figure 5-24. *Relative rate of microbial kinetics as a function of temperature based on the assumed activation energies and the minimum, optimum, and maximum temperatures for microbial activity of 5 °C, 25 °C, and 60 °C, respectively. The actual rate depends on other factors, including the concentrations of either organic carbon or hydrogen and of sulfate ions.*

Given the large number of temperature-dependent parameters and the complexity of spatially and temporally varying temperature, it is difficult to identify which of these processes is controlling the sulfide flux. Based on the time dependence of the extent of sulfate reduction, however, it appears that the behaviour observed in Figure 5-25 is a result of the effect of temperature on the microbial kinetics rather than on the availability of Fe(II) as a sink for sulfide. Figure 5-26 shows the time dependence of the cumulative extent of organotrophic sulfate reduction (by far the more important of the two pathways) for the Base Case and Therm1 variant case simulations. The extent of sulfate reduction is higher in the variant case for the first 10 000 a, after which slightly more sulfate reduction occurs in the Base Case. This time corresponds approximately to the period during which the corrosion depth is greater for the variant case (Figure 5-25).

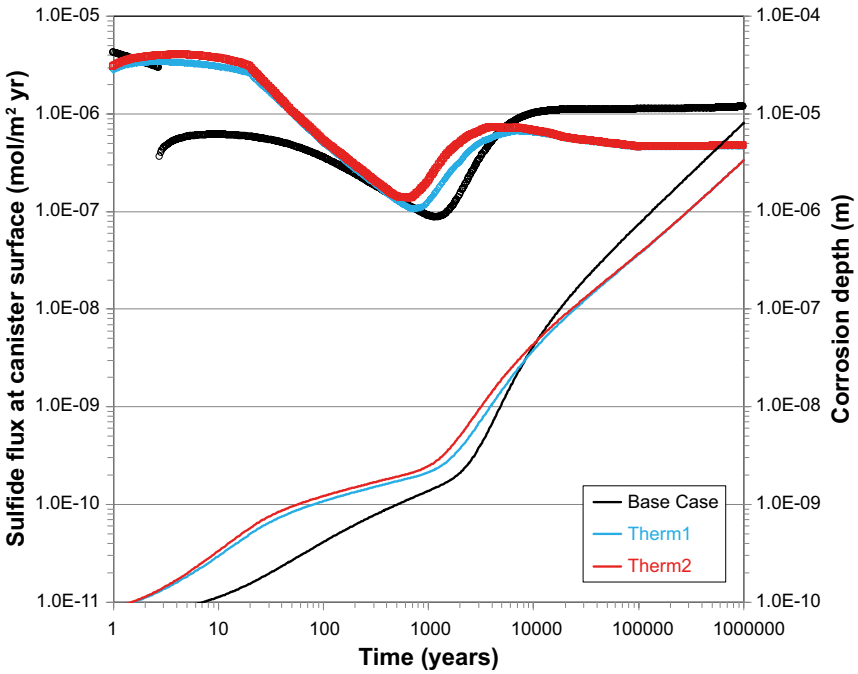

Figure 5-25. *Effect of spatially and temporally varying temperatures on the flux of sulfide to the canister (open symbols) and the depth of corrosion (solid lines) for simulation times up to 10^6 a. The same colour is used for the symbols and lines for a given simulation.*

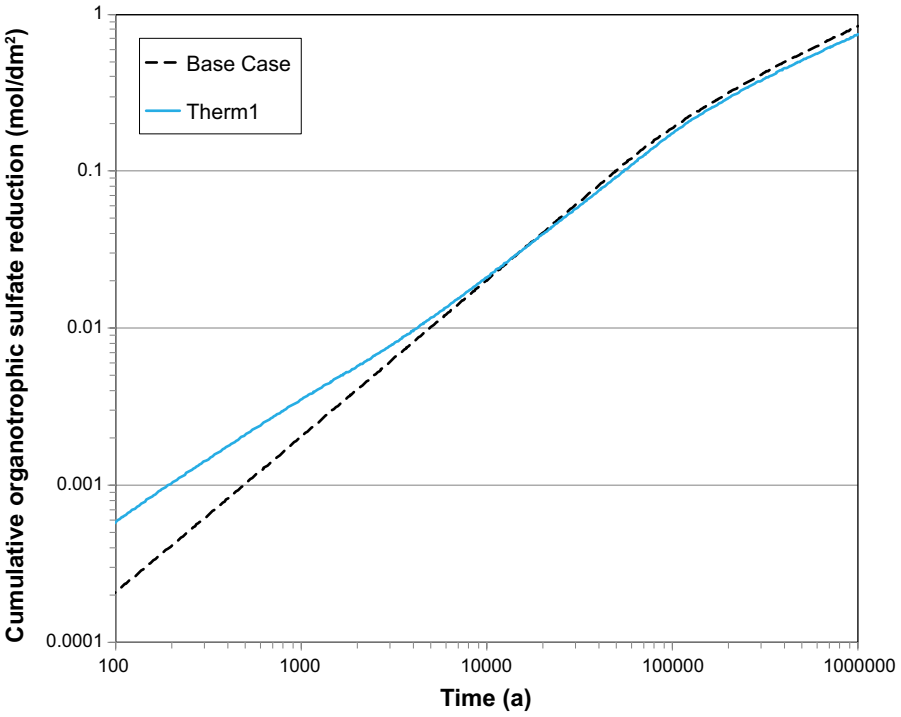

Figure 5-26. *Time dependence of the cumulative amount of organotrophic sulfate reduction for the Base Case and Therm1 variant case simulations up to 10^6 a.*

On the assumption that the rate of the microbial sulfate reduction is the primary temperature-dependent process, the question is then which individual process is rate controlling. As described in Section 2.3.7 and, specifically, by Equations (2-61) – (2-64), the temperature dependence of the Monod kinetics in the CSM are described by an optimum and by minimum and maximum temperatures. The optimum temperature, at which the rate of sulfate reduction is at a maximum, is 25 °C for the current simulations to correspond to that specified for the model inter-comparison simulations (Appendix D). Thus, all other factors being equal, the rate of sulfate reduction would be expected to have been highest for the isothermal Base Case simulation. That this is not the case, therefore, suggests that a temperature-dependent process associated with the availability of either sulfate or dissolved organic material is responsible for the temperature dependence observed. Since gypsum exhibits retrograde solubility, i.e., the solubility decreases with increasing temperature, the temperature-dependent dissolution of sulfate would not seem to be controlling. Furthermore, since the solubility of SOM is assumed to be temperature independent, the observed temperature dependence could be due to either the rate of dissolution of SOM to produce dissolved organics (although this seems unlikely based on the sensitivity analyses presented in Section 5.3.2.9) or the diffusion of dissolved sulfate and organic material from the backfill (and buffer) to the RTI.

5.3.2.8 Groundwater composition

Three variant case simulations were carried out in which the composition of the ground water was modified compared with that specified for the Base Case (see Section 5.2.2.7). The three variants involved adding either 460 mg/L SO_4^{2-} (GW1), or 25 mg/L DOM (GW2), or 0.02 mg/L HS^- (GW3) to the ground water.

Figure 5-27 compares the results of the three variant cases and that for the Base Case and shows that the variations in ground water composition have no effect on the predicted behaviour. This conclusion is perhaps not surprising since neither sulfate nor organic matter are limiting in the Base Case. Although adding HS^- to the ground water represents an additional source of sulfide, that source is some distance from the canister (12.3 m in the model) and there is an excess of Fe(II) in the system to precipitate any sulfide diffusing in from the right-hand boundary of the model. More importantly, however, the supply of sulfide from the groundwater is limited because the effective diffusion coefficient of sulfide in the host rock is small.

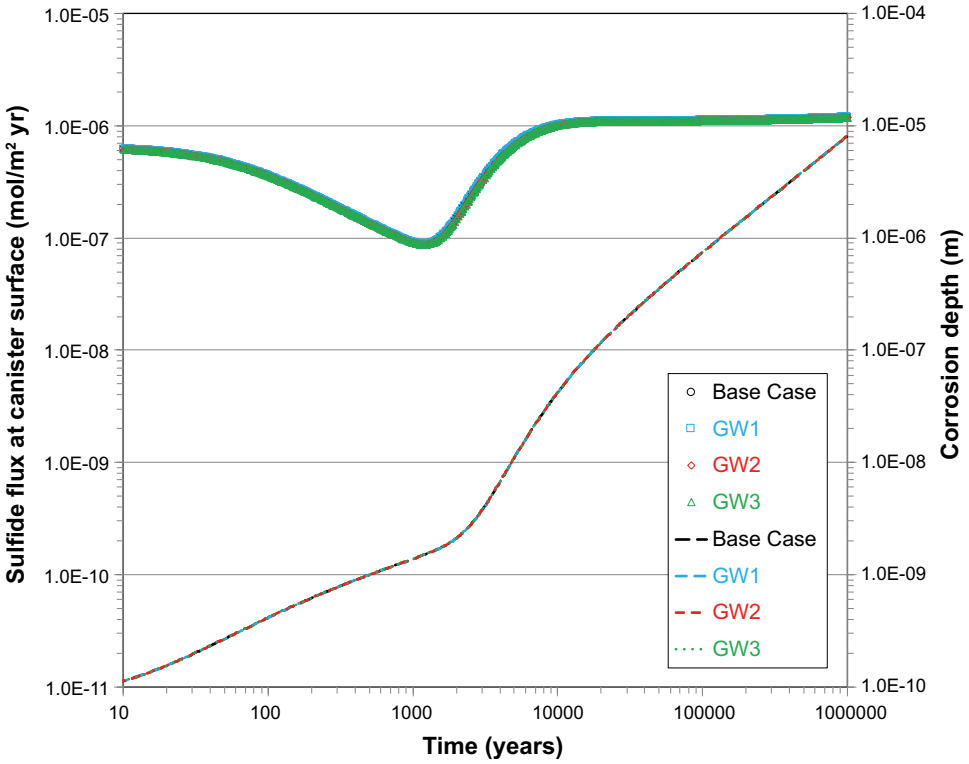

Figure 5-27. *Effect of additions of sulfate, DOM, or sulfide ions to the ground water on the flux of sulfide to the canister (open symbols) and the depth of corrosion (dashed lines) for simulation times up to 10^6 a. The same colour is used for the symbols and lines for a given simulation.*

5.3.2.9 Kinetic rates

In order to assess the sensitivity of the predictions to the Monod kinetics, the value of the maximum specific growth rate was increased by a factor of ten for either the organotrophic pathway (variant case K1), the chemotrophic pathway (K2), or both pathways (K3).

The results in Figure 5-28 show that there was no impact on the predicted sulfide flux or the depth of corrosion for any of these variant cases. Since the chemotrophic pathway is relatively minor (due to the lack of H_2), it is not surprising that increasing the rate constant for this process has no effect. The fact that increasing the rate constant for organotrophic sulfate reduction also has no effect suggests that some other process, possibly the supply of SO_4^{2-} or of organic material, is rate determining, which is consistent with the conclusion drawn from the effect of elevated temperature discussed in Section 5.3.2.7.

5.3.2.10 Fineness of the interface grid spacing

Because microbial activity is restricted to the 0.3-m-wide RTI in the Base Case simulation, two additional variant cases were run to determine the effect of grid spacing in this region. The number of grid points and the mean spacing in the RTI was adjusted as follows: 33 grid points/9.1 mm spacing (Base Case), 48 grid points/6.3 mm spacing (variant case "Fine"), and 104 grid points/2.9 mm spacing (variant case "Finer").

The results illustrated in Figure 5-29 indicate no effect of the RTI discretisation on the predicted sulfide flux or depth of corrosion, providing confidence that the data presented here are free from numerical artefacts associated with the execution of the code.

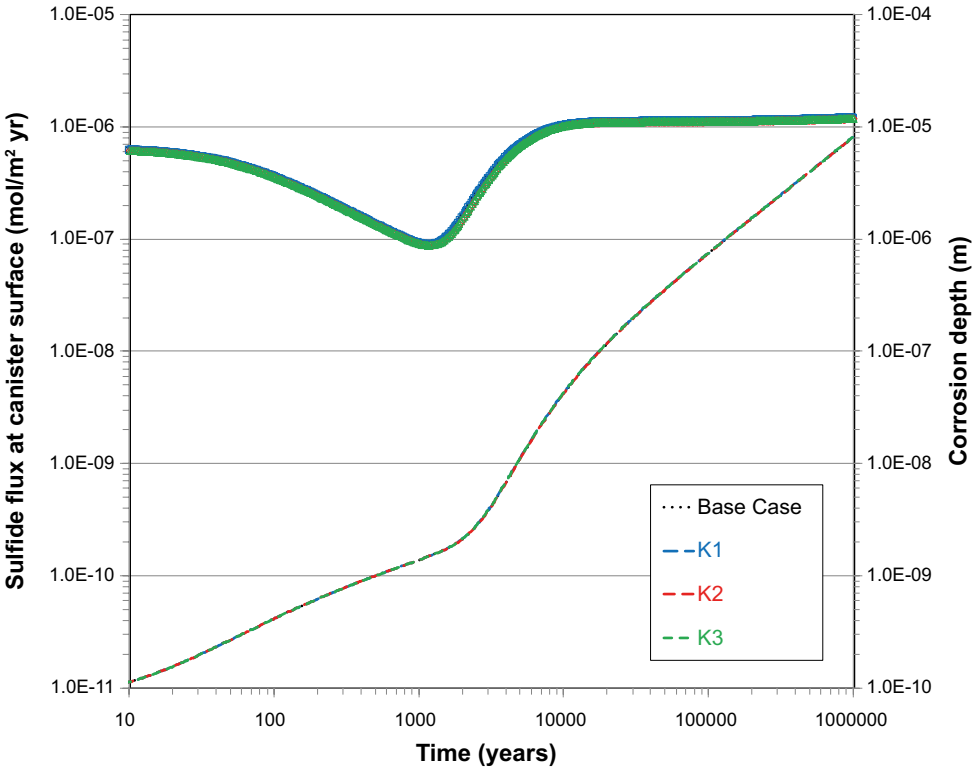

Figure 5-28. *Effect of variations in the rate of the Monod rate constants for organotrophic and chemotrophic sulfate reduction on the flux of sulfide to the canister (open symbols) and the depth of corrosion (dashed lines) for simulation times up to 10^6 a. The same colour is used for the symbols and lines for a given simulation.*

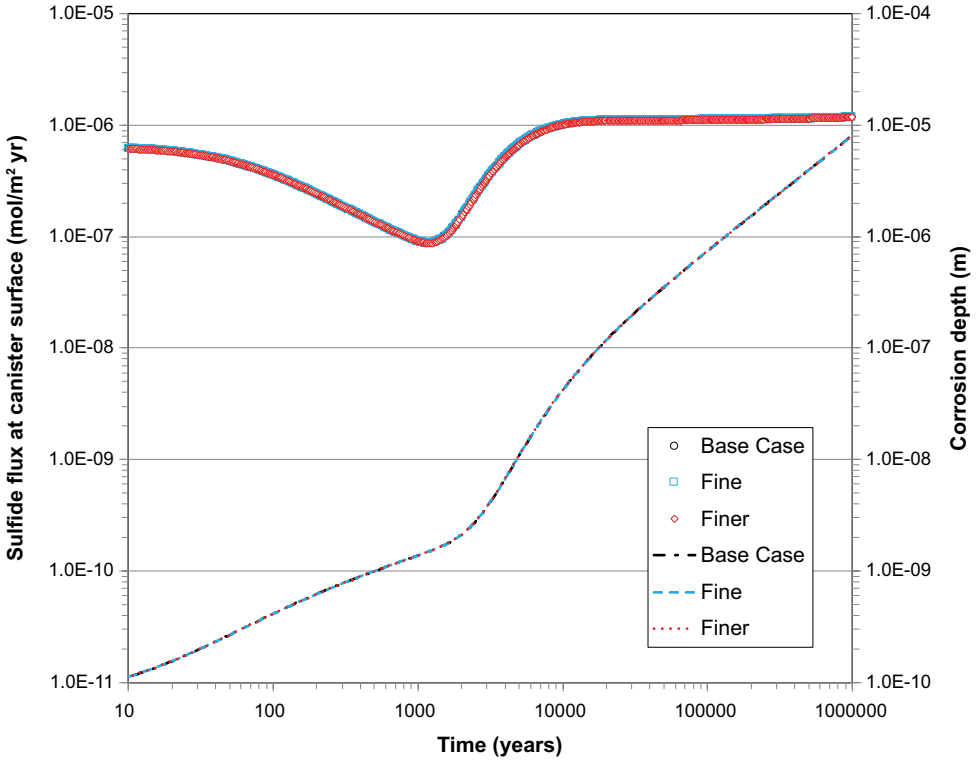

Figure 5-29. *Effect of RTI discretisation on the flux of sulfide to the canister (open symbols) and the depth of corrosion (dashed lines) for simulation times up to 10^6 a. The same colour is used for the symbols and lines for a given simulation.*

5.3.3 Discussion of the results of the Base Case and variant cases

A number of general conclusions can be drawn from the results of the Base Case and variant case simulations. Despite the fact that these simulations were run using a series of hypothetical scenarios, the results are consistent with those from the best-estimate analysis presented in Section 4 in terms of the extent of corrosion. The predicted depth of corrosion after 10^6 a was less than 10 µm, except for those cases where the location of microbial activity was moved closer to the canister by removing the backfill layer (i.e., variant cases Buff0, Buff1, IDe3, and IDe4), where siderite was removed from the system (variant case Fe4), or where microbial activity was permitted in the backfill coupled with slow dissolution of Fe(II) minerals (variant cases Back1 and Back2).

For all simulations, the main factor that limited the extent of corrosion was the precipitation of the majority of the sulfide as FeS prior to it reaching the canister surface. On simple mass-balance grounds, the systems modelled contain a vast excess of Fe(II) in the form of soluble siderite, with an equally large amount of sulfate present in the form of gypsum, especially in the backfill. In contrast, for simulations in which there is only buffer material, the availability of gypsum is limiting. The extent of chemotrophic sulfate reduction was small in all cases because the only source of H_2 is anaerobic corrosion of the canister by sulfide produced by the organotrophic pathway. The organic material was not completely consumed for the Base Case and for the majority of the variant case analyses, even over a period of 10^6 a.

The results also show the importance of the relative distance between sulfide production and the canister surface and, by inference, of the dimensionality of the model (Figure 5-1). Moving the location of microbial activity from the RTI (6.81 m from the canister) to the RDI closer to the canister (0.83 m from the canister) results in a factor of 28 times more corrosion after 10^6 a, even though the overall inventory of organic material in the buffer is only one eight of that in the backfill. The steeper sulfide gradient and the absence of siderite in the buffer both result in a higher flux of sulfide to the canister surface. This sensitivity to the distance between the source of microbial activity and the canister also suggests that differences would be observed between the predicted corrosion behaviour for 1-D and 3-D versions of the CSM.

The current results also have implications for the specification of the buffer and backfill materials. Clearly, a source of soluble Fe(II), such as siderite, is an important consideration and, given the limited amount of organic material, it should not be difficult to specify materials that will provide an excess of ferrous minerals. Although reducing the amount of organic material would reduce the total extent of sulfate reduction, there is little benefit to be attained in doing so provided there is an excess of soluble Fe(II) in the buffer or backfill. Limiting microbial activity in the buffer is considered to be desirable, although the results of the backfill variant cases suggest that microbial activity in the backfill does not lead to excessive corrosion of the canister provided there is a source of Fe(II) to precipitate the sulfide produced.

6 Discussion

6.1 Nature of the repository environment and the evolution of the corrosion behaviour of the canister

By coupling the interfacial electrochemical processes to reactions and mass transport in the buffer, backfill, and host rock, the CSM allows the evolution of the corrosion behaviour of the canister to be predicted as the repository environment evolves back to the pre-excavation, undisturbed state. Predictions of the time dependence of the corrosion potential E_{CORR} and of the corrosion rate are useful in assessing the extent of various corrosion processes that are, and are not, expected to occur over extended time periods. Furthermore, the CSM, like other reactive-transport models (e.g. Idiart et al. 2019 and Pękala et al. 2019), provides insights into the nature of the repository environment and how it evolves over time.

From a corrosion perspective, the nature of the environment in a KBS-3 style deep geological repository can be characterised as follows:

- Oxygen-deficient, limited to that trapped in the unsaturated fraction of the pores in the buffer and backfill materials at the time of emplacement. What oxygen is present is expected to be consumed within a period of a few weeks to a few years, although copper(II) species produced by the homogeneous oxidation of Cu(I) by O_2, may persist for a longer time.
- Slow rates of mass transport of reactants towards, and of corrosion products away from, the canister surface through the compacted clay-based buffer and backfill materials. Effective diffusivities of species in the buffer and backfill are of the order of 10^{-7} cm^2/s, approximately two orders of magnitude lower than in bulk solution, with diffusion path lengths of up to several metres.
- Initially warm (maximum canister surface temperature of 80–90 °C), with temperatures diminishing to close to ambient within a few tens of thousands of years.
- Initially partially water-saturated, but becoming completely saturated within a period of a few decades to few centuries following repository closure (Åkesson et al. 2010).
- Inhospitable for microbes close to the canister surface, although microbial activity is possible in the surrounding rock and, depending on the specific properties, may be possible in the tunnel backfill.
- Limited amount of organic carbon restricted to that present in the buffer and backfill materials used to seal the repository. Only a fraction of the total organic material is expected to be available to support microbial activity.
- Large quantities of sulfate, present both as an accessory mineral in the buffer and backfill in the form of gypsum and in the ground water itself.
- Large quantities of ferrous minerals, present both in the host rock and as accessory minerals in the buffer and back materials.

As a consequence of these environmental conditions, the extent of corrosion of the copper canisters is expected to be extremely limited, even over timescales of 10^6 a or longer. Based on the “best-estimate” simulation in Section 4, the total depth of general corrosion is predicted to be 9 µm after 10^6 a, of which approximately 70 % results from the initially trapped O_2 and 30 % from sulfide produced by microbial activity in the backfill and rock and present in the ground water itself. Although the predicted depth of corrosion varies to some degree based on the assumed location of the microbial activity and the inventories of organic material and Fe(II) minerals, the results of the CSM predictions presented here demonstrate that the extent of general corrosion is small and will not result in canister failure in less than 10^6 a.

6.2 Implications of CSM predictions for localised corrosion and SCC of the canister

In addition to the prediction of the rate of general corrosion, the CSM also predicts the evolution of E_{CORR} which is a useful parameter for assessing the probability of other forms of corrosion, as well as for characterising the overall corrosion behaviour. In particular, the value of E_{CORR} can indicate the likelihood of localised corrosion (in the form of pitting) and stress corrosion cracking (SCC).

6.2.1 Pitting

Pitting is the result of spatial separation of the anodic and cathodic reactions due to the breakdown of a passive film. Pit initiation occurs if the value of E_{CORR} exceeds the pitting or breakdown potential (E_B). The breakdown potential depends on a number of factors, especially environmental parameters such as the temperature, pH, and the concentration of aggressive ions, notably Cl^- (Cong et al. 2009). Once initiated, a pit will propagate until the surface re-passivates as the E_{CORR} falls below the re-passivation potential (E_{RP}). The value of E_{RP} tends to be less dependent on environmental conditions, as pit growth is affected more by the maintenance of the critical chemistry inside the pit. Nevertheless, both E_B and E_{RP} are distributed parameters because of the stochastic nature of film breakdown and because of the variability in the surface condition of the copper.

Together with values for the film breakdown and repassivation potentials, predictions of the time dependence of E_{CORR}, such as that shown in Figure 4-1, can be used to assess the probability of pit initiation and the duration of any subsequent propagation. The depth of pit propagation cannot be estimated based on the CSM predictions and would need to be independently assessed. Even if E_{CORR} does exceed E_B under some circumstances, however, the corresponding corrosion rates in Figure 4-2 suggest that propagation would be limited. During the short Phase A which only last 4 months, the rate of (general) corrosion is of the order of 10–20 μm a^{-1}, and attack would have to be highly localised for any significant damage to occur. Once the surface re-wets, corrosion rates during Phase C are only of the order 1–10 nm a^{-1} and, even though this phase is longer, it again seems unlikely that significant damage would result. The durations of Phases A–C depend on the saturation characteristics of the repository, but the general lack of oxidant within the repository and the competing reactions for the available O_2 (Giroud et al. 2018, Müller et al. 2017) make it unlikely that extensive pitting could occur.

It has been suggested that copper is susceptible to pitting due to the localised breakdown of a passive Cu_2S film (Kong et al. 2017a, b, Macdonald et al. 2016, Mao et al. 2014). As discussed in more detail in Section 6.5, all of the experimental evidence on which the CSM is based is consistent with a porous Cu_2S film that would not be susceptible to localised breakdown and pitting. However, regardless of the properties of the Cu_2S film, it is evident from the "best-estimate" CSM predictions that the supply of HS^- to the canister surface would not be sufficient to sustain a pitting process. Corrosion rates are of the order of 0.001 nm a^{-1} during Phases E and F (Figure 4-2) as a result of the limited extent of microbial sulfate reduction and, more importantly, because the vast majority of the sulfide produced is precipitated as mackinawite before it reaches the canister surface.

Although the CSM is useful for predicting the long-term evolution of E_{CORR} for use in assessing the probability of pitting, it must be emphasised that the model is based on the assumption of an active copper surface rather than passive conditions. Thus, if conditions exist within the repository under which the canister surface could be passivated during the early aerobic phase, for instance, due to an elevated pH or a high bicarbonate ion concentration (Qin et al. 2017), then the consequences of this passive film would need to be incorporated into the CSM. Under anaerobic conditions in the presence of sulfide, the supporting experimental evidence suggests that the Cu_2S film is porous and, hence, the treatment of the film properties in the CSM is appropriate (Section 6.5).

6.2.2 Stress corrosion cracking

Copper is known to be susceptible to SCC under aerobic conditions in certain specific environments (King and Newman 2010) and it has been suggested that cracking may also occur in the presence of millimolar concentrations of sulfide (Becker and Öijerholm 2017, Taniguchi and Kawasaki 2008). Under aerobic conditions, cracking has only been reported at potentials and pH values above the Cu_2O/CuO equilibrium line (King and Newman 2010, King et al. 2010). In sulfide environments, cracking is associated with a threshold $[HS^-]$ between 10^{-4} mol/L and 0.001 mol/L (Becker and Öijerholm 2017, Taniguchi and Kawasaki 2008).

Predictions from the CSM can be used to assess the likelihood of SCC in a similar manner to that for pitting. Values of E_{CORR} can be compared against the apparent threshold potentials for cracking, although the CSM does not predict the evolution of the interfacial pH upon which the occurrence of SCC also depends. Furthermore, the existence of an apparent threshold related to the Cu_2O/CuO equilibrium implies some requirement for passivation of the copper surface which, as noted above, is not incorporated into the model. Of more importance, however, is whether the required SCC agent (nitrite, ammonia, or acetate) is present at the canister surface in sufficient concentration at the same time that the potential and interfacial pH exceed the threshold values (King and Newman 2010).

Cracking in sulfide environments is associated with a threshold concentration, rather than a threshold potential (and pH). Despite the fact that there is some question about whether copper is susceptible to SCC in sulfide environments, there have been no reports of "cracking" at (bulk solution) HS^- concentrations of less than 10^{-4}–10^{-3} mol/L (SKB 2019). Based on the "best-estimate" CSM predictions in Section 4, the maximum sulfide concentration at any location in the repository is of the order of 10^{-5} mol/L (Figure 4-13) and, because of the restrictive mass-transport conditions, of the order of 10^{-6} mol/L at the canister surface (Figure 4-4). Regardless of whether the crack-like features reported are in fact SCC cracks, cracking seems highly unlikely under repository conditions because of the low $[HS^-]$.

6.3 Cathodic reaction under anaerobic conditions

Identification of the appropriate cathodic reaction(s) for the model is important as it impacts the predicted E_{CORR} value. It has been suggested that H_2O is the cathodic reactant in sulfide solutions (Macdonald et al. 2016), whereas HS^- has always been treated as the species undergoing electron transfer in the cathodic reaction in the CSM (King 2008, King et al. 2011a, b). The distinction is important as H_2O is present in almost unlimited amounts whereas, as is apparent from the results presented in Sections 4 and 5, relatively little HS^- reaches the canister surface. In addition, the equilibrium potential for the reduction of H_2O is more-positive than that for the evolution of H_2 from HS^- (Figure 6-1). If the anodic reaction is transport limited, as is the case for the sulfidation of copper, the E_{CORR} would be expected to be close to the equilibrium potential for the cathodic reaction.

The attempts at including the reduction of H_2O in the CSM (Version 1.2e, Section 2.3.5) provide some insight into the nature of the cathodic reactions occurring under anaerobic conditions. Based on kinetic data for the reduction of H_2O on copper in sulfide-free solutions (Sharifi-Asl and Macdonald 2013, Appendix A), the predicted E_{CORR} values are inconsistent with those observed experimentally if this reaction is included as an additional cathodic reaction in the CSM. Values of > 0.4 V_{SCE} are predicted for the long-term evolution of E_{CORR} as the repository environment becomes anaerobic (Figure 3-11), which are inconsistent with values in the range -0.9 V_{SCE} to -1.1 V_{SCE} observed experimentally in the presence of sulfide (King et al. 2011a, Smith et al. 2007b).

We are left to conclude, therefore, that either the kinetics of H_2O reduction on copper in the presence of sulfide are quite different from those in sulfide-free solutions, which is quite possible, or that H_2O is not the species undergoing electron transfer, which is also possible. Until such time that additional information is available, the reduction of H_2O will not be included in future simulations using the CSM.

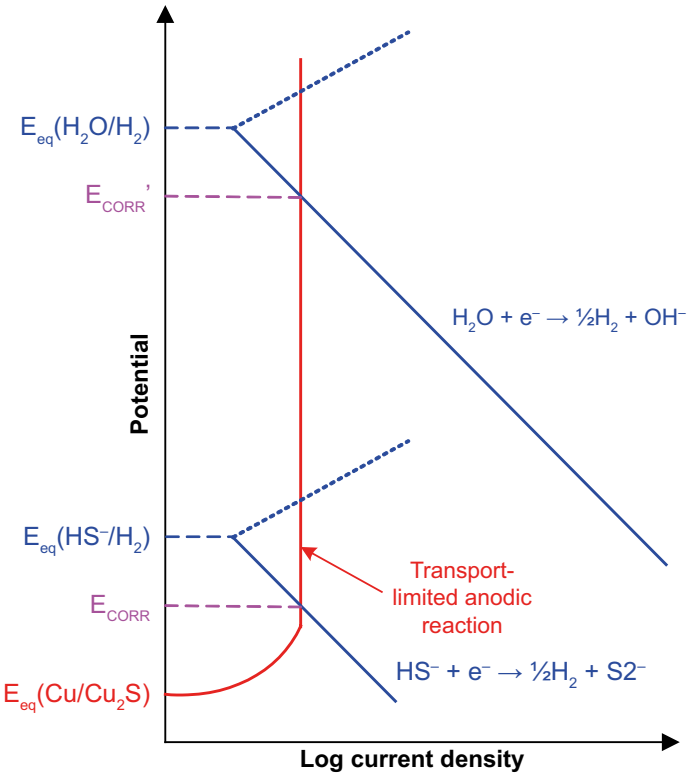

Figure 6-1. *Schematic Evans diagram for two possible cathodic reactions coupled to the transport-limited sulfidation of copper illustrating the effect on E_{CORR} of the equilibrium potential of the cathodic reaction.*

6.4 Spatial separation of anodic and cathodic processes

Another important consideration is the location of the cathodic reaction. The default assumption underlying the CSM is that both anodic and cathodic reactions occur on the same surface, namely the exposed copper surface at the base of pores in the Cu_2S film (or, prior to film formation, equally over the entire surface area). The Cu_2S film is semi-conducting and could sustain electrochemical reactions on the surface. If the cathode:anode surface area ratio exceeds one then the value of E_{CORR} could be ennobled, i.e., shift to more-positive values (Figure 6-2), with implications for the possibility of pitting and SCC. Ennoblement would be more likely if the cathodic reactant was present in high concentration, as in the case of the reduction of H_2O, although that possibility is currently considered unlikely as noted above.

Version 1.3 of the CSM incorporates the possibility of different cathode:anode surface area ratios based on the cathodic reduction of HS^- occurring on either the exposed Cu_2S film surface or on the surface of the film plus the internal surfaces of the pores. These two cases lead to cathode:anode surface area ratios of between 9 and 3.2×10^5, respectively, for the simulations performed here (Section 3.3).

However, despite this large difference in the respective surface areas, the degree of ennoblement is relatively small, ranging from approximately 50 to 250 mV for the range of surface area ratios. The greatest ennoblement occurs at later times with relatively thick Cu_2S films which result in the largest cathode areas on the internal surfaces of the pores. It should be emphasised that the shift of E_{CORR} to more-positive values does not correspond to an increase in corrosion rate, since the rate remains limited by the rate of supply of HS^- to the canister surface. The ennoblement of E_{CORR} is only of concern if it increases the probability of pit initiation but, given the porous nature of the Cu_2S films, this possibility if considered unlikely regardless of the value of E_{CORR}. Had H_2O been included as an oxidant, it is likely that the degree of ennoblement would have been greater.

The fact that the predicted E_{CORR} does shift to more-positive values with increasing surface area ratio does have implications for the nature of the rate-controlling processes under repository conditions. If both anodic and cathodic reactions were transport-controlled by the rate of supply of HS^-, then E_{CORR} would be independent of the areas of the cathodes and anodes since the rate of supply of sulfide is determined by the geometric surface area which is the same for both reactions. The positive shift in

E_{CORR} with increasing surface area ratio (Figure 6-3) suggests, therefore, that the cathodic reaction is under (partial) kinetic control (Figure 6-2). This is consistent with the non-zero interfacial [HS^-] predicted using the CSM (Figure 4-4). Overall, however, it is reasonable to conclude that the rate of corrosion is sulfide-transport limited.

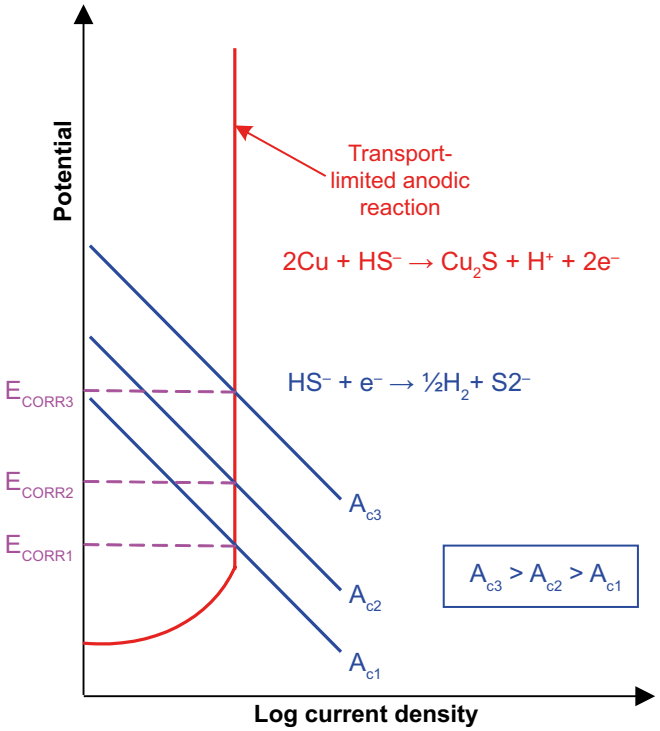

Figure 6-2. *Schematic Evans diagram for the coupling of a transport-limited anodic process and a kinetically limited cathodic reaction occurring at locations of increasing surface area.*

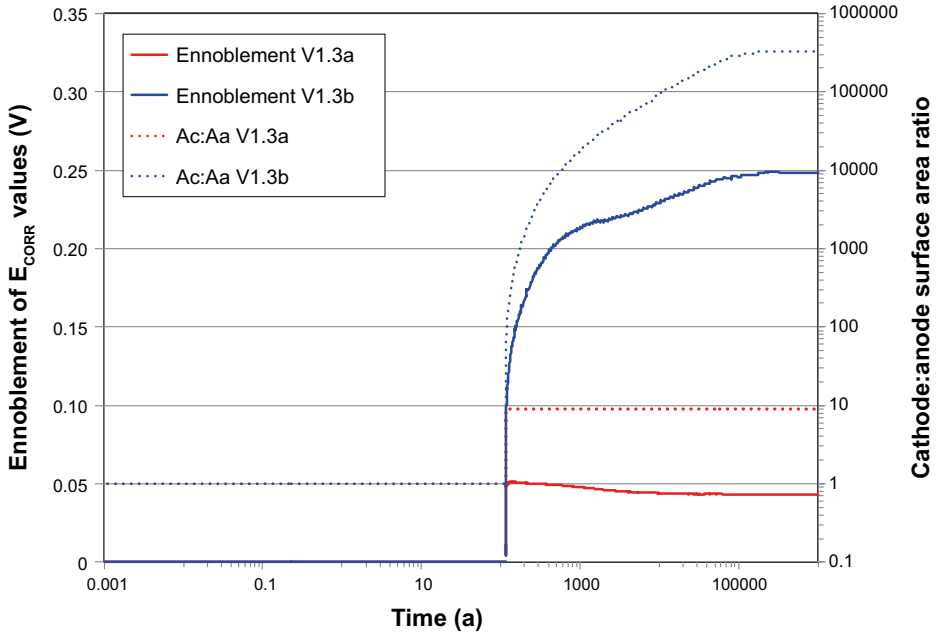

Figure 6-3. *Effect of cathode:anode surface area ratio on the ennoblement of E_{CORR} predicted using CSM Version 1.3. For simulations V1.3a and V1.3b, the cathodic reduction of HS^- was assumed to occur either only on the surface of the Cu_2S film or both on the exposed surface and the internal surfaces of the pores in the film, respectively. The anodic reaction was limited to the exposed copper surface at the base of the pores in the film. The degree of ennoblement of E_{CORR} was determined as the difference between the value predicted based on Version 1.3 and the value estimated using the full Version 1.2a-f code (Figure 3-24). The cathode:anode surface area ratio is denoted Ac:Aa in the figure legend.*

6.5 The nature of the Cu_2S film

Another important aspect of the CSM is the treatment of the formation and properties of the precipitated Cu_2S film. Cuprous sulfide is highly insoluble and will form a Cu_2S film on the canister surface. In the CSM, this film is treated as being porous with the interfacial reactions occurring at the base of the pores, with the possibility of the cathodic reaction occurring on the surface and/or within the pores of the Cu_2S film in Version 1.3. Others consider the film to be passive and report potential-independent currents as evidence of passivity (Kong et al. 2017a, b, Macdonald et al. 2016, Mao et al. 2014). The nature of the film structure is not only important for how it is modeled in the CSM but, as discussed above, also has implications for the possibility of localised corrosion. A porous, partially protective film will not exhibit localized film breakdown and pitting corrosion. The structure and properties of Cu_2S films depend on a number of factors, including: the $[HS^-]$, electrochemical potential, the $[Cl^-]$:$[HS^-]$ ratio, and the rate of HS^- transport (Chen et al. 2010, 2011a, b, 2012, 2014a, b, 2017, Martino et al. 2014, 2017, Smith et al. 2006, 2007a, b). Under conditions relevant to the corrosion of the canister (open-circuit potential, low $[HS^-]$ and low rate of transport), the film structure is porous and grows at a constant rate, inconsistent with the behaviour expected of a passive film (Chen et al. 2010). It is interesting to note that the reported "passive current densities" increase with increasing $[HS^-]$ consistent with transport control (Kong et al. 2017a), and exhibit a value of 0.46 mA/cm^2 in 0.005 mol/L solution, equivalent to a corrosion rate of 11 mm/yr. In contrast, all of the experimental data on which the interfacial mechanisms in the CSM are based are consistent with the transport-limited growth of a porous Cu_2S film and this is how it is treated in the model.

6.6 Effect of gaseous H_2S

A preliminary simulation has been performed to determine the effect of gaseous H_2S on the early corrosion behaviour of the canister. The duration of this gas-phase sulfidation process depends in part on the saturation time for the buffer and backfill materials. Gaseous species diffuse relatively rapidly in unsaturated buffer and backfill, but desiccation of the backfill also limits the extent of possible microbial sulfate reduction, which has been shown to be the primary source of $H_2S(g)$. Volatilisation of dissolved sulfide in the host rock does not appear to be a significant source of gaseous H_2S because the low porosity limits the amount of sulfide that can be released to the gas phase.

The results of this preliminary simulation suggest that early formation of a Cu_2S film may occur as a result of gas-phase processes. The properties of such a film and the consequences for subsequent aqueous corrosion processes once the repository has saturated have still to be determined.

The current reaction scheme for the effects of gaseous H_2S is considered to be conservative as it does not include any other reactions that could act as a sink for sulfide. In contrast, the precipitation of FeS is shown to account for > 99 % of the dissolved HS^- produced in the repository and acts as a significant sink for sulfide, thus limiting the extent of corrosion of the canister. Further developments of the CSM V1.2a-h should include additional reactions between gaseous H_2S and other components in the buffer and backfill.

Although Cu_2S film formation is predicted to occur under unsaturated conditions, the extent of gas-phase sulfidation is no greater than that expected over the entire one million year simulation period as a result of corrosion under saturated conditions. The sensitivity of the extent of the gas phase reaction on factors such as the saturation time, the effect of desiccation on microbial activity, the availability of sulfate and of sulfide sinks, etc should be considered in further simulations.

6.7 Status and future development of the CSM

The CSM Version 1.2a-g is based on our current mechanistic understanding of the corrosion behaviour of copper under both aerobic and anaerobic conditions representative of those expected in a KBS-3 design repository. The incorporation of the more-detailed kinetic description of the microbial reduction of sulfate represents a significant improvement in the treatment of this important source of sulfide. Further improvements to the code may be required as and when additional mechanistic insight is developed in the companion experimental programme at the University of Western Ontario. In addition, the

impact of the reversible precipitation/dissolution of mackinawite should be considered since Cu_2S is less soluble than FeS, as well as the possibility that FeS will convert to a more-thermodynamically-stable, less-soluble, iron sulfide phase, although phase transformation may be kinetically hindered in near-neutral-pH environments. In the meantime, the current version of the code is considered to provide a reliable prediction of the long-term corrosion behaviour of the canister and of the evolution of the near-field corrosive environment.

One area requiring additional work is the implementation of the single inter-layer porosity model in the CSM. Although the Donnan equilibrium between ions across different interfaces has been implemented in Version 2.0 of the code, it is premature to conclude that the single porosity model leads to greater corrosion than the traditional multi-porosity model, as suggested by the preliminary simulations performed to date.

Additional validation of the CSM is also required. There has been limited validation so far involving a comparison of predictions from Version 1.1 against a single experimental E_{CORR} measurement with a clay-covered electrode immersed in a sulfide-containing Cl^- solution (King et al. 2011a). It would be helpful to validate Version 1.2a-g against these same data, as well as any other E_{CORR} and corrosion rate measurements available in the literature or planned as part of future experimental work. It may also be feasible to validate the CSM against the microbial activity measurements of Bengtsson et al. (2017). Although these tests did not involve measurement of E_{CORR}, these authors do report corrosion depth measurements (in the form of the amount of labelled Cu_2S formed on copper coupons), albeit using a complex geometrical layout that might be difficult to simulate using the 1-D CSM.

The inter-model comparison exercise conducted as part of the ISP has highlighted some of the (known) limitations of 1-D codes, such as the CSM. When modelling processes that are transport controlled or for which diffusion plays an important role, it is necessary to consider the possibility of enhanced transport due to radial or spherical diffusion effects. For example, when modelling the transport of sulfide produced in the interface region around the deposition hole to the canister surface, the increased radial flux (compared to a 1-D linear model) would be approximately proportional to the ratio of the radii of the deposition hole to that of the canister. Now that the underlying mechanism of the CSM has been further developed, it would seem appropriate to consider extending the model from 1-D to 3-D to better represent the more-complex mass-transport regime within the repository.

7 Conclusions

Various improvements and additions have been made to the Copper Sulfide Model. Some of these updates are based on an improved mechanistic understanding of the underlying corrosion processes and environmental conditions and others have been made to correct errors or omissions in an earlier version of the model. Of particular note is the improved treatment of microbial sulfate reduction, which now accounts for both organotrophic and chemotrophic processes as well as possible limitation by the availability of organic carbon and/or sulfate. The importance of mackinawite precipitation as a sink for sulfide is also now incorporated in the model.

The various applications of the model have also been extended to address issues such as the spatial separation of anodic and cathodic processes, of gaseous H_2S under unsaturated conditions, and of the implications of the bentonite pore-water model used to describe mass transport.

The CSM is capable of predicting not only the long-term corrosion behaviour of the copper canister but also the evolution of the corrosive environment in the repository. From a corrosion perspective, the CSM predictions suggest that the repository environment can be characterised as:

- Oxygen-deficient, limited to that trapped in the unsaturated fraction of the pores in the buffer and backfill materials at the time of emplacement.
- Restrictive mass transport of reactants towards, and of corrosion products away from, the canister surface through the compacted clay-based buffer and backfill materials.
- Initially warm (maximum canister surface temperature of 80–90 °C), with temperatures diminishing to close to ambient within a few tens of thousands of years.
- Inhospitable for microbes close to the canister surface, although microbial activity may occur elsewhere in the near- and far-fields.
- Containing a limited amount of organic carbon restricted to that present in the buffer and backfill materials used to seal the repository, but large quantities of both sulfate and Fe(II) minerals.

As a result of these environmental conditions, the extent of corrosion is predicted to be limited. Based on the best-estimate simulation, the depth of general corrosion due to both the initially trapped oxygen and sulfide produced by microbial activity or present in the ground water is predicted to be < 10 μm after one million years. During this time, the corrosion potential evolves from relatively positive values during the aerobic phase to more-negative values as conditions become anaerobic. Once sulfide reaches the canister surface, E_{CORR} is predicted to decrease to long-term values in the range to −0.9 V_{SCE} to −1.0 V_{SCE} as the corrosion behaviour becomes dominated by the presence of sulfide.

References

SKB's (Svensk Kärnbränslehantering AB) publications can be found at www.skb.com/publications.

Åkesson M, Kristensson O, Börgesson L, Dueck A, Hernelind J, 2010. THM modelling of buffer, backfill and other system components. Critical processes and scenarios. SKB TR-10-11, Svensk Kärnbränslehantering AB.

Astakhova R K, Krasikov B S, 1971. Electrochemical behaviour of copper in chloride electrolytes. Applied Chemistry USSR 44, 356–362.

Bacarella A L, Griess J C, 1973. The anodic dissolution of copper in flowing sodium chloride solutions from 25 ºC and 175 ºC. Electrochemical Society 120, 459–465.

Barbour J C, Sullivan J P, Campin M J, Wright A F, Wissert N A, Braithwaite J W, Zavadil K R, Sorensen N R, Lucero S J, Breiland W G, Moffat H K, 2002. Mechanisms of atmospheric copper sulfidation and evaluation of parallel experimentation techniques. Sandia Report SAND2002-0699, Sandia National Laboratories, New Mexico.

Becker R, Öijerholm J, 2017. Slow strain rate testing of copper in sulfide rich chloride containing deoxygenated water at 90 °C. Technical Report 2017:02, Swedish Radiation Safety Authority.

Bengtsson A, Blom A, Hallbeck B, Heed C, Johansson L, Stalén J, Pedersen K, 2017. Microbial sulphide-producing activity in water saturated MX-80, Asha and Calcigel bentonite at wet densities from 1 500 to 2 000 kg m^{-3}. SKB TR-16-09, Svensk Kärnbränslehantering AB.

Bertocci U, Turner D R, 1974. Copper. Bard A J (ed). In Encyclopedia of the elements, Volume II. New York: Marcel Dekker, Chapter II-6, Table 1.1.2.

Birgersson M, Karnland O, 2009. Ion equilibrium between montmorillonite interlayer space and an external solution – Consequences for diffusional transport. Geochimica et Cosmochimica Acta 73, 1908−1923.

Bradbury M H, Baeyens B, 2003. Porewater chemistry in compacted re-saturated MX-80 bentonite. Journal of Contaminant Hydrology 61, 329–338.

Brown A D, 1990. Microbial water stress physiology: principles and perspectives. Chichester: Wiley.

Byegård J, Selnert E, Tullborg E-L, 2008. Bedrock transport properties. Data evaluation and retardation model. Site descriptive modelling SDM-Site Forsmark. SKB R-08-98, Svensk Kärnbränslehantering AB.

Chen J, Qin Z, Shoesmith D W, 2010. Kinetics of corrosion film growth on copper in neutral chloride solutions containing small concentrations of sulfide. Journal of The Electrochemical Society 157, C338–C345.

Chen J, Qin Z, Shoesmith D W, 2011a. Long-term corrosion of copper in a dilute anaerobic sulfide solution. Electrochimica Acta 56, 7854–7861.

Chen J, Qin Z, Shoesmith D W, 2011b. Rate controlling reactions for copper corrosion in anaerobic aqueous sulphide solutions. Corrosion Engineering, Science and Technology 46, 138–141.

Chen J, Qin Z, Shoesmith D W, 2012. Copper corrosion in aqueous sulfide solutions under nuclear waste repository conditions. In Scientific basis for nuclear waste management XXXV: symposium held in Buenos Aires, Argentina, 2–7 October 2011. Warrendale, PA: Materials Research Society. (Materials Research Society Symposium Proceedings 1475), 465–470.

Chen J, Qin Z, Shoesmith D W, 2014a. Key parameters determining structure and properties of sulphide films formed on copper corroding in anoxic sulphide solutions. Corrosion Engineering, Science and Technology 49, 415–419.

Chen J, Qin Z, Wu L, Noël J J, Shoesmith D W, 2014b. The influence of sulphide transport on the growth and properties of copper sulphide films on copper. Corrosion Science 87, 233–238.

Chen J, Qin Z, Martino T, Shoesmith D W, 2017. Effect of chloride on Cu corrosion in anaerobic sulphide solutions. Corrosion Engineering, Science and Technology 52, 40–44.

Chen J, Qin Z, Martino T, Guo M, Shoesmith D W, 2018. Copper transport and sulphide sequestration during copper corrosion in anaerobic aqueous sulphide solutions. Corrosion Science 131, 245–251.

Cong H, Michels H T, Scully J R, 2009. Passivity and pit stability behaviour of copper as a function of selected water chemistry variables. Journal of the Electrochemical Society 156, C16–C27.

CRC, 1982. Handbook of chemistry and physics: a ready-reference book of chemical and physical data. 63rd ed. Boca Raton, FL: CRC Press.

Dixon D G, 2000. Analysis of heat conservation during copper sulphide heap leaching. Hydrometallurgy 58, 27–41.

Dixon D A, Chandler N A, Stroes-Gascoyne S, Kozak E, 2001. The isothermal buffer-rock-concrete plug interaction test: final report. Report 06819−REP−01200−10056−R00, Ontario Power Generation, Nuclear Waste Management Division, Canada.

Fontana A, Van Muylder J, Winand R, 1985. Etablissement de diagrammes tension-pH cinetiques du cuivre en milieu de chlorures. Electrochimica Acta 30, 641−647. (In French.)

Garisto F, D'Andrea A, Gierszewski P, Melnyk T, 2004. Third Case Study – reference data and codes. Report 06819-REP-01200-10107-R00, Ontario Power Generation, Nuclear Waste Management Division, Canada.

Giroud N, Tomonaga Y, Wersin P, Briggs S, F King, Kipfer R, Diomidis N, 2018. On the fate of oxygen in a spent fuel emplacement drift in Opalinus Clay. Applied Geochemistry 97, 270–278.

Graedel T E, Franey J P, Gualtieri G J, Kammlott G W, Malm D L, 1985. On the mechanism of silver and copper sulfidation by atmospheric H_2S and OCS. Corrosion Science 25, 1163–1180.

Hallbeck L, Pedersen K, 2008. Characterization of microbial processes in deep aquifers of the Fennoscandian Shield. Applied Geochemistry 23, 1796–1819.

Hartley L, Hoek J, Swan D, Appleyard P, Baxter S, Roberts D, Simpson T, 2013. Hydrogeological modelling for assessment of radionuclide release scenarios for the repository system 2012. Posiva Working Report 2012-42, Posiva Oy, Finland.

Hellä P, Pitkänen P, Löfman J, Partamies S, Vuorinen U, Wersin P, 2014. Safety case for the disposal of spent nuclear fuel at Olkiluoto. Definition of reference and bounding groundwaters, buffer and backfill porewaters. Posiva Report 2014-04, Posiva Oy, Finland.

Hurlen T, 1961. Dissolution of copper by oxidation agents in acid chloride solution. Acta Chemica Scandinavica 15, 1239–1245.

ICT, 1926. International critical tables of numerical data, physics, chemistry and technology. New York: McGraw-Hill.

Idiart A, Pękala M, 2016. Models for diffusion in compacted bentonite. SKB TR-15-06, Svensk Kärnbränslehantering AB.

Idiart A, Coene E, Bagaria F, Román-Ross G, Birgersson M, 2019. Reactive transport modelling considering transport in interlayer water – new model, sensitivity analyses and results from the Integrated Sulfide Project inter-model comparison exercise. SKB TR-18-07, Svensk Kärnbränslehantering AB.

Jin Q, Roden E E, Giska J R, 2013. Geomicrobial kinetics: Extrapolating laboratory studies to natural environments. Geomicrobiology Journal 30, 173–185.

Johnson L H, LeNeveu D M, Shoesmith D W, Oscarson D W, Gray M N, Lemire R J, Garisto N C, 1994. The disposal of Canada's nuclear fuel waste: the vault model for postclosure assessment. Report AECL-10714, COG-93-4, Atomic Energy of Canada Limited.

King F, 2008. Mixed-potential modelling of the corrosion of copper in the presence of sulphide. Posiva Working Report 2007-63, Posiva Oy, Finland.

King F, 2009. Microbiologically influenced corrosion of nuclear waste containers. Corrosion 65, 233–251.

King F, 2013. A review of the properties of pyrite and the implications for corrosion of the canister. SKB TR-13-19, Svensk Kärnbränslehantering AB.

King F, Kolář M, 2000. The copper container corrosion model used in AECL's second case study. Report 06819REP-01200-10041-R00, Ontario Power Generation, Nuclear Waste Management Division, Canada.

King F, Kolář M, 2006. Simulation of the consumption of oxygen in long-term *in situ* experiments and in the Third Case Study repository using the copper corrosion model CCM-UC.1.1. Report No: 06819-REP-01300-10084, Ontario Power Generation, Nuclear Waste Management Division, Canada.

King F, Kolář M, 2012. Simulation of the anaerobic corrosion of carbon steel used fuel containers using the Steel Corrosion Model Version 1.0 (SCM V1.0). NWMO TR-2012-07, Nuclear Waste Management Organization, Canada.

King F, Newman R, 2010. Stress corrosion cracking of copper canisters. SKB TR-10-04, Svensk Kärnbränslehantering AB.

King F, Litke C D, Quinn M J, LeNeveu D M, 1995a. The measurement and prediction of the corrosion potential of copper in chloride solutions as a function of oxygen concentration and mass-transfer coefficient. Corrosion Science 37, 833–851.

King F, Quinn M J, Litke C D, 1995b. Oxygen reduction on copper in neutral NaCl solution. Electroanalysis Chemistry 385, 45–55.

King F, Kolář M, Shoesmith D W, 1996. Modelling the effects of porous and semi-permeable layers on corrosion processes. In Proceedings of CORROSION 96, Denver, Colorado, 24–29 March 1996. Houston, TX: NACE International, paper 380. (Also published as Atomic Energy of Canada Limited Report AECL-11592, COG-96-273).

King F, Kolář M, Stroes-Gascoyne S, Bellingham P, Chu J, Dawe P V, 1999. Modelling the activity of sulphate-reducing bacteria and the effects on container corrosion in an underground nuclear waste disposal vault. In Wronkiewicz D J, Lee J L (eds). Scientific basis for nuclear waste management XXII: symposium held in Boston, Massachusetts, 30 November – 4 December 1998. Warrendale, PA: Materials Research Society. (Materials Research Society Symposium Proceedings 556), 1167–1174.

King F, Kolář M, Stroes-Gascoyne S, 2002. Theory manual for the microbiological copper corrosion model CCM-MIC.0. Report 06819-REP-01200-10091, Ontario Power Generation Nuclear Waste Management Division, Canada.

King F, Kolář M, Stroes-Gascoyne S, 2003. Preliminary simulations of the long-term activity of microbes in a deep geologic repository using CCM-MIC.0 and the implications for corrosion of copper containers. Report 06819-REP-01200-10116-R00, Ontario Power Generation, Nuclear Waste Management Division, Canada.

King F, Jack T R, Kolář M, Worthingham R G, 2004a. A permeable coating model for predicting the environment at the pipe surface under CP-compatible coatings. In Proceeding of CORROSION 2004, New Orleans, Louisiana, 28 March – 1 April 2004. NACE International, paper 04158.

King F, Kolář M, Stroes-Gascoyne S, Maak P, 2004b. Model for the microbiological corrosion of copper containers in a deep geologic repository. In Oversby V M, Werme L O (eds). Scientific basis for nuclear waste management XXVII: symposium held in Kalmar, Sweden, 15–19 June 2003. Warrendale, PA: Materials Research Society. (Materials Research Society Symposium Proceedings 807), 811–816.

King F, Kolář M, Maak P, 2008. Reactive-transport model for the prediction of the uniform corrosion behaviour of copper used fuel containers. Journal of Nuclear Materials 379, 133–141.

King F, Lilja C, Pedersen K, Pitkänen P, Vähänen M, 2010. An update of the state-of-the-art report on the corrosion of copper under expected conditions in a deep geologic repository. SKB TR-10-67, Svensk Kärnbränslehantering AB.

King F, Kolář M, Vähänen M, 2011a. Reactive-transport modelling of the sulphide-assisted corrosion of copper nuclear waste containers. In Féron D, Kursten B, Druyts F (eds). Sulphur-assisted corrosion in nuclear disposal systems. Leeds: Maney Publishing. (European Federation of Corrosion Publication 59), 152–164.

King F, Kolář M, Vähänen M, Lilja C, 2011b. Modelling the long-term corrosion behaviour of copper canisters in a KBS-3 repository. Corrosion Engineering, Science and Technology 46, 217–222.

King F, Kolář M, Keech P G, 2014. Simulations of long-term anaerobic corrosion of carbon steel containers in Canadian deep geological repository. Corrosion Engineering, Science and Technology 49, 455–459.

King F, Hall D S, Keech P G, 2017a. Nature of the near-field environment in a deep geological repository and the implications for the corrosion behaviour of the container. Corrosion Engineering, Science and Technology 52 sup1, 25–30.

King F, Chen J, Qin Z, Shoesmith D, Lilja C, 2017b. Sulphide transport control of the corrosion of copper canisters. Corrosion Engineering, Science and Technology 52 sup1, 210–216.

Kinoshita K, 1992. Electrochemical oxygen technology. New York: Wiley.

Kolář M, 2016. Transient. Available at: http://transient.mkolar.org/

Kong D, Dong C, Xu A, Man C, He C, Li X, 2017a. Effect of sulfide concentration on copper corrosion in anoxic chloride-containing solutions. Journal of Materials Engineering and Performance 26, 1741–1750.

Kong D, Xu A, Dong C, Mao F, Xiao K, Li X, Macdonald D D, 2017b. Electrochemical investigation and *ab initio* computation of passive film properties on copper in anaerobic sulphide solutions. Corrosion Science 116, 34–43.

Kukkonen I, 2015. Thermal properties of rocks at Olkiluoto: Results of laboratory measurements 1994–2015. Posiva Working Report 2015-30, Posiva Oy, Finland.

Lovley D R, Klug M J, 1986. Model for the distribution of sulfate reduction and methanogenesis in freshwater sediments. Geochimica et Cosmochimica Acta 50, 11–18.

Luther G W, Theberge S M, Rozan T F, Rickard D, Rowlands C C, Oldroyd A, 2002. Aqueous copper sulfide clusters as intermediates during copper sulfide formation. Environmental Science & Technology 36, 394–402.

Macdonald D D, Mao F, Dong C, Sharifi-Asl S, 2016. Measurement of parameter values for predicting corrosion phenomena on copper in Swedish HLNW repositories. Phase IV: Impact of chloride ion on the passivity and pitting of copper. Report 2016:30, Swedish Radiation Safety Authority.

Maia F, Puigdomenech I, Molinero J, 2016. Modelling rates of bacterial sulfide production using lactate and hydrogen as energy sources. SKB TR-16-05, Svensk Kärnbränslehantering AB.

Malmström M, Banwart S, Duro L, Wersin P, Bruno J, 1995. Biotite and chlorite weathering at 25 ºC: The dependence of pH and (bi)carbonate on weathering kinetics, dissolution stoichiometry, and solubility; and the relation to redox conditions in qranitic aquifers. SKB TR 95-01, Svensk Kärnbränslehantering AB.

Man A, Martino J B, 2009. Thermal, hydraulic and mechanical properties of sealing materials. NWMO TR-2009-20, Nuclear Waste Management Organization, Canada.

Mao F, Dong C, Sharifi-Asl S, Lu P, Macdonald D D, 2014. Passivity breakdown on copper: influence of chloride ion. Electrochimica Acta 144, 391–399.

Martino T, Partovi-Nia R, Chen J, Qin Z, Shoesmith D W, 2014. Mechanisms of film growth on copper in aqueous solutions containing sulphide and chloride under voltammetric conditions. Electrochimica Acta 127, 439–447.

Martino T, Chen J, Qin Z, Shoesmith D W, 2017. The kinetics of film growth and their influence on the susceptibility to pitting of copper in aqueous sulphide solutions. Corrosion Engineering, Science and Technology 52, 61–64.

Masurat P, Eriksson S, Pedersen K, 2010. Microbial sulphide production in compacted Wyoming bentonite MX-80 under *in situ* conditions relevant to a repository for high-level radioactive waste. Applied Clay Science 47, 58–64.

Miller D G, Rard J A, Eppstein L B, Robinson R A, 1980. Mutual diffusion coefficients, electrical conductances, osmotic coefficients, and ionic transport coefficients l_{ij} for aqueous $CuSO_4$ at 25 ºC. Journal of Solution Chemistry 9, 467–496.

Müller H R, Garitte B, T Vogt, Köhler S, Sakaki T, Weber H, Spillmann T, Hertrich M, Becker J K, Giroud N, V Cloet, Diomidis N, Vietor T, 2017. Implementation of the full-scale emplacement (FE) experiment at the Mont Terri rock laboratory. Swiss Journal of Geosciences 110, 287–306.

Nethe-Jaenchen R, Thauer R K, 1984. Growth yields and saturation constant of *Desulfovibrio vulgaris* in chemostat culture. Archives of Microbiology 137, 236–240.

Oscarson D W, Hume H B, Sawatsky N G, Cheung S C H, 1992. Diffusion of iodide in compacted bentonite. Soil Science Society of America 56, 1400–1406.

Palmer D A, 2011. Solubility measurements of crystalline Cu_2O in aqueous solution as a function of temperature and pH. Journal of Solution Chemistry 40, 1067–1093.

Pastina B, Hellä P (eds), 2006. Expected evolution of a spent fuel repository at Olkiluoto. Revised October 2007. Posiva 2006-05, Posiva Oy, Finland.

Paulamäki S, Paananen M, Gehör S, Kärki A, Front K, Aaltonen I, Ahokas T, Kemppainen K, Mattila J, Wikström L, 2006. Geological model of the Olkiluoto site. Version 0. Posiva Working Report 2006-37, Posiva Oy, Finland.

Pedersen K, 2012a. Subterranean microbial populations metabolize hydrogen and acetate under in situ conditions in granitic groundwater at 450 m depth in the Äspö Hard Rock Laboratory, Sweden. FEMS Microbiology Ecology 81, 217–229.

Pedersen K, 2012b. Influence of H_2 and O_2 on sulfate-reducing activity of a subterranean community and the coupled response in redox potential. FEMS Microbiology Ecology 82, 653–665.

Pękala M, Alt-Epping P, Wersin P, 2019. 3D and 1D dual-porosity reactive transport simulations – model improvements, sensitivity analyses, and results from the Integrated Sulfide Project inter-model comparison exercise. Posiva Working Report 2018-31, Posiva Oy, Finland.

Peters D G, Cruser S A, 1965. Cathodic chronopotentiometry of copper(I) and copper(II) in chloride media. Electrochemical Society 9, 27–40.

Posiva, 2012. Safety case for the disposal of spent nuclear fuel at Olkiluoto – Description of the disposal system 2012. Posiva 2012-05, Posiva Oy, Finland.

Posiva, 2013. Safety case for the disposal of spent nuclear fuel at Olkiluoto – Models and data for the repository system 2012. Posiva 2013-01, Posiva Oy, Finland.

Qin Z, Deljeet R, Ai M, Farhangi N, Noël J, Ramamurthy S, Shoesmith D, King F, Keech P, 2017. The active/passive conditions for copper corrosion under nuclear waste repository environment. Corrosion Engineering, Science and Technology 52 sup1, 45–49.

Robinson R A, Stokes R H, 1959. Electrolyte solutions: the measurement and interpretation of conductance, chemical potential and diffusion in solutions of simple electrolytes. 2nd ed. London: Butterworths.

Ryan S R, King F, 1994. The adsorption of Cu(II) on sodium bentonite in a synthetic saline groundwater. Report AECL-11062, COG-I-94-125, Atomic Energy of Canada Limited.

Saanio T, Ikonen A, Keto P, Kirkkomäki T, Kukkola T, Nieminen J, Raiko H, 2013. Design of the disposal facility 2012. Posiva Working Report 2013-17, Posiva Oy, Finland.

Salmon S U, Malmström M E, 2004. Geochemical processes in mill tailings deposits: modelling of groundwater composition. Applied Geochemistry19, 1–17.

Sander R, 1999. Compilation of Henry's law constants for inorganic and organic species of potential importance in environmental chemistry. Version 3. Mainz, Germany: Max-Planck Institute of Chemistry. Available at: https://www.ft.unicamp.br/~mariaacm/ST405/Lei%20de%20Henry.pdf

Sharifi-Asl S, Macdonald D D, 2013. Investigation of the kinetics and mechanism of the hydrogen evolution reaction on copper. Journal of The Electrochemical Society 160, H382–H391.

Sharma V K, Millero F J, 1988. The oxidation of Cu(I) in electrolyte solutions. Journal of Solution Chemistry 17, 581–599.

SKB, 2006a. Long-term safety for KBS-3 repositories at Forsmark and Laxemar – a first evaluation. Main report of the SR-Can project. SKB TR-06-09, Svensk Kärnbränslehantering AB.

SKB, 2006b. Data report for the safety assessment SR-Can. Swedish Nuclear Fuel Supply Company, SKB Report TR-06-25.

SKB, 2006c. Platsundersökning Forsmark. Årsrapport 2005. Svensk Kärnbränslehantering AB.

SKB, 2010. Corrosion calculations report for the safety assessment SR-Site. SKB TR-10-66, Svensk Kärnbränslehantering AB.

SKB, 2019. Supplementary information on canister integrity issues. Swedish Nuclear Fuel and Waste Management Company Report, SKB Report TR-19-15.

Smith J, Qin Z, King F, Werme L, Shoesmith D W, 2006. The electrochemistry of copper in aqueous sulphide solutions. In Van Iseghem P (ed). Scientific basis for nuclear waste management XXIX: proceedings of a meeting held in Ghent, Belgium, 12–16 September 2005. Warrendale, PA: Materials Research Society. (Materials Research Society Symposium Proceedings 932), 869–876.

Smith J M, Wren J C, Odziemkowski M, Shoesmith D W, 2007a. The electrochemical response of preoxidized copper in aqueous sulfide solutions. Journal of The Electrochemical Society 154, C431–C438.

Smith J, Qin Z, King F, Werme L, Shoesmith D W, 2007b. Sulfide film formation on copper under electrochemical and natural corrosion conditions. Corrosion 63, 135–144.

Smyrl W H, 1985. Digital impedance for Faradaic analysis. Part II. Electrodissolution of Cu in HCl. Electrochemical Society 132, 1555–1562.

Stroes-Gascoyne S, Haveman S A, Vilks P, 1997. The change in bioavailability of organic matter associated with clay-based buffer materials as a result of heat and radiation treatment. In Gray W J, Triay I R (eds). Scientific basis for nuclear waste management XX: symposium held in Boston, Massachusetts, USA, 2–6 December 1996. Pittsburgh, PA: Materials Research Society. (Materials Research Society Symposium Proceedings 465), 987–994.

Stroes-Gascoyne S, Hamon C J, Vilks P, 2000. Microbial analysis of the Isothermal Test at AECL's Underground Research Laboratory. Report 06819-REP-01200-10023-R00 Ontario Power Generation, Nuclear Waste Management Division, Canada.

Suleimenov O M, Seward T M, 1997. A spectrophotometric study of hydrogen sulfide ionization in aqueous solutions to 350 °C. Geochimica et Cosmochimica Acta 61, 5187–5198.

Sun W, Nešić S, Young D, Woollam R C, 2008. Equilibrium expressions related to the solubility of the sour corrosion product mackinawite. Industrial & Engineering Chemistry Research 47, 1738–1742.

Taniguchi N, Kawasaki M, 2008. Influence of sulfide concentration on the corrosion behaviour of pure copper in synthetic seawater. Journal of Nuclear Materials 379, 154–161.

Tran T T M, Fiaud C, Sutter E M M, Villanova A, 2003. The atmospheric corrosion of copper by hydrogen sulphide in underground conditions. Corrosion Science 45, 2787–2802.

Tran T T M, Fiaud C, Sutter E M M, 2005. Oxide and sulphide layers on copper exposed to H_2S containing moist air. Corrosion Science 47, 1724–1737.

Truche L, Berger G, Destrigneville C, Pages A, Guillaume D, Giffaut E, Jacquot E, 2009. Experimental reduction of aqueous sulphate by hydrogen under hydrothermal conditions: implication for the nuclear waste storage. Geochimica et Cosmochimica Acta 73, 4824–4835.

Truche L, Berger G, Destrigneville C, Guillaume D, Giffaut E, 2010. Kinetics of pyrite to pyrrhotite reduction by hydrogen in calcite buffered solutions between 90 and 180 °C: implications for nuclear waste disposal. Geochimica et Cosmochimica Acta 74, 2894–2914.

van Bodegom P M, 2007. Microbial maintenance: a critical review on its quantification. Microbial Ecology 53, 513–523.

Vaittinen T, Hellä P, Nummela J, Tammisto E, Paulamäki S, Front K, 2005. Bedrock model of the Olkiluoto site, KR5 sub-volume, Version 2002/1. Posiva Working Report 2004-56, Posiva Oy, Finland.

Van Muylder J, de Zoubov N, Pourbaix M, 1961. Diagrammes d'equilibres tension-pH des systemes Cu-H_2O et Cu-Cl^--H_2O a 25 ºC. Report 755, CEBELCOR (Centre Belges D'Etudes de la Corrosion), Belgium. (In French.)

Vaughan D J, 2005. Minerals/Sulphides. In Selley R C, CocksL R M, Plimer I A (eds). Encyclopedia of geology. Amsterdam: Elsevier, 574–586.

Vilks P, Stroes-Gascoyne S, Goulard M, Haveman S A, Bachinski D H, 1998. The release of organic material from clay based buffer materials and its potential implications for radionuclide transport. Radiochim. Acta 82, 385–391.

Wagman D D, Evans W H, Parker V B, Schumm R H, Halow I, Bailey S M, Churney K L, Nuttall R L, 1982. The NBS tables of chemical thermodynamic properties. Selected values for inorganic and C_1 and C_2 organic substances in SI units. Journal of Physical and Chemical Reference Data 11, Supplement 2.

Wersin P, Alt-Epping P, Pitkänen P, Román-Ross G, Trinchero P, Molinero J, Smith P, Snellman M, Filby A, Kiczka M, 2014. Sulphide fluxes and concentrations in the spent nuclear fuel repository at Olkiluoto. Posiva 2014-01, Posiva Oy, Finland.

Appendix A

Derivation of parameter values for cathodic reduction of H_2O on copper

Data for the cathodic reduction of H_2O on Cu are largely taken from:

Sharifi-Asl S, Macdonald D D, 2013. Investigation of the kinetics and mechanism of the hydrogen evolution reaction on copper. Journal of The Electrochemical Society 160, H382–H391.

This study was performed in sulfide-free solution and, in the absence of other data, it is assumed that the kinetics of H_2O reduction on Cu in the presence of HS^- (and, by extension, on Cu_2S) are the same.

The Butler–Volmer expression for the reduction of H_2O on Cu is given by Equation (2-34) of the main text.

k_F (kFroom)

The standard rate constant for the reduction of H_2O on Cu is taken from the expression for the exchange-current density (Equation (12) of Sharifi-Asl and Macdonald):

$$i_0 = 0.2 \exp\left(-\frac{31268.9}{RT}\right)[H_2]^{0.31}[H^+]^{-0.13} \quad \text{(A-1)}$$

where i_0 is the exchange current density in $A \cdot cm^{-2}$, $[H_2]$ is the concentration of dissolved H_2 in $mol \cdot kg^{-1}$, and $[H^+]$ is the hydrogen ion concentration in $mol \cdot cm^{-3}$.

The exchange current density is equivalent to the term $n_F F k_F$ in Equation (2-34).

It is assumed here that the bentonite pore-water pH is pH 8 and that the H_2 partial pressure will (eventually) be 5 MPa (50 atm). The concentration of dissolved H_2 was determined from the Henry's law constant of 7.8×10^{-4} $mol \cdot dm^{-3} \cdot atm^{-1}$ at 25 °C (Sander 1999). At 50 atm H_2 at 25 °C, the concentration of dissolved H_2 in water is 0.039 $mol \cdot dm^{-3}$, taken to be equivalent to the molality of H_2 in the bentonite pore water at the same H_2 pressure and temperature.

Based on these values, the exchange current density is equal to 6.546×10^{-6} $A \cdot cm^{-2}$ at 25 °C, p_{H2} = 5 MPa, pH 8.0.

In turn, the value of $k_F = 6.79 \times 10^{-9}$ $mol \cdot dm^{-2} s^{-1}$.

ΔH_F (DeHF)

The activation energy for k_F of 31 200 J/mol is taken directly from the study of Sharifi-Asl and Macdonald (2013).

n_F (nF)

Based on the stoichiometry of Reaction (2-33) in the main text, the number of electrons transferred in the cathodic reduction of H_2O, $n_F = 1$.

α_F (alfaF)

Sharifi-Asl and Macdonald (2013) report that the value of the cathodic transfer coefficient α_C varies linearly with temperature between temperatures of 20 °C and 80 °C (Sharifi-Asl and Macdonald 2013, Figure 5(d)). However, the variation is not large (0.13 to 0.175), and here a constant value of 0.15 is assumed.

E_F^0 (E0Froom)

The standard potential (here adjusted for the pore-water pH and expected H_2 pressure) is given by

$$E_F^0(V_{SHE}) = 0.000 - \frac{2.3RT}{F}pH - \frac{2.3RT}{2F}\log p_{H_2} \quad \text{(A-2)}$$

At 25 °C, pH 8, p_{H2} = 5 MPa, the value of E_F^0 = −0.764 V_{SCE}.

dE_F^0/dT (DeE0F)

The temperature dependence of E_F^0 was determined by calculating the value of Equation (A-2) at various temperatures and assuming a linear dependence on temperature, to give dE_F^0/dT = −0.0019 V/K.

Appendix B

Derivation of surface area factor for cathodic reaction on surface and within pores of Cu_2S film

B1 CSM V1.3 – Total Pore Surface

Let us consider two bounding cases for the pore structure of the precipitated Cu_2S film:

- The pores can be described by a series of parallel cylinders extending through the entire thickness of the film.
- The pores are perfect spheres distributed uniformly throughout the film.

B1.1 Pores as parallel cylinders

B1.1.1 Uniform pore diameter

The pores are in the form of cylinders of uniform diameter d and length L (corresponding to the thickness of the film). For unit surface area of film of volume $1 \times L$, the total volume of pores is given by

$$\varepsilon_{film} L = N \frac{\pi d^2}{4} L \tag{B-1}$$

where ε_{film} is the film porosity and N is the number of cylindrical pores

$$N = \frac{4\varepsilon_{film}}{\pi d^2} \tag{B-2}$$

Thus, the total interior surface area of these N pores is $N\pi dL$. (Here, we do not include the surface areas of the two ends of the cylindrical pores since they are already included in the term ε_{film}).

The total surface area of pores within a film of thickness L and unit cross-sectional area is the effective fractional surface area factor of interest (ε_{pore}) which, substituting for N from Equation (B-2) gives

$$\varepsilon_{pore} = N\pi dL = \frac{4}{d}\varepsilon_{film} L \tag{B-3}$$

B1.1.2 Distribution of pore diameters

Now let us assume that, instead of pores of uniform diameter, the cylinders exhibit a distribution of diameters around a mean value of $\bar{d}$, where

$$\overline{d} = \frac{1}{N}\sum_i d_i \tag{B-4}$$

where d_i is the diameter of the i^{th} cylindrical pore. The mean value of the square of d_i is given by

$$\overline{d^2} = \frac{1}{N}\sum_i d_i^2 = d_{rms}^2 \tag{B-5}$$

where d_{rms} is the root-mean square of d_i (also referred to as the quadratic mean)

$$d_{rms} = \sqrt{\frac{1}{N}\sum_i d_i^2} \tag{B-6}$$

and

$$d_{rms}^2 = \overline{d}^2 + \sigma_d^2 \tag{B-7}$$

where σ_d is the standard deviation of d_i.

As for the case of cylinders of uniform diameter, the volume of pores in one unit area of film is given by (Equations (B-1) and (B-6))

$$\varepsilon_{film} L = \frac{\pi L}{4}\sum_i d_i^2 = \frac{\pi L}{4} N d_{rms}^2 \tag{B-8}$$

from which

$$N = \frac{4\varepsilon_{film}}{\pi d_{rms}^2} \tag{B-9}$$

The total internal pore surface area per unit cross section is

$$\varepsilon_{pore} = \pi L \sum_i d_i = N\pi\overline{d}L \quad \text{(B-10)}$$

which, combining with Equation (B-9), gives

$$\varepsilon_{pore} = 4\varepsilon_{film} L \frac{\overline{d}}{d_{rms}^2} \equiv 4\varepsilon_{film} L f_2 \quad \text{(B-11)}$$

Substituting Equation (B-7) gives

$$\varepsilon_{pore} = 4\varepsilon_{film} L \frac{1}{\overline{d}} \left(\frac{1}{1+\frac{\sigma_d^2}{\overline{d}^2}} \right) \quad \text{(B-12)}$$

Equation (B-12) has the same form as Equation (B-3) with an additional factor

$$\left(\frac{1}{1+\frac{\sigma_d^2}{\overline{d}^2}} \right) \leq 1 \quad \text{(B-13)}$$

Note, that if $\sigma_d = 0$ (i.e., all of the pores are of identical diameter), Equation (B-13) is the same as Equation (B-3).

B1.2 Pores as perfect spheres

B1.2.1 Uniform pore diameter

Let us assume that there are N perfectly spherical pores of uniform diameter d per unit cross section of film of thickness L. The volume of these pores is then

$$\varepsilon_{film} L = N \frac{\pi d^3}{6} \quad \text{(B-14)}$$

and

$$N = \frac{6\varepsilon_{film} L}{\pi d^3} \quad \text{(B-15)}$$

The internal surface area of these N spherical pores is

$$\varepsilon_{pore} = N\pi d^2 = \frac{6}{d}\varepsilon_{film} L \quad \text{(B-16)}$$

B1.2.2 Distribution of pore diameters

If we now assume a collection of spheres with a distribution of diameters d_i, the cubic mean diameter $\bar{d}_c$ is given by

$$\overline{d_c} = \sqrt[3]{\frac{1}{N}\sum_i d_i^3} \quad \text{(B-17)}$$

The arithmetic mean ($\bar{d}$), quadratic mean (d_{rms}), and cubic mean ($\bar{d}_c$) are linked by the inequality

$$\overline{d} \leq d_{rms} \leq \overline{d_c} \quad \text{(B-18)}$$

As before, the volume of pores is given by

$$\varepsilon_{film} L = \frac{\pi}{6}\sum_i d_i^3 = \frac{\pi}{6} N \overline{d_c}^3 \quad \text{(B-19)}$$

so that

$$N = \frac{6\varepsilon_{film} L}{\pi \overline{d_c}^3} \quad \text{(B-20)}$$

Similarly, the internal pore surface area is given by

$$\varepsilon_{pore} = \pi \sum_i d_i^2 = N\pi d_{rms}^2 \quad \text{(B-21)}$$

which, substituting for N (Equation (B-20)) and rearranging, gives

$$\varepsilon_{pore} = 6\varepsilon_{film} L \frac{d_{rms}^2}{\overline{d_c}^3} = \frac{6}{\overline{d}} \varepsilon_{film} L \frac{\overline{d}}{d_{rms}} \left(\frac{d_{rms}}{\overline{d_c}}\right)^3 \quad \text{(B-22)}$$

where

$$\frac{\overline{d}}{d_{rms}} \left(\frac{d_{rms}}{\overline{d_c}}\right)^3 \leq 1 \equiv f_3 \quad \text{(B-23)}$$

where the factor f_3 decreases with increasing variation in the values of d_i.

B1.3 Conclusions

Each of the derived relations for ε_{pore} have the form

$$\varepsilon_{pore} = F_{pore} \frac{\varepsilon_{film} L}{\overline{d}} \quad \text{(B-24)}$$

The factor F_{pore} varies from 4 for perfect cylinders of uniform diameter, to 6 for perfect spheres of uniform diameter. For real pores of variable diameter, the value of F_{pore} is decreased by the pore-width variability and varies from $4f_2$ to $6f_3$.

Because real pores are generally elongated rather than spherical, the value of F_{pore} (for uniform pores) would be expected to be closer to 4 than 6. This value will be decreased because of the variability in pore diameter, so the best estimate value would be 4, with a range of 1 to 5 to assess the sensitivity of the results to the value of F_{pore}.

Appendix C

Data input file

C1 Sources of Input Data

Each input parameter is identified by the symbol used to describe the parameter in the code in the left-hand margin, followed by a paragraph containing the parameter definition, mathematical symbol if defined (in parentheses), typical value and units [in brackets], and a discussion of the source of the data.

The input parameters are grouped under the following headings: Control Parameters, Layer-dependent Parameters, and Material, Rate and Environment Parameters. Control parameters determine, amongst other things, the speed and accuracy of the computer code; the layer-dependent parameters define both the nature and dimensions of the different mass-transport layers and their properties; and material, rate and environment parameters describe the various mass-transport, chemical and electrochemical processes.

With some exceptions, the input data are generally expressed in units of mol, dm, kg, s and K.

C1.1 Control Parameters

The following are the control parameters for the subroutine TRANSIENT (Kolář 2016) and are common to all programs that include this subroutine, including the current model.

monitor	Level of diagnostic output (monitor = 2). Four settings of monitor between 0 and 3 determine the amount of information displayed on-screen during the execution.
CmntC	Comment character to mark the beginning of a comment statement (#).
steady	Designates type of solution (steady = 0). The code can calculate either a transient (steady = 0), a steady-state solution (steady = 1), or calculate the steady-state solution and then use it as input for the transient solution (steady = 2).
Tau	The degree of implicitness for the differencing scheme (tau = 0.5). Tau = 0 corresponds to a fully implicit solution, 0.5 to a Crank–Nicholson solution and 1 to an explicit solution. Generally, the Crank–Nicholson solution is used.
nIter	Desired number of Newton–Raphson iterations in each time step (20).
tStart	Initial time in s (0 s). Start of integration.
tEnd	Final time in s (3.16×10^{13} s). End of integration.
tStepInit	Length of the initial time step (0.0001 s).
tStepMin	Minimum length of time step (0 s).
tStepMax	The largest time step allowed in s (−0.1 s). For tStepMax ≤ 0, there is no limitation on the time step.
tOutInit	Initial output time tOut in s for the concentration profiles (43 200 s).
tOutMulF	Multiplication factor to determine the next value of tOut (1.6). Thus, $tOut_{n+1} = tOut_n + tOut_{n-1}tOutMulF$.
nOutOTH	Number of profiles calculated between consecutive tOut values (10).
sepProf	Parameter determining how output files are stored (1). For sepProf = 0, all output files are stored in a single file; for sepProf = 1, profiles for each time output are stored in a separate file.
strict	Parameter determining extent to which cDiffMax is used to calculate the next time step (0). Using strict < 0, cDiffMax is not used at all in determining the next time step; strict = 0, cDiffMax is not exceeded too much; strict > 0, cDiffMax is strictly enforced (within 18 %). In general, the higher the value of strict, the more accurate, but slower, the code execution.

init_from_file	Name of file containing initial profiles. Used when profiles other than determined by initial concentrations are to be used as the input data. Useful for re-starting stalled runs.
cDiffMaxf	Maximum difference in concentration of any species from one time step to the next. cDiffMaxf varies with time.

C1.2 Layer-dependent parameters

The layer-dependent parameters define the dimensions and properties of the spatial grid, which in turn describes geometry of the model. In general, an arbitrary number of layers can be defined, each defining a particular mass-transport barrier (or part of a mass-transport barrier) in the repository. Each layer is characterised by the composition and dimensions of the layer (e.g., highly compacted bentonite buffer) and specific properties (e.g., the content of pyrite accessory mineral, the time-dependent degree of saturation, etc). Different layers are used to define different repository geometries.

Nmedia	Number of separate layers in the model [9].
mediumNo_O2flux	Layer number at which flux of O_2 is calculated [6]. The flux of O_2 is used in the calculation of the O_2 balance to ensure that all of the initial inventory of oxygen is accounted for in the simulation as a quality check.
NMlayer1	Name of Layer 1 [Cu2S_film]. The first layer is the Cu_2S film of variable thickness. This layer grows in response to the predicted precipitation of Cu_2S.
Mfilm	Molecular mass of Cu_2S [159.1 g/mol] (CRC 1982).
L1	Length of Cu_2S layer [variable]. The length (width) of the Cu_2S layer changes during the course of the simulation as the layer grows.
eps1E	Effective porosity for mass transport of the Cu_2S film (ε_e) [0.1 unitless]. Assumed value.
eps1S	Storage porosity of the Cu_2S film (ε_s) [0 unitless]. Assumed value based on assumption that all porosity of Cu_2S film is interconnected through-porosity.
eps1N	Non-accessible porosity of the Cu_2S film (ε_{na}) [0 unitless]. Assumed value based on the assumption that all porosity is the Cu_2S film is accessible to solutes.
rho1	Particle density of the Cu_2S film (ρ) [5.6 kg/dm^3] (CRC 1982).
S_MIC1	Threshold degree of saturation above which microbial activity in the Cu_2S film is possible (S_{MIC}) [1 unitless]. There is strong evidence that microbial activity only occurs above a threshold water activity or, for porous media, a threshold degree of saturation (King 2009, King et al. 2002, 2003). Since the degree of saturation cannot exceed 1, the default parameter value is equivalent to assuming that no microbial activity occurs in the Cu_2S film.
c5max1	Maximum adsorption capacity of Cu(II) on Cu_2S film (c_5^{max}) [0 mol/kg]. It is assumed that Cu_2S does not adsorb Cu(II).
AP1	Surface area of pyrite per unit volume of Cu_2S layer (A_p) [0 dm^{-1}]. There is no pyrite in the Cu_2S layer.
tau1	Tortuosity factor of Cu_2S layer (τ_f) [0.1 unitless]. Assumed value.
S1_in	File name for the time-dependent degree of saturation of the Cu_2S layer [S1_in]. Since the growing Cu_2S layer is adjacent to the initial sub-layer of bentonite, the time dependence of S1 is taken to be the same as that for S2 (see below).

K1_in File name for the dependence of the thermal conductivity of Cu_2S on the degree of saturation [K1_in]. Data for the thermal conductivity of Cu_2S are sparse and estimates for the dependence of K of a porous layer on the degree of saturation are not available. For a study of the heat conservation during the heap leaching of copper sulfide, Dixon (2000) adopted a value for K of 0.1 $W \cdot dm^{-1} \cdot K^{-1}$, which is used here as the value for partially saturated Cu_2S. The thermal conductivity of saturated Cu_2S will be higher and here is arbitrarily assigned a value of 0.2 $W \cdot dm^{-1} \cdot K^{-1}$. The shape of the dependence of K on S is assumed to be the same as that for bentonite (see below).

Degree of saturation S	Thermal conductivity K ($W \cdot dm^{-1} \cdot K^{-1}$)
0	0.1
0.2	0.1
0.8	0.2
1.0	0.2

Cp1 Heat capacity of Cu_2S (C) [845 $J \cdot kg^{-1} \cdot K^{-1}$]. In the absence of other data, taken to be the same as that for bentonite (see below).

NMlayer2 Name of layer 2 [Bent1]. The second layer is the first of three sub-layers representing the highly compacted bentonite (HCB) buffer material. The HCB is represented by three sub-layers to better represent the spatial dependence of the time-dependent degree of saturation, but otherwise all properties are identical.

L2 Thickness of layer 2 [2 dm]. The total thickness of the HCB layer is based on the ratio of the volume of the buffer in the repository to the surface area of the canister. In this way, the amount of initially trapped atmospheric O_2 per unit area of canister is simulated properly in the 1-D CSM. The canister surface area and buffer volume are based on Figure 4-4 of SKB (2006a), giving a volume:surface area ratio of 6.93 dm. This thickness is arbitrarily divided into three layers of thickness 2 dm, 2 dm, and 2.93 dm.

eps2E Effective porosity for diffusive transport in layer 2 (ε_e) [0.05 unitless]. The total porosity of the HCB at the reference density of 1.65 $Mg \cdot m^{-3}$ is 0.40, based on Figure 4-16 of Pastina and Hellä (2006) and the accessible (external) porosity is 0.1. Canadian studies indicate that the accessible porosity is equally divided between effective porosity for diffusive transport and storage porosity associated with dead-end pores (King et al. 1996). Thus, the effective porosity for HCB is taken to be 0.05.

eps2S Storage porosity in layer 2 (ε_s) [0.05 unitless]. The total porosity of the HCB at the reference density of 1.65 $Mg \cdot m^{-3}$ is 0.40, based on Figure 4-16 of Pastina and Hellä (2006) and the accessible (external) porosity is 0.1. Canadian studies indicate that the accessible porosity is equally divided between effective porosity for diffusive transport and storage porosity associated with dead-end pores (King et al. 1996). Thus, the storage porosity for HCB is taken to be 0.05.

eps2N Non-accessible porosity for layer 2 (ε_{na}) [0.3 unitless]. The total porosity of the HCB at the reference density of 1.65 Mg m^{-3} is 0.40, based on Figure 4-16 of Pastina and Hellä (2006) and the accessible (external) porosity is 0.1. The non-accessible porosity is, therefore, 0.3.

rho2 Density of solids in HCB (ρ) [2.7 $kg \cdot dm^{-3}$]. This is the density of the solid particles in the HCB and is not to be confused with the dry density of 1.65 $Mg \cdot m^{-3}$ (Pastina and Hellä 2006, Section 4.4.3).

S_MIC2 Threshold degree of saturation above which microbial activity in the HCB is possible (S_{MIC}) [1 unitless]. There is strong evidence that microbial activity only occurs above a threshold water activity or, for porous media, a threshold degree of saturation (King 2009, King et al. 2002, 2003). Since the degree of saturation cannot exceed 1, the default parameter value is equivalent to assuming that no microbial activity occurs in the HCB.

c5max2 Maximum adsorption capacity for Cu(II) in layer 2 (c_5^{max}) [0.09375 mol·kg^{-1}]. Based on a cation exchange capacity for MX-80 clay of 75 meq/100g (Pastina and Hellä 2006, Table 4-4) and accessible and total porosities of 0.1 and 0.4, respectively (see above). Thus, Cu(II) can only adsorb on accessible exchange sites on the bentonite.

AP2 Surface area of pyrite per unit volume of layer 2 (A_p) [0.139 dm^{-1}]. Based on a pyrite content of 0.07 wt% in MX-80 bentonite (Pastina and Hellä 2006, Table 4-4), a HCB dry density of the bentonite blocks of 1 650 kg·m^{-3} (Pastina and Hellä 2006, Table 4-5), and a specific surface area for pyrite of 12.0 cm^3·g^{-1} (based on an assumed spherical particle diameter of 1 mm and a pyrite density of 5.01 g·cm^{-3}, CRC 1982).

tau2 Tortuosity factor for HCB (τ_f) [0.1 unitless]. Based on value for 50:50 sand:bentonite buffer material (Oscarson et al. 1992).

c02 Initial (calculated) concentration of dissolved O_2 in the pore water in layer 2 (c_0) [0.000361 mol·dm^{-3}]. An important feature of the CSM is that the initial O_2 inventory in the buffer and backfill layers is properly accounted for and that the extent of corrosion is not under-estimated. The initial O_2 inventory is calculated based on a dissolved [O_2] of 0.00022 mol·dm^{-3} in the saturated fraction of the pores (based on the solubility of O_2 in water in contact with air at 25 °C (0.00025 mol·dm^{-3}), reduced slightly to account for salting-out due to the salinity of the pore water) and a gaseous [O_2] in the unsaturated pores of 0.00855 mol·dm^{-3} (based on the volume of an ideal gas at 25 °C of 24.5 dm^3·mol^{-1} and the mole fraction of O_2 in air of 0.209, CRC 1982). Because the dissolved and gaseous O_2 are treated as being in equilibrium in the CSM V1.1eq (Section 2.2.1), the initial dissolved [O_2] must be specified so that it is in equilibrium with the gaseous fraction in order to avoid numerical instability when the code is executed. However, the Henry's law constant is temperature-dependent and varies spatially due to the initial temperature profile. Therefore, for each initially unsaturated layer (i.e., the three buffer sub-layers, the two backfill sub-layers, and the EDZ and EdZ), the initial dissolved O_2 concentration is calculated so that (i) the temperature-dependent (spatially variable) equilibrium is maintained and (ii) the total calculated O_2 inventory is equal to that based on the initial dissolved and gaseous [O_2] of 0.00022 mol·dm^{-3} and 0.00855 mol·dm^{-3}, respectively.

c62 Initial concentration of Cl^- in the pore water in layer 2 (c_6) [0.096 mol·dm^{-3}]. Based on the modelled pore water composition of 0.0675 mol·dm^{-3} for a dry density of 1 500 kg·m^{-3} (Pastina and Hellä 2006, Table 6-5), corrected for the actual dry density of 1 650 kg·m^{-3} and the mean initial degree of saturation of 0.77 for the bentonite blocks and rings (Pastina and Hellä 2006, Table 4-5).

c72 Initial concentration of Fe(II) in layer 2 (c_7) [0 mol·dm^{-3}]. The HCB pore water is assumed to be initially free of dissolved Fe(II).

c92 Initial concentration of dissolved sulfide in the HCB pore water (c_9) [0 mol·dm^{-3}]. The HCB is assumed to be initially free of HS^- because of the aerobic conditions.

cP2 Initial concentration of pyrite in layer 2 (c_{10}) [0.00963 mol·dm^{-3}]. Based on the pyrite content of MX-80 bentonite of 0.07 wt% (Pastina and Hellä 2006, Table 4-4), a HCB dry density of the bentonite blocks of 1 650 kg·m^{-3} (Pastina and Hellä 2006, Table 4-5), and the molecular mass of FeS_2 of 120 g·mol^{-1} (CRC 1982).

cS2 Initial concentration of dissolved sulfate in the pore water in layer 2 (c_{11}) [0.149 mol·dm^{-3}]. Based on modelled pore water composition of 0.104 mol·dm^{-3} for a dry density of 1 500 kg·m^{-3} (Pastina and Hellä 2006, Table 6-5), corrected for the actual dry density of 1 650 kg·m^{-3} and the mean initial degree of saturation of 0.77 for the bentonite blocks and rings (Pastina and Hellä 2006, Table 4-5).

S2_in File name for the time dependence of the degree of saturation in layer 2 [S2_in]. The initial value is a mean value for the HCB blocks and rings (Pastina and Hellä 2006, Table 4-5). Complete saturation of the repository is assumed to occur after 200 a. At intermediate times, the assumed values are chosen to reflect the fact that the HCB closest to the canister will exhibit the most extensive desiccation. The degree of saturation at times other than those indicated in the table is calculated based on the assumption of the linear variation of S with log t.

Time (a)	S	Time (a)	S
0	0.78	50	0.166
0.01	0.77	73	0.225
0.2	0.5	95	0.29
0.4	0.4	105	0.335
0.6	0.3	110	0.38
0.8	0.2	120	0.46
0.9	0.15	130	0.54
1.0	0.12	140	0.62
1.122	0.107	150	0.7
1.5	0.1	190	0.95
2	0.098	198	0.99
4	0.095	200.5	0.997
7	0.098	205	0.999
10	0.1	210	1
25	0.118	1 000 000	1

Kbent_in — File name for the saturation-dependence of the thermal conductivity of HCB [Kbent_in]. Based on SKB (2006b).

Cp2 — Specific heat of layer 2 (C) [845 $J \cdot kg^{-1} \cdot K^{-1}$]. Generic value for clay/rock/sand (King and Kolář 2000).

NMlayer3 — Name of layer 3 [Bent2]. The third layer is the second of three sub-layers representing the highly compacted bentonite (HCB) buffer material. The HCB is represented by three sub-layers to better represent the spatial dependence of the time-dependent degree of saturation.

L3 — Thickness of layer 3 [2 dm]. The total thickness of the HCB layer is based on the ratio of the volume of the buffer in the repository to the surface area of the canister. In this way, the amount of initially trapped atmospheric O_2 per unit area of canister is simulated properly in the 1-D CSM. The canister surface area and buffer volume are based on Figure 4-4 of SKB (2006a), giving a volume:surface area ratio of 6.93 dm. This thickness is arbitrarily divided into three layers of thickness 2 dm, 2 dm, and 2.93 dm.

eps3E — Effective porosity for diffusive transport in layer 3 (ε_e) [0.05 unitless]. The total porosity of the HCB at the reference density of 1.65 $Mg \cdot m^{-3}$ is 0.40, based on Figure 4-16 of Pastina and Hellä (2006) and the accessible (external) porosity is 0.1. Canadian studies indicate that the accessible porosity is equally divided between effective porosity for diffusive transport and storage porosity associated with dead-end pores (King et al. 1996). Thus, the effective porosity for HCB is taken to be 0.05.

eps3S — Storage porosity in layer 3 (ε_s) [0.05 unitless]. The total porosity of the HCB at the reference density of 1.65 $Mg \cdot m^{-3}$ is 0.40, based on Figure 4-16 of Pastina and Hellä (2006) and the accessible (external) porosity is 0.1. Canadian studies indicate that the accessible porosity is equally divided between effective porosity for diffusive transport and storage porosity associated with dead-end pores (King et al. 1996). Thus, the storage porosity for HCB is taken to be 0.05.

eps3N — Non-accessible porosity for layer 3 (ε_{na}) [0.3 unitless]. The total porosity of the HCB at the reference density of 1.65 $Mg \cdot m^{-3}$ is 0.40, based on Figure 4-16 of Pastina and Hellä (2006) and the accessible (external) porosity is 0.1. The non-accessible porosity is, therefore, 0.3.

rho3 — Density of solids in HCB (ρ) [2.7 $kg \cdot dm^{-3}$]. This is the density of the solid particles in the HCB and is not to be confused with the dry density of 1.65 $Mg \cdot m^{-3}$ (Pastina and Hellä 2006, Section 4.4.3).

S_MIC3 — Threshold degree of saturation above which microbial activity in the HCB is possible (S_{MIC}) [1 unitless]. There is strong evidence that microbial activity only occurs above a threshold water activity or, for porous media, a threshold degree of saturation (King 2009, King et al. 2002, 2003). Since the degree of saturation cannot exceed 1, the default parameter value is equivalent to assuming that no microbial activity occurs in the HCB.

c5max3 Maximum adsorption capacity for Cu(II) in layer 3 (c_5^{max}) [0.09375 mol·kg^{-1}]. Based on a cation exchange capacity for MX-80 clay of 75 meq/100g (Pastina and Hellä 2006, Table 4-4) and accessible and total porosities of 0.1 and 0.4, respectively (see above). Thus, Cu(II) can only adsorb on accessible exchange sites on the bentonite.

AP3 Surface area of pyrite per unit volume of layer 3 (A_p) [0.139 dm^{-1}]. Based on a pyrite content of 0.07 wt% in MX-80 bentonite (Pastina and Hellä 2006, Table 4-4), a HCB dry density of the bentonite blocks of 1 650 kg·m^{-3} (Pastina and Hellä 2006, Table 4-5), and a specific surface area for pyrite of 12.0 cm^3·g^{-1} (based on an assumed spherical particle diameter of 1 mm and a pyrite density of 5.01 g·cm^{-3}, CRC 1982).

tau3 Tortuosity factor for HCB (τ_f) [0.1 unitless]. Based on value for 50:50 sand:bentonite buffer material (Oscarson et al. 1992).

c03 Initial (calculated) concentration of dissolved O_2 in the pore water in layer 3 (c_0) [0.000256 mol·dm^{-3}]. Calculated based on the requirements to (i) conserve the correct initial O_2 inventory and (ii) ensure equilibrium between dissolved and gaseous O_2 initially. See more-detailed explanation for c02, above.

c63 Initial concentration of Cl^- in the pore water in layer 3 (c_6) [0.096 mol·dm^{-3}]. Based on modelled pore water composition of 0.0675 mol·dm^{-3} for a dry density of 1 500 kg·m^{-3} (Pastina and Hellä 2006, Table 6-5), corrected for the actual dry density of 1 650 kg·m^{-3} and the mean initial degree of saturation of 0.77 for the bentonite blocks and rings (Pastina and Hellä 2006, Table 4-5).

c73 Initial concentration of Fe(II) in layer 3 (c_7) [0 mol·dm^{-3}]. The HCB pore water is assumed to be initially free of dissolved Fe(II).

c93 Initial concentration of dissolved sulfide in the HCB pore water (c_9) [0 mol·dm^{-3}]. The HCB is assumed to be initially free of HS^- because of the aerobic conditions.

cP3 Initial concentration of pyrite in layer 3 (c_{10}) [0.00963 mol·dm^{-3}]. Based on the pyrite content of MX-80 bentonite of 0.07 wt% (Pastina and Hellä 2006, Table 4-4), a HCB dry density of the bentonite blocks of 1 650 kg·m^{-3} (Pastina and Hellä 2006, Table 4-5), and the molecular mass of FeS_2 of 120 g·mol^{-1} (CRC 1982).

cS3 Initial concentration of dissolved sulfate in the pore water in layer 3 (c_{11}) [0.149 mol·dm^{-3}]. Based on modelled pore water composition of 0.104 mol·dm^{-3} for a dry density of 1 500 kg·m^{-3} (Pastina and Hellä 2006, Table 6-5), corrected for the actual dry density of 1 650 kg·m^{-3} and the mean initial degree of saturation of 0.77 for the bentonite blocks and rings (Pastina and Hellä 2006, Table 4-5).

S3_in File name for the time dependence of the degree of saturation in layer 3 [S3_in]. The initial value is a mean value for the HCB blocks and rings (Pastina and Hellä 2006, Table 4-5). Complete saturation of the repository is assumed to occur after 200 a. At intermediate times, the assumed values are chosen to reflect the fact that the HCB closer to the canister will exhibit more desiccation. The degree of saturation at times other than those indicated in the table is calculated based on the assumption of the linear variation of S with log t.

Time (a)	S	Time (a)	S
0	0.78	25	0.27
0.01	0.77	50	0.4
0.2	0.52	77	0.56
0.4	0.44	100	0.7
0.6	0.36	110	0.76
0.8	0.28	120	0.82
0.93	0.235	130	0.88
1.05	0.208	140	0.94
1.2	0.2	148	0.99
2	0.192	150	0.996
4	0.19	155	0.998
7	0.192	160	1
10	0.2	1 000 000	1
15	0.222		

Kbent_in — File name for the saturation-dependence of the thermal conductivity of HCB [Kbent_in]. Based on SKB (2006b).

Cp3 — Specific heat of layer 3 (C) [845 $J \cdot kg^{-1} \cdot K^{-1}$]. Generic value for clay/rock/sand (King and Kolář 2000).

NMlayer4 — Name of layer 4 [Bent3]. The fourth layer is the third of three sub-layers representing the highly compacted bentonite (HCB) buffer material. The HCB is represented by three sub-layers to better represent the spatial dependence of the time-dependent degree of saturation, but otherwise all properties are identical.

L4 — Thickness of layer 4 [2.93 dm]. The total thickness of the HCB layer is based on the ratio of the volume of the buffer in the repository to the surface area of the canister. In this way, the amount of initially trapped atmospheric O_2 per unit area of canister is simulated properly in the 1-D CSM. The canister surface area and buffer volume are based on Figure 4-4 of SKB (2006a), giving a volume:surface area ratio of 6.93 dm. This thickness is arbitrarily divided into three layers of thickness 2 dm, 2 dm, and 2.93 dm.

eps4E — Effective porosity for diffusive transport in layer 4 (ε_e) [0.05 unitless]. The total porosity of the HCB at the reference density of 1.65 $Mg \cdot m^{-3}$ is 0.40, based on Figure 4-16 of Pastina and Hellä (2006) and the accessible (external) porosity is 0.1. Canadian studies indicate that the accessible porosity is equally divided between effective porosity for diffusive transport and storage porosity associated with dead-end pores (King et al. 1996). Thus, the effective porosity for HCB is taken to be 0.05.

eps4S — Storage porosity in layer 4 (ε_s) [0.05 unitless]. The total porosity of the HCB at the reference density of 1.65 $Mg \cdot m^{-3}$ is 0.40, based on Figure 4-16 of Pastina and Hellä (2006) and the accessible (external) porosity is 0.1. Canadian studies indicate that the accessible porosity is equally divided between effective porosity for diffusive transport and storage porosity associated with dead-end pores (King et al. 1996). Thus, the storage porosity for HCB is taken to be 0.05.

eps4N — Non-accessible porosity for layer 4 (ε_{na}) [0.3 unitless]. The total porosity of the HCB at the reference density of 1.65 $Mg \cdot m^{-3}$ is 0.40, based on Figure 4-16 of Pastina and Hellä (2006) and the accessible (external) porosity is 0.1. The non-accessible porosity is, therefore, 0.3.

rho4 — Density of solids in HCB (ρ) [2.7 $kg \cdot dm^{-3}$]. This is the density of the solid particles in the HCB and is not to be confused with the dry density of 1.65 $Mg \cdot m^{-3}$ (Pastina and Hellä 2006, Section 4.4.3).

S_MIC4 — Threshold degree of saturation above which microbial activity in the HCB is possible (S_{MIC}) [1 unitless]. There is strong evidence that microbial activity only occurs above a threshold water activity or, for porous media, a threshold degree of saturation (King 2009, King et al. 2002, 2003). Since the degree of saturation cannot exceed 1, the default parameter value is equivalent to assuming that no microbial activity occurs in the HCB.

c5max4 — Maximum adsorption capacity for Cu(II) in layer 4 (c_5^{max}) [0.09375 $mol \cdot kg^{-1}$]. Based on a cation exchange capacity for MX-80 clay of 75 meq/100g (Pastina and Hellä 2006, Table 4-4) and accessible and total porosities of 0.1 and 0.4, respectively (see above). Thus, Cu(II) can only adsorb on accessible exchange sites on the bentonite.

AP4 — Surface area of pyrite per unit volume of layer 4 (A_p) [0.139 dm^{-1}]. Based on a pyrite content of 0.07 wt% in MX-80 bentonite (Pastina and Hellä 2006, Table 4-4), a HCB dry density of the bentonite blocks of 1 650 $kg \cdot m^{-3}$ (Pastina and Hellä 2006, Table 4-5), and a specific surface area for pyrite of 12.0 $cm^3 \cdot g^{-1}$ (based on an assumed spherical particle diameter of 1 mm and a pyrite density of 5.01 $g \cdot cm^{-3}$, CRC 1982).

tau4 — Tortuosity factor for HCB (τ_f) [0.1 unitless]. Based on value for 50:50 sand:bentonite buffer material (Oscarson et al. 1992).

c04 Initial (calculated) concentration of dissolved O_2 in the pore water in layer 4 (c_0) [0.000223 mol·dm^{-3}]. Calculated based on the requirements to (i) conserve the correct initial O_2 inventory and (ii) ensure equilibrium between dissolved and gaseous O_2 initially. See more-detailed explanation for c02, above.

c64 Initial concentration of Cl^- in the pore water in layer 4 (c_6) [0.096 mol·dm^{-3}]. Based on modelled pore water composition of 0.0675 mol·dm^{-3} for a dry density of 1 500 kg·m^{-3} (Pastina and Hellä 2006, Table 6-5), corrected for the actual dry density of 1 650 kg·m^{-3} and the mean initial degree of saturation of 0.77 for the bentonite blocks and rings (Pastina and Hellä 2006, Table 4-5).

c74 Initial concentration of Fe(II) in layer 4 (c_7) [0 mol·dm^{-3}]. The HCB pore water is assumed to be initially free of dissolved Fe(II).

c94 Initial concentration of dissolved sulfide in the HCB pore water (c_9) [0 mol·dm^{-3}]. The HCB is assumed to be initially free of HS^- because of the aerobic conditions.

cP4 Initial concentration of pyrite in layer 4 (c_{10}) [0.00963 mol·dm^{-3}]. Based on the pyrite content of MX-80 bentonite of 0.07 wt% (Pastina and Hellä 2006, Table 4-4), a HCB dry density of the bentonite blocks of 1 650 kg·m^{-3} (Pastina and Hellä 2006, Table 4-5), and the molecular mass of FeS_2 of 120 g·mol^{-1} (CRC 1982).

cS4 Initial concentration of dissolved sulfate in the pore water in layer 4 (c_{11}) [0.149 mol·dm^{-3}]. Based on modelled pore water composition of 0.104 mol·dm^{-3} for a dry density of 1 500 kg·m^{-3} (Pastina and Hellä 2006, Table 6-5), corrected for the actual dry density of 1 650 kg·m^{-3} and the mean initial degree of saturation of 0.77 for the bentonite blocks and rings (Pastina and Hellä 2006, Table 4-5).

S4_in File name for the time dependence of the degree of saturation in layer 4 [S4_in]. The initial value is a mean value for the HCB blocks and rings (Pastina and Hellä 2006, Table 4-5). Complete saturation of the repository is assumed to occur after 200 a. At intermediate times, the assumed values are chosen to reflect the fact that the HCB further from the canister will exhibit less desiccation. The degree of saturation at times other than those indicated in the table is calculated based on the assumption of the linear variation of S with log t.

Time (a)	S	Time (a)	S
0	0.78	28	0.39
0.01	0.77	50	0.5
0.2	0.54	77	0.66
0.4	0.48	100	0.8
0.6	0.42	110	0.84
0.8	0.36	120	0.88
0.93	0.335	130	0.92
1.05	0.308	140	0.96
1.2	0.3	148	0.992
2	0.292	150	0.997
4	0.29	155	0.999
7	0.292	160	1
10	0.3	1 000 000	1
15	0.322		

Kbent_in File name for the saturation-dependence of the thermal conductivity of HCB [Kbent_in]. Based on SKB (2006b).

Cp4 Specific heat of layer 4 (C) [845 J·kg^{-1}·K^{-1}]. Generic value for clay/rock/sand (King and Kolář 2000).

NMlayer5 Name of layer 5 [Back1]. The fifth layer is the first of two sub-layers representing the backfill material. The backfill is represented by two sub-layers to better represent the spatial dependence of the time-dependent degree of saturation, but otherwise all properties are identical.

L5 Thickness of layer 5 [40 dm]. The total thickness of the backfill layer is based on the ratio of the volume of the backfill in the repository to the surface area of the canisters. In this way, the amount of initially trapped atmospheric O_2 per unit area of canister is simulated properly in the 1-D CSM. The canister surface area and backfill volume are based on Figure 4-4 of SKB (2006a) and an average borehole spacing of 5 m, giving a volume:surface area ratio of 87 dm. This thickness is arbitrarily divided into two layers of thickness 40 dm and 47 dm.

eps5E Effective porosity for diffusive transport in layer 5 (ε_e) [0.22 unitless]. For the current purposes, the backfill is assumed to comprise a mixture of 70 wt% crushed rock plus 30 wt% Deponit Ca-N bentonite, a dry density of 2 120 kg·m^{-3}, total porosity of 0.22, and an initial degree of saturation of 0.8, based on the properties of the dense backfill defined by Ontario Power Generation for their Third Case Study (Garisto et al. 2004). Because of the relatively low clay content, and in the absence of other information, the entire porosity is assumed to be accessible, interconnected porosity that contributes to mass transport.

eps5S Storage porosity in layer 5 (ε_s) [0 unitless]. Because of the relatively low clay content, and in the absence of other information, the entire porosity of the dense backfill is assumed to be accessible, interconnected porosity that contributes to mass transport. Therefore, the storage porosity is assumed to be zero.

eps5N Non-accessible porosity for layer 5 (ε_{na}) [0 unitless]. Because of the relatively low clay content, and in the absence of other information, the entire porosity of the dense backfill is assumed to be accessible, interconnected porosity that contributes to mass transport. Therefore, the non-accessible porosity is assumed to be zero.

rho5 Density of solids in the backfill (ρ) [2.7 kg·dm^{-3}]. This is the density of the solid particles in the backfill and is not to be confused with the assumed dry density of 2 120 kg·m^{-3}.

S_MIC5 Threshold degree of saturation above which microbial activity in the backfill is possible (S_{MIC}) [0.75 unitless]. There is strong evidence that microbial activity only occurs above a threshold water activity or, for porous media, a threshold degree of saturation (King 2009, King et al. 2002, 2003, 2004b). The degree of saturation corresponding to the threshold water activity of 0.96 depends on the suction potential, which in turn is dependent on the clay content and density of the material. A value of 0.75 is selected here as an intermediate value between that for a 50:50 bentonite:sand mixture and that for the dense backfill containing 5 wt% bentonite (King et al. 2004b).

c5max5 Maximum adsorption capacity for Cu(II) in layer 5 (c_5^{max}) [0.105 mol·kg^{-1}]. Based on a cation exchange capacity for Deponit CA-N clay of 70 meq/100g (Pastina and Hellä 2006, Table 4-4), a clay content of 30 wt% in the backfill, and the assumption that all porosity is accessible porosity.

AP5 Surface area of pyrite per unit volume of layer 5 (A_p) [0.382 dm^{-1}]. Based on a pyrite content of 0.5 wt% in Deponit CA-N bentonite (Pastina and Hellä 2006, Table 4-4), a clay content of 30 wt%, an assumed backfill dry density of 2 120 kg·m^{-3}, and a specific surface area for pyrite of 12.0 cm^3·g^{-1} (based on an assumed spherical particle diameter of 1 mm and a pyrite density of 5.01 g·cm^{-3}, CRC 1982). The surface area of pyrite in the crushed rock component of the backfill is assumed to be negligible.

tau5 Tortuosity factor for the backfill (τ_f) [0.1 unitless]. Assumed value based on the value for 50:50 sand:bentonite buffer material (Oscarson et al. 1992).

c05 Initial (calculated) concentration of dissolved O_2 in the pore water in layer 5 (c_0) [0.0002213 mol·dm^{-3}]. Calculated based on the requirements to (i) conserve the correct initial O_2 inventory and (ii) ensure equilibrium between dissolved and gaseous O_2 initially. See more-detailed explanation for c02, above.

c65 Initial concentration of Cl^- in the pore water in layer 5 (c_6) [0.036 mol·dm^{-3}]. Based on the modelled pore water composition for MX-80 bentonite clay of 0.0675 mol·dm^{-3} for a dry density of 1 500 kg·m^{-3} (Pastina and Hellä 2006, Table 6-5), corrected for the backfill dry density of 2 120 kg.m^{-3}, the mean initial degree of saturation of 0.8, the lower clay content (30 wt% of the backfill) and the assumption that the halite impurity content of Deponit CA-N clay is the same as that for MX-80 clay.

c75 Initial concentration of Fe(II) in layer 5 (c_7) [0 mol·dm^{-3}]. The backfill pore water is assumed to be initially free of dissolved Fe(II), consistent with the presence initially of dissolved and gaseous O_2.

c95 Initial concentration of dissolved sulfide in the backfill pore water (c_9) [0 mol·dm^{-3}]. The backfill is assumed to be initially free of HS^- because of the aerobic conditions.

cP5 Initial concentration of pyrite in layer 5 (c_{10}) [0.0265 mol·dm^{-3}]. Based on the pyrite content of Deponit CA-N bentonite of 0.5 wt% (Pastina and Hellä 2006, Table 4-4), a backfill dry density of 2 120 kg·m^{-3}, a clay content of 30 wt%, and the molecular mass of FeS_2 of 120 g·mol^{-1} (CRC 1982).

cS5 Initial concentration of dissolved sulfate in the pore water in layer 5 (c_{11}) [0.479 mol·dm^{-3}]. Based on the anhydrite content of Deponit CA-N bentonite (18 g·kg^{-1}, Pastina and Hellä 2006, Table 4-4), a dry density of 2 120 kg·m^{-3}, a clay content in the backfill of 30 wt%, the backfill porosity of 0.22, initial degree of saturation of 0.8, and the molecular mass of anhydrite $CaSO_4$ of 136 g·mol^{-1}. In order to avoid under-estimating the amount of sulfate available for microbial sulfate reduction, the entire inventory of SO_4^{2-} is assumed to be initially dissolved in the pore water.

S5_in File name for the time dependence of the degree of saturation in layer 5 [S5_in]. The initial degree of saturation of 0.8 is assumed to be the same as for the dense backfill defined by Garisto et al. (2004). Complete saturation of the repository is assumed to occur after 200 a. At intermediate times, the assumed values are chosen to reflect the fact that the backfill will dry out to a lesser extent than the HCB that is closer to the canister. The layer of backfill in contact with the EDZ will dry out to a greater extent because some of the initial moisture content will be re-distributed to the EDZ which is assumed to almost completely dry out during repository construction. The degree of saturation at times other than those indicated in the table is calculated based on the assumption of the linear variation of S with log t.

Time (a)	S	Time (a)	S
0	0.8	30	0.8
0.9	0.8	45	0.8805
1.25	0.799	51	0.902
1.6	0.795	60	0.93
3	0.77	100	0.95
5	0.74	110	0.96
8	0.709	120	0.97
9	0.702	130	0.98
10	0.7	140	0.99
11.5	0.701	150	1
13	0.706	1 000 000	1
20	0.74		

Kback_in File name for the saturation-dependence of the thermal conductivity of the backfill [Kback_in]. Based on the thermal conductivity of dense backfill defined by Garisto et al. (2004).

Cp5 Specific heat of layer 5 (C) [845 $J \cdot kg^{-1} \cdot K^{-1}$]. Generic value for clay/rock/sand (King and Kolář 2000).

NMlayer6 Name of layer 6 [Back2]. The sixth layer is the second of two sub-layers representing the backfill material. The backfill is represented by two sub-layers to better represent the spatial dependence of the time-dependent degree of saturation, but otherwise all properties are identical.

L6 Thickness of layer 6 [47 dm]. The total thickness of the backfill layer is based on the ratio of the volume of the backfill in the repository to the surface area of the canisters. In this way, the amount of initially trapped atmospheric O_2 per unit area of canister is simulated properly in the 1-D CSM. The canister surface area and backfill volume are based on Figure 4-4 of SKB (2006a) and an average borehole spacing of 5 m, giving a volume:surface area ratio of 87 dm. This thickness is arbitrarily divided into two layers of thickness 40 dm and 47 dm.

eps6E Effective porosity for diffusive transport in layer 6 (ε_e) [0.22 unitless]. For the current purposes, the backfill is assumed to comprise a mixture of 70 wt% crushed rock plus 30 wt% Deponit Ca-N bentonite, a dry density of 2 120 $kg \cdot m^{-3}$, total porosity of 0.22, and an initial degree of saturation of 0.8, based on the properties of the dense backfill defined by Ontario Power Generation for their Third Case Study (Garisto et al. 2004). Because of the relatively low clay content, and in the absence of other information, the entire porosity is assumed to be accessible, interconnected porosity that contributes to mass transport.

eps6S Storage porosity in layer 6 (ε_s) [0 unitless]. Because of the relatively low clay content, and in the absence of other information, the entire porosity of the dense backfill is assumed to be accessible, interconnected porosity that contributes to mass transport. Therefore, the storage porosity is assumed to be zero.

eps6N Non-accessible porosity for layer 6 (ε_{na}) [0 unitless]. Because of the relatively low clay content, and in the absence of other information, the entire porosity of the dense backfill is assumed to be accessible, interconnected porosity that contributes to mass transport. Therefore, the non-accessible porosity is assumed to be zero.

rho6 Density of solids in the backfill (ρ) [2.7 $kg \cdot dm^{-3}$]. This is the density of the solid particles in the backfill and is not to be confused with the assumed dry density of 2 120 $kg \cdot m^{-3}$.

S_MIC6 Threshold degree of saturation above which microbial activity in the backfill is possible (S_{MIC}) [0.75 unitless]. There is strong evidence that microbial activity only occurs above a threshold water activity or, for porous media, a threshold degree of saturation (King 2009, King et al. 2002, 2003, 2004b). The degree of saturation corresponding to the threshold water activity of 0.96 depends on the suction potential, which in turn is dependent on the clay content and density of the material. A value of 0.75 is selected here as an intermediate value between that for a 50:50 bentonite:sand mixture and that for the dense backfill containing 5 wt% bentonite (King et al. 2004b).

c5max6 Maximum adsorption capacity for Cu(II) in layer 6 (c_5^{max}) [0.105 $mol \cdot kg^{-1}$]. Based on a cation exchange capacity for Deponit CA-N clay of 70 meq/100g (Pastina and Hellä 2006, Table 4-4), a clay content of 30 wt% in the backfill, and the assumption that all porosity is accessible porosity.

AP6 Surface area of pyrite per unit volume of layer 6 (A_p) [0.382 dm^{-1}]. Based on a pyrite content of 0.5 wt% in Deponit CA-N bentonite (Pastina and Hellä 2006, Table 4-4), a clay content of 30 wt%, an assumed backfill dry density of 2 120 $kg \cdot m^{-3}$, and a specific surface area for pyrite of 12.0 $cm^3 \cdot g^{-1}$ (based on an assumed spherical particle diameter of 1 mm and a pyrite density of 5.01 $g \cdot cm^{-3}$, CRC 1982). The surface area of pyrite in the crushed rock component of the backfill is assumed to be negligible.

tau6 Tortuosity factor for the backfill (τ_f) [0.1 unitless]. Assumed value based on the value for 50:50 sand:bentonite buffer material (Oscarson et al. 1992).

c06 Initial (calculated) concentration of dissolved O_2 in the pore water in layer 6 (c_0) [0.000205 mol·dm^{-3}]. Calculated based on the requirements to (i) conserve the correct initial O_2 inventory and (ii) ensure equilibrium between dissolved and gaseous O_2 initially. See more-detailed explanation for c02, above.

c66 Initial concentration of Cl^- in the pore water in layer 6 (c_6) [0.036 mol·dm^{-3}]. Based on modelled pore water composition for MX-80 bentonite clay of 0.0675 mol·dm^{-3} for a dry density of 1 500 kg·m^{-3} (Pastina and Hellä 2006, Table 6-5), corrected for the backfill dry density of 2 120 kg·m^{-3}, the mean initial degree of saturation of 0.8, the lower clay content (30 wt% of the backfill), and the assumption that the halite impurity content of Deponit CA-N clay is the same as that for MX-80 clay.

c76 Initial concentration of Fe(II) in layer 6 (c_7) [0 mol·dm^{-3}]. The backfill pore water is assumed to be initially free of dissolved Fe(II), consistent with the presence initially of dissolved and gaseous O_2.

c96 Initial concentration of dissolved sulfide in the backfill pore water (c_9) [0 mol·dm^{-3}]. The backfill is assumed to be initially free of HS^- because of the aerobic conditions.

cP6 Initial concentration of pyrite in layer 6 (c_{10}) [0.0265 mol·dm^{-3}]. Based on the pyrite content of Deponit CA-N bentonite of 0.5 wt% (Pastina and Hellä 2006, Table 4-4), a backfill dry density of 2 120 kg·m^{-3}, a clay content of 30 wt%, and the molecular mass of FeS_2 of 120 g·mol^{-1} (CRC 1982).

cS6 Initial concentration of dissolved sulfate in the pore water in layer 6 (c_{11}) [0.479 mol·dm^{-3}]. Based on the anhydrite content of Deponit CA-N bentonite (18 g·kg^{-1}, Pastina and Hellä 2006, Table 4-4), a dry density of 2 120 kg·m^{-3}, a clay content in the backfill of 30 wt%, the backfill porosity of 0.22, initial degree of saturation of 0.8, and the molecular mass of anhydrite $CaSO_4$ of 136 g·mol^{-1}. In order to avoid under-estimating the amount of sulfate available for microbial sulfate reduction, the entire inventory of SO_4^{2-} is assumed to be initially dissolved in the pore water.

S6_in File name for the time dependence of the degree of saturation in layer 6 [S6_in]. The initial degree of saturation of 0.8 is assumed to be the same as for the dense backfill defined by Garisto et al. (2004). Complete saturation of the repository is assumed to occur after 200 a. At intermediate times, the assumed values are chosen to reflect the fact that the backfill will dry out to a lesser extent than the HCB that is located closer to the canister. The layer of backfill in contact with the EDZ will dry out to a greater extent because some of the initial moisture content will be re-distributed to the EDZ which is assumed to almost completely dry out during repository construction. The degree of saturation at times other than those indicated in the table is calculated based on the assumption of the linear variation of S with log t.

Time (a)	S	Time (a)	S
0	0.8	11.5	0.601
0.009	0.8	13	0.606
0.0125	0.79995	20	0.646
0.019	0.79945	30	0.725
0.03	0.7983	45	0.8705
0.05	0.796	4 706	0.889
0.2	0.78	51	0.902
0.4	0.76	60	0.913
0.6	0.74	100	0.95
0.8	0.72	110	0.96
1	0.7	120	0.97
1.4	0.689	130	0.98
2	0.677	140	0.99
5	0.637	147	0.9976
8	0.609	150	0.9994
9	0.602	154	1
10	0.6	1 000 000	1

Kback_in — File name for the saturation-dependence of the thermal conductivity of the backfill [Kback_in]. Based on the thermal conductivity of dense backfill defined by Garisto et al. (2004).

Cp6 — Specific heat of layer 6 (C) [845 $J \cdot kg^{-1} \cdot K^{-1}$]. Generic value for clay/rock/sand (King and Kolář 2000).

NMlayer7 — Name of layer 7 [EDZ]. The seventh layer is the first of two layers representing the damage resulting from excavation of the underground openings. The region closest to the openings, and hence closest to the canister, is referred to as the excavation-damaged zone (EDZ). The EDZ is a zone of irreversible deformation of the rock and may contain new fractures (Pastina and Hellä 2006).

L7 — Thickness of layer 7 [5 dm]. The thickness and permeability of the EDZ depends on the method of excavation (Pastina and Hellä 2006). Drill and blasting can result in a zone a few tens of cm up to a metre wide, with a permeability 100–1 000-fold higher than that of the sparsely fractured host rock. A tunnel boring machine results in less damage, with an EDZ thickness of a few cm and an increase in permeability of the order of a factor of 10. Here a value representative of a drill and blast technique is used.

eps7E — Effective porosity for diffusive transport in layer 7 (ε_e) [0.006 unitless]. Based on values for the 'inner EDZ' defined by Garisto et al. (2004). The entire porosity is assumed to be accessible, interconnected porosity that contributes to mass transport.

eps7S — Storage porosity in layer 7 (ε_s) [0 unitless]. The entire EDZ porosity is assumed to be accessible, interconnected porosity that contributes to mass transport. Therefore, the storage porosity is assumed to be zero.

eps7N — Non-accessible porosity for layer 7 (ε_{na}) [0 unitless]. The entire EDZ porosity is assumed to be accessible, interconnected porosity that contributes to mass transport. Therefore, the non-accessible porosity is assumed to be zero.

rho7 — Density of solids in the EDZ (ρ) [2.7 $kg \cdot dm^{-3}$]. This is the density of the solid particles in the EDZ.

S_MIC7 — Threshold degree of saturation above which microbial activity in the EDZ is possible (S_{MIC}) [0 unitless]. A value of 0 is selected here since it is assumed that microbial activity is possible in the host rock and damaged zones at all times.

c5max7 — Maximum adsorption capacity for Cu(II) in layer 7 (c_5^{max}) [0 $mol \cdot kg^{-1}$]. In the absence of information to the contrary, it is assumed that there is negligible adsorption of Cu(II) in the host rock or damaged zones.

AP7 — Surface area of pyrite per unit volume of layer 7 (A_p) [0 dm^{-1}]. Although there is pyrite in the host rock, it is assumed that all exposed pyrite surfaces are oxidised during the operational phase, so that the effective pyrite surface area in the EDZ is zero.

tau7 — Tortuosity factor for the EDZ (τ_f) [0.1 unitless]. Assumed value.

c07 — Initial (calculated) concentration of dissolved O_2 in the pore water in layer 7 (c_0) [0.000204 $mol \cdot dm^{-3}$]. Calculated based on the requirements to (i) conserve the correct initial O_2 inventory in the EDZ and (ii) ensure equilibrium between dissolved and gaseous O_2 initially. See more-detailed explanation for c02, above.

c67 — Initial concentration of Cl^- in the pore water in layer 7 (c_6) [0.1 $mol \cdot dm^{-3}$]. Assumed representative ground water concentration. The assumed value does not account for the possibility of the evaporative concentration of EDZ pore water during the operational phase.

c77 — Initial concentration of Fe(II) in layer 7 (c_7) [0 $mol \cdot dm^{-3}$]. The EDZ pore water is assumed to be initially free of dissolved Fe(II), consistent with the presence initially of dissolved and gaseous O_2.

c97 Initial concentration of dissolved sulfide in the EDZ pore water (c_9) [1.0×10^{-5} mol·dm^{-3}]. Based on the maximum at-closure value reported in Table 2-2 of King et al. (2010). The concentration of 1.0×10^{-5} mol·dm^{-3} is equivalent to approximately 0.3 mg/L. The assumption of a finite HS^- initial concentration is conservative as it is inconsistent with the assumption that the EDZ pore water is initially aerobic, which would result in the oxidation of HS^- to SO_4^{2-}.

cP7 Initial concentration of exposed pyrite in layer 7 (c_{10}) [0 mol·dm^{-3}]. Based on the assumption that the available pyrite in the EDZ is oxidised during the operational phase.

cS7 Initial concentration of dissolved sulfate in the pore water in layer 7 (c_{11}) [0.0094 mol·dm^{-3}]. Based on the maximum at-closure value reported in Table 2-2 of King et al. (2010). The defined value does not account for the possibility of the evaporative concentration of EDZ pore water during the operational phase.

S7_in File name for the time dependence of the degree of saturation in layer 7 [S7_in]. It is assumed that the EDZ dries out extensively during the operational phase. The degree of saturation at times other than those indicated in the table is calculated based on the assumption of the linear variation of S with log t.

Time (a)	S	Time (a)	S
0	0.197	75	0.535
0.01	0.2	89	0.568
0.2	0.26	100	0.6
0.4	0.32	105	0.628
0.6	0.38	110	0.668
0.8	0.44	120	0.76
0.9	0.475	130	0.84
0.98	0.495	140	0.92
1.1	0.499	147	0.979
1.4	0.5	150	0.998
50	0.5	154	1
64	0.515	1 000 000	1

Krock_in File name for the saturation-dependence of the thermal conductivity of the EDZ [Krock_in]. Based on the thermal conductivity of granite rock defined by Garisto et al. (2004).

Cp7 Specific heat of layer 7 (C) [845 J·kg^{-1}·K^{-1}]. Generic value for clay/rock/sand (King and Kolář 2000).

NMlayer8 Name of layer 8 [EdZ]. The eighth layer is the second of two layers representing the damage resulting from excavation of the underground openings. The region between the EDZ and the intact host rock is referred to as the excavation-disturbed zone (EdZ). The EdZ is a zone of stress redistribution, elastic strains, and small changes in permeability (Pastina and Hellä 2006).

L8 Thickness of layer 8 [20 dm]. The EdZ can be several metres thick (Pastina and Hellä 2006).

eps8E Effective porosity for diffusive transport in layer 8 (ε_e) [0.003 unitless]. Based on values for the 'outer EDZ' defined by Garisto et al. (2004). The entire porosity is assumed to be accessible, interconnected porosity that contributes to mass transport.

eps8S Storage porosity in layer 8 (ε_s) [0 unitless]. The entire EdZ porosity is assumed to be accessible, interconnected porosity that contributes to mass transport. Therefore, the storage porosity is assumed to be zero.

eps8N Non-accessible porosity for layer 8 (ε_{na}) [0 unitless]. The entire EdZ porosity is assumed to be accessible, interconnected porosity that contributes to mass transport. Therefore, the non-accessible porosity is assumed to be zero.

rho8 Density of solids in the EdZ (ρ) [2.7 kg·dm^{-3}]. This is the density of the solid particles in the EdZ.

S_MIC8 Threshold degree of saturation above which microbial activity in the EdZ is possible (S_{MIC}) [0 unitless]. A value of 0 is selected here since it is assumed that microbial activity is possible in the host rock and damaged zones at all times.

c5max8 Maximum adsorption capacity for Cu(II) in layer 8 (c_5^{max}) [0 mol·kg^{-1}]. In the absence of information to the contrary, it is assumed that there is negligible adsorption of Cu(II) in the host rock or damaged zones.

AP8 Surface area of pyrite per unit volume of layer 8 (A_p) [50 dm^{-1}]. Based on the estimated surface area of fractures at Stripa (1 000 dm^2/dm^3) (Malmström et al. 1995) and an estimate that 5 % of the fracture surface is covered by FeS_2, with calcite as the predominant fracture-filling mineral (Paulamäki et al. 2006).

tau8 Tortuosity factor for the EdZ (τ_f) [0.1 unitless]. Assumed value.

c08 Initial (calculated) concentration of dissolved O_2 in the pore water in layer 8 (c_0) [0.000204 mol·dm^{-3}]. Calculated based on the requirements to (i) conserve the correct initial O_2 inventory in the EdZ and (ii) ensure equilibrium between dissolved and gaseous O_2 initially. See more-detailed explanation for c02, above.

c68 Initial concentration of Cl^- in the pore water in layer 8 (c_6) [0.1 mol·dm^{-3}]. Assumed representative ground water concentration. The assumed value does not account for the possibility of the evaporative concentration of EDZ pore water during the operational phase.

c78 Initial concentration of Fe(II) in layer 8 (c_7) [0 mol·dm^{-3}]. The EdZ pore water is assumed to be initially free of dissolved Fe(II), consistent with the presence initially of dissolved and gaseous O_2.

c98 Initial concentration of dissolved sulfide in the EdZ pore water (c_9) [1.0×10^{-5} mol·dm^{-3}]. Based on the maximum at-closure value reported in Table 2-2 of King et al. (2010). The concentration of 1.0×10^{-5} mol×dm^{-3} is equivalent to approximately 0.3 mg/L. The assumption of a finite HS^- initial concentration is conservative as it is inconsistent with the assumption that the EdZ pore water is initially aerobic.

cP8 Initial concentration of exposed pyrite in layer 8 (c_{10}) [21 mol·dm^{-3}]. This parameter represents the concentration of pyrite in the EdZ available for reaction during the course of the simulation. Even over geological timescales, pyrite in the host rock away from fracture surfaces will not be available for reaction. Only the pyrite in the vicinity of the fracture surfaces is included. This is, therefore, a complex and uncertain calculation. The pyrite content of the EdZ is based on an assumed fracture surface area in the EdZ area of 50 dm^2/dm^3 (a factor of 20 smaller than the surface area of fractures in the EDZ at Stripa of 1 000 dm^2/dm^3, Malmström et al. 1995), an assumed thickness of pyrite in the fracture of 1 mm (based on the report by Vaittinen et al. (2005) of 5-mm-thick pyrite deposits at Olkiluoto), a pyrite density of 5 g·cm^{-3}, and a pyrite molecular mass of 120 g·mol^{-1}.

cS8 Initial concentration of dissolved sulfate in the pore water in layer 8 (c_{11}) [0.0094 mol·dm^{-3}]. Based on the maximum at-closure value reported in Table 2-2 of King et al. (2010). The defined value does not account for the possibility of the evaporative concentration of EDZ pore water during the operational phase.

S8_in File name for the time dependence of the degree of saturation in layer 8 [S8_in]. It is assumed that the EdZ dries out to a limited degree during the operational phase due to evaporation at the surface of the openings. The EdZ is assumed to dry out to a lesser degree, and re-saturates faster, than the EDZ. The degree of saturation at times other than those indicated in the table is calculated based on the assumption of the linear variation of S with log t.

Time (a)	S	Time (a)	S
0	0.5	10	0.7
0.9	0.5	15	0.72
1	0.501	40	0.773
1.2	0.503	50	0.8
2	0.518	92	0.97
3	0.54	99	0.995
6	0.625	110	1
8	0.675	1 000 000	1

Krock_in — File name for the saturation-dependence of the thermal conductivity of the EdZ [Krock_in]. Based on the thermal conductivity of granite rock defined by Garisto et al. (2004).

Cp8 — Specific heat of layer 8 (C) [845 $J \cdot kg^{-1} \cdot K^{-1}$]. Generic value for clay/rock/sand (King and Kolář 2000).

NMlayer9 — Name of layer 9 [Rock]. The ninth layer in the simulation is the layer of intact host rock between the EdZ and the right-hand boundary of the model geometry, representing a ground-water-bearing fracture.

L9 — Thickness of layer 9 [20 dm]. The thickness of the host rock layer is arbitrarily chosen to represent a location in the far-field at which a ground-water-bearing fractures maintains constant geochemical conditions.

eps9E — Effective porosity for diffusive transport in layer 9 (ε_e) [0.003 unitless]. Based on values for the host rock defined by Garisto et al. (2004). The entire porosity is assumed to be accessible, interconnected porosity that contributes to mass transport.

eps9S — Storage porosity in layer 9 (ε_s) [0 unitless]. The entire host rock porosity is assumed to be accessible, interconnected porosity that contributes to mass transport. Therefore, the storage porosity is assumed to be zero.

eps9N — Non-accessible porosity for layer 9 (ε_{na}) [0 unitless]. The entire host-rock porosity is assumed to be accessible, interconnected porosity that contributes to mass transport. Therefore, the non-accessible porosity is assumed to be zero.

rho9 — Density of solids in the host rock (ρ) [2.7 $kg \cdot dm^{-3}$]. This is the density of the solid particles in the host rock, excluding porosity.

S_MIC9 — Threshold degree of saturation above which microbial activity in the host rock is possible (S_{MIC}) [0 unitless]. A value of 0 is selected here since it is assumed that microbial activity is possible in the host rock at all times.

c5max9 — Maximum adsorption capacity for Cu(II) in layer 9 (c_5^{max}) [0 $mol \cdot kg^{-1}$]. In the absence of information to the contrary, it is assumed that there is negligible adsorption of Cu(II) in the host rock.

AP9 — Surface area of pyrite per unit volume of layer 9 (A_p) [5 dm^{-1}]. Based on the estimated surface area of fractures at Stripa (1 000 dm^2/dm^3) (Malmström et al. 1995), reduced by a factor of 10 to account for the lower fracture density in the intact host rock, and an estimate that 5 % of the fracture surface is covered by FeS_2, with calcite as the predominant fracture-filling mineral (Paulamäki et al. 2006).

tau9 — Tortuosity factor for the host rock (τ_f) [0.1 unitless]. Assumed value.

c09 — Initial concentration of dissolved O_2 in the pore water in layer 9 (c_0) [0 $mol \cdot dm^{-3}$]. The ground water in the host rock is treated as anoxic based on the redox potentials given by King et al. (2010).

c69 — Initial concentration of Cl^- in the pore water in layer 9 (c_6) [0.1 $mol \cdot dm^{-3}$]. Assumed representative ground water concentration.

c79 Initial concentration of Fe(II) in layer 9 (c_7) [1×10^{-5} mol·dm^{-3}]. The ground water in the host rock is treated as anoxic and saturated with Fe(II). The defined value is assumed to approximate the solubility of Fe(II) in deep granitic ground waters.

c99 Initial concentration of dissolved sulfide in the host-rock ground water (c_9) [1.0×10^{-5} mol·dm^{-3}]. Based on the maximum at-closure value reported in Table 2-2 of King et al. (2010). The concentration of 1.0×10^{-5} mol·dm^{-3} is equivalent to approximately 0.3 mg/L.

cP9 Initial concentration of exposed pyrite in layer 9 (c_{10}) [2.1 mol·dm^{-3}]. This parameter represents the concentration of pyrite in the host rock available for reaction during the course of the simulation. Even over geological timescales, pyrite in the host rock away from fracture surfaces will not be available for reaction. Only the pyrite in the vicinity of the fracture surfaces is included. This is, therefore, a complex and uncertain calculation. The pyrite content of the host rock is based on an assumed fracture surface area per unit volume of rock of 5 dm^2/dm^3 (a factor of 200 smaller than the surface area of fractures in the EDZ at Stripa of 1 000 dm^2/dm^3, Malmström et al. 1995), an assumed thickness of pyrite in the fracture of 1 mm (based on the report by Vaittinen et al. (2005) of 5-mm-thick pyrite deposits at Olkiluoto), a pyrite density of 5 g·cm^{-3}, and a pyrite molecular mass of 120 g·mol^{-1}.

cS9 Initial concentration of dissolved sulfate in the pore water in layer 9 (c_{11}) [0.0094 mol·dm^{-3}]. Based on the maximum at-closure value reported in Table 2-2 of King et al. (2010).

S9_in File name for the time dependence of the degree of saturation in layer 9 [S9_in]. It is assumed that the host rock is saturated at all times.

Time (a)	S	Time (a)	S
0	1	1 000 000	1

Krock_in File name for the saturation-dependence of the thermal conductivity of the host rock [Krock_in]. Based on the thermal conductivity of granite rock defined by Garisto et al. (2004).

Cp9 Specific heat of layer 9 (C) [845 J·kg^{-1}·K^{-1}]. Generic value for clay/rock/sand (King and Kolář 2000).

C1.3 Rate Constants, Diffusivities, Activation Energies, Solubilities, and Electrochemical Parameters

k1room Rate constant for the homogeneous oxidation of $CuCl_2^-$ by O_2 (k_1) [a spatially and temporally varying function of T and [Cl$^-$] calculated within the model]. The included temperature dependence is taken directly from Sharma and Millero (1988), and is equivalent to an activation energy of 39 500 J·mol^{-1}.

k2room Rate constant for the hydrolysis of $CuCl_2^-$ (k_2) [1 s^{-1} at 25 °C]. The mechanism for the formation of Cu_2O is unknown, but is assumed here to result from the hydrolysis of $CuCl_2^-$. The value of k_2 is set a factor of 10 larger than k_{-2} in order to simulate the experimentally observed formation of Cu_2O.

DeH2 Temperature dependence of k_2 (ΔH_2) [60 000 J·mol^{-1}]. Estimated value based on a typical ΔH for chemical processes.

km2room Rate constant for the dissolution of Cu_2O (k_{-2}) [0.1 s^{-1} at 25 °C]. Some experimental data are available on the dissolution rate of Cu_2O in Cl^- solutions as a function of pH (King and Legere, unpublished data), including an activation energy, the dependence on pH and [Cl^-] and estimated values for the rate constant in units of $mol \cdot cm^{-2} \cdot s^{-1}$. The reaction is pH-dependent, but independent of [Cl^-]. However, k_{-2} is expressed in terms of the rate of Cu_2O dissolution per unit volume. Consequently, a value for the specific surface area of Cu_2O ($cm^2 \cdot mol^{-1}$) is required to convert the experimentally accessible rate constant to k_{-2}. The specific surface area of Cu_2O is unknown and will depend on the environmental conditions under which precipitation occurs. Therefore, the value of k_{-2} of 0.1 s^{-1} is an assumed value.

DeHm2 Temperature dependence of k_{-2} (ΔH_{-2}) [40 000 $J \cdot mol^{-1}$]. Based on experimental data on Cu_2O dissolution at pH 5 (King and Legere, unpublished data).

k3room Rate constant for the precipitation of $CuCl_2 \cdot 3Cu(OH)_2$ (k_3) [$1 \times 10^{-5} \times s^{-1}$ at 25 °C]. There are no kinetic data for the rate of precipitation of $CuCl_2 \cdot 3Cu(OH)_2$. The precipitation rate constant is 10 times higher than the dissolution rate constant to account for the experimental observation of precipitated $CuCl_2 \cdot 3Cu(OH)_2$. The value of k_3 of 1×10^{-5} s^{-1} is assumed.

DeH3 Temperature dependence of k_3 (ΔH_3) [60 000 $J \cdot mol^{-1}$]. Estimated value based on a typical ΔH for chemical processes.

km3room Rate constant for the dissolution of $CuCl_2 \cdot 3Cu(OH)_2$ (k_{-3}) [1×10^{-6} s^{-1} at 25 °C]. There are a limited number of measurements on the dissolution rate of $CuCl_2 \cdot 3Cu(OH)_2$ (King and Strandlund, unpublished data). However, as in the case of the dissolution of Cu_2O (k_{-2}), k_{-3} contains a term for the specific surface area of precipitated $CuCl_2 \cdot 3Cu(OH)_2$, an unknown parameter. Therefore, an assumed value of k_{-3} is used.

DeHm3 Temperature dependence of k_{-3} (ΔH_{-3}) [60 000 $J \cdot mol^{-1}$]. Estimated value based on a typical ΔH for chemical processes.

k4room Rate constant for the adsorption of Cu^{2+} on Na-bentonite (k_4) [2×10^{-3} $dm^3 \cdot mol^{-1} \cdot s^{-1}$ at 25 °C]. The rate of Cu^{2+} adsorption is based on unpublished data (King and Ryan) from studies on loose clay. The form of the kinetic adsorption expression is consistent with the nature of the equilibrium Langmuir isotherm observed experimentally (Ryan and King 1994).

DeH4 Temperature dependence of k_4 (ΔH_4) [0 $J \cdot mol^{-1}$]. Various equilibrium sorption studies of Cu^{2+} on loose montmorillonite clay report both positive and negative enthalpies (Ryan and King 1994). Therefore, in the absence of other data, the adsorption of Cu^{2+} will be assumed to be independent of temperature.

km4room Rate constant for the desorption of Cu^{2+} (k_{-4}) [1×10^{-6} s^{-1} at 25 °C]. The desorption rate constant is an estimated value based on the observation of extremely slow desorption in loose clay systems (King and Ryan, unpublished data).

DeHm4 Temperature dependence of k_{-4} (ΔH_{-4}) [0 $J \cdot mol^{-1}$]. Various equilibrium sorption studies of Cu^{2+} on loose montmorillonite clay report both positive and negative enthalpies (Ryan and King 1994). Therefore, in the absence of other data, the desorption of Cu^{2+} will be assumed to be independent of temperature.

k5room Rate constant for the consumption of FeS_2 by oxidation by O_2 (k_5) [6.6×10^{-11} $mol^{1/2} \cdot dm^{-1/2} \cdot s^{-1}$ at 25 °C]. The overall oxidation of FeS_2 is given by (see Section 2.3.2):

$$FeS_2 + H_2O + 3.5O_2 \rightarrow Fe^{2+} + 2SO_4^{2-} + 2H^+$$

The rate of the oxidation of FeS_2 to sulfate and Fe(II) is ½-order with respect to the concentration of O_2 and is pH-dependent (Salmon and Malmström 2004). In terms of the rate of consumption of FeS_2, the specific rate constant (per unit area of pyrite) is $8.7 \times 10^{-12}[H^+]^{-0.11}$ $mol^{1/2} \cdot dm^{-1/2} \cdot s^{-1}$ or 6.6×10^{-11} $mol^{1/2} \cdot dm^{-1/2} \cdot s^{-1}$ at pH 8, the assumed pH of the pore water. The use of this rate constant to describe the rate of the overall oxidation reaction implicitly assumes that the subsequent oxidation of Fe(II) to Fe(III) is fast.

DeH5 Temperature dependence of k_5 (ΔH_5) [56 900 $J \cdot mol^{-1}$]. Activation energy from Salmon and Malmström (2004).

k6room — Rate constant for the reaction between Cu^{2+} and Fe(II) (k_6) [10 $dm^3 \cdot mol^{-1} \cdot s^{-1}$ at 25°C]. No experimental data are available. The value is based on the assumption that the homogeneous kinetics are rapid, as is the case for the redox reactions involving O_2 and $CuCl_2^-$ and O_2 and Fe(II) discussed above.

DeH6 — Temperature dependence of k_6 (ΔH_6) [40 000 $J \cdot mol^{-1}$]. Activation energy assumed to be the same as that for k_1.

k7room — Rate constant for the precipitation of FeS (k_7) [1 $dm^3 \cdot mol^{-1} \cdot s^{-1}$ at 25 °C]. Assumed value to reflect relatively fast precipitation of mackinawite.

DeH7 — Temperature dependence of k_7 (ΔH_7) [60 000 $J \cdot mol^{-1}$]. Activation energy based on typical value for a chemical reaction.

k9room — Rate constant for the microbial consumption of O_2 (k_9) [2.2×10^{-10} s^{-1} at 25 °C]. If the degree of saturation exceeds the threshold value of microbial activity, then the consumption of O_2 by aerobic respiration is permitted. The value for the rate constant is derived from the Isothermal Test (ITT) at AECL's Underground Research Laboratory (Dixon et al. 2001). Over the 6.5 a duration of the test, the composition of the atmosphere in the test was observed to decrease from an initial O_2:Ar ratio of 20.2 to between 16.4 and 18.3. Microbial activity was known to have occurred in the test (Stroes-Gascoyne et al. 2000) and the decrease in O_2 content was ascribed to aerobic microbial respiration at a rate equivalent to an O_2 half-life of 10 a (King and Kolář 2006), resulting in a zero-order rate constant of 2.2×10^{-9} s^{-1}. Simulations of various large-scale in situ tests using this value suggested the rate of O_2 consumption was over-estimated, so the value used for the CSM was decreased by one order of magnitude.

DeH9 — Temperature dependence of k_9 (ΔH_9) [60 000 $J \cdot mol^{-1}$]. Activation energy based on typical value for a chemical reaction.

k10room — Rate constant for the microbial reduction of sulfate to sulfide (k_{10}) [6.0×10^{-15} $mol \cdot dm^{-3} \cdot s^{-1}$ at 25 °C]. The zero-order rate constant is derived from the data of Masurat et al. (2010) who measured the rate of Cu_xS formation on copper coupons embedded in a microbially active system containing compacted bentonite. Based on the rate of sulfide production (equivalent to the rate of sulfate reduction, assuming all HS^- produced was consumed in the formation of Cu_xS) of 3.4×10^{-14} $mol \cdot mm^{-2} \cdot day^{-1}$ and the assumption that the sulfide was produced throughout the bentonite plug used in the experiments, the rate of sulfate reduction per unit volume of pore water is estimated to be 6.0×10^{-15} $mol \cdot dm^{-3} \cdot s^{-1}$.

DeH10 — Temperature dependence of k_{10} (ΔH_{10}) [60 000 $J \cdot mol^{-1}$]. Activation energy based on typical value for a chemical reaction.

R0room — Instantaneous rate of the anaerobic dissolution (expressed as the Fe(II) release rate) of pyrite (R_0) [2×10^{-14} $mol \cdot dm^{-2} \cdot s^{-1}$ at 25 °C]. In the absence of kinetic data for the anaerobic dissolution of FeS_2 (King 2013), the rate and mechanism of pyrite dissolution are assumed to be the same as for biotite. The model used for predicting the release rate of Fe(II) from biotite dissolution is based on the experimental observation that an Fe(II)−depleted layer of constant thickness forms on the biotite surface. A similar surface layer develops for the oxidative dissolution of pyrite and it is not unreasonable to assume that a similar surface layer may develop under anaerobic conditions. During the transient period, the thickness of this layer grows. At steady-state (i.e., once a constant film thickness has been achieved), the dissolution rate of the film (and, hence, the release rate of Fe(II)) is determined by the dissolution rate of the least soluble component. The value of R_0 is based on the data of Malmström et al. (1995) at pH 7.

DeHR0 — Temperature dependence of R_0 (ΔH_{R_0}) [59 000 $J \cdot mol^{-1}$]. An activation energy of 59 000 $J \cdot mol^{-1}$ was suggested by Johnson et al. (1994) to describe the general dissolution behaviour of biotite. Here the same value is used for the temperature dependence of R_0, R_1 and α_p.

R1room — Steady-state pyrite anaerobic dissolution rate (R_1) [7.4×10^{-15} $mol \cdot dm^{-2} \cdot s^{-1}$]. Taken from Malmström et al. (1995) at pH 7.

DeHR1 Temperature dependence of R_1 (ΔH_{R_1}) [59 000 J·mol^{-1}]. See comment for ΔH_{R_o}.

alfaProom Time constant for the dissolution of pyrite (α_p) [1×10^{-6} s^{-1}]. Taken from Malmström et al. (1995) for the dissolution of biotite.

DeHalfaP Temperature dependence of α_p (ΔH_{α_p}) [59 000 J·mol^{-1}]. See comment for ΔH_{R_o}.

DAroom Diffusion coefficient of O_2 in air (D_A) [0.00165 dm^2·s^{-1} at 25 °C]. Based on the value of 0.00178 dm^2·s^{-1} at 0 °C (CRC 1982, p F-51) corrected for temperature based on the value of ΔH_{D_A}.

DeHDA Temperature dependence of D_A (ΔH_{D_A}) [−2 060 J·mol^{-1}]. Based on the temperature dependence of the increase in viscosity of air with temperature for temperatures between 0 °C and 74 °C (CRC 1982, p F-47). By analogy with the temperature-dependence of aqueous diffusion coefficients which is determined by the effect of temperature on viscosity.

D0room Pore-solution diffusion coefficient of O_2 (D_0) [1.7×10^{-7} dm^2·s^{-1} at 25 °C]. From data of King et al. (1995a).

DeHD0 Temperature dependence of D_0 (ΔH_{D_o}) [15 000 J·mol^{-1}]. The activation energy for the diffusion of dissolved species is taken to be the same as that for the temperature dependence of the viscosity of H_2O. Ionic mobility is closely related to the viscosity of the fluid (Robinson and Stokes 1959), from which it follows that the temperature dependence of the diffusivity is similar to that for the viscosity of the solution.

D1room Pore-solution diffusion coefficient of $CuCl_2^-$ (D_1) [6×10^{-8} dm^2·s^{-1} at 25 °C]. From data of Smyrl (1985).

DeHD1 Temperature dependence of D_1 (ΔH_{D1}) [18 800 J·mol^{-1}]. From Bacarella and Griess (1973).

D3room Pore-solution diffusion coefficient of Cu^{2+} (D_3) [6×10^{-8} dm^2·s^{-1} at 25 °C]. From data of Miller et al. (1980) in $CuSO_4$ solutions and Peters and Cruser (1965) in Cl^- solution.

DeHD3 Temperature dependence of D_3 (ΔH_{D_3}) [15 000 J·mol^{-1}]. The activation energy for the diffusion of dissolved species is taken to be the same as that for the temperature dependence of the viscosity of H_2O.

D6room Pore-solution diffusion coefficient of Cl^- (D_6) [2×10^{-7} cm^2·s^{-1} at 25 °C]. From Fontana et al. (1985).

DeHD6 Temperature dependence of D_6 (ΔH_{D_6}) [15 000 J·mol^{-1}]. The activation energy for the diffusion of dissolved species is taken to be the same as that for the temperature dependence of the viscosity of H_2O.

fD6 Enhancement factor to account for the effect of gravitational mixing of saline rock-mass fluids (f_{D_6}) [variable]. Not used for the current simulations.

D7room Pore-solution diffusion coefficient of Fe(II) (D_7) [5×10^{-8} dm^2·s^{-1} at 25 °C]. From International Critical Tables (ICT 1926).

DeHD7 Temperature dependence of D_7 (ΔH_{D_7}) [15 000 J·mol^{-1}]. The activation energy for the diffusion of dissolved species is taken to be the same as that for the temperature dependence of the viscosity of H_2O.

D9room Pore-solution diffusion coefficient of HS^- (D_9) [5×10^{-8} dm^2·s^{-1} at 25 °C]. Assumed value by analogy with value for Fe(II).

DeHD9 Temperature dependence of D_9 (ΔH_{D_9}) [15 000 J·mol^{-1}]. The activation energy for the diffusion of dissolved species is taken to be the same as that for the temperature dependence of the viscosity of water.

D11room Pore-solution diffusion coefficient of SO_4^{2-} (D_{11}) [1×10^{-7} dm^2·s^{-1} at 25 °C]. Assumed value characteristic of the diffusivity of ions in aqueous solution.

DeHD11 Temperature dependence of D_{11} ($\Delta H_{D_{11}}$) [15 000 J·mol^{-1}]. The activation energy for the diffusion of dissolved species is taken to be the same as that for the temperature dependence of the viscosity of water.

HeOroom Inverse Henry's law constant for O_2 at 25 °C ($\widetilde{H}_o$) [31.4 unitless]. Based on data from Sander (1999) and calculation in Section 2.2.1.

DeHHeO Temperature dependence of $\widetilde{H}_o$ ($\Delta H_{\widetilde{H}_o}$) [−14 100 J/mol]. Mean activation energy for the Henry' law constant given by Sander (1999) with opposite sign for the inverse constant.

c1satRoom Concentration of $CuCl_2^-$ in equilibrium with Cu_2O (c_1^{sat}) [3.4×10^{-3} mol·dm^{-3} at 25 °C in 1 mol·dm^{-3} Cl^-, pH 7]. The concentration of $CuCl_2^-$ at which Cu_2O precipitation occurs is estimated based on the total concentration of dissolved Cu(I) species (Cu^+, $CuCl_2^-$, Cu(OH) and $Cu(OH)_2^-$) in equilibrium with Cu_2O. No Cu(II) species are included in the equilibrium calculations. The solubility of Cu_2O is a function of [Cl^-] and temperature. Since, in the pH and [Cl^-] ranges of interest (King and Kolář 2000), $CuCl_2^-$ is the dominant species, the solubility of Cu_2O is proportional to [Cl^-]^2. The pH is assumed to be constant in the model.

DeH1sat Temperature dependence of c_1^{sat} (ΔH_1^{sat}) [24 000 J·mol^{-1}]. Determined from the effect of temperature on the solubility of Cu_2O (Palmer 2011).

c3satRoom Concentration of Cu^{2+} in equilibrium with $CuCl_2 \times 3Cu(OH)_2$ (c_3^{sat}) [4.3×10^{-7} mol·dm^{-3} at 25 °C, pH 7]. The concentration of Cu^{2+} in equilibrium with $CuCl_2 \cdot 3Cu(OH)_2$ is equated to the sum of the concentrations of all major dissolved species, namely; Cu^{2+}, $Cu(OH)^+$, $Cu(OH)_2$, $Cu(OH)_4^{2-}$ and $CuCl^+$ (D.J. Jobe, private communication). No Cu(I) species are considered in the equilibrium calculations. The relative proportions of these various species is a function of T, [Cl^-] and pH. At [Cl^-] < 0.1 mol·dm^{-3}, the solubility of $CuCl_2 \cdot 3Cu(OH)_2$ is proportional to [Cl^-]$^{-0.5}$, as would be expected from the stoichiometry. At higher [Cl^-] (0.1 < [Cl^-] <1.0 mol·dm^{-3}), the solubility is approximately independent of [Cl^-]. Therefore, c_3^{sat} is assumed to be independent of [Cl^-] for the present calculations.

DeH3 Temperature dependence of c_3^{sat} (ΔH_3^{sat}) [19 000 J × mol^{-1}]. The temperature dependence of c_3^{sat} varies with temperature. The value quoted is a mean of several values determined between 25 °C and 100 °C (D.J. Jobe, private communication).

c7satRoom Concentration of dissolved Fe(II) in equilibrium with FeS (c_7^{sat}) [1.56×10^{-12} mol^2·dm^{-6} at 25 °C]. The value of c_7^{sat} is based on the solubility product K_{sp} for FeS given by Sun et al. (2008) and is calculated for unit concentration of HS^- and pH 8.

DeH7sat Temperature dependence of c_7^{sat} (ΔH_7^{sat}) [24 000 J·mol^{-1}]. Based on data from Sun et al. (2008).

FaradC Faraday constant (F) [96 485.33 C·mol^{-1}]. CODATA Value, U.S. National Institute of Standards and Technology, NIST database accessed August 1, 2018 (https://physics.nist.gov/cgi-bin/cuu/Value?f).

n0 Number of electrons transferred in the reduction of O_2 (n_0) [4 unitless]. From King et al. (1995a).

alfaC Cathodic transfer coefficient for the reduction of O_2 (α_C) [0.37 unitless]. The transfer coefficient is a function of [O_2] (King et al. 1995b). The value used is that for aerated solution.

kCroom Electrochemical rate constant for the reduction of O_2 (k_C) [1.7×10^{-9} dm·s^{-1} at 25 °C]. From King et al. (1995a).

DeHC Temperature dependence of k_C (ΔH_C) [60 000 J·mol^{-1}]. From Kinoshita (1992).

E0Croom Standard potential for the reduction of O_2 (E_C^0) [0.16 V_{SCE} at 25 °C]. E_C^0 is calculated for pH 7, so that the exponential term in the expression for the equilibrium potential for the reduction of O_2 is not pH-dependent.

DeE0C Temperature dependence of E_C^0 (ΔE_C^0) [-1.23×10^{-4} V·K^{-1}]. Calculated on the assumption of a linear temperature dependence of E_C^0 between 298.2 K and 368.2 K. The values of E_C^0 at these temperatures were calculated using the convention that the free energy of the standard hydrogen electrode (SHE) is zero only at 298.2 K. Therefore, the standard potential of the SHE changes with temperature.

nA Number of electrons transferred during the oxidation of Cu (n_A) [1 unitless]. From King et al. (1995a).

E0Aroom Standard potential for the anodic dissolution of copper (E_A^0) [−0.105 V_{SCE} at 25 °C]. From King et al. (1995a).

DeE0A Temperature dependence of E_A^0 (ΔE_A^0) [-6.35×10^{-4} V·K^{-1}]. From Bertocci and Turner (1974).

kAroom Combined electrochemical rate constant for the anodic dissolution of Cu (k_A) [3.3×10^{-4} dm·s^{-1} at 25 °C]. k_A is a combined rate constant, equivalent to $k_{AF}k_{BF}/k_{AB}$ (Table 2-3). The value of k_A is a mean value from 0.1 mol·dm^{-3} and 1.0 mol·dm^{-3} Cl^- solution (King et al. 1995a).

DeHA Temperature dependence of k_A (ΔH_A) [60 000 J·mol^{-1}]. Assumed value.

kBBroom Rate constant for the reverse reaction involving the precipitation of $CuCl_{ADS}$ from dissolved $CuCl_2^-$ (k_{BB}) [1.42×10^{-3} dm·s^{-1} at 25 °C]. From King et al. (1995a).

DeHBB Temperature dependence of k_{BB} (ΔH_{BB}) [60 000 k·mol^{-1}]. Assumed value.

nD Number of electrons transferred for the reduction of Cu^{2+} (n_D) [1 unitless].

kDroom Electrochemical rate constant for the reduction of Cu^{2+} (k_D) [2×10^{-8} dm·s^{-1} at 25 °C]. Value derived from i/E curves of Hurlen (1961).

DeHD Temperature dependence of k_D (ΔH_D) [45 000 J·mol^{-1}]. From Astakhova and Krasikov (1971).

alfaD Transfer coefficient for the reduction of Cu^{2+} (α_D) [0.5 unitless]. Assumed value based on facile electron transfer reaction.

E0Droom Standard potential for the reduction of Cu^{2+} (E_D^0) [0.223 V_{SCE} at 25 °C]. From Van Muylder et al. (1961) and Peters and Cruser (1965).

DeE0D Temperature dependence of E_D^0 (ΔE_D^0) [0 V·K^{-1}]. Temperature dependence unknown.

nE Number of electrons transferred for the reduction of HS^- (n_E) [1 unitless].

kEroom Electrochemical rate constant for the evolution of H_2 from the reduction of HS^- (k_E) [2×10^{-8} dm·s^{-1} at 25 °C]. Estimated from the data of Smith et al. (2007b).

DeHD Temperature dependence of k_E (ΔH_E) [60 000 J·mol^{-1}]. Assumed value.

alfaE Transfer coefficient for the evolution of H_2 from the cathodic reduction of HS^- (α_E) [0.5 unitless]. Assumed value based on facile electron transfer reaction.

E0Eroom Standard potential for the evolution of H_2 from the cathodic reduction of HS^- (E_E^0) [−1.005 V_{SCE} at 25 °C]. Calculated from standard free energy of formation data (Wagman et al. 1982).

DeE0E Temperature dependence of E_E^0 (ΔE_E^0) [0 V × K^{-1}]. Temperature dependence unknown.

nS Number of electrons transferred in the rate-determining step for the sulfidation of copper (n_S) [1 unitless].

kSroom Electrochemical rate constant for the sulfidation of copper (k_S) [600 dm^4·mol^{-1}·s^{-1} at 25 °C). k_S is a composite rate constant equal to $k_{S1}k_{S3}/k_{S2}$. Based on analysis of the data of Smith et al. (2007b).

DeHS Temperature dependence of k_S (ΔH_S) [60 000 J·mol^{-1}]. Assumed value.

alfaS3 Transfer coefficient for the rate-determining electron-transfer step for the sulfidation of Cu (α_{S3}) [0.5 unitless]. Based on observed Tafel slope of 40 mV/dec (Smith et al. 2007b).

E0S12room Standard potential for the first electron-transfer step in the sulfidation of copper (E_{S12}^0) [−0.747 V_{SCE} at 25 °C]. Calculated from standard free energy of formation data (Wagman et al. 1982).

DeE0S12 Temperature dependence of E_{S12}^0 (ΔE_{S12}^0) [0 V·K^{-1}]. Temperature dependence unknown.

E0S3room Standard potential for the first electron-transfer step in the sulfidation of copper (E^0_{S3}) [−0.747 V_{SCE} at 25 °C]. Calculated from standard free energy of formation data (Wagman et al. 1982).

DeE0S3 Temperature dependence of E^0_{S3} (ΔE^0_{S3}) [0 $V \cdot K^{-1}$]. Temperature dependence unknown.

cAR Boundary condition for gaseous O_2 at the RHS boundary (fracture) [−1 $mol \cdot dm^{-3}$]. If cAR < 0, saturation concentration for cA used instead of the specified value.

c0R Boundary condition for dissolved O_2 at the RHS boundary (fracture) [0 $mol \cdot dm^{-3}$].

c6R Boundary condition for Cl^- at the RHS boundary (fracture) [0.1 $mol \cdot dm^{-3}$].

c7R Boundary condition for dissolved Fe(II) at the RHS boundary (fracture) [−1 $mol \cdot dm^{-3}$]. If c7R < 0, saturation concentration for c7 used instead of the specified value.

c9R Boundary condition for HS^- at the RHS boundary (fracture) [1.0×10^{-5} $mol \cdot dm^{-3}$].

c11R Boundary condition for SO_4^{2-} at the RHS boundary (fracture) [0.0094 $mol \cdot dm^{-3}$].

rhoW Groundwater density at 0 °C [1.0204 $kg \cdot dm^{-3}$].

Rgas Gas constant (R) [8.314 $J \cdot K^{-1} \cdot mol^{-1}$].

hkmin Humidity value below which surface reaction rates are zero [0.6 unitless].

hkmax Humidity value above which surface reaction rates equal their maximum values (corresponding to saturated conditions) [0.7 unitless].

t_hk1 Time when surface humidity is still > hkmin [0.2 a]. If t_hk1 < 0, humidity never passes through hkmin on desaturation.

t_hk2 Time when surface humidity is already < hkmin on desaturation [0.4 a].

t_hk3 Time when surface humidity is still < hkmin [110 a]. If t_hk3 < 0, humidity never passes through hkmin on resaturation.

t_hk4 Time when surface humidity is already > hkmin on resaturation [120 a].

rhsT_in Name of file with RHS temperature boundary condition (i.e., temperature at the RHS fracture) [tempFract.txt]. Two-column format: time (a) temperature (°C).

Time (a)	T (°C)	Time (a)	T (°C)
0	10.5	2 000	19.5
20	40.5	3 000	17
30	39	4 000	16.5
40	38	5 000	16
50	36.5	6 000	15
60	35	7 000	14.5
70	34	8 000	14.5
80	33	9 000	14
90	32.5	10 000	14
100	32	20 000	12.5
200	28.5	30 000	12
300	26.5	40 000	11.5
400	26	50 000	11
500	25	60 000	11
600	24.5	70 000	11
700	24	80 000	10.5
800	23.5	90 000	10.5
900	23	100 000	10.5
1 000	22.5	1 000 000	10.5

H0 Parameter used to define treatment of canister surface temperature in model [−0.072 unitless]. If negative, use the LHS temperature boundary condition file (lhsT_in); otherwise: use canister heat output file (heat_in) and scale it by H0.

lhsT_in Name of file with LHS temperature boundary condition [tempCont.txt]. Two-column file format: time (a) temperature (°C). Used when H0 is negative.

Time (a)	T (°C)	Time (a)	T (°C)
0	45	2 000	31
20	75.5	3 000	26.5
30	74.5	4 000	23
40	72.5	5 000	21.5
50	71	6 000	20.5
60	69	7 000	20
70	67.5	8 000	19
80	66.5	9 000	18.5
90	65	10 000	18
100	64	20 000	14.5
200	59	30 000	13.5
300	56.4	40 000	13
400	54	50 000	12.5
500	52	60 000	12
600	50	70 000	11.5
700	47.5	80 000	11
800	46	90 000	11
900	43.5	100 000	10.5
1 000	42.5	1 000 000	10.5

heat_in Name of file with heat source [HeatSource.txt]. Two-column file format: time (a) heat output (W.dm^{-2}). Used when H0 ≥ 0.

initT_in Name of file with initial temperature distribution in the various slayers [initTemp.txt]. Two-column file format: x (dm) temperature (°C).

x (dm)	T (°C)	x (dm)	T (°C)
0	45	3.5	16
1	45	4	15
1.5	44	20	15
2	40	30	10.5
2.5	30	10 000	10.5
3	20		

Appendix D

Definition of Base Case and Variant calculations for WP3 of the Integrated Sulfide Project

Please note that this Appendix was initially written by the members of the Work Package 3 (WP3) of the Posiva-SKB Integrated Sulfide Project as well as by participants of the steering group, work package leaders, etc. The members of the WP3 were: A. Idiart (Amphos 21, Spain), M. Birgersson (ClayTech, Sweden), F. King (ICC, Canada), M. Pękala, P. Alt-Epping and P. Wersin (Univ. Bern, Switzerland). Several other persons contributed to the definition of the base and variant cases: P. Pitkänen (Posiva, Finland), P. Hellä (Saanio & Riekkola, Finland), and C. Lilja and I. Puigdomenech (SKB, Sweden).

D1 Base case for WP3 of the Integrated Sulfide Project

D1.1 Introduction

The key motivation for the Integrated Sulfide Project (ISP) co-financed by Posiva and SKB is the assessment of copper sulfide corrosion and the different processes concerning sulfide production, transport and consumption.

The ISP is divided in three different work packages (WP), as follows:

1. WP1 – Geosphere.
2. WP2 – The buffer and backfill system.
3. WP3 – Integration with Safety Case; develop reactive transport modelling tools that are able to describe and simulate sulfide evolution (sources and sinks) and fluxes in the different parts of the near field of a KBS-3 repository (buffer, backfill, rock-backfill interface, rock bolts).

The numerical models developed in WP3 should be limited to the near-field of the repository, i.e. approximately a 10-to-20 meters square box around a single deposition hole, see **Figure D-1** for a sketch of the KBS-3 concept.

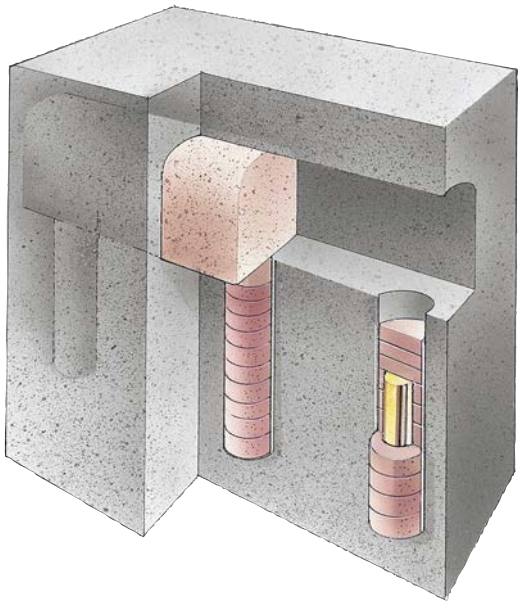

Figure D-1. *The KBS-3 system with canisters deposited one by one in vertical holes. From SKB (2006c).*

In such a system the rock may be envisaged as a homogeneous medium of low porosity, while the rock-backfill interface and possibly a damaged zone adjacent to the deposition holes, due to e.g. thermal spalling, will have a higher porosity. Fractures reaching the deposition tunnel and/or the deposition hole may be sources of inflowing water rich in sulfur (either sulfate and/or sulfide) and dissolved organic matter, cf. **Figure D-2**.

In the repository near field, important sources of sulfur are accessory minerals in the backfill and buffer (calcium sulfates, and sulfides to a minor extent) and dissolved sulfate and sulfide in inflowing groundwater (it must be noted, however, that in the base case described below the concentrations of both sulfate and sulfide are set initially to zero in the rock groundwater). Sulfate (SO_4^{2-}) may be reduced by sulfate reducing bacteria (SRB) if they have access to reductants and nutrients. Some organic compounds may be used as reductants by SRB, but the preferred reductant by SRB is molecular hydrogen, H_2, which may be produced by the corrosion of metals. **Figure D-3** shows the main sulfur fluxes near a canister in a KBS-3 repository.

D1.1.1 Modelling teams

Three modelling teams participate in the WP3 of the ISP:

- The rock-water interaction group at the Institute of Geological Sciences of Bern University. This team will use both a single-porosity 3D model and dual-porosity Donnan 1D models.
- A collaboration team including ClayTech AB (Sweden) and Amphos 21 (Spain). Both traditional models and hybrid (including Donnan ionic equilibria) 1D models will be used.
- Integrity Corrosion Consulting Ltd. (Canada) using its own Copper Sulfide Model (CSM).

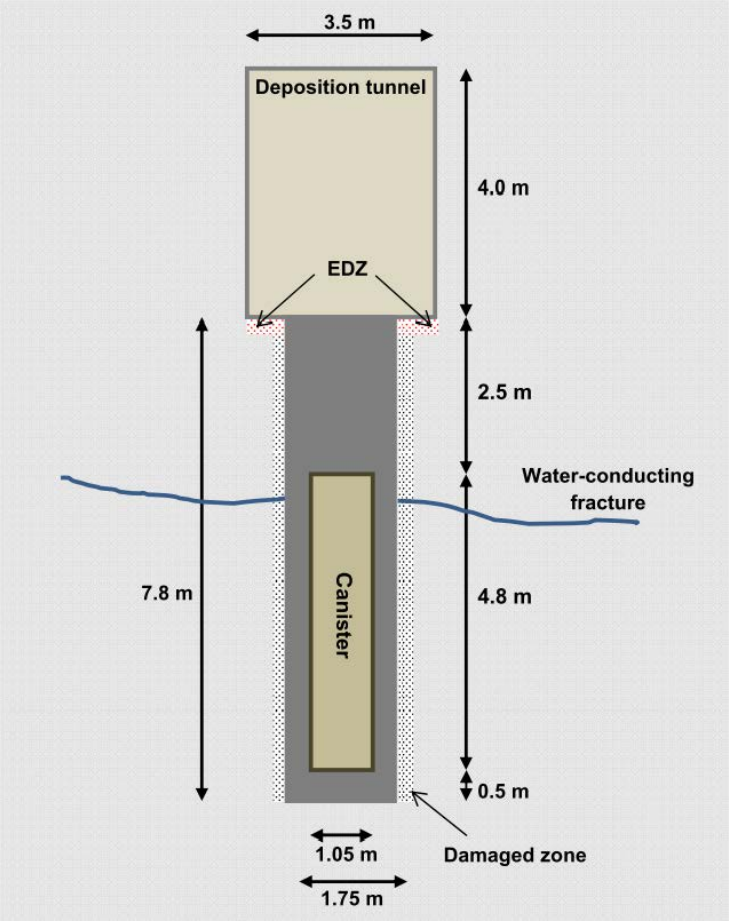

Figure D-2. *Dimensions of the near-field in a Posiva KBS-3 repository for OL1&2 canisters, from Wersin et al. (2014). Note that the depth of the deposition hole (in fact 7.83 m) is to the bottom of the rock-backfill interface (here denoted "EDZ"), as indicated in Saanio et al. (2013, Figure 3-5).*

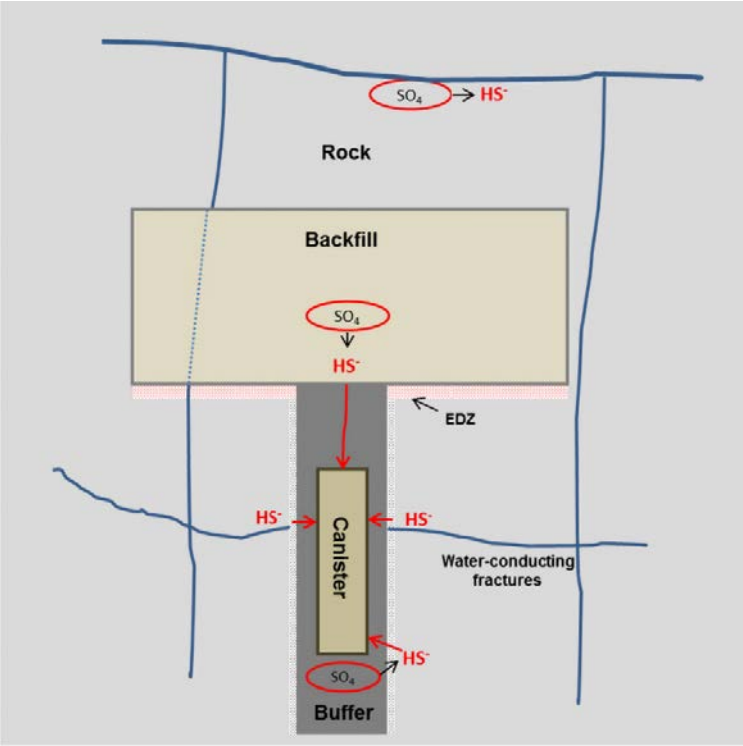

Figure D-3. *Sulfate and sulfide fluxes in the near field (Wersin et al. 2014).*

D1.2 WP3 calculations

An essential part of testing the modelling tools developed within WP3 is the definition and performance of a "base" calculation case. An additional set of variant cases will be defined where parameters are varied one at a time or a single feature (process affecting sulfide) is added to the models.

For all calculations of WP3, chemical equilibrium between species will be defined by the set of equilibrium constants available through version 9b of Thermochimie (www.thermochimie-tdb.com).

The following conditions are applied to the WP3 calculations:

- Temperature coefficients will be needed if temperature changes are to be included in the calculations of variant cases.
- Models may use a subset of the reactions in the Thermochimie database.
- Chemical equilibria may be represented by equivalent kinetically-controlled forward and backward reaction.
- Because pyrite (Fe_2S) is known to form irreversibly, chemical equilibrium with pyrite will be *excluded* from the calculations. An additional reason for this is that dissolution-precipitation reactions involving Fe(II)-monosulfides result in higher sulfide equilibrium concentrations, which in turn will result in pessimistic sulfide corrosion consequences.
- Mackinawite (rather than amorphous iron(II) monosulfide) will be used to control the solubility of sulfide and Fe(II).
- Redox disequilibrium: to simulate microbial sulfate reduction, redox equilibrium between SO_4^{2-} and HS^- must be disabled. To simulate H_2 utilisation by SRB, redox equilibrium involving H_2 must also be disabled.

Diffusion coefficients in aqueous solution and effective diffusion coefficients for anion and neutral species or cations will be defined, if needed tortuosities should be derived from these. If temperature effects are to be considered, then activation energies for the diffusion coefficients will also be needed. For models that can not use species-specific diffusion coefficients average values should be used.

Threshold relative humidity expressions for interfacial electrochemical reactions will be needed only if saturation effects are to be included in any variant case.

D1.2.1 The Base Case

The Base Case should include the most important sulfide-related processes that are possible to handle by each of the models developed within WP3. There can, however, be differences in the way the processes are implemented in the models because of conceptual differences of the models. For example, Donnan equilibrium (ionic equilibria), may be used to describe diffusive transport in bentonite, but other models are described in the scientific literature. Chemical reactions and processes not directly related to sulfide transport or its generation or depletion do not need to be included (for example, weathering reactions, precipitation-dissolution of calcite, etc).

A *hypothetical initial state* (i.e., fully saturated repository, no remaining O_2, thermally equilibrated to 25 °C) will be used in the Base Case to describe the evolution of the repository near field.

The maximum simulated time for a base case should be 100 000 years. The rationale behind this choice is that *it is expected* that the initial transient conditions caused by the presence of bentonite accessory mineral (such as gypsum and sulfide minerals) will stabilise in time periods shorter than 100 000 years.

In the Base Case the temperature in all parts of the system to be simulated is 25 °C.

D1.2.1.1 Geometry

The geometry of a typical KBS-3 repository is shown in **Figure D-2**, see also Hellä et al. (2014), Posiva (2013) and Saanio et al. (2013). Deviations may occur due to the nature of different models, which may be in one, two or three dimensions. The size of the intact rock domain should be large enough to act as a diffusion sink, around three or more times the thickness of the rock-backfill interface (Section D1.2.1.3), for example 5 m. The minimum spacing between deposition holes is 7.5 m, and therefore a 3D model should include 7.5 m of backfilled tunnel.

When considering 1D models, both a radial model centred on the canister, or a vertical model (also centred on the canister) would provide useful comparisons with 3D models. The radial 1D model would be 1 m high, and the vertical model would have a 1 m^2 cross-section.

D1.2.1.2 Intact rock

In the Base Case intact rock is included as a ECPM (Equivalent Continuous Porous Medium) representation of the rock matrix and fractures. The porosity should correspond to a fractured rock, i.e., it must include the fracture porosity, see table below. Transport of substances between the intact rock and the backfill/buffer/rock-backfill interface is by diffusion. In a variant case fractures are considered explicitly.

- Groundwater. The sulfate-rich brackish water defined in Hellä et al. (2014) is the reference groundwater. To simplify matters sulfur concentrations are set to zero initially. The concentration of sodium or calcium might have to be adjusted in some models to achieve electrical neutrality.
  - SO_4^{2-} concentration in groundwater is initially zero. This is a simplification for the base case. The sulfate concentration in the rock groundwater will vary with time because of diffusion from the backfill or buffer into the rock. In a variant case sulfate may be added to the groundwater.
  - Sulfide concentration in groundwater is initially zero. This is a simplification for the base case. The sulfide concentration in the rock groundwater will vary with time because of diffusion from the backfill into the rock. Equilibrium precipitation of iron(II) sulfide in the rock matrix assuming pH = 7.6 and $[Fe(II)]_{TOT} = 5.7 \times 10^{-6}$ M. These values corresponds to the sulfate-rich brackish water in Hellä et al. (2014, Table 6-3). In a variant case the concentration of sulfide in the groundwater might not be zero.
  - The concentration of reductants (H_2, hydrocarbons, other organic matter) in the groundwater set initially to zero in the Base Case. The concentration of organic matter and other components in the intact rock will vary with time because of diffusion from the backfill or buffer into the rock. In a variant case H_2 and/or DOC might be added to the groundwater.

  - Initial concentration of Fe(II) = 5.7×10^{-6} M assumed in the groundwater in the intact rock. This Fe(II) may diffuse into the rock-backfill interface, into the backfill and into the buffer. A constant value assumed at the outer rock boundaries.
  - Initial O_2 concentration in the groundwater set to zero.
  - Initial concentration of Cl^- = 0.1131 M (4 010 mg/L) assumed in the groundwater in the intact rock. The value corresponds to the sulfate-rich brackish water in Hellä et al. (2014, Table 6-3). This chloride may diffuse into the rock-backfill interface, into the backfill and into the buffer. A constant value assumed at the outer rock boundaries.
- Solid sulfide initial concentration in the rock matrix (for example pyrite) is simplified to be zero.
- No groundwater flow around the modelled system (deposition tunnel etc).
- Diffusion coefficients: see table below from Posiva (2013).
- Constant boundary properties (fixed groundwater concentrations) may be assumed at a distance of 5 m from the backfill/buffer interfaces.
- No SRB activity in the intact rock. Might be added in a variant case.
- No sorption processes considered in the intact rock.

Geosphere data (Posiva 2013): Other flow-related parameters.		
Total porosity (θ)	0.515 %	Matrix porosity and interconnected porosity to be used in an ECPM representation of the rock (matrix and fractures). From the rock matrix porosity (0.5 %) and a kinematic porosity of 0.15 % of Hartley et al. (2013, Table 2-5 and Table 4-2).
Diffusion accessible porosity (Rock matrix porosity)	0.5 %	Groundwater flow modelling in Hartley et al. (2013) referred to in Posiva (2013, Section 6.1 and Section 7.8, Table 7-13).
Molecular diffusion coefficient in water (D_w)	1.0×10^{-9} m^2/s	Posiva (2013, Table I-1).
Effective diffusion coefficient (D_e) for intact rock matrix	6×10^{-14} m^2/s	Posiva (2013, Table I-1).
Effective diffusion coefficient (D_e) for fractured rock	2×10^{-13} m^2/s	Estimated in this project to provide diffusion in a ECPM representation of the intact rock (rock matrix and fractures).

D1.2.1.3 Rock-backfill interface and rock-buffer interface (thermally spalled rock volume)

The rock-tunnel interface will be denoted **RTI**, and the rock-deposition hole interface will be denoted **RDI**. These interfaces are represented as volumes of ECPM (Equivalent Continuous Porous Medium). The RTI and the RDI are arbitrarily represented by a porosity that is about 4 times higher than the porosity of the intact rock, see table below. The thickness of the RDI is 0.1 m around deposition holes and for the RTI it is 0.4 m below the tunnel floor and 0.3 m on other parts of the tunnel perimeter. When considering 7.5 m of backfilled tunnel, the area of the RTI in contact with the tunnel is 110.1 m^2, and its volume is 35.4 m^3, for the RDI the area in contact with the deposition hole is 45.3 m^2 and the volume is 2.45 m^3.

UNDERGROUND OPENINGS DATA (Posiva 2013)		
Rock-backfill interface (RTI)		
Thickness, except below tunnel floor	0.3 m	Agreed in this project.
Thickness below tunnel floor	0.4 m	Hartley et al. (2013, Section 5.1.5 and Table E-1).
Hydraulic conductivity	2.5×10^{-8} m/s	Hartley et al. (2013, p 91 and p 234).
Porosity	1 %	Hartley et al. (2013, Table E-1).
Effective diffusion coefficient (D_e) for fractured rock	5×10^{-13} m^2/s	Estimated as $D_e = D_w F_f$ with the formation factor estimated using an Archie's law: $F_f = 0.71\ \theta^{1.58}$ (see Byegård et al. 2008, Figure 3-5) and $\theta = 0.01$.
Damaged rock around deposition holes (RDI)		
Thickness of affected area	0.1 m	Hartley et al. (2013, p 74 and Table E-1).
Hydraulic conductivity	2.5×10^{-8} m/s	Hartley et al. (2013, p 234).
Porosity of affected area	2 %	Hartley et al. (2013, Table E-1).
Effective diffusion coefficient (D_e) for fractured rock	1.5×10^{-12} m^2/s	Estimated as $D_e = D_w F_f$ with the formation factor estimated using an Archie's law: $F_f = 0.71\ \theta^{1.58}$ (see Byegård et al. 2008, Figure 3-5) and $\theta = 0.02$.

- Groundwater. The same groundwater as for the intact rock is initially present in the fragmented rock. The sulfate-rich brackish water defined in Hellä et al. (2014, Table 6-3) is the reference water. To simplify matters sulfur concentrations are set to zero initially. The concentration of sodium or calcium might have to be adjusted in some models to achieve electrical neutrality.
- No metals such as rock bolts and stretch metal are present in the base case. Metal corrosion is a source of H_2, which will be used by SRB, and Fe(II), which could remove sulfide through precipitation. A variant case will include both rock bolts and stretch metal.
- Initially there are no reductants in these interface volumes (DOC, H_2, etc). Out- and in-diffusion of substances (SO_4^{2-}, organic carbon, H_2, etc) from/to the backfill or buffer and to the intact rock
- SRB activity is expected to be possible in these repository volumes.
- **Biomass:**
  - *Fraction of SRB.* The proportion between the total number of microorganisms and SRB is quite uncertain; in Table 6 of Hallbeck and Pedersen (2008) 35 % of the bacteria are SRB in borehole KJ0052F01, while Figures 1 and 2 in Pedersen (2012a) indicate 20 % of SRB, but the data in Table 1 of Pedersen (2012b) suggest 50 % SRB. For WP3 simulations a value of 20 % may be used.
  - *Attached cells on fracture surfaces.* At Äspö, $\approx 10^{5.6}$ cells/cm^2 were found on glass surfaces (Pedersen 2012a). One can assume the same cell density on fracture surfaces. For the RTI with 1 % porosity, the volume occupied by "fractures" is 5 L, and if the average "fracture" aperture is 0.1 mm, then the area of the fractures should be at least 100 m^2 per m^3 of ECPM, resulting in 8.0×10^{10} attached SRB cells per m^3 of ECPM. For the RDI (2 % porosity) the fracture surface is at least 300 m^2 per m^3 of ECPM, resulting in 2.4×10^{11} attached SRB cells per m^3 of ECPM.
  - *Suspended cells in groundwater.* The number microorganisms is based on a TNC of 10^5 cells/mL, see Figure 2(b) in Pedersen (2012b). For the RTI with 1 % porosity, the volume occupied by "fractures" is 5 L, resulting in 1×10^8 suspended SRB cells per m^3 of ECPM. For the RDI (2 % porosity) the fracture volume is 15 L per m^3 of ECPM, resulting in 3×10^8 suspended SRB cells per m^3 of ECPM.
  - *Biomass composition.* To transform cells to mg of biomass, an average cell dry mass of 5×10^{-13} g will be used in the base case, and an average formula of $C_5H_7O_2N$ (113.115 g/mol).
  - *Total biomass.* From the data above, the biomass concentration in the RTI is calculated to be 3.54×10^{-4} mol/m^3 of ECPM, and in the RDI it is 1.06×10^{-3} mol/m^3 of ECPM. The biomass is kept constant as a function of time.

- **Rate:** *Monod kinetics* may be written as;

$$\frac{d[SO_4^{2-}]}{dt} = -\frac{d[HS^-]}{dt} = -[X] \cdot k_{max} \frac{[H_2]}{K_{H2} + [H_2]} \frac{[SO_4^{2-}]_{Tot}}{K_{SO_4} + [SO_4^{2-}]_{Tot}}$$

where [*X*] is the biomass concentration given above. If the process involves organic matter, then [*org*] and K_{org} should be used instead of $[H_2]$ and K_{H2}. To calculate the concentration of organic matter, [*org*], a stoichiometric composition equivalent to that of acetate ($C_2H_4O_2$) may be used. If needed, first order kinetics (on biomass) for SO_4^{2-} reduction may be assumed. Monod kinetics gives a slower reduction rate at low concentrations of substrates, and therefore, a first order kinetics should be pessimistic.

The Monod rate equation from Jin et al. (2013) for SO_4 reduction using organic matter (acetate) will be used in the base case, although the composition of the organic matter is not specified in the base case. Their Table 3 gives $k = 1.3 \times 10^{-6}$ mol (g biomass)$^{-1}$ s^{-1} (equivalent to $k = 1.5 \times 10^{-4}$ s^{-1}). For SO_4^{2-} reduction using H_2 as electron donor, the rate constants in the literature from laboratory studies are in the range (1.6 to 6.4) $\times 10^{-5}$ s^{-1} (Maia et al. 2016). In the base case the fastest rate will be used: 6.4×10^{-5} s^{-1}.

Half saturation constants: the reported values of K_{H2} are between 1.3 and 20 µM (Maia et al. 2016) and a value of 4×10^{-6} M will be adopted for the base case. The value of $K_{SO4} = 1 \times 10^{-5}$ M (Nethe-Jaenchen and Thauer 1984) will be used; note that (Jin et al. 2013, Table 3) selected $K_{SO4} = 6.8 \times 10^{-5}$ M. For K_{org} the value 5×10^{-6} M will be used, corresponding to that of acetate when used as reductant (Jin et al. 2013, Table 3).

- **Stoichiometry:** The sulfate reduction reaction will be taken to be:
  $2(CH_2O) + SO_4^{2-} \rightarrow HS^- + 2HCO_3^- + H^+$. Biomass production will not be included in the base case.
- Sulfate and organic matter is provided by diffusion from the backfill (dissolution of gypsum). Hydrogen (H_2), originating from the sulfide corrosion of the canister, reaches these repository volumes by diffusion through the backfill and/or the buffer.
- Solid sulfide (pyrite and mackinawite) initial concentration assumed to be zero.
- FeS (mackinawite) precipitation included either as an equilibrium or kinetic process, where Fe(II) diffuses from/to the intact rock.
- Diffusion coefficients set to those of the intact rock.
- No sorption processes considered in the fragmented rock.

D1.2.1.4 Backfill

As stated above, a *hypothetical initial state* (i.e., fully saturated backfill, no remaining O_2, thermally equilibrated to 25 °C) will be used. In the Base Case the backfill is modelled as a medium that is initially homogeneous.

- Porosity and diffusion coefficients have been agreed in the project, see table below.

BACKFILL DATA **Effective diffusion coefficients and porosity in backfill; values agreed upon by the members of the project. The temperature is 25 °C.**	
All neutral species and ions	
Pore diffusivity D_p (m^2/s)	5.00×10^{-11}
ε (physical bulk porosity)	43 %
Effective diffusivity D_e (m^2/s) = ($D_p \times \varepsilon$)	2.15×10^{-11}

- Dry density defined in Hellä et al. (2014, Table 7-11) , i.e. 1 720 kg/m^3.

- Mineral composition defined as those in Hellä et al. (2014, Table 7-11). Initial amount of gypsum also set to the values reported in Hellä et al. (2014, Table 7-11). Considering the porosity and dry density defined above this gives: 189.8 (mol gypsum)·m^{-3} and 467.2 (mol calcite + dolomite)·m^{-3}.
- Availability of iron(II) phases to produce and precipitate sulfide set to Hellä et al. (2014, Table 7-11). Considering the porosity and dry density defined above this gives: 163.3 (mol $FeCO_3$)·m^{-3}. FeS (mackinawite) and $FeCO_3$ precipitation/dissolution included.
- Porewater composition from Posiva (2013), Appendix F, Table F-2, p.715, column "Reference porewaters – Brackish water".
- Dimensions of the deposition tunnel: see Section D1.2.1.1. The cross-section area is 14 m^2, with a length of 7.5 m the total volume is 105 m^3.
- SRB activity absent in the base case.
- For the amount of organic carbon, the limit value (1 wt%) reported in Posiva (2012) will be used, but only 10 % of the organic carbon will be assumed to be mobile (soluble) and degradable by SRB (i.e. 0.1 wt% of C). Considering the porosity and dry density defined above this gives: 143.2 (mol organic C)·m^{-3}. The availability of organic carbon will be varied in a variant case. Considering the concentration of DOC in the porewater will be maintained at 2 mg/L (mg of C), by an equilibrium reaction, until all degradable organic carbon (10 % of 1 % of the backfill in weight) is exhausted. Because in the base case SRB activity is absent in the backfill, the DOC may diffuse to the buffer (where SRB activity is also absent), to the RTI and to the RDI (where SRB activity is present).

D1.2.1.5 Buffer

As stated above, a *hypothetical initial state* (i.e., fully saturated buffer, no remaining O_2, thermally equilibrated to 25 °C) will be used. In the Base Case the buffer is modelled as a medium that is initially homogeneous.

- Porosity and diffusion coefficients have been agreed in the project, see table below.

BUFFER DATA **Effective diffusion coefficient and porosity in buffer; values agreed upon by the project members. Grain density for the buffer 2 760 kg/m^3. The temperature is 25 °C.**	
All neutral species and ions	
Pore diffusivity D_p (m^2/s)	5.00×10^{-11}
ε (physical bulk porosity)	43 %
Effective diffusivity D_e (m^2/s) = ($D_p \times \varepsilon$)	2.15×10^{-11}

- Dry density defined in Hellä et al. (2014, Table 7-5), i.e. 1 570 kg/m^3.
- Porewater composition from Posiva (2013, Appendix E, Table E-2, p.707, column "Reference porewaters – Brackish water").
- Mineral composition defined as those in Hellä et al. (2014, Table 7-5). Initial amount of gypsum set to the values reported in Hellä et al. (2014, Table 7-5). Considering the porosity and dry density defined above this gives: 36.48 (mol gypsum)·m^{-3} and 327 (mol calcite + dolomite)·m^{-3}.
- CEC (cation exchange capacity) from Posiva (2013, Appendix E, Table E-2), i.e. 2 873 meq/L.
- Siderite is not considered in the initial composition so that the Fe concentration in the porewater (1.1×10^{-5} M) is not changed. Note that in order to compare single-porosity models with Donnan models, the CEC in the single-porosity model of the buffer must be equilibrated with the initial Fe(II) concentration (1.1×10^{-5} M). FeS (mackinawite) and $FeCO_3$ precipitation included.
- SRB activity absent.
- Dimensions: see Section D1.2.1.1. The volume is 14.6 m^3.

- For the amount of organic carbon, the limit value (1 wt%) reported in Posiva (2012) will be used, but only 10 % of the organic carbon will be assumed to be mobile (soluble) and degradable by SRB (i.e. 0.1 wt% of C). Considering the porosity and dry density defined above this gives: 130.7 (mol organic C)·m^{-3}. The availability of organic carbon will be varied in a variant case. The concentration of DOC in the porewater will be maintained at 2 mg/L (mg of C), by an equilibrium reaction, until all degradable organic carbon (10 % of 1 % of the buffer in weight) is exhausted. Because SRB activity is absent in the buffer, the DOC may diffuse to the backfill (where SRB activity is also absent in the base case), to the RTI and to the RDI (where SRB activity is present).

D1.2.1.6 Canister

The canister corrosion will be either described fully, or depending on each model's shortcomings it may be treated as an ideal surface where sulfide will be converted according to: $2Cu + HS^- + H^+ \rightarrow Cu_2S + H_2(aq)$. The hydrogen molecules thus formed will diffuse through the bentonite buffer. Assuming a perfect cylinder the surface area of the canister is 17.57 m^2.

The full corrosion model requires:

- Definition of interfacial electrochemical reactions.
- Standard potentials for interfacial electrochemical reactions (and their temperature dependence if temperature changes are considered).
- Interfacial rate constants for electrochemical reactions (and their activation energies if temperature changes are considered).
- Transfer coefficient α for each interfacial reaction from which the Tafel slope can be calculated.
- Number of electrons for each interfacial electrochemical reactions.

Values for these parameters may be obtained from Fraser King.

D1.3 Summary of input data

Domain	Groundwater/Porewater	Minerals (equilibrium)		Kinetic reactions	Cation exchange	Transport Properties	Dimensions
		Primary	Secondary				
Intact rock	B-SO_4 (Hellä et al. 2014, Table 6-3) SO_4^{2-} and sulfide concs. = 0 Ca or Na: charge balance $[Fe(II)]_{TOT} = 5.7 \times 10^{-6}$ M OM: 0 Anoxic conditions Cl^-: 0.1131 M (4 010 mg/L) No SRB activity. No sorption processes	-	calcite, mackinawite	-	-	Porosity = 0.00515 $D_{eff} = 2.0 \times 10^{-13}$ m^2/s	5 m from the interfaces Vol = 2 050 m^3
RTI (rock - tunnel interface)	B-SO_4 (Hellä et al. 2014, Table 6-3) SO_4^{2-} & sulfide concs. = 0 DOC: Initially set to 0 Charge balance on Na No sorption processes. SRB activity: Yes	-	calcite, mackinawite	Biotic SO_4 reduction with: C-org: k = 1.5×10^{-4} s^{-1} H_2(aq): k = 6.4×10^{-5} s^{-1} [biomass]: 3.54×10^{-4} mol/m^3 $K_{orgC} = 5.0 \times 10^{-6}$ M; $K_{H2} = 4.0 \times 10^{-6}$ M; $K_{SO4} = 1.0 \times 10^{-5}$ M;	-	Porosity = 0.01 $D_{eff} = 5.0 \times 10^{-13}$ m^2/s	0.3 m, except below tunnel floor, where it is 0.4 m Tunnel contact = 110.1 m^2 Vol = 35.4 m^3
RDI (rock - deposition hole interface)	B-SO_4 (Hellä et al. 2014, Table 6-3) SO_4^{2-} & sulfide concs. = 0 DOC: Initially set to 0 Charge balance on Na No sorption processes SRB activity: Yes	-	calcite, mackinawite	Biotic SO_4 reduction with: C-org: k = $1.5 \times 10-4$ s^{-1} H_2(aq): k = 6.4×10^{-5} s^{-1} [biomass]: 1.06×10^{-3} mol/m^3 $K_{orgC} = 5.0 \times 10^{-6}$ M; $K_{H2} = 4.0 \times 10^{-6}$ M; $K_{SO4} = 1.0 \times 10^{-5}$ M;	-	Porosity = 0.02 $D_{eff} = 1.5 \times 10^{-12}$ m^2/s	0.1 m Contact with deptn. hole = 45.3 m^2 Vol = 2.45 m^3
Backfill	Brackish water (Posiva 2013, Table F-2) DOC = 2 mg/L of C SOM(s) = 0.1 wt% of C (143.2 mol/m^3) SRB activity: No	Gypsum 189.8 mol/m^3 Calcite 467 mol/m^3 Siderite 163.3 mol/m^3 (Hellä et al. 2014, Table 7-11)	mackinawite	-	CEC = 2 120 meq/L = 0.47 eq/kg (Posiva 2013, Table F-2)	Porosity = 0.43 $D_{eff} = 2.15 \times 10^{-11}$ m^2/s	4 m height, 3.5 m wide, 7.5 m long (distance btwn deptn. holes). Vol = 105 m^2 Cross section = 14 m^2
Buffer	Brackish water (Posiva 2013, Table E-2) DOC = 2 mg/L of C SOM = 0.1 wt% of C (130.7 mol/m^3) SRB activity: No	Gypsum 36.5 mol/m^3 Calcite 327 mol/m^3 (Hellä et al. 2014, Table 7-5)*	siderite, mackinawite	-	CEC = 2 873 meq/L = 0.79 eq/kg (Posiva 2013, Table E-2)	Porosity = 0.43 $D_{eff} = 2.15 \times 10^{-11}$ m^2/s	7.8 m height, outer diam. 1.75m, inner diam. 1.05m. Vol = 14.6m^3
Canister	-	-	-	-	-	-	4.8 m height, 1.05 m diam, Area = 17.6 m^2
TDB	Thermodynamic database. Thermochimie version 9b: all equilibrium constants; sulfate/sulfide decoupled; hydrogen from corrosion decoupled.						

DOC = dissolved organic matter; SOM = solid organic matter.
B-SO_4 = Brackish-sulfate groundwater.
CEC = Cation Exchange Capacity.
SRB = Sulfate Reducing Bacteria.
* No siderite is considered in the buffer initially, to keep the porewater Fe concentration as in Table E-2.
OM = organic matter.

D2 Variant calculation cases for WP3 of the Integrated Sulfide Project

D2.1 Introduction

For the sake of simplicity, the reader is referred to the document defining the Base Case for a short description of the project, acronym definition, etc.

D2.1.1 Evolution of a KBS-3 repository

Three cases in the evolution of a KBS-3 repository deserve special attention, when focussing on the near field: the initial unsaturated period, a saturated period where the bentonite buffer acts as a diffusion barrier, and the special "bentonite erosion case".

D2.1.1.1 The unsaturated period

Within WP3, modelling tools will *not* be developed to model gas transport of H_2S (though gaseous H_2S will be built into the CSM code outside the ISP). Similarly, the modelling tools will not be able to deal with the possible SRB (Sulfate Reducing Bacteria) activity in biofilms growing in the rock surfaces during the unsaturated period.

D2.1.1.2 The saturated period

The main features that affect sulfide production and transport, in addition to access to sulfate, reductants and nutrients, are volumes where SRB (sulfate reducing bacteria) can grow: interfaces between buffer/backfill and rock due to e.g. thermal spalling, head crown in the backfill, low density backfill, and partially "eroded" buffer.

D2.1.1.3 The bentonite erosion case

It may be shown, through careful safety assessment studies, that the most detrimental case for a KBS-3 spent nuclear fuel repository is, potentially in combination with a rock shear, when a highly transmissive fracture reaching a deposition hole causes enough removal of bentonite buffer so that advective conditions in the deposition whole are obtained. Such a case is often named the "bentonite erosion case".

There are important conceptual questions concerning the geometry and properties (porosity etc) of the erosion cavity. These conceptual questions can not be solved by the WP3. Modelling the bentonite erosion case would be highly speculative. Therefore, in this study two extreme cases of buffer mass loss are considered to scope the impacts of a bentonite erosion case;

i. Reduced density of the buffer that allows bacterial activity.
ii. Loss of buffer mass such that a cavity filled with water is formed.

D2.1.2 Structure of WP3

Three modelling teams participate in the WP3 of the ISP:

- The rock-water interaction group at the Institute of Geological Sciences of Bern University.
- A collaboration team including ClayTech AB (Sweden) and Amphos 21 (Spain).
- Integrity Corrosion Consulting Ltd. (Canada) using its own Copper Sulfide Model (CSM).

D2.2 Identification of calculation cases

D2.2.1 Base case

The "base case" is defined in a complementary document.

D2.2.2 Variant cases

Variant cases are suggested to cover following topics:

D2.2.2.1 High priority cases

- One fracture intersecting the deposition hole will act as a line source of sulfide, sulfate and DOC. The fracture will be located midway of the canister height. In this case the groundwater will include concentrations of sulfate, sulfide, and DOC (contrary to the Base Case). The concentration of sulfate and sulfide will be those specified for the brackish sulfate type groundwater (Hellä et al. 2014, Table 6-3). The concentration of DOC will be 10 mg/L. The matrix rock porosity is then decreased, from the Base Case value to that of intact rock matrix. Three flow rates in the fracture will be modelled: 10^{-4}, 10^{-3} and 10^{-2} m^2/y (m^3 of flow per m or fracture width per year).
- Buffer: localized loss of density so that bacterial sulfate reduction is possible. The affected volume in the buffer may defined as a toroid geometry with a rectangular cross-section with a height equal to the width of the buffer around the canister.

  This volume will be assumed to have such properties that bacterial sulfate reduction is possible. This eroded volume will be positioned midway in the canister height. Two cases are envisaged.

  – In the first case SRB (sulfate reducing bacteria) are assumed to be active in this volume of the buffer but all other parameters are left unchanged. Note that this is an unrealistic case, as the required dry density for SRB activity is lower than in the base case, but leaving all other parameters unchanged allows distinct comparisons with the base case. The biomass in the porewater of the buffer is 2×10^8 cells/L, that is, 8.8×10^{-7} mol/L of porewater (using a dry cell mass of 5×10^{-13} g/cell and a molecular weight of 113.115 g/mol).
  – In the second case this buffer volume is considered to be a cavity empty of bentonite (but full of groundwater). Suspended cells in groundwater: The number microorganisms is based on a TNC of 10^5 cells/mL, see Figure 2(b) in Pedersen (2012b). As in the base case, 20 % of these cells are postulated to be SRB.
- Backfill porosity low enough to sustain SRB activity, in the whole of its volume. In order to make an easier comparison with the base case, all other parameters are left unchanged. The biomass in the porewater of the backfill is 2×10^8 cells/L, that is, 8.8×10^{-7} mol/L of porewater (using a dry cell mass of 5×10^{-13} g/cell and a molecular weight of 113.115 g/mol).
- Interface volumes: higher effective diffusivities. The base case diffusivity of RTI is 5×10^{-13} m^2/s and 1.5×10^{-12} m^2/s for RDI. At least one order of magnitude higher (maybe two) will be tested in this variant case.
- The effect of corroding rock bolts and stretch metal in the backfill next to the rock producing hydrogen (H_2) and magnetite. The metal in the walls and ceiling of the deposition tunnel will be regularly distributed and the amount will be 14 kg/(m of tunnel). The corrosion rate of the metal will be 2.8 µm/y and the metal will be modelled to be cylindrical in shape with a diameter of 3 mm. The density of steel will be 7 800 kg/m^3. For models that discretize space into finite volumes, the thickness of the backfill compartment containing the steel may be between 5 and 10 cm thick.
- Check the numerical accuracy of 3D models by increased discretization, especially at the canister surface.

D2.2.2.2 Medium priority cases

- Increased contents of organic carbon available for sulfate reduction in the buffer and backfill by a factor of ten.
- Amount of reactive Fe(II) minerals that may react with sulfide (i.e. carbonates) in the buffer and backfill. For the buffer a value of 0.5 % for siderite will be used (Hellä et al. 2014, Table 7-5) while for the backfill a value of 2.2 % will be tested.

D2.2.2.3 Low priority cases

- Including sulfate and/or iron(II) and/or DOC in the groundwater in the intact rock (when specific fractures are not modelled). The concentrations of sulfate and Fe(II) in the groundwater will be those for the brackish sulfate type groundwater (Hellä et al. 2014, Table 6-3). For DOC a value of 10 mg/L will be used.
- Faster kinetics for SRB (sulfide reduction) and/or kinetics for organic matter degradation/dissolution in the backfill. A decrease and an increase by a factor of ten will be used.
- Temperature evolution. This case is modelled by ICC which already has a temperature variation as a function of time.

Other additional cases could be envisaged, such as crown space in the backfill, etc, but they are not included in the WP3.

Thermal properties.

Name	Value	Unit	min	max	Reference	detail ref.	Component	Sub-component	comments	applicable T
Thermal conductivity	36	W/(m·K)			Posiva (2013)	Table D-1	Canister	Canister iron insert	Cast iron	
- " -		W/(m·K)	52	63	- " -	- " -	- " -	Canister steel casette	Steel	
- " -	391	W/(m·K)			- " -	- " -	- " -	Canister copper shell/overpack	Copper	
Volumetric heat capacity	2.4	MJ/(m^3·K)			- " -	- " -	- " -		BWR (OL1-2)	
- " -	2.5	MJ/(m^3·K)			- " -	- " -	- " -		VVER-40 (LO1-2)	
- " -	2.7	MJ/(m^3·K)			- " -	- " -	- " -		PWR (EPR) (OL3-4)	
Thermal conductivity	0.3				Posiva (2013)	Table E-1	Buffer		Dry conditions	25
- " -	1				- " -	- " -	- " -		Initial conditions	25
- " -	1.3				- " -	- " -	- " -		Saturated conditions	25
Heat capacity	830	J/(kg·K)			- " -	- " -	- " -			25
Heat capacity (volumetric)	2.4	MJ/(m^3·K)			- " -	- " -	- " -			25
Thermal conductivity (all samples)	2.77	W/(m·K)			Kukkonen (2015)		Geosphere			25 °C
- " -	2.71	W/(m·K)			- " -		- " -			60 °C
- " -	2.62	W/(m·K)			- " -		- " -			100 °C
Specific heat capacity (all samples)	728	J/(kg·K)			- " -		- " -			25 °C
- " -	786	J/(kg·K)			- " -		- " -			60 °C
- " -	838	J/(kg·K)			- " -		- " -			100 °C

D2.2.2.4 Overview table of variant cases

In the following table the variant cases modelled by each WP3 team are indicated. The type of model is listed as well: single porosity "traditional" model or dual porosity "hybrid" model, and one or three dimensional models.

Case ID	Description	Models used	Dimension	Uni. Bern	Amphos +CT	ICC
FRACTURES	A fracture or set of fractures intersecting the deposition hole and tunnel, acting as line sources/sinks of sulfide, sulfate and DOC			X		
BUFFER DENSITY	Buffer: localized loss of density so that SRB is active	Traditional	1D			X
		Traditional	3D	X		
BACKFILL DENSITY	Backfill density low enough to sustain SRB activity in its entire volume	Traditional	1D			X
		Traditional *and* Hybrid	1D	X	X	
		Traditional	3D	X		
INTERFACE METALS	Metal corrosion: effect of rock bolts and stretch metal producing H_2 and magnetite	Traditional *and* Hybrid	1D		X	
		Traditional	3D	X		
3D MODELS	3D modelling: check numerical accuracy by increased discretization			X		
INTERFACE De	Interfaces diffusivities: Higher effective diffusivities in the interfaces	Traditional	1D			X
ORGANIC MATTER	Organic matter: Effect of changing organic content in buffer & backfill	Traditional	1D			X
		Traditional *and* Hybrid	1D		X	
Fe(II) MINERALS	Fe(II) minerals: amount of Fe(II) minerals that can react with sulfide (i.e. siderite) in the buffer and backfill	Traditional	1D			X
		Traditional *and* Hybrid	1D		X	
THERMAL EFFECTS	Temperature evolution: assess the thermal effects on diffusion and reaction processes	Traditional	1D			X
GROUNDWATER COMPOSITION	Groundwater in the intact rock: include sulfate and/or Fe(II) and/or DOC (when specific fractures are not modelled)	Traditional	1D			X
KINETIC RATES	Effect of slower/faster SRB kinetics in the interfaces	Traditional	1D			X

D3 Definition and values for CSM V1.2a-g constant input parameters for the inter-model comparison exercise

Table D-1. List of constant input parameters used for the benchmarking Base Case and variant case simulations.

Parameter symbol	Value	Units	Parameter description
Troom	298.15	K	Room temperature at which all the “room” values are given
DAroom	1×10^{-7}	dm^2/s	Diffusion coefficient for gaseous O_2
DeHDA	−2 060	J/mol	Activation energy for DA
D0room	1×10^{-7}	dm^2/s	Diffusion coefficient for dissolved O_2
DeHD0	15 000	J/mol	Activation energy for D0
D1room	1×10^{-7}	dm^2/s	$CuCl_2^-$ diffusion coefficient
DeHD1	18 800	J/mol	Activation energy for D1
D3room	1×10^{-7}	dm^2/s	Cu^{2+} diffusion coefficient
DeHD3	15 000	J/mol	Activation energy for D3
fD6	1	unitless	Enhancement 3D simulation factor for D6
D6room	1×10^{-7}	dm^2/s	Cl^- diffusion coefficient
DeHD6	15 000	J/mol	Activation energy for D6
D7room	1×10^{-7}	dm^2/s	Fe(II) diffusion coefficient
DeHD7	15 000	J/mol	Activation energy for D7
D9room	1×10^{-7}	dm^2/s	Fe(II) diffusion coefficient
DeHD9	15 000	J/mol	Activation energy for D9
D11room	1×10^{-7}	dm^2/s	SO_4^{2-} diffusion coefficient
DeHD11	15 000	J/mol	Activation energy for D11
D12room	1×10^{-7}	dm^2/s	Diffusion coefficient for dissolved H_2
DeHD12	15 000	J/mol	Activation energy for D12
D13room	1×10^{-7}	dm^2/s	Diffusion coefficient for gaseous H_2
DeHD13	−2 060	J/mol	Activation energy for D13
D16room	1×10^{-7}	dm^2/s	Pore-solution diffusion coefficient of dissolved acetic acid
DeHD16	15 000	J/mol	Activation energy for the diffusion coefficient of dissolved acetic acid
HeOroom	31.4	unitless	Inverse Henry constant for O_2
DeHHeO	−14 100	J/mol	Activation energy for HeO
HeHroom	52.4	unitless	Inverse Henry constant for H_2
DeHHeH	−4 500	J/mol	Activation energy for HeH
c1sat1Room	0.0034	$mol \cdot dm^{-3}$	Saturation value of c1 at c6 = 1 $mol \cdot dm^{-3}$
DeH1sat	24 000	J/mol	Activation energy for c1sat
c3satRoom	4.3×10^{-7}	$mol \cdot dm^{-3}$	Saturation value of c3
DeH3sat	19 000	J/mol	Activation energy for c3sat
c7sat1Room	1.56×10^{-12}	$mol \cdot dm^{-3}$	Saturation value of c7 at c9 = 1 $mol \cdot dm^{-3}$

Parameter symbol	Value	Units	Parameter description
DeH7sat	24 000	J/mol	Activation energy for c7sat
c7satFeCO3Room	1×10^{-7}	mol·dm^{-3}	Saturation value of c7 in presence of $FeCO_3$
DeH7satFeCO3	0	J/mol	Activation energy for c7satFeCO3room
c11satRoom	0.01523	mol/dm3	Saturated concentration of c11 at 25 °C
$c_{11}^{sat} = 8.292306 \times 10^{-9} \cdot t^3 - 2.384728 \times 10^{-6} \cdot t^2 + 1.472958 \times 10^{-4} \cdot t + 1.290774 \times 10^{-2}$ where t is the temperature in °C			
c16satRoom	8.33×10^{-5}	mol·dm^{-3}	Saturation value of c16
DeH16sat	0	J/mol	Activation energy for c16sat
k1room	computed	dm^3·mol^{-1}·s^{-1}	Computed within the code, alternatively value can be set to zero
k2room	1	1/s	Homogeneous reaction rate
DeH2	60 000	J/mol	Activation energy for k2
km2room	0.1	1/s	Homogeneous reaction rate
DeHm2	40 000	J/mol	Activation energy for km2
k3room	1×10^{-5}	1/s	Homogeneous reaction rate
DeH3	60 000	J/mol	Activation energy for k3
km3room	1×10^{-6}	1/s	Homogeneous reaction rate
DeHm3	60 000	J/mol	Activation energy for km3
k4room	0.002	dm^3 mol^{-1} s^{-1}	Homogeneous reaction rate
DeH4	0	J/mol	Activation energy for k4
km4room	1×10^{-6}	1/s	Homogeneous reaction rate
DeHm4	0	J/mol	Activation energy for km4
k5room	6.6×10^{-11}	mol$^{1/2}$ dm$^{-1/2}$ s^{-1}	Homogeneous reaction rate
DeH5	56 900	J/mol	Activation energy for k5
k6room	10	dm^3 mol^{-1} s^{-1}	Homogeneous reaction rate
DeH6	40 000	J/mol	Activation energy for k6
k7room	1	dm^3 mol^{-1} s^{-1}	Homogeneous reaction rate
DeH7	60 000	J/mol	Activation energy for k7
DeH9	60 000	J/mol	Activation energy for k9 for all layers
k11room	1.99	dm^3 mol^{-1} s^{-1}	Homogeneous reaction rate
DeH11	60 000	J/mol	Activation energy for k11
k12room	8×10^{-6}	1/s	Dissolution rate constant for gypsum
DeH12	60 000	J/mol	Activation energy for gypsum dissolution
k13room	8×10^{-6}	1/s	Dissolution rate constant for $FeCO_3$
DeH13	60 000	J/mol	Activation energy for $FeCO_3$ dissolution
km13room	8×10^{-6}	1/s	Precipitation rate constant for $FeCO_3$
DeHm13	60 000	J/mol	Activation energy for $FeCO_3$ precipitation
k14room	2.2×10^{-9}	1/s	Dissolution rate constant for organic carbon
DeH14	60 000	J/mol	Activation energy for organic C dissolution

Parameter symbol	Value	Units	Parameter description
R0room	2×10^{-14}	mol dm^{-2} s^{-1}	Rate for transient dissolution of biotite
R1room	7.4×10^{-15}	mol dm^{-2} s^{-1}	Rate for steady-state dissolution of biotite
DeHR0	59 000	J/mol	Activation energy for R0
DeHR1	59 000	J/mol	Activation energy for R1
alfaGroom	1×10^{-6}	1/s	Time constant for dissolution of biotite
DeHalfaG	59 000	J/mol	Activation energy for alfaG
E0Aroom	−0.105	V_{SCE}	Standard potential for dissolution of Cu as $CuCl_2^-$
DeE0A	−0.00064	V/K	Linear temperature dependence coefficient for E0A
E0Croom	0.16	V_{SCE}	Standard potential for reduction of O_2
DeE0C	−0.00012	V/K	Linear temperature dependence coefficient for E0C
E0Droom	0.223	V_{SCE}	Standard potential for reduction of Cu^{2+}
DeE0D	0	V/K	Linear temperature dependence coefficient for E0D
E0Eroom	−1.005	V_{SCE}	Standard potential for reduction of HS^-
DeE0E	0	V/K	Linear temperature dependence coefficient for E0E
E0S12room	−0.747	V_{SCE}	Standard potential for dissolution of Cu to form Cu_2S
DeE0S12	0	V/K	Linear temperature dependence coefficient for E0S12
E0S3room	−0.747	V_{SCE}	Standard potential for dissolution of Cu to form Cu_2S
DeE0S3	0	V/K	Linear temperature dependence coefficient for E0S3
E0Froom	−0.764	V_{SCE}	Standard potential for the reduction of H_2O
DeE0F	−0.0019	V/K	Linear temperature dependence coefficient for E0F
E0_iF_cutoff	−0.5	V_{SCE}	Value of the corrosion potential (E_0 or E_{corr}) above which the current iF = 0
kAroom	0.00033	dm^4 mol^{-1} s^{-1}	Anodic rate constant
DeHA	60 000	J/mol	Activation energy for kA
kBBroom	0.00142	dm/s	Anodic rate constant
DeHBB	60 000	J/mol	Activation energy for kBB
kCroom	1.7×10^{-9}	dm/s	Cathodic rate constant
DeHC	60 000	J/mol	Activation energy for kC
kDroom	2×10^{-8}	dm/s	Cathodic rate constant
DeHD	45 000	J/mol	Activation energy for kD
kEroom	2×10^{-8}	dm/s	Cathodic rate constant
DeHE	60 000	J/mol	Activation energy for kE
kSroom	600	dm^4 mol^{-1} s^{-1}	Anodic rate constant
DeHS	60 000	J/mol	Activation energy for kS
kFroom	0	mol dm^{-2} s^{-1}	Cathodic rate constant
DeHF	31 200	J/mol	Activation energy for kF
c0R	0	mol·dm^{-3}	Boundary conc of O_2 at the RHS fracture
c6R	0.1131	mol·dm^{-3}	Boundary conc of Cl^- at the RHS fracture
c7R	−1	mol·dm^{-3}	Boundary conc of Fe(II) at the RHS fracture; c7R<0: saturation concentration used instead

Parameter symbol	Value	Units	Parameter description
c9R	0	$mol \cdot dm^{-3}$	Boundary conc of HS^- at the RHS fracture
c11R	0	$mol \cdot dm^{-3}$	Boundary conc of SO_4^{2-} at the RHS fracture
c12R	0	$mol \cdot dm^{-3}$	Boundary conc of H_2 at the RHS fracture
c16R	0	$mol \cdot dm^{-3}$	Boundary conc of Acetic Acid at the RHS fracture
rhoW	1.0204	kg/dm^3	Groundwater density at 0 °C
Rgas	8.314	J/(K·mol)	Gas constant
FaradC	96 485.33	C/mol	Faraday constant
alfaC	0.37	unitless	Transfer coefficient for the reduction of O_2
alfaD	0.5	unitless	Transfer coefficient for the reduction of Cu^{2+}
alfaE	0.5	unitless	Transfer coefficient for the reduction of HS^-
alfaS3	0.5	unitless	Transfer coefficient for the dissolution of Cu
alfaF	0.15	unitless	Transfer coefficient for the reduction of H_2O
m_iE	1	unitless	Exponent for c_9 in the expression for current i_E
n0	4	unitless	Number of electrons transferred in the reduction of O_2
nA	1	unitless	Number of electrons transferred in the oxidation of Cu
nD	1	unitless	Number of electrons transferred in the reduction of Cu^{2+}
nE	1	unitless	Number of electrons transferred in the reduction of HS^-
nS	1	unitless	Number of electrons transferred in the dissolution of Cu
nF	1	unitless	Number of electrons transferred in the cathodic reduction of H_2O
hkmin	0.6	unitless	Humidity value below which surface reaction rates are 0
hkmax	0.7	unitless	Humidity value above which surface reaction rates equal their maximum values (corresponding to saturated conditions)
t_hk1	0.2	a	Time (a) when surface humidity is still > hkmin; if t_hk1 < 0: humidity never passes through hkmin on desaturation
t_hk2	0.4	a	Time (a) when surface humidity is already < hkmin on desaturation
t_hk3	110	a	Time (a) when surface humidity is still < hkmin; if t_hk3 < 0: humidity never passes through hkmin on resaturation
t_hk4	120	a	Time (a) when surface humidity is already > hkmin on resaturation
FG	0.008841	$mol\ g_{cells}^{-1}$	Conversion factor for the number of moles of microbes per g of microbial cell material
FR	0.0221	$mol\ g_{cells}^{-1}$	Conversion factor for the number of moles of acetic acid per g of microbial cell material
a1B	0	$g_{cells}\ mol^{-1}$	Biomass production from acetate for organotrophic sulfate reduction
a2B	0	$g_{cells}\ mol^{-1}$	Biomass production from acetate for chemotrophic sulfate reduction
b1B	0	1/s	Death rate due to cell maintenance for organotrophic sulfate reduction
b2B	0	1/s	Death rate due to cell maintenance for chemotrophic sulfate reduction
v1max	1.3×10^{-6}	$mol\ g_{cells}^{-1}\ s^{-1}$	Specific Monod reaction rate of organotrophic sulfate reduction
v2max	5.7×10^{-7}	$mol\ g_{cells}^{-1}\ s^{-1}$	Specific Monod reaction rate of chemotrophic sulfate reduction
K111	1×10^{-5}	$mol \cdot dm^{-3}$	Half-saturation concentration for SO_4^{2-} for organotrophic sulfate reduction
K16	5×10^{-6}	$mol \cdot dm^{-3}$	Half-saturation concentration for acetic acid for organotrophic sulfate reduction
K112	1×10^{-5}	$mol \cdot dm^{-3}$	Half-saturation concentration for SO_4^{2-} for chemotrophic sulfate reduction
K12	4×10^{-6}	$mol \cdot dm^{-3}$	Half-saturation concentration for H_2 for chemotrophic sulfate reduction
KR1	0	unitless	Fraction of dead cells recycled into AA for organotrophic sulfate reduction

Parameter symbol	Value	Units	Parameter description
KR2	0	unitless	Fraction of dead cells recycled into AA for chemotrophic sulfahte reduction
Tmin1	278.15	K	Minimum temperature for organotrophic sulfate reducers
Topt1	298.15	K	Optimum temperature for organotrophic sulfate reducers
Tmax1	333.15	K	Maximum temperature for organotrophic sulfate reducers
DeHB1lTo	60 000	J/mol	Activation energy for organotrophic sulfate reducers at T < Topt1
DeHB1gTo	−60 000	J/mol	Activation energy for organotrophic sulfate reducers at T > Topt1
Tmin2	278.15	K	Minimum temperature for chemotrophic sulfate reducers
Topt2	298.15	K	Optimum temperature for chemotrophic sulfate reducers
Tmax2	333.15	K	Maximum temperature for chemotrophic sulfate reducers
DeHB2lTo	60 000	J/mol	Activation energy for chemotrophic sulfate reducers at T < Topt2
DeHB2gTo	−60000	J/mol	Activation energy for chemotrophic sulfate reducers at T > Topt2
rhsT_in	tempFract.txt	-	Name of file with RHS temperature b.c.: time (a) temp (°C)
H0	−0.072	unitless	If negative: Use LHS temperature b.c. file (lhsT_in); otherwise: use canister heat output file (heat_in) and scale it by H0
lhsT_in	tempCont.txt	-	Name of file with LHS temperature b.c.: time (a) temp (°C)
heat_in	HeatSource.txt	-	Name of the file with heat source: time (a) Output ($W \cdot dm^{-2}$)
initT_in	InitTemp.txt	-	Name of file with initial temperature: x (dm) temp (°C)

Arkitektkopia AB, Bromma, 2020

SKB is responsible for managing spent nuclear fuel and radioactive waste produced by the Swedish nuclear power plants such that man and the environment are protected in the near and distant future.

skb.se